

---

Sea Level Variations  
derived from Mass Conserving  
Finite Element Sea-Ice Ocean Model

Study of Major Contributions to Sea Level Change  
in the Recent Past

---

Sandra-Esther Brunnabend



Universität Bremen 2010

---

Sea Level Variations  
derived from Mass Conserving  
Finite Element Sea-Ice Ocean Model

Study of Major Contributions to Sea Level Change  
in the Recent Past

---

Vom Fachbereich für Physik und Elektrotechnik  
der Universität Bremen

zur Erlangung des akademischen Grades eines  
Doktor der Naturwissenschaften (Dr. rer. nat.)  
genehmigte Dissertation

von

Sandra-Esther Brunnabend M.Sc. (ESPACE)  
aus Bremerhaven

1. Gutachter: Prof. Dr. Peter Lemke
2. Gutachter: Prof. Dr.-Ing. Jürgen Kusche

Eingereicht am: 02. Dezember 2010  
Tag des Promotionskolloquiums: 17. Februar 2011

# Abstract

During the last century sea level rise strongly increased compared to sea level change in the last 2000 years. The present study investigates global and regional sea level change, simulated with the finite element sea-ice ocean model (FESOM). The major goal is to separate sea level change into steric and eustatic contributions and to estimate the influence of Greenland and Antarctic ice sheet melt on global and regional sea level.

Modeled steric height variations show realistic regional geophysical patterns compared with steric height variations derived from altimetry measurements and GRACE. Compared to the time before the 1990's, an increased global trend in steric sea level rise is found in estimates derived from the model and from satellite measurements. Modeled ocean mass exhibits reasonable spatial structures. However, the trend in the global model mean cannot be trusted in FESOM as it strongly depends on the mass budget of the model, which is determined by uncertain mass fluxes. To account for this, global mean ocean mass variations need to be optimized to realistic values. To this end results from GRACE in combination with GPS data is used.

Greenland and Antarctic ice sheet melting influence the global sea level mainly through the additional mass. The eustatic sea level rises by about 0.3 mm/yr for 100 Gt/yr of melt water. Additionally, the fresh water causes local steric variations in sea level that are transported farther by ocean currents. The ice sheet mass loss yields a decrease in gravitational attraction causing a sea level fall near the source of mass loss but also to a slight increase at long distance. This effect is computed for the Greenland ice sheet mass loss using Green's functions. It leads to a decreased sea level near the Greenland coast and to a slightly increased sea level in the Southern Ocean. The effect of different melting scenarios is investigated.

# Zusammenfassung

Während des letzten Jahrhunderts ist der Meeresspiegel stärker angestiegen als in den vergangenen 2000 Jahren. Diese Studie untersucht globale und regionale Veränderungen des Meeresspiegels, die mit dem Finite-Elemente-Meereis-Ozean-Modell (FESOM) simuliert werden. Das Hauptziel ist es, sterische und eustatische Beiträge in den Meeresspiegeländerungen zu separieren. Ausserdem wird der Einfluss des Schmelzwassers der beiden grossen Eisschilde auf Grönland und der Antarktis auf den regionalen Meeresspiegel untersucht.

Modellierte sterische Höhenänderungen zeigen realistische regionale geophysikalische Strukturen, ähnlich denen, die aus Altimetriedaten und GRACE abgeleitet worden sind. Verglichen mit der Zeit vor den 1990er Jahren, ist ein erhöhter Trend im globalen sterischen Meeresspiegelanstieg sowohl in den Modellergebnissen als auch in den Satellitenmessungen zu beobachten. Modellierte Ozeanmassenvariationen zeigen angemessene räumliche Strukturen. Dem Trend der globalen mittleren Massenvariationen ist normalerweise mit einem grossen Fehler versehen, da dieser stark von der Massenbilanz des Modells abhängt, die durch unsichere Massenflüsse bestimmt ist. Daher muss die Beschreibung der globalen mittleren Massenvariationen optimiert werden. Hierfür werden Ergebnisse von GRACE in Kombination mit GPS Daten verwendet.

Das Schmelzwasser der Eisschilde in Grönland und der Antarktis beeinflusst den globalen Meeresspiegel. Die Simulationen zeigen einen eustatischen Meeresspiegelanstieg von etwa 0,3 mm pro Jahr, wenn Schmelzwasser in Höhe von 100 Gt pro Jahr in den Ozean fliessen. Das zusätzliche Süswasser verursacht lokale sterische Variationen des Meeresspiegels, die durch die Meeresströmungen in weiter entfernte Regionen transportiert werden. Ausserdem verursacht der Massenverlust eine Verringerung der Anziehungskraft des Eisschildes. Dies führt zu einem verringerten Meeresspiegel in der Nähe des Eisschildes und zu einer leichten Erhöhung in weiter entfernten Regionen. Dieser Effekt wird für die Grönlandeisschmelze mit Hilfe von Green's Funktionen berechnet. Er verursacht einen Meeresspiegelanstieg in der Nähe der Grönländischen Küste und einem leichten Anstieg im

Südozean. Der Effekt von verschiedenen Schmelzszenarien wird untersucht.

# Contents

|          |  |           |
|----------|--|-----------|
| <b>1</b> | <b>Introduction</b>  | <b>1</b>  |
| <b>2</b> | <b>Model Description</b>   | <b>6</b>  |
| 2.1      | Method of Finite Elements . . . . .                              | 6         |
| 2.2      | Finite Element Sea-Ice Ocean Model . . . . .                     | 7         |
| 2.2.1    | Finite Element Sea-Ice Model . . . . .                           | 7         |
| 2.2.2    | Finite Element Ocean Model . . . . .                             | 8         |
| 2.2.3    | Coupling . . . . .   | 10        |
| 2.3      | Subgrid-Scale Processes . . . . .                                | 12        |
| 2.4      | Surface Heat Budget . . . . .                                    | 13        |
| 2.5      | Sea Level Equation . . . . .                                     | 14        |
| 2.6      | Spatial Discretization . . . . .                                 | 15        |
| 2.7      | Atmospheric Forcing . . . . .                                    | 16        |
| 2.7.1    | NCEP/NCAR Data . . . . .   | 18        |
| 2.7.2    | ERA40 Data . . . . .   | 18        |
| 2.7.3    | Operational ECMWF data . . . . .                                 | 19        |
| 2.7.4    | ERA Interim . . . . .  | 20        |
| 2.7.5    | GPCP Precipitation . . . . .                                     | 21        |
| 2.7.6    | Reference Model Simulation and Sensitivity Experiments . . . . . | 22        |
| <b>3</b> | <b>Variations of Ocean Mass</b>                                  | <b>23</b> |
| 3.1      | Land-Ocean Mass Exchange . . . . .                               | 24        |
| 3.2      | Mass Exchange between Atmosphere and Ocean . . . . .             | 27        |
| 3.3      | Mass Balance in FESOM . . . . .                                  | 30        |
| 3.4      | Weekly Ocean Bottom Pressure Anomalies . . . . .                 | 33        |
| 3.5      | Error Estimation of Modeled Ocean Mass Variations . . . . .      | 35        |
| 3.5.1    | Influence of Spatial Discretization . . . . .                    | 36        |

---

|          |  |            |
|----------|--|------------|
| 3.5.2    | FESOM and the Large Scale Geostrophic Model . . . . .                  | 38         |
| 3.5.3    | Influence of Atmospheric Forcing . . . . .                             | 40         |
| 3.6      | Gravity Recovery and Climate Experiment . . . . .                      | 42         |
| 3.7      | Joint Inversion . . . . .  | 48         |
| 3.7.1    | Impacts of modeled OBP Error to the Inversion . . . . .                | 49         |
| 3.7.2    | Global Mass Correction derived from Inversion . . . . .                | 50         |
| 3.8      | Ocean Bottom Pressure Recorders . . . . .                              | 53         |
| 3.8.1    | Correlation with OBPR . . . . .  | 54         |
| 3.8.2    | OBPR for Regional Mean Mass Variations . . . . .                       | 60         |
| 3.8.3    | Validation of modeled OBP error . . . . .                              | 66         |
| 3.9      | Conclusion . . . . .   | 68         |
| <b>4</b> | <b>Sea Surface Topography and Steric Sea Level</b>                     | <b>70</b>  |
| 4.1      | Modeled Surface Heat Flux . . . . .                                    | 71         |
| 4.2      | Surface Heat Flux Correction . . . . .                                 | 75         |
| 4.3      | Modeled Sea Surface Topography . . . . .                               | 76         |
| 4.4      | Variations in Sea Level . . . . .                                      | 78         |
| 4.5      | Modeled Steric Height Variations . . . . .                             | 81         |
| 4.6      | Satellite Altimetry . . . . .  | 83         |
| 4.7      | Multi-Mission Altimetry Measurements . . . . .                         | 85         |
| 4.8      | Identification of Modeled Steric Height Changes in Altimetry . . . . . | 86         |
| 4.9      | Conclusion . . . . .   | 88         |
| <b>5</b> | <b>Sea Level Change due to Ice Sheet Melting</b>                       | <b>90</b>  |
| 5.1      | Definition of Ice sheets . . . . .                                     | 91         |
| 5.2      | Loading and Self Attraction . . . . .                                  | 92         |
| 5.3      | Melting of the Antarctic Ice sheet . . . . .                           | 94         |
| 5.4      | Mass Variations of the Greenland Ice Sheet . . . . .                   | 97         |
| 5.4.1    | Constant Melt Rates . . . . .  | 99         |
| 5.4.2    | Sea Level Evolution in Coastal Regions . . . . .                       | 104        |
| 5.4.3    | Varying Melt Rates . . . . .   | 105        |
| 5.5      | Conclusion . . . . .   | 108        |
| <b>6</b> | <b>Summary and Outlook</b>   | <b>111</b> |
|          | <b>Bibliography</b>  | <b>118</b> |

---

|   |            |
|---|------------|
| <b>Appendix</b>   | <b>133</b> |
| A List of Acronyms . . . . .  | 133        |
| B Global Positioning System . . . . .                                 | 135        |
| C Comparison of OBPR and FESOM Timeseries . . . . .                   | 136        |
| D Comparison of time series from OBPR and Inverse Solutions . . . . . | 149        |
| E Comparison of time series from OBPR and GRACE Solutions . . . . .   | 162        |
| F Comparison of time series from OBPR and corrected FESOM . . . . .   | 175        |

# List of Figures

|      |   |    |
|------|---|----|
| 1.1  | Satellite measurements and ocean modelling . . . . .                            | 5  |
| 2.1  | Spatial discretization and bottom topography . . . . .                          | 15 |
| 2.2  | Accumulation of water fluxes . . . . .  | 20 |
| 2.3  | Global Sum of GPCP Precipitation . . . . .                                      | 21 |
| 3.1  | River runoff . . . . .  | 25 |
| 3.2  | Global river runoff . . . . .   | 26 |
| 3.3  | Difference in SSH due to different river runoff . . . . .                       | 27 |
| 3.4  | Global integral of precipitation minus evaporation . . . . .                    | 28 |
| 3.5  | Ten year mean precipitation . . . . .   | 29 |
| 3.6  | Correlation of 10yr mean precipitation to GPCP . . . . .                        | 30 |
| 3.7  | Ratio of 10yr mean precipitation from GPCP and ECMWF . . . . .                  | 30 |
| 3.8  | Global fresh water flux . . . . .   | 31 |
| 3.9  | Variations of global mean ocean mass . . . . .                                  | 32 |
| 3.10 | Variations in ocean bottom pressure, if the heat flux is set to 0 . . . . .     | 33 |
| 3.11 | Global mean OBP variations modeled with FESOM . . . . .                         | 34 |
| 3.12 | Weekly mean pressure of ocean and atmosphere . . . . .                          | 35 |
| 3.13 | Monthly and weekly mean OBP anomalies . . . . .                                 | 36 |
| 3.14 | First EOF of difference and its principle component . . . . .                   | 37 |
| 3.15 | Volume transport through Drake Passage . . . . .                                | 37 |
| 3.16 | Global mean of modeled OBP using different grids . . . . .                      | 38 |
| 3.17 | Global mean variations of modeled OBP simulated by FESOM and LSG . . . . .      | 39 |
| 3.18 | OBP anomalies derived with LSG and FESOM . . . . .                              | 39 |
| 3.19 | Regional trends of OBP anomalies . . . . .                                      | 40 |
| 3.20 | Mean ocean mass variations modeled with different atmospheric forcing . . . . . | 41 |
| 3.21 | Estimated error of OBP anomalies . . . . .                                      | 42 |
| 3.22 | Weekly GRACE background models . . . . .  | 45 |

---

|      |   |    |
|------|---|----|
| 3.23 | Global mean ocean mass variations derived with GRACE . . . . .                      | 46 |
| 3.24 | Correlation and STD of OBP anomalies from GRACE and FESOM . . . . .                 | 47 |
| 3.25 | Weekly mean global ocean mass variations . . . . .                                  | 49 |
| 3.26 | Inverse solutions . . . . .   | 51 |
| 3.27 | Ocean Mass Correction . . . . .   | 52 |
| 3.28 | Comparison of ocean bottom pressure time series with OBPR . . . . .                 | 54 |
| 3.29 | Correlation with OBPR . . . . .   | 58 |
| 3.30 | Histogram of differences between correlations with OBPR and OBP estimates . . . . . | 59 |
| 3.31 | Locations of OBPR . . . . .   | 60 |
| 3.32 | Ocean bottom pressure time series of North Polar Region . . . . .                   | 61 |
| 3.33 | Ocean bottom pressure variations in the Arctic Ocean . . . . .                      | 62 |
| 3.34 | Mean ocean bottom pressure variations at the Kuroshio current . . . . .             | 62 |
| 3.35 | Mean ocean bottom pressure variations in the Mid Atlantic Ocean . . . . .           | 63 |
| 3.36 | Mean ocean bottom pressure variations in the Fram Strait . . . . .                  | 63 |
| 3.37 | Mean ocean bottom pressure variations in the ACC . . . . .                          | 64 |
| 3.38 | Mean ocean bottom pressure variations near Kerguelen Islands . . . . .              | 65 |
| 3.39 | Mean ocean bottom pressure variations in the Drake Passage . . . . .                | 65 |
| 3.40 | Mean ocean bottom pressure variations in the North Pacific . . . . .                | 66 |
| 3.41 | Validation of modeled OBP error using OBPR measurements . . . . .                   | 67 |
| 4.1  | Modeled ten year mean surface heat fluxes for the open ocean . . . . .              | 72 |
| 4.2  | Modeled ten year mean surface heat fluxes for the ice covered ocean . . . . .       | 73 |
| 4.3  | Ten year mean net heat flux . . . . .   | 74 |
| 4.4  | Global yearly mean net heat flux . . . . .  | 75 |
| 4.5  | Tangent hyperbolic function . . . . .   | 76 |
| 4.6  | Mean sea surface topography of year 2007 . . . . .                                  | 77 |
| 4.7  | Modeled mean dynamic topography and horizontal velocity . . . . .                   | 78 |
| 4.8  | Mean dynamic topography . . . . .   | 79 |
| 4.9  | Difference of mean dynamic topography . . . . .                                     | 80 |
| 4.10 | Variations of global mean sea level . . . . .                                       | 81 |
| 4.11 | Trends of regional sea level change . . . . .                                       | 81 |
| 4.12 | El Niño-Southern Oscillation . . . . .  | 82 |
| 4.13 | Monthly variations of modeled steric sea level . . . . .                            | 83 |
| 4.14 | Modeled steric height anomalies . . . . .   | 83 |
| 4.15 | Altimetry . . . . .   | 84 |
| 4.16 | Mean sea surface topography derived from altimetry . . . . .                        | 86 |

---

|      |   |     |
|------|---|-----|
| 4.17 | Weekly steric height anomalies (GRACE) . . . . .                              | 87  |
| 4.18 | Weekly steric height anomalies (inversion) . . . . .                          | 87  |
| 4.19 | Weekly global mean steric height variations . . . . .                         | 88  |
| 5.1  | Definition of ice sheets . . . . .  | 91  |
| 5.2  | Antarctic ice sheet and bedrock elevation . . . . .                           | 94  |
| 5.3  | Relative sea level change due to 100Gt/yr West Antarctic ice sheet melting    | 96  |
| 5.4  | Fresh water inflow due to melting of the West Antarctic ice sheet . . . . .   | 97  |
| 5.5  | Temperature and salinity change due to 100 Gt/yr Antarctic ice sheet melt     | 98  |
| 5.6  | Greenland ice sheet and bedrock elevation . . . . .                           | 99  |
| 5.7  | Fresh water inflow due to Greenland ice sheet melting . . . . .               | 99  |
| 5.8  | Response of global mean sea level to melting of the Greenland (GIS) . . . . . | 100 |
| 5.9  | Relative sea level change due to Greenland ice sheet melting . . . . .        | 101 |
| 5.10 | Temperature and salinity change due to 200 Gt/yr Greenland ice sheet melt     | 103 |
| 5.11 | Regional sea level change due to Greenland ice sheet melting . . . . .        | 104 |
| 5.12 | Local sea level change . . . . .  | 105 |
| 5.13 | Sea level change at the coast of the North Sea . . . . .                      | 106 |
| 5.14 | Total Greenland ice sheet melt and fresh water flux in 2007 . . . . .         | 107 |
| 5.15 | Response of global mean sea level to melt in Greenland . . . . .              | 107 |
| 5.16 | Comparison of steric height variations and surface net heat flux . . . . .    | 108 |
| 5.17 | Relative sea level due to Greenland ice sheet melting of 161 Gt/yr . . . . .  | 109 |
| 5.18 | Relative sea level change due to the gravitational effect . . . . .           | 110 |
| 6.1  | Global mean sea level . . . . .   | 112 |

# List of Tables

|     |   |     |
|-----|---|-----|
| 2.1 | Albedo . . . . .                                    | 13  |
| 2.2 | z-Levels . . . . .                                  | 15  |
| 2.3 | Atmospheric datasets . . . . .                      | 17  |
| 3.1 | GRACE Solutions . . . . .                           | 43  |
| 3.2 | OBPR Correlation . . . . .                          | 56  |
| 3.3 | Correlations at the Kuroshio (KESS) array . . . . . | 57  |
| 4.1 | Mean Dynamic Topography . . . . .                   | 77  |
| 5.1 | Antarctic Ice Mass Balance . . . . .                | 95  |
| 5.2 | Greenland Ice Mass Balance . . . . .                | 100 |

# Chapter 1

## Introduction

In the last century the global sea level has risen substantially as humans involuntarily intervened in the global climate system. This has become a serious problem for civilization as various cities where many people live are located in coastal regions. An increase of about 1-2 m would have strong impacts on humanity, as these cities would be flooded. Industrialization has strongly influenced the global climate for example by the CO<sub>2</sub> emissions supporting the absorption of heat. As a consequence the ocean gains more heat. The resulting thermal expansion leads to an increase in global mean sea level. If a sea water column of 1000 m warms by 0.1°C the water column expands by 1 to 2 cm (Church et al., 2010). Nowadays, thermal expansion is a major contributor to sea level rise and important for regional sea level change. From 1995 to 1998 Levitus et al. (2005) observed an increase in ocean temperature of 0.037°C in the upper 3000 m not considering temperature biases that might occur from using different instrumentation. Based on this data, Church et al. (2001), Antonov et al. (2005), and Ishii et al. (2006) reported a rise in steric sea level between 0.3 and 0.4 mm/yr for the same time period (1955-2003). In the upper ocean (to about 700 m depth) steric sea level rise of about 0.4 mm/yr have been observed for the period from 1955 to 2003. Its trend has accelerated to about 1.6 mm/yr in the last 10 years of the investigation period (Willis et al., 2004; Levitus et al., 2005; Ishii et al., 2006; Bindoff et al., 2007).

Steric sea level is also varying due to salinity variations (halosteric), but its contribution to global sea level is much smaller than from thermosteric effects. It is observed as  $0.05 \pm 0.02$  mm/yr for the years 1957 to 1994 and to  $0.04 \pm 0.01$  mm/yr for the years 1955 to 2003 (Antonov et al., 2002; Ishii et al., 2006). Regionally, it is an important factor for the freshening of the ocean, especially in the Polar Regions with sea-ice cover.

Temperature and salinity variations in the upper 2000 m of the ocean can be measured

with ARGO Array of floats, which are globally distributed over the ocean. About 100,000 new temperature and salinity profiles become available every year. However, investigations suffer from the sparse observational data in greater depth yielding to an underestimation of steric height change. Wenzel and Schröter (2007b) showed that the deep ocean below 500 m depth similarly contributes to steric sea level as the upper ocean. By assimilation of different data sets in an ocean model they derive substantial warming below 2000 m depth.

Sea level also changes due to variations in ocean mass, which result from mass exchange between ocean and atmosphere via precipitation and evaporation. Also fresh water is introduced by river runoff and groundwater discharge. The sum of these contributions shows a seasonal signal resulting from the water storage in the land hydrology. In addition, fresh water from continental ice sheets and glaciers flows into the ocean, if melting of the land ice mass occurs. It increases global mean sea level proportional to the amount of melting, which causes regional steric variations in sea level, mainly due to the freshening and the modified mixing of ocean water. For example, the melting of the Greenland ice sheet leads to a freshening of the North Atlantic, causing modifications in ocean circulation. Also the gravitational effect of the reduced ice mass on Greenland leads to a decreased sea level near the source of melting, but to an increase at farther regions (Mitrovica et al., 2001). Near the Greenland ice sheet the total sea level would fall because the gravitational effect due to the mass loss of the ice sheet becomes larger than the amount of additional ocean mass and the changes in its density. This is dependent on the amount of melting.

The Greenland ice sheet is subject to increased melting in the last decade. Several studies, such as Luthcke et al. (2006), van den Broeke et al. (2009), Velicogna (2009), and Wu et al. (2010), observed melt rates between 100 Gt/yr in the beginning of the 21st century, and 200 Gt/yr during the last few years. A melt rate of 100 Gt/yr is equivalent to an increase in global mean sea level of about 0.3 mm/yr. If the whole mass of the Greenland ice sheet would be added to the ocean, global sea level would rise by about 7 m, not accounting for steric effects (Lemke et al., 2007).

On the Antarctic continent the largest ice sheet is found. In comparison to the Greenland ice sheet, it is more stable. Only, at coastal regions and in the West Antarctic ice losses occur, which amount to about 100 Gt/yr as shown for example by Velicogna (2009), Gunter et al. (2009), and Wu et al. (2010). The melt of sea-ice, which is located in the Arctic and Southern Oceans is not increasing global mean sea level as no additional mass is introduced. But significant steric effects occur locally, due to the freshening, especially in the Arctic Ocean, where strong melt happened in the last years. In the near future, the CryoSat mission will improve the capability to measure the extent and thickness of sea-ice

and continental ice sheets.

To estimate future changes in sea level, it is important to understand the behavior of the ocean in the recent past. Before global measurement techniques became available, sea level change has mostly been studied with tide gauges. In the recent past, research in the field of sea level variations has changed, as different space geodetic techniques have been developed, such as the Gravity Recovery and Climate Experiment (GRACE) and satellite altimetry, measuring the change in ocean mass and variations of the geometric shape of the Earth. The GRACE satellite mission enables the scientific community to directly estimate time-variable ocean mass on a global scale (Chambers et al., 2004; Ilk et al., 2005; Chambers, 2006; Macrander et al., 2009). Mass estimates are operationally provided by the three centers that form the GRACE science data system (GFZ, CSR, JPL) and a few others (Bonn University, GRGS Toulouse, TU Delft). They are using different processing techniques and different temporal resolution, which range from daily to monthly mass estimates. For most applications the solutions have to be filtered because of (anisotropic) errors. Different filter techniques have been applied, such as the Gauss filter (Wahr and Molenaar, 1998), the pattern filter (Böning et al., 2008), or the de-correlation filter (Kusche, 2007). The major disadvantage of filtering is that it reduces not only the aliasing effects but also the signals under consideration.

Locally, measurements of ocean mass variation at many locations from ocean bottom pressure recorders (OBPR) are available nowadays. These in-situ measurements are useful to validate measurements from satellites and model simulations. GRACE solutions already fit reasonably well with in-situ measurements from OBPR (Rietbroek et al., 2006), (Böning et al., 2008), (Böning, 2009) and (Macrander et al., 2009) in the polar regions (with correlations mostly higher than 0.5) (Macrander et al., 2009). In many other regions the correlation between GRACE and OBPR measurements is weaker. A particular problem is geocenter motion, which cannot be measured by GRACE as the two satellites fly with respect to center of mass of the Earth system. On the other hand the total ocean mass and thus OBP is sensitive to geocenter movements. To solve this issue and to increase the correlation of ocean mass variations with OBPR, different studies combining GRACE gravity solutions with other terrestrial data sets have been performed. For example, Rietbroek et al. (2009) combined GRACE gravity data, GPS site displacements and ocean bottom pressure (OBP) modeled with FESOM to estimate surface loading with higher accuracy than GRACE only estimates, including geocenter motion.

Altimetry enables to measure the sea level. An increased trend sea level rise (3.1 mm/yr) has been estimated by Bindoff et al. (2007) between the years 1993 and 2003. The relative contribution of the different sources to the trend is subject of current research.

Church et al. (2001) suggest that about 60% originates from thermosteric effects. The different estimated melt rates between 100 and 200 Gt/yr, in case of Greenland ice mass loss, induce an uncertainty range of 0.3 mm/yr. However, when measuring global ocean mass variations with GRACE, no trend is observed, which can be directly referred to land ice mass change yielding to assumptions that current sea level change originates from steric effects. On the other hand current studies show an decreased trend in steric sea level rise (Cazenave et al., 2008). Trends in GRACE must be corrected for glacial isostatic adjustment (GIA) which introduces a substantial uncertainty (Wu et al., 2010; Mitrovica et al., 2007). Therefore, the quantities of the different contributions are still associated with large error bars.

The aim of this study is to investigate changes in global and regional sea level caused by the major contributions through heat and mass variations. This includes sea level change due to changes of inflow as well as temperature and salinity variations. In addition, the response of the North Atlantic Ocean to melting of the Greenland ice sheet is investigated in more detail. In Chapter 3 variations of ocean mass are estimated, using the finite element sea-ice ocean model (FESOM), which is presented in Chapter 2. Here, ocean bottom pressure anomalies are simulated that can be easily converted to ocean mass. Results are compared with another ocean model, with in-situ bottom pressure measurements, and GRACE measurements (Figure 1.1). The atmosphere strongly influences ocean circulation. Hence, the error of modeled OBP is estimated by alternative model simulations, using different atmospheric forcing fields. FESOM calculates the OBP and simultaneously estimates the error of the calculation. Both fields, pressure and error estimate, vary in space and time. The estimated error of modeled OBP strongly influences a combined inversion of GRACE gravity data, GPS site displacements and modeled OBP (Rietbroek et al., 2009). In Chapter 4 the global sea surface topography as well as sea level change due to steric variations of the ocean are investigated. The results are validated using dynamic sea surface topography from multi-mission altimetry measurements, which are provided by DGFI München (Bosch and Savcenko, 2008). To compute steric height variations from the altimetry measurements different ocean mass data sets, like GRACE gravity or the results of the joint inversion (Rietbroek et al., 2009) are used. In Chapter 5, the influence of ice sheet melting in Greenland on the sea level is analyzed. In addition, variations in sea level caused by mass loss of the West Antarctic ice sheet are presented. Finally the results are summarized and discussed in Chapter 6.

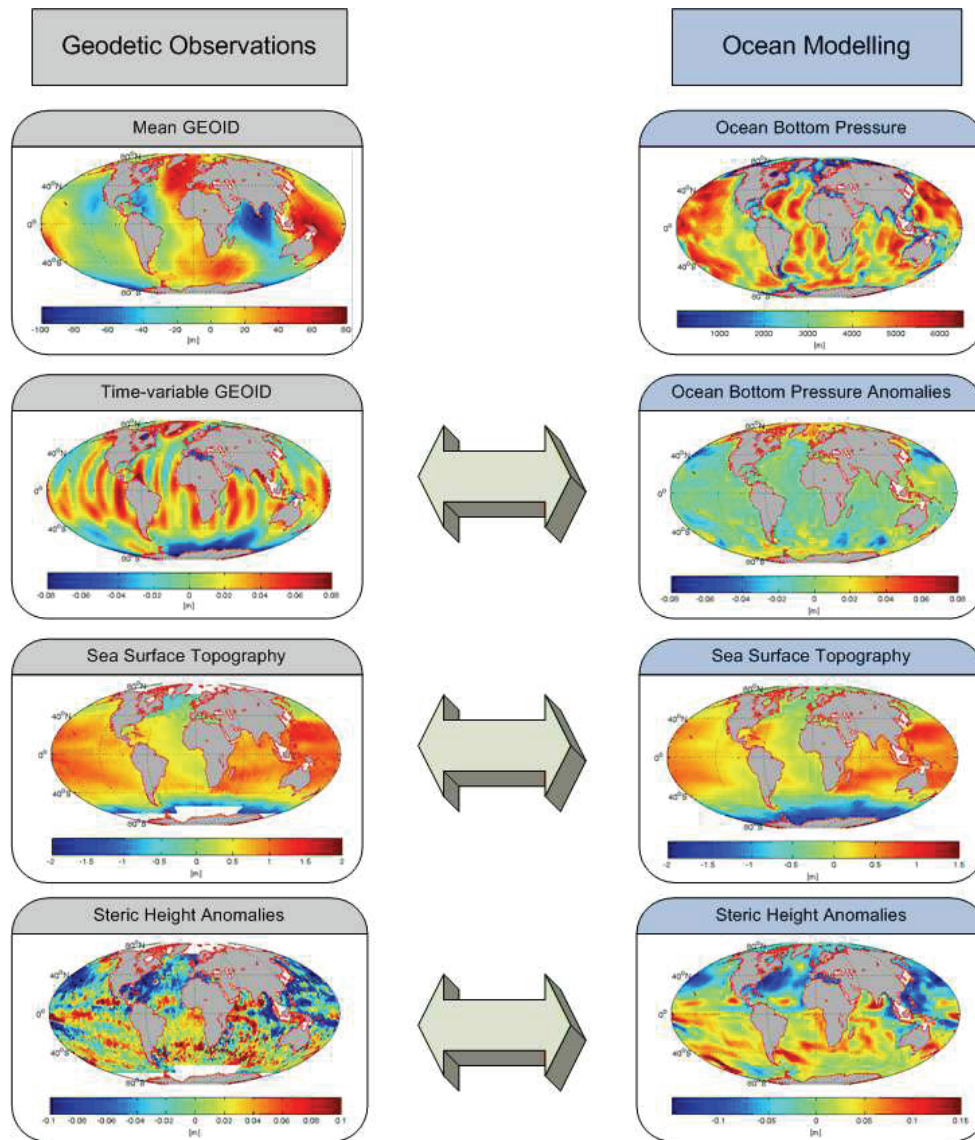


Figure 1.1: Comparison between estimates from satellite measurements (left) and ocean modelling (right)

# Chapter 2

## Model Description

The finite element sea-ice ocean model (FESOM, Timmermann et al. (2009), Böning (2009)) is used to simulate ocean mass redistribution and steric sea level change. Simulations are performed on a global and regular grid. As the name already suggest the model applies the finite element method, which is described in the following.

### 2.1 Method of Finite Elements

The finite element (FE) method first came up with Galerkin (1915). It is a numerical technique to solve partial differential equations of complex systems like the ocean, where small-scale geometries, such as islands, sea mountains, or steep slopes are important to be taken into account to realistically describe the state of the ocean. First, the method splits the region of interest into a number of finite small regions, for example triangles for two dimensions or tetrahedrons in case of three dimensions. Using FE to model the ocean state on an unstructured grid is possible, whereby small features in the ocean and regions of scientific interest can be discretized with a higher spatial resolution than other regions. The resulting elements can then be described by a finite amount of parameters.

Basis functions are defined within the elements and substituted into the differential equation to be solved. Together with the initial and boundary conditions, a linear system of equations is defined that is generally solved numerically is defined. Here, an advantage is that the system of equations can be solved for each element because the basis functions are zero outside the cluster of neighbors. The numerical solution generally represents a good approximation to the solution of the differential equations. The size of the system of equations to be solved depends on the amount of finite elements. With increasing amount of nodes and increasing complexity of the possibly unstructured grid the computational

cost becomes higher and different approaches like parallelization have to be implemented to achieve affordable costs.

## 2.2 Finite Element Sea-Ice Ocean Model

The finite element sea-ice ocean model (FESOM, Timmermann et al. (2009)) couples the finite element ocean model (FEOM) (Danilov et al., 2004) and (Danilov et al., 2005), which solves the hydrostatic primitive equations, with the finite element sea-ice model (FESIM, Danilov and Yakovlev (2003)).

Various aspects of the FESOM model have been described by Timmermann et al. (2009), Böning (2009), Böning et al. (2008), and Rollenhagen (2008). Beside the model basics, this section concentrates on aspects that are important for this study, such as the treatment of surface heat and fresh water fluxes and the sea level equation.

### 2.2.1 Finite Element Sea-Ice Model

The sea-ice model FESIM is a dynamic-thermodynamic model, which simulates mean sea-ice concentration and thickness as well as velocities of sea-ice drift. It mainly uses methods of Parkinson and Washington (1979), Hibler III (1979), Lemke et al. (1990), and Owens and Lemke (1990). Within a grid cell the surface can be either sea-ice, open ocean, or only partly sea-ice, where the areal proportion of sea-ice in a grid cell is described by the sea-ice concentration. Sea-ice thickness is defined as mean thickness of sea-ice, which is assumed as evenly distributed over the grid cell. The mean sea-ice thickness or sea-ice concentration may vary due to melting or freezing. Also sea-ice drift is a possible source of variations in sea-ice. It is determined by wind stress, oceanic currents, sea surface tilt and internal forces in the sea-ice. The model includes a snow pack on top of the sea-ice and a possible snow-ice conversion. It does not consider internal heat storage and blowing snow (Timmermann et al., 2009). The prognostic equations for sea-ice concentration ( $A$ ), sea-ice thickness ( $h$ ) and snow thickness ( $h_s$ ) are described by

$$\frac{\partial h}{\partial t} + \nabla \cdot (\vec{u}_i h) = S_h \quad (2.1)$$

$$\frac{\partial h_s}{\partial t} + \nabla \cdot (\vec{u}_i h_s) = S_{h_s} \quad (2.2)$$

$$\frac{\partial A}{\partial t} + \nabla \cdot (\vec{u}_i A) = S_A \text{ with } (0 \leq A \leq 1) \quad (2.3)$$

In these equations the first term describes the regional change over time. The second term defines the effect of advection. Ice and snow drift velocity are determined from the momentum balance

$$m \left( \frac{\partial}{\partial t} f(\vec{k}x) \right) \vec{u} = A(\vec{\tau}_{ai} - \vec{\tau}_{io}) + \vec{F} - mg\nabla\eta \quad (2.4)$$

which approximates large scale sea-ice as a continuum in two dimensions and uses the scaling of ice/ocean stresses suggested by Connolley et al. (2004):

$$\vec{\tau}_{io} = c_{d,io}\rho_o(\vec{u} - \vec{u}_w)|\vec{u} - \vec{u}_w|$$

The mass of sea-ice and snow per unit area is defined by  $m$ . The drift velocity is  $\vec{u}$  and the mean density of ocean water is  $\rho_o = 1027 \text{ kg/m}^3$ . The mean density of sea-ice is  $910 \text{ kg/m}^3$  and for snow  $290 \text{ kg/m}^3$ . The gravitational acceleration  $g = 9.806 \text{ m/s}^2$ ,  $\vec{\tau}_{ai}$  is the wind stress,  $c_{d,io}$  the sea-ice/snow drag coefficient, and  $\vec{F}$  the contribution from internal stress. The wind stress at the boundary of atmosphere and sea-ice is denoted as  $\vec{\tau}_{ai}$ , and the surface stress between ocean and ice is denoted by  $\vec{\tau}_{io}$ . The last term on the right hand side of equation 2.4 describes the effect of the sea surface tilt.

## 2.2.2 Finite Element Ocean Model

The FEOM model is a hydrostatic ocean circulation model with a spherical geometry and solves the primitive equations. Partial differential equations are defined to represent the prognostic variables potential temperature, salinity, and horizontal velocity, here formulated in Cartesian coordinates. The temporal evolution of these variables are described by the momentum equations, the continuity equation, the equation for salinity and potential temperature balance, and the non-linear equation of state:

$$\frac{\partial u}{\partial t} + \vec{u} \cdot \nabla u - fv = -\frac{\partial \Phi}{\partial x} + F^u + D^u \quad (2.5)$$

$$\frac{\partial v}{\partial t} + \vec{u} \cdot \nabla v + fu = -\frac{\partial \Phi}{\partial y} + F^v + D^v \quad (2.6)$$

$$0 = -\frac{\partial \Phi}{\partial z} - \frac{\rho g}{\rho_o} \quad (2.7)$$

The momentum equations 2.5 and 2.6 (horizontal momentum balance) describe the horizontal velocities  $u$  and  $v$  in the direction of the horizontal coordinates  $x$  and  $y$ . Here, the

first term describes the local temporal change, and the second term the variation of the velocity field ( $\vec{u} = (u, v)$ ) due to advection. The third term on the left hand side defines the Coriolis force where  $f$  represents the Coriolis parameter ( $f = \frac{4\pi}{86400} \cdot \sin \phi$  with  $\phi = \text{latitude}$ ). The right hand side includes the pressure gradient as a function of the dynamic pressure ( $\Phi = \frac{P}{\rho_0}$ ), and the force and dissipation ( $F$  and  $D$ ) associated with turbulent flows. These equations include the Boussinesq approximation, where density anomalies are only considered in the buoyancy term of the vertical momentum equation. The vertical momentum balance in the hydrostatic approximation converts to the hydrostatic balance as defined by equation 2.7, where  $\rho$  is the in-situ density. The vertical velocity is computed from the continuity equation

$$\frac{\partial u}{\partial x} + \frac{\partial v}{\partial y} + \frac{\partial w}{\partial z} = 0 \quad (2.8)$$

which describes ocean water as incompressible fluid. The potential temperature  $T$  and salinity  $S$  balance equations

$$\frac{\partial T}{\partial t} + \vec{u} \cdot \nabla T = F^T + D^T \quad (2.9)$$

$$\frac{\partial S}{\partial t} + \vec{u} \cdot \nabla S = F^S + D^S \quad (2.10)$$

describe the dynamics of  $T$  and  $S$ , which includes advection, as well as local sources ( $F$ ) and the diffusion ( $D$ ) due to turbulent flows. The non-linear equation of state

$$\rho = \rho(T, S, z) \quad (2.11)$$

defines the in-situ density as a function of potential temperature, salinity and depth.

The Boussinesq approximation used here simplifies the continuity equation from

$$\frac{\partial \rho}{\partial t} + \nabla \cdot (\rho \mathbf{v}) = 0 \quad (2.12)$$

to

$$\nabla \cdot (\mathbf{v}) = 0 \quad (2.13)$$

with  $\mathbf{v} = (u, v, w)$ ; c.f. eq. 2.8, which leads to a conservation of volume (rather than mass) with the assumption that density change has small impact on other forces. In order to be able to use the Boussinesq approximations, ocean velocities must be much smaller than speed of sound. Also vertical velocities must be small. To achieve a mass-conserving

ocean within FESOM, a correction term after Greatbatch (1994) is applied (Böning, 2009). Equation 2.14 recovers steric effects, which are neglected in the Boussinesq approximation. Compared with the original Greatbatch correction (Greatbatch, 1994) the correction is applied locally at every (surface) grid note, by adding

$$- \int_{-H}^{\eta} \frac{1}{\rho} \frac{D\rho}{Dt} dz \quad (2.14)$$

to the sea level equation (described in section 2.5).

### 2.2.3 Coupling

The FESIM and FEOM models are coupled by the flux-averaging method (Timmermann et al., 2002), where heat, fresh water and momentum are exchanged. Morison et al. (1987) defined heat exchange ( $Q_{oi}$ ) between the bottom of the sea-ice and the ocean to be

$$Q_{oi} = \rho_w c_{p,w} c_{h,oi} u_* (T_0 - T_f) \quad (2.15)$$

where the friction velocity  $u_*$  is defined by the relative velocity at the boundary between sea-ice and ocean.

$$u_* = \sqrt{c_{d,oi}} |\vec{u}_w - \vec{u}_i| \quad (2.16)$$

The density of water is  $\rho_w$ , the specific heat of water at constant pressure  $c_{p,w}$ , and the heat transfer coefficient  $c_{h,oi} = 1.2 \cdot 10^{-2}$ .  $\vec{u}_w$  is the ocean surface velocity, and  $c_{d,oi} = 3 \cdot 10^{-3}$  being the oceanic drag coefficient.  $T_0$  is the temperature of the surface layer of FEOM. The in-situ freezing temperature  $T_f$  is computed as a function of salinity (Millero, 1978). If there is no sea-ice in an element and the ocean temperature is cooled down to the freezing point, sea-ice formation starts as soon as additional heat is lost.

The exchange of heat between atmosphere and open ocean/sea-ice is defined after Parkinson and Washington (1979). It is described in section 2.4 in more detail as heat exchange is important for thermosteric variations, which is a major contribution to sea level change. The total amount of heat reaching the ocean ( $Q_o$ ) is described by

$$Q_o = (1 - A) \cdot Q_{ow} + A \cdot Q_{oi} \quad (2.17)$$

where the heat exchange for ice-free ocean (open water) is defined by

$$Q_{ow} = Q_{ao} + \rho_i L_i \left( \frac{\partial h}{\partial t} \right)_{ow} \quad (2.18)$$

where the last term in the right hand side denotes the heat flux associated with the freezing rate in an open ocean element, with  $L_i$  being the latent heat of fusion.

Salt fluxes ( $F_i^S$ ) between sea-ice and ocean occur due to melting and freezing of ice and melting of snow. It is defined as

$$F_i^S = (S_o - S_i) \frac{\rho_i}{\rho_w} \left( \frac{\partial h}{\partial t} \right)_{th} + (S_o) \frac{\rho_{sn}}{\rho_w} \left( \frac{\partial h_s}{\partial t} \right)_{th} \quad (2.19)$$

Salinity of sea-ice  $S_i$  is assumed to be 5 psu and of snow 0 psu. Sea-ice and snow have a constant density of  $\rho_i = 910 \text{ kg/m}^3$  and  $\rho_{sn} = 290 \text{ kg/m}^3$ . Here, only thermodynamic variations of sea-ice and snow denoted by the subscript  $th$  are taken into account because snow accumulation and increase in sea-ice volume due to convergent sea-ice drift do not contribute to the salt flux. Also a constant sea surface salinity is assumed to be  $S_o = 34$  psu here to ensure global conservation of salt. In the parts where sea-ice is existing, net precipitation enters the ocean as rain if the temperature  $T$  is higher than the freezing point of fresh water. If the temperature is below the freezing point, precipitation falls as snow on top of the ice covered part. In the open ocean, precipitation is generally a fresh water flux into the ocean, independent of temperature (equation 2.20). The resulting total salt flux  $F^S = F_i^S + F_{ow}^S$  defines the salt balance at the surface nodes of the ocean model, with

$$F_{ow}^S = S_o \cdot \begin{cases} (P - E) & \text{if } T_a \geq 0^\circ C \\ (1 - A) \cdot (P - E) & \text{if } T_a < 0^\circ C \end{cases} \quad (2.20)$$

The total stress at the ocean surface is computed by

$$\vec{\tau}_o = A \cdot \vec{\tau}_{io} + (1 - A) \cdot \vec{\tau}_{ao} \quad (2.21)$$

where the stress between ocean and sea-ice is computed with the bulk formula

$$\vec{\tau}_{io} = \rho_0 c_{d,oi} |\vec{u} - \vec{u}_w| (\vec{u} - \vec{u}_w) \quad (2.22)$$

with  $c_{d,oi} = 3 \cdot 10^{-3}$ . The stress between atmosphere and open ocean is implemented by

$$\vec{\tau}_{ao} = \rho_0 c_{d,oi} |\vec{u}_{10}| \vec{u}_{10} \quad (2.23)$$

using  $c_{d,ao} = 1 \cdot 10^{-3}$ . Here, the velocity of the ocean at the surface is neglected as it is very small compared to the 10 m wind velocity. The stress between atmosphere and sea-ice ( $\vec{\tau}_{ai}$ ) is computed in the same way as  $\vec{\tau}_{ao}$ , only  $c_{d,ai}$  is set to  $1.32 \cdot 10^{-3}$ .

## 2.3 Subgrid-Scale Processes

The effects of subgrid-scale processes are parameterized after Redi (1982) applying tracer mixing along isopycnals. Gent and McWilliams (1990) and Gent et al. (1995) provide the scheme to model advective flux arising from an eddy-induced bolus velocity.

Lateral and vertical mixing are described by the harmonic operator

$$D^x = \nabla(v^x \nabla x) \quad (2.24)$$

It defines the terms of viscosity and diffusion ( $D^x$ ) in the momentum equations (eq. 2.5 and 2.6) and in the balance equations for salinity and temperature (eq. 2.10 and 2.9).

Viscosity  $v^{u,v}$  and diffusivity  $v^{TS}$  [m<sup>2</sup>/s] are linear functions of the spatial resolution

$$v^{u,v} = \frac{1}{10^5 s} \Delta_{\vec{i}} \quad (2.25)$$

$$v^{T,S} = \frac{4}{10^2 s} \cdot v^{u,v} \quad (2.26)$$

with  $\Delta_{\vec{i}}$  [m<sup>2</sup>] being the size of the element. Numerical instabilities in cases of very steep surfaces of neutral density<sup>1</sup> are avoided in the Gent and McWilliams (1990) scheme by tapering the parametrization of lateral diffusivity according to the scheme of Griffies (2004).

Vertical viscosity is implemented after Pacanowski and Philander (1981) to achieve continuously increasing mixing of potential temperature and salinity with weakening stratification. An upper limitation of  $v_{max}^x = 0.01$  m<sup>2</sup>/s is implemented, to avoid spurious deep convection in the Southern Ocean. Unrealistic shallow mixed layers, which might occur in summer, are avoided by introducing an additional diffusivity of 0.01 m<sup>2</sup>/s over a depth defined by the Monin-Obukhov-length (Timmermann and Beckmann, 2004). A constant viscosity of  $2 \cdot 10^{-3}$  m<sup>2</sup>/s is applied for vertical mixing of momentum. Bottom drag is computed by a quadratic function, multiplying the bottom velocity with the bottom friction coefficient  $C_d = 0.0025$  (Beckmann et al. (1999))

---

<sup>1</sup>e.g. occurring in mixed layers and in places of deep convection

Table 2.1: Albedo

| albedo          | surface type                     |
|-----------------|----------------------------------|
| $\alpha = 0.85$ | dry snow                         |
| $\alpha = 0.75$ | wet snow                         |
| $\alpha = 0.75$ | sea-ice without snow pack on top |
| $\alpha = 0.66$ | melting ice                      |
| $\alpha = 0.10$ | open water                       |

## 2.4 Surface Heat Budget

Following Parkinson and Washington (1979) the net heat flux at the surface of the open ocean or sea-ice ( $Q_s$ ) is described as follows

$$Q_s = Q_{SW}^{\downarrow} + Q_{SW}^{\uparrow} + Q_{LW}^{\downarrow} + Q_{LW}^{\uparrow} + Q_l + Q_s \quad (2.27)$$

where  $Q_{SW}^{\downarrow}$  is the downward shortwave radiation (solar radiation) going into the ocean/sea-ice (Zillmann (1972), Laevastu (1960)). Outgoing shortwave radiation  $Q_{SW}^{\uparrow}$  is computed by  $\alpha Q_{SW}^{\downarrow}$ , where  $\alpha$  defines the albedo. It differs depending on the type of the surface and its temperature, see Table 2.1 (Fischer, 1995).

Net infrared radiation is the sum of downward atmospheric and upward surface components,  $Q_{LW}^{\downarrow} + Q_{LW}^{\uparrow}$ , which are computed as

$$Q_{LW}^{\uparrow} = \epsilon_s \sigma T_s^4 \quad (2.28)$$

and

$$Q_{LW}^{\downarrow} = \epsilon_a \sigma T_a^4 \quad (2.29)$$

with

$$\epsilon_a = 0.765 + 0.22 \cdot A_c^3$$

where  $a$  stands for atmosphere and  $s$  for surface (open ocean or sea-ice). The temperature is denoted as  $T$ ,  $\sigma$  is the Stefan-Boltzmann constant ( $5.67 \cdot 10^{-8} \text{ W}/(\text{m}^2 \text{ K}^4)$ ), and  $\epsilon$  is the emissivity. The emissivity of the surface ( $\epsilon_s$ ) is taken to be 0.97. For the atmosphere the emissivity  $\epsilon_a$  is a function of the total cloud cover  $A_c$  (Koenig-Langlo and Augstein, 1994). Latent ( $Q_l$ ) and sensible ( $Q_s$ ) heat flux are computed by the bulk formulas

$$Q_l = \rho_a L C_l |u_{10}| (q_s - q_a) \quad (2.30)$$

and

$$Q_s = \rho_a c_p C_s |u_{10}| (T_s - T_a) \quad (2.31)$$

where  $\rho_a = 1.3 \text{ kg/m}^3$  (air density above surface),  $c_p = 1004 \text{ J/(kg K)}$  (latent heat capacity),  $L = 2.5 \cdot 10^6 \text{ J/kg}$  and  $L = 2.834 \cdot 10^6 \text{ J/kg}$  (specific heat of evaporation of water and sublimation of sea-ice, respectively), and  $C_s = C_l = 1.75 \cdot 10^{-3}$  (sensible and latent heat transfer coefficients) (Maykut (1977), Parkinson and Washington (1979)). The wind velocity 10 m above the surface ( $u_{10}$ ), the air temperature 2 m above the surface ( $T_a$ ), the specific humidity of the atmosphere 2 m above the surface ( $q_a$ ), and the total cloud cover are given as atmospheric forcing fields (see section 2.7). If only the dew point temperature ( $T_d$ ) is available, the specific humidity  $q_a$  is computed as

$$q_a = \frac{0.622}{p} \cdot 6.11 \cdot e^{a \cdot \frac{T_d}{T_d+b}} \quad (2.32)$$

where  $p$  is atmospheric pressure and  $a$  and  $b$  are constants dependent on the surface type (Murray, 1967). If the surface is only sea-ice, then  $a = 21.9^\circ\text{C}$  and  $b = 265.5^\circ\text{C}$ . If the surface is only open water, then  $a = 17.3^\circ\text{C}$  and  $b = 237.3^\circ\text{C}$ . And if it is a mixture, then  $a = 19.0^\circ\text{C}$  and  $b = 250^\circ\text{C}$ .

## 2.5 Sea Level Equation

The model comprises a free surface, so that variations in sea level can result from the divergence of volume via the continuity equation, from steric effects due to thermal and haline expansion, or from mass flux at the ocean surface. In the model the evolution of the sea level ( $\eta$ ) is computed by

$$\frac{\partial \eta}{\partial t} + \nabla \cdot \int_{-H}^{\eta} \vec{u} dz = - \int_{-H}^{\eta} \frac{1}{\rho} \frac{D\rho}{Dt} dz + (P - E) + R + F + \frac{DM}{Dt} \quad (2.33)$$

where  $\frac{\partial \eta}{\partial t}$  is the local temporal change of sea level (Böning, 2009). The horizontal transport divergence is calculated as  $\nabla \cdot \int_{-H}^{\eta} \vec{u} dz$ . Steric effects are related to density changes in the water column, caused by salinity and temperature variations and are computed by  $-\int_{-H}^{\eta} \frac{1}{\rho} \frac{D\rho}{Dt} dz$ . The surface mass budget is introduced by  $(P - E) + R$ , with  $P$  being precipitation,  $E$  being evaporation, and  $R$  being the river runoff<sup>2</sup> (see also section 3.3).

---

<sup>2</sup>Surface runoff on the model does not include fluxes due to land ice melting, e.g. ice melt from glaciers, ice sheets, or shelves. In Chapter 5 an additional term is introduced to the right hand side of equation 2.33 to account for meltwater from the Greenland and West Antarctic ice sheets.

The water flux due to melting and freezing of sea-ice and snow is defined by  $F$ . Finally,  $M$  is the volume of sea-ice and snow converted to equivalent water height. The transfer to equivalent water height is performed by applying the density ratios  $\frac{\rho_{ice}}{\rho_0}$  and  $\frac{\rho_{sw}}{\rho_0}$ , where  $\rho_i$  is  $910 \text{ kg/m}^3$  and  $\rho_{sw}$  is  $290 \text{ kg/m}^3$ . The total mass of the ocean does not change through the exchange of mass between ocean and sea-ice. However,  $F$  and  $M$  have to be included in the equation 2.33 to account for advection of sea-ice (and snow). This is needed as sea-ice and snow have a drift speed different from ocean currents, so that horizontal redistribution of sea-ice/snow has to be accounted for explicitly.

## 2.6 Spatial Discretization

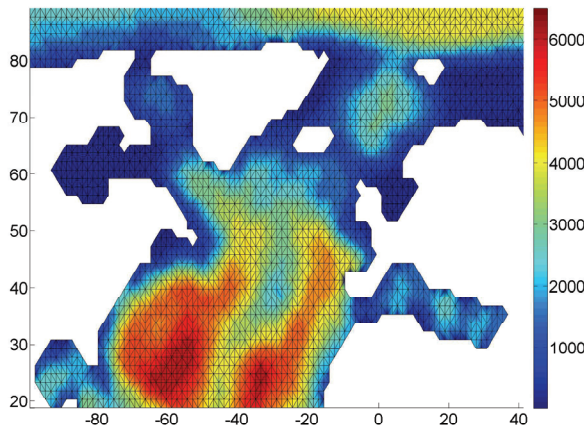


Figure 2.1: Spatial discretization and Bottom topography in the North Atlantic and the Arctic Ocean

| z-level | depth | z-level | depth |
|---------|-------|---------|-------|
| 1       | 0     | 14      | 2000  |
| 2       | 10    | 15      | 2500  |
| 3       | 30    | 16      | 3000  |
| 4       | 50    | 17      | 3500  |
| 5       | 75    | 18      | 4000  |
| 6       | 100   | 19      | 4250  |
| 7       | 150   | 20      | 4500  |
| 8       | 200   | 21      | 4750  |
| 9       | 300   | 22      | 5000  |
| 10      | 425   | 23      | 5250  |
| 11      | 600   | 24      | 5500  |
| 12      | 1000  | 25      | 6000  |
| 13      | 1500  | 26      | 6500  |

Table 2.2: z-Levels

Although the FESOM can provide simulations on unstructured grids, here a regular grid is used. The ocean and sea-ice use the same horizontal discretization on a regular grid, which consists of a mesh of triangles separated horizontally by  $1.5^\circ \times 1.5^\circ$ <sup>3</sup>. Vertically the nodes of the 26 z-levels (Table 2.2) are aligned under the surface nodes, forming tetrahedral structured elements. The ocean bottom topography used to create the 3D mesh is provided by the Rand Corporation/Scripps Institution of Oceanography (Gates and Nelson, 1975a,b). The global bathymetry has a spatial resolution of 1 degree and is interpolated to the model grid. For illustration the spatial discretization of the North Atlantic and the Arctic Ocean around Greenland are shown in Figure 2.1. The ocean depth in the model

<sup>3</sup>Note, that all global data sets used during this study are interpolated to the model grid.

(in meter) is represented by the colors.

To avoid a mesh with a stepwise bottom topography and to receive a realistic bathymetry, the nodes of the lowest elements may deviate from the z-levels. The tetrahedrons are deformed in such a way that the bottom nodes align directly at the ocean bottom (similar to a shaved-cells approach described by Wang (2007)). To minimize pressure gradient errors, only density anomalies are considered and a constant reference pressure as a function of depth is subtracted<sup>4</sup>.

Linear basis functions in three dimensions are used for the tracers  $T$  and  $S$ , and the velocity  $\vec{u}_0$ . Two dimensional linear basis functions are used for the surface elevation  $\eta$ . The variables are then represented as the sum of nodal values ( $x_i$ ) multiplied with the basis functions  $\Psi_i$ :

$$x \simeq \sum_{i=1}^N x_i \Psi_i \quad (2.34)$$

where  $x$  has to be replaced by the variable under discussion, and  $N$  is the total amount of nodes, depending on the dimension of the variable. The basis functions are 1 at node  $i$ , linearly decreasing to 0 at the neighboring nodes, and are 0 outside.

## 2.7 Atmospheric Forcing

In the climate system the atmosphere plays a major role as it transports heat from the equatorial region to the higher latitudes and is the main driver of ocean circulation. The near-surface winds cause a surface stress (momentum input), which is transmitted downwards within the Ekman layer by internal friction. In addition, atmospheric pressure gradients drive ocean current via the inverse barometer effect. Also the exchange of heat at the ocean surface as well as the exchange of mass through precipitation and evaporation have major influence to the ocean state. Realistic atmospheric forcing fields are therefore important ingredients of any ocean model simulation.

An overview of the parameters used from the different atmospheric data sets is shown in Table 2.3. Some aspects that are important when using these forcing fields in FESOM, are described in the following sections<sup>5</sup>.

---

<sup>4</sup>Pressure gradient errors might occur if the vertical discretization is not following the geopotential surface or if there are not enough orders of basis functions to approximate pressure or density accurately (Wang, 2007)

<sup>5</sup>Atmospheric forcing with the NCAR/NCEP reanalysis has been already implemented by Timmermann et al. (2009) and Böning et al. (2008)

Table 2.3: Atmospheric datasets

| Field                 | Source   | time period   | temporal resolution  | spatial resolution   | description   |
|-----------------------|--|---|--|--|---|
| u-wind                | NCAR/NCEP<br>ERA40<br>ERA interim<br>op. ECMWF         | 1958-2008<br>1958-2002<br>1989-2008<br>2002-2007              | daily mean<br>6-hourly<br>6-hourly<br>6-hourly               | $1.875^\circ \times 1.875^\circ$<br>$2.5^\circ \times 2.5^\circ$<br>$1.5^\circ \times 1.5^\circ$<br>$1.125^\circ \times 1.125^\circ$                     | mean zonal wind at 10 m height in m/s   |
| v-wind                | NCAR/NCEP<br>ERA40<br>ERA interim<br>op. ECMWF         | 1958-2008<br>1958-2002<br>1989-2008<br>2002-2007              | daily mean<br>6-hourly<br>6-hourly<br>6-hourly               | $1.875^\circ \times 1.875^\circ$<br>$2.5^\circ \times 2.5^\circ$<br>$1.5^\circ \times 1.5^\circ$<br>$1.125^\circ \times 1.125^\circ$                     | mean meridional wind at 10 m height in m/s  |
| latent heat flux      | NCAR/NCEP  | 1958-2008   | daily mean   | $1.875^\circ \times 1.875^\circ$   | evaporation in FESOM is computed from latent heat flux:<br>$F_w[m/s] = \frac{Q_l}{\Gamma_{evap} \rho_w}$                              |
| 2m temperature        | NCAR/NCEP<br>ERA40<br>ERA interim<br>op. ECMWF         | 1958-2008<br>1958-2002<br>1989-2008<br>2002-2007              | daily mean<br>6-hourly<br>6-hourly<br>6-hourly               | $1.875^\circ \times 1.875^\circ$<br>$2.5^\circ \times 2.5^\circ$<br>$1.5^\circ \times 1.5^\circ$<br>$1.125^\circ \times 1.125^\circ$                     | mean air temperature at 2 m height in $^\circ C$  |
| dew point temperature | ERA40<br>ERA interim<br>op. ECMWF                      | 1958-2002<br>1989-2008<br>2002-2007                           | 6-hourly<br>6-hourly<br>6-hourly                             | $2.5^\circ \times 2.5^\circ$<br>$1.5^\circ \times 1.5^\circ$<br>$1.125^\circ \times 1.125^\circ$   | mean dew point temperature at 2 m height in $^\circ C$  |
| specific humidity     | NCAR/NCEP  | 1958-2008   | daily mean   | $1.875^\circ \times 1.875^\circ$   | mean specific humidity at 2 m height in kg/kg   |
| atmospheric pressure  | NCAR/NCEP<br>ERA40<br>ERA interim<br>op. ECMWF         | 1958-2008<br>1958-2002<br>1989-2008<br>2002-2007              | daily mean<br>6-hourly<br>6-hourly<br>6-hourly               | $1.875^\circ \times 1.875^\circ$<br>$2.5^\circ \times 2.5^\circ$<br>$1.5^\circ \times 1.5^\circ$<br>$1.125^\circ \times 1.125^\circ$                     | mean sea level pressure in Pa   |
| total precipitation   | NCAR/NCEP<br>ERA40<br>ERA interim<br>op. ECMWF<br>GPCP | 1958-2008<br>1958-2002<br>1989-2008<br>2002-2007<br>1997-2008 | daily mean<br>6-hourly<br>6-hourly<br>daily mean<br>6-hourly | $1.875^\circ \times 1.875^\circ$<br>$2.5^\circ \times 2.5^\circ$<br>$1.5^\circ \times 1.5^\circ$<br>$1^\circ \times 1^\circ$<br>$1^\circ \times 1^\circ$ | mean precipitation rate at surface in m/s<br>op. ECMWF: total precipitation is stratiform precipitation plus convective precipitation |
| evaporation           | ERA40<br>ERA interim<br>op. ECMWF                      | 1958-2002<br>1989-2008<br>2002-2007                           | 6-hourly<br>6-hourly<br>daily mean                           | $2.5^\circ \times 2.5^\circ$<br>$1.5^\circ \times 1.5^\circ$<br>$1^\circ \times 1^\circ$   | mean evaporation rate at surface in m/s   |
| total cloud cover     | NCAR/NCEP<br>ERA40<br>ERA interim                      | 1958-2008<br>1958-2002<br>1989-2008                           | daily mean<br>6-hourly<br>6-hourly                           | $1.875^\circ \times 1.875^\circ$<br>$2.5^\circ \times 2.5^\circ$<br>$1.5^\circ \times 1.5^\circ$   | mean total cloud cover with range:[0...1]   |

### 2.7.1 NCEP/NCAR Data

The National Centers for Environmental Prediction provide the daily NCAR/NCEP reanalysis, which includes data sets of atmospheric conditions from 1948 to present (Kalnay et al., 1996). For consistency the assimilation system has been unchanged for the entire reanalysis period. On the other hand, data records are still influenced by changes in the input data, as all useful data available at a given point of time are included into the processing system. This is done to be as accurate as possible during the 50 year period. For data processing from August 1989 to September 1991 the European Center for Medium-Range Weather Forecasts (ECMWF) filled some data gaps in the wind field and provided a sea ice database for the NCEP reanalysis.

The atmospheric data fields are classified into four classes (A to D) according to the influence of observations and models. Variables that are denoted as class A are mainly influenced by measured data, and are defined to be most reliable. No data set used in this study is denoted as class A. The class B variables are strongly influenced by observation, but also model results highly influence the analysis value. For example, sea level pressure, specific humidity, and temperature and wind at 2 m height are assigned to class B (Kalnay et al., 1996). The precipitation field as well as latent heat flux is classified to "C", which means that the data set is estimated by models (forced by data assimilation). Although the precipitation field should be used with caution, Kalnay et al. (1996) did several comparison with observations and climatology and found good agreement on timescales of a few days to inter-annual variability.

The NCEP data set has a spatial resolution of  $1.875^\circ \times 1.875^\circ$  and is used as the default atmospheric forcing in the FESOM model. This includes 10-m wind u-component, 10-m wind v-component, 2-m temperature, specific humidity, total cloudiness, atmospheric pressure, precipitation, and evaporation. Evaporation is computed from NCEP's latent heat flux by

$$E = \frac{Q_l}{\rho_w \cdot l_{evap}} \quad (2.35)$$

where the density of water is defined as  $\rho_w = 1000 \text{ kg/m}^3$  and the latent heat of evaporation is  $l_{evap} = 2.5 \cdot 10^6 \text{ J/kg}$ .

### 2.7.2 ERA40 Data

As an alternative atmospheric forcing the ERA40 reanalysis can be used for the period from September 1957 to August 2002 (S.M.Uppala et al., 2005). Here, the data sets used are

10-m wind zonal-component, 10-m wind meridional-component, 2-m temperature, 2-m dew point temperature, total cloudiness, atmospheric pressure, precipitation, and evaporation. They have a spatial resolution of  $2.5^\circ \times 2.5^\circ$ . The model converts dew point temperature to specific humidity by equation (2.32).

As in all data sets, also the ERA40 reanalysis has errors. For example, the total precipitation has spurious variability and strong trends over the ocean, which need to be taken into account when scaling the fresh water budget to reasonable bounds in FESOM (section 3.3). Especially in the tropical regions precipitation is overestimated (chapter 3.2 and (Hagemann et al., 2005)). Until the 1990's, the precipitation field was affected by an incorrect bias correction in the assimilation of Special Sensor Microwave Imager (SSM/I). This error source was eliminated in 1993, improving the representation of the water exchange between atmosphere and ocean (Hagemann et al., 2005). In addition, uncertainties due to assimilation of High Resolution Infrared Radiation Sounder (HIRS) data from a new satellite mission were introduced, as its bias correction was tuned to the current state of the atmosphere. It was strongly distorted by aerosols originating from the volcanic eruption of the Pinatubo (Hagemann et al., 2005). This error has been corrected in 1996.

### 2.7.3 Operational ECMWF data

For the years from 2002 to 2007 operational ECMWF data are available for this study (ECWFMF, 1995), where the same data sets as in the ERA40 reanalysis are used in the model. The only difference is that precipitation is separated in convective precipitation and stratiform precipitation. Convective precipitation, also called thermodynamic precipitation, originates from convective clouds. The showers have strongly varying intensity and fall locally for a relatively short period of time. Stratiform precipitation, also called dynamic precipitation, originates from lifting of air due to processes causing lower level convergence and divergence in the upper level. This process is due to the fact that the relative humidity of air increases when unsaturated air is rising and cooling. If the air is saturated and is still lifting, clouds are formed. The resulting rain is less intense, but lasts longer than convective rain.

Freshwater fluxes of the operational ECMWF data are accumulated over 12 hours (Figure 2.2). Therefore, daily mean precipitation and evaporation rates in  $[m/s]$  are computed with

$$\frac{P_1 + P_2}{86400 \text{ s}} \quad (2.36)$$

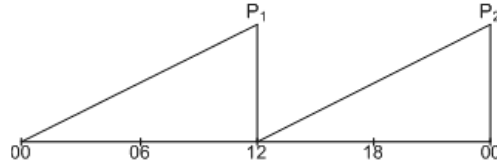


Figure 2.2: Accumulation of water fluxes

where  $P_1$  and  $P_2$  are the accumulated fresh water fluxes after 12 and 24 hours per day.

The operational ECMWF data sets have a major disadvantage against the ERA40 and NCAR/NCEP data sets. The data processing is not homogeneous, i.e. all modifications of the analysis model are included in the data set, which has the potential to create spurious trends and longer-term variability in ocean simulations forced with such data. For this reason, operational ECMWF data are not used as forcing in FESOM during this study.

#### 2.7.4 ERA Interim

The ERA Interim reanalysis is more suitable for ocean modeling than the operational ECMWF analysis because the ERA Interim reanalysis uses the same processing technique during the complete time period (Berrisford et al., 2009). This data set has been developed after the ERA40 reanalysis has finished. It has been derived from the operational system using a 12-hour 4D-VAR data assimilation system (Simmons et al., 2006). It covers the period from 1989 to near real time and will be ongoing until 2013. The spatial resolution with  $1.5^\circ \times 1.5^\circ$  is higher than the resolution of the ERA40 data set. The time series overlaps the ERA40 reanalysis during the period 1989-2002. With a few exceptions ERA interim uses the same data sets for processing as for the ERA40 reanalysis operational ECMWF analysis. The exceptions are not relevant in the following and will not be discussed here, please refer to <http://www.ecmwf.int/research/era/> for more details. The ERA-interim reanalysis system solved different problems of the ERA40 reanalysis system like the too strong oceanic precipitation in the tropical regions (Simmons et al., 2006).

The ECMWF compared the ERA-Interim data sets with other data sets available, to estimate the quality of the data sets. It was found that the data sets are improved especially in the long-term homogeneity, compared to the ERA40 reanalysis. Generally, the improvements are due to further developed processing systems as well as due to new types of satellite data, like the Global Positioning System (GPS) assimilated into the processing scheme (Dee et al., 2008). The GPS system provides among others temperature and humidity profiles from the troposphere to the lower stratosphere using the radio occultation (Healy and Thépaut, 2006). The observations are converted to bending angles and impact

parameters. These are used to compute the refractivity, through which the atmospheric parameters are determined. These measurements have global coverage and high vertical resolution. The GPS system provides data under all weather conditions (Ao et al., 2003).

### 2.7.5 GPCP Precipitation

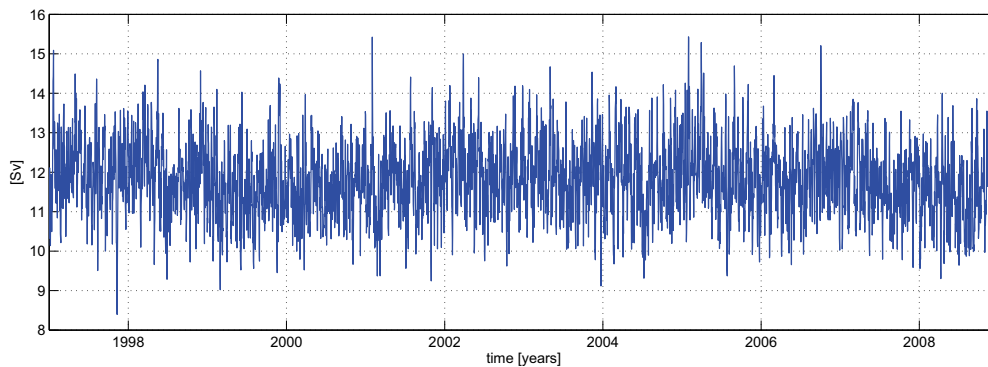


Figure 2.3: Global Sum of GPCP Precipitation

The Global Precipitation Climatology Project (GPCP) of the World Climate Research Program (WCRP) combines observations from different sources to quantify the distribution of precipitation on a global grid (Adler et al., 2003). Primary datasets are gauge measurements from the Global Precipitation Climatology Center (GPCC) of the Deutsche Wetterdienst (DWD) and the Climate Prediction Center of NOAA. Also estimates from several satellite missions are used as input data, like infrared precipitation estimated by different geostationary (GEO) satellites, estimates from atmospheric infrared sounders (AIRS) of low earth orbit (LEO) satellites, data from Special Sensor/Microwave Imager (SSM/I), which provides fractional occurrence of precipitation, and from TIROS Operational Vertical Sounders (TOVS). A description of the data sets used as input to compute the global precipitation fields can be found in Huffman and Bolvin (2009) and on the website of the GPCP project (<http://www.gewex.org/gpcp/html>).

Monthly data sets from 1979 to present and a climatology are available on a  $2.5^\circ * 2.5^\circ$  grid. Also daily one-degree precipitation fields are available from 1997 to present (Huffman et al., 2001). The daily dataset is chosen to be most suitable in the following as it has highest spatial resolution and the temporal resolution is most appropriate for investigation that require weekly time scales. As the GPCP precipitation strictly uses only observations, a disadvantage occurs. It includes missing values and missing days, which

have to be taken care of. These data gaps are filled with a mean value, computed with

$$\bar{P}^d(\gamma, \theta) = \frac{1}{12} \sum_y P_y^d(\gamma, \theta) \quad (2.37)$$

with  $y = (1997\dots 2008)$  ([mm/s]). During this study the GPCP precipitation is used for a comparison of precipitation fields from the different atmospheric data sets (chapter 3.2).

### 2.7.6 Reference Model Simulation and Sensitivity Experiments

Multi-decadal time series of observations have become an important source for analyzing oceanic processes. However, analyzing long term trends is not possible with the atmospheric data sets because in the time period of the reanalysis measurements techniques have been changed. This is in particular the case in the 1990's where more satellite measurements became available.

The atmospheric forcing data set for the reference model simulation is provided by the NCAR/NCEP reanalysis (Kalnay et al., 1996). ERA40 (S.M.Uppala et al., 2005) and ERA Interim reanalysis (Berrisford et al., 2009) are used when running an alternative model simulation, which is used to estimate the error of modeled OBP (section 3.5.3).

The model runs with time steps of 2h from 1958 to 2008. It is initialized with temperature and salinity from the January mean data set of the World Ocean Atlas (WOA01). Sea-ice thickness is initialized with 1 m and a concentration of 0.9 where the sea surface temperature is smaller  $-1^\circ\text{C}$ . On top of the sea-ice an initial layer of snow with a height of 0.1 m is defined. For more details about the FESOM model version used in this study, please refer to Timmermann et al. (2009), and Böning (2009).

# Chapter 3

## Variations of Ocean Mass

The ocean takes part in the hydrological cycle of the Earth, where different sources exist, which can modify ocean mass. Generally, fresh water is transferred from ocean to atmosphere by evaporation. Part of it condensates and falls back into the ocean by precipitation. The other part remains in the atmosphere and is transported to the over land by the wind systems. There, it falls as precipitation, which can be stored for many years if it falls as snow on glaciers, ice caps or ice sheets. Precipitation falling as rain feeds plants, or flows into rivers, lakes or the groundwater system. Some water on land is transferred back to the atmosphere via evaporation, evapotranspiration or sublimation. Meltwater from glaciers, ice caps or ice sheets also feeds the groundwater system as well as the rivers before it flows into the ocean via surface runoff, closing the hydrological cycle of the Earth.

Variations in atmospheric pressure changes the regional distribution of mass in the ocean but not its total mass (e.g. due to the inverse barometer effect). Regional density variations occur due to melting and freezing of sea-ice and redistribution of mass within the ocean. Here, the difference between sea-ice drift and ocean velocities is of major importance (see Section 2.5). Redistribution of ocean mass also happens due to currents, such as the Gulf Stream or the Kuroshio Current. The same is true for eddies, i.e. small scale turbulences, which additionally account for mixing. They are not modeled in this study as their scale is generally too small for the chosen spatial resolution of the model.

In the following, contributions from mass exchange between land, ocean, and atmosphere via surface runoff, precipitation, and evaporation are analyzed. Weekly mean variations of ocean mass are modeled with FESOM, including changes in total ocean mass, which is quite uncertain in the model as its accuracy directly depends on the given input variables. Continental ice sheet and glacier melting are not considered in this Chapter. The simulation results are used within a combination of individual data sets (joint inversion)

with the aim to estimate the redistribution of ocean mass with higher temporal resolution, as it has been done before Rietbroek et al. (2009). For the combination, the estimation of the modeled OBP error is of major importance as the contributions of the different data sets are weighted by their errors. Hence, different possible error sources of modeled OBP have been investigated. The inversion also provides a mass correction term, which can be used to optimize modeled global mean ocean mass variations. Finally, all results are validated with measurements from the GRACE satellite mission as well as with in-situ bottom pressure measurements.

### 3.1 Land-Ocean Mass Exchange

The mass budget in FESOM includes surface runoff from land. The river runoff is provided on a rectangular grid of  $1^\circ \times 1^\circ$  spatial resolution and is interpolated to the nearest coastal nodes of the model grid. The daily volume flux is included into the model after converting it to fresh water flux ( $[m/s]$ ) by dividing it with the surrounding cluster area of the coastal node. The cluster area defined as  $1/3$  of the area of the corresponding triangles around the node. Here, the temperature of the fresh water flux is the same as the temperature at the location, the fresh water is flowing into the ocean (Böning, 2009). The FESOM model has been extended to use river runoff provided by an alternative hydrological model. The two data sets are compared and their influence on the model results is investigated.

The given river runoff is provided by the hydrological discharge model (HDM), which was developed to compute the global continental hydrology (Hagemann and Duemenil, 1998b). It estimates the lateral water flows from continents to oceans and was originally used in coupled applications within climate models (Hagemann and Duemenil, 1998a). It also provides estimates of the impacts of the hydrological cycle on Earth's rotation parameters (Walter, 2008). The model has a resolution of  $0.5^\circ$  with daily time stepping. It is forced with atmospheric data sets from the ECMWF. The model covers all sources of water outflow from land to atmosphere and ocean, except the flow due to sublimation and melting in ice covered regions. The model provides daily estimates of runoff into the ocean, which are included in the FESOM model to close the mass budget of the ocean.

Alternatively, data provided by the Land Surface Discharge Model (LSDM) from GFZ Potsdam (Dill, 2008) is implemented as river runoff in FESOM. The model is a further development of the Hydrological Discharge Model (HDM) from the TU Dresden. It considers water storage via inflow to reservoirs like lakes, rivers and groundwater. Precipitation is defined as snow according to the atmospheric temperature. Below  $-1.1^\circ C$  precipitation

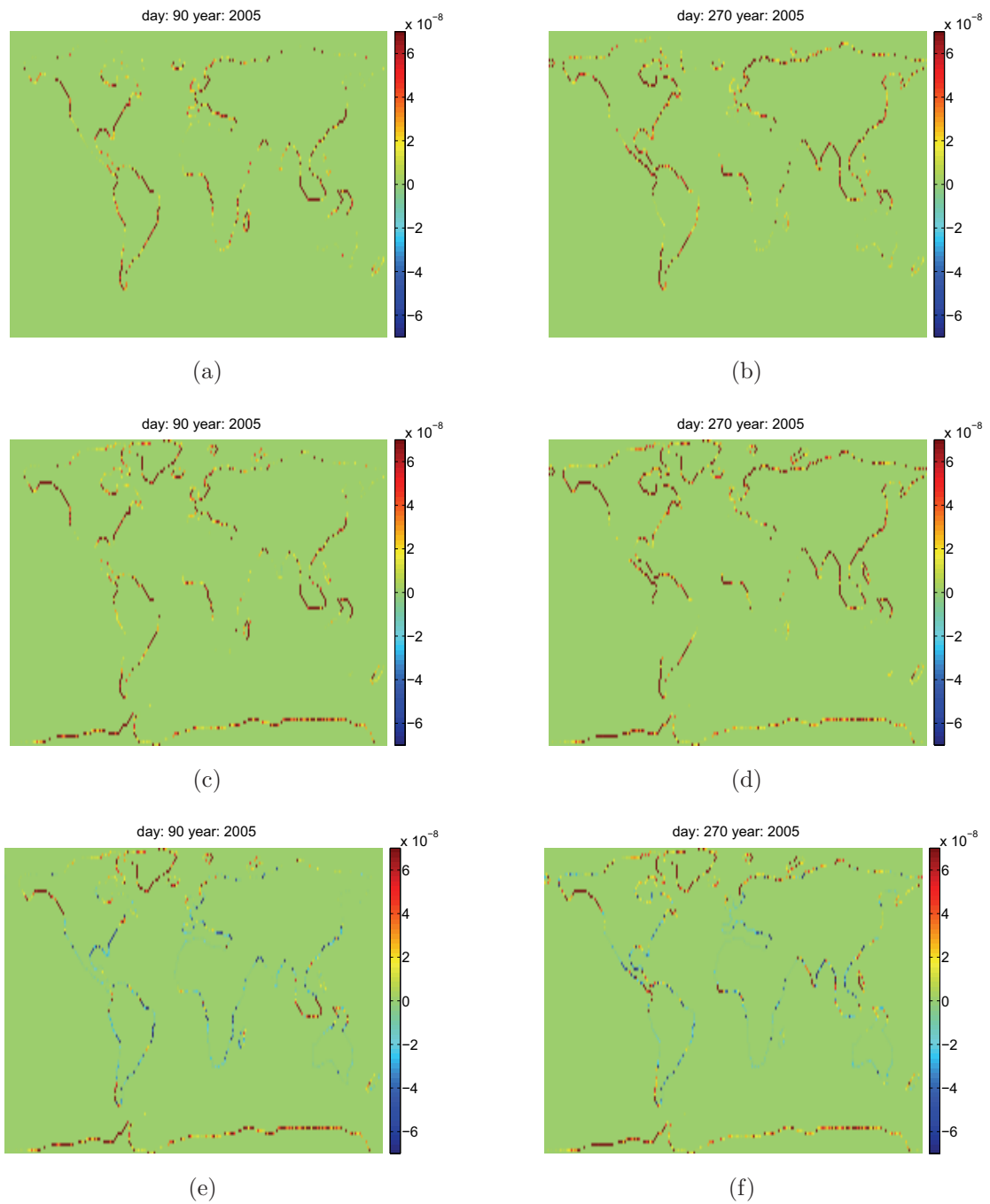


Figure 3.1: River runoff of day 90 and 270 in 2005; HDM model (a) and (b); LSDM model (c) and (d); difference (e) and (f)

is added to the snow pack and above  $+3.3^{\circ}\text{C}$  precipitation is falls as rain. In-between precipitation is assumed as a linear mixture. Compared to the HDM model the LSDM model included a seasonal driven discharge model for ice covered regions, such as for the ice sheets of Greenland and Antarctica. It makes sure that snow accumulation and melting is covered, but it does not consider long term ice mass change and transport of ice mass. No present day melting of the Greenland and Antarctic ice sheets is considered.

Comparing the runoff of the two hydrological models (Figure 3.1), the LSDM model shows runoff at the Antarctic coast, which is not the case for the HDM model. At the coast of Greenland the river runoff is higher in the LSDM model. Comparing the runoff from end of March and end of September 2005, in both models a clear seasonal cycle is visible poleward of 40 degree latitude. In the Southern Ocean it is not as significant. At the coast of India a strong seasonal signal occurs, due to the monsoon. This leads to very low precipitation in winter and high precipitation rates in summer. The difference of the two models show less runoff in the subtropical regions and higher runoff in polar regions in the LSDM model. In the equatorial regions runoff is very similar in both data sets. It is slightly higher in summer in the LSDM model. Global mean river runoff of both models are compared in Figure 3.2. Here, the amplitude and phase are very similar, which is also true for the long term trend. Only since 2001 the trend in the LSDM is a bit smaller than the trend in the HDM model.

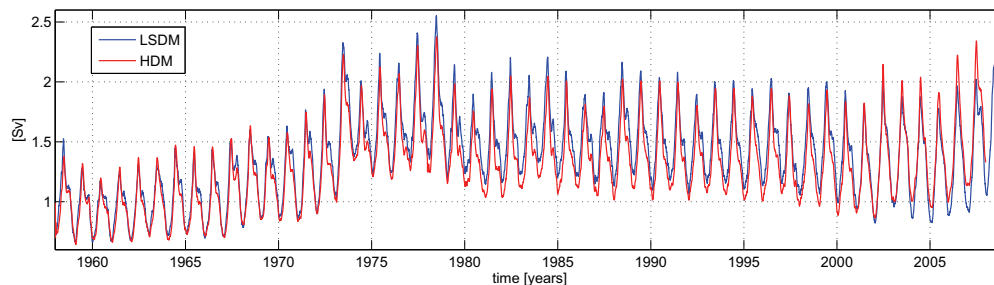


Figure 3.2: Global river runoff in Sverdrup (Sv) provided by the HDM model (red) and by the LSDM model (blue)

The fresh water flux influences the sea surface height (SSH). Simulating SSH, using LSDM model instead of the HDM model as river runoff (same atmospheric forcing), result in increased annual mean SSH. Around Greenland, ocean density changes due to the increased fresh water flux in the years 1965 (Figure 3.3a) and 2005 (Figure 3.3b). In addition, strong fluctuations appear in the Southern Ocean as the surface runoff of LSDM model includes fresh water inflow at the Antarctic coast. This changes the ocean density in the

Southern Ocean, which is transported around the globe within the Antarctic Circumpolar Current (ACC). A typical error pattern appears, which is always excited when model parameters change. In the Gulf of Mexico a decrease in SSH occurs, which is due to reduced water inflow of the Mississippi when using LSDM model results. As a consequence, surface runoff provided by the LSDM model is used within FESOM as river runoff, because of the main advantage of including runoff at the Greenland and Antarctic coasts.

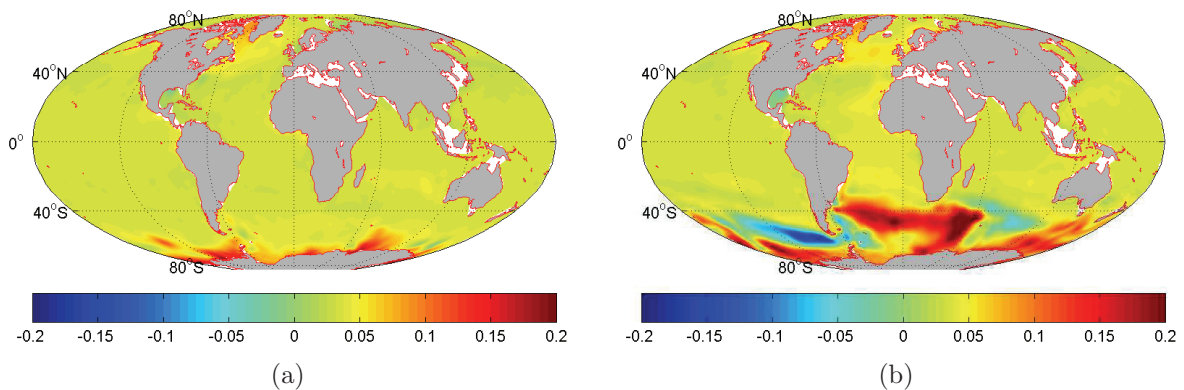


Figure 3.3: Difference in annual mean SSH in meter due to different river runoff used in FESOM (LSDM and HDM); (a): year 1965 and (a): year 2005

## 3.2 Mass Exchange between Atmosphere and Ocean

The second important parameter of global ocean mass change is precipitation minus evaporation, called net precipitation. It is included in the model as atmospheric forcing field taken from the NCAR/NCEP reanalysis. Although this yields an inconsistency as the LSDM model employs atmospheric data from the ECMWF to estimate river runoff, the use of data from the NCAR/NCEP reanalysis in FESOM results in better oceanic circulation and better representation of sea-ice as compared to using ECMWF data sets, described in Chapter 2.7. Using net precipitation from the different data sets leads to strong differences in regional and global mass redistribution. Hence, comparing all available precipitation data sets major differences are found (Figure 3.4).

Here, daily mean precipitation and evaporation is first interpolated to the model grid as the different data sets have different resolution ranging from  $1^\circ \times 1^\circ$  to  $2.5^\circ \times 2.5^\circ$ . Generally net precipitation is negative over the ocean as only part of the evaporated water falls back into the ocean as rain or snow. The other part is transported by the atmospheric

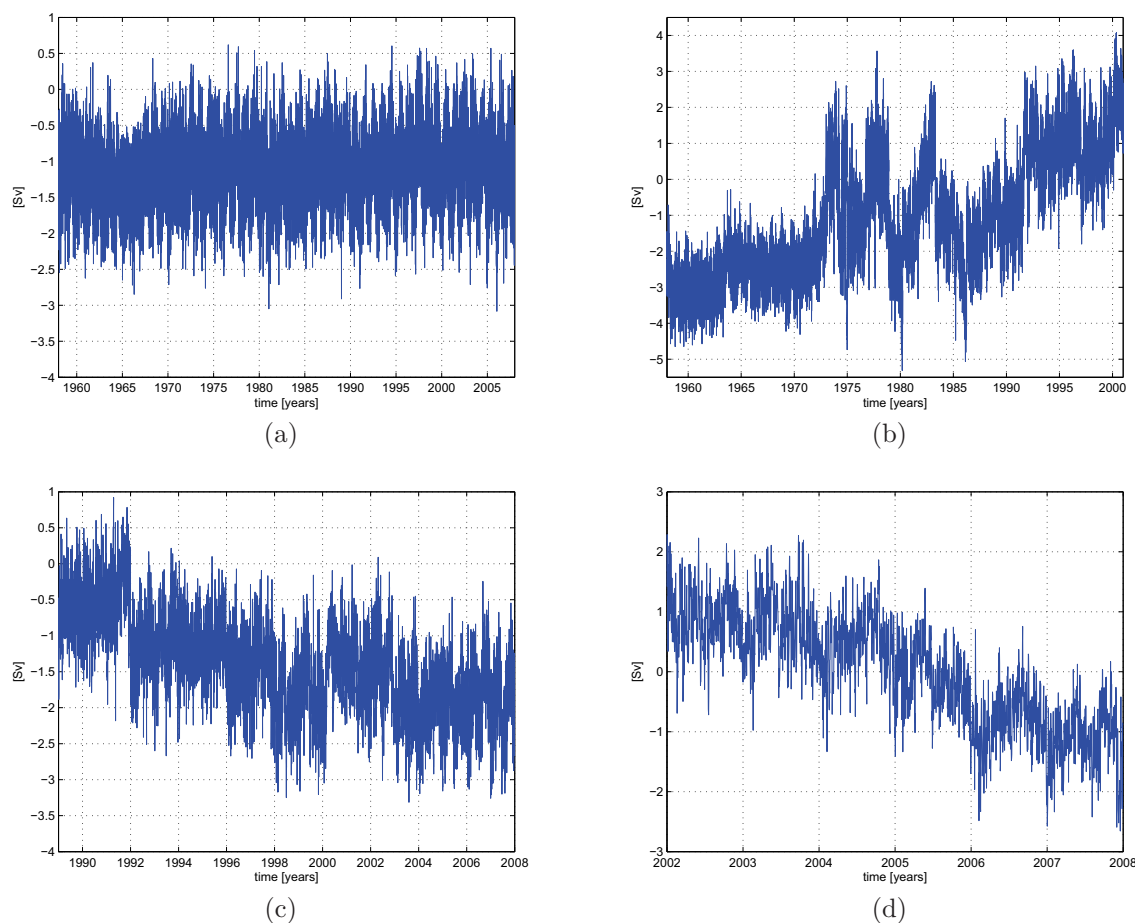


Figure 3.4: Global integral of precipitation minus evaporation over the ocean (in Sv) computed from different data sets; (a): NCAR/NCEP reanalysis, (b): ERA40 reanalysis, (c): ERA Interim reanalysis, (d): operational ECMWF data

circulation to the continents, where it precipitates as rain or snow. Here, the water is a source for the land hydrology and might be stored for many years. The NCAR/NCEP data sets shows almost no trend in the global sum (see Figure 3.4a). The global sum of net precipitation from the ERA40 reanalysis, shows highest long term trends (Figure 3.4b). These are changing over time, especially in the 1970's. Since the year 1986 the trend remains positive. However, the data centers don't claim that their global mean is correct. This is in particular the case for all ECMWF data sets. Here, net precipitation is also negative in the ERA Interim reanalysis (Figure 3.4c), but not in the operational ECMWF data (Figure 3.4d). All ECMWF data sets include strong trends. For the ERA Interim reanalysis and the operational ECMWF data it is a clear negative trend.

To validate precipitation from the different data sets, they are compared with a data set

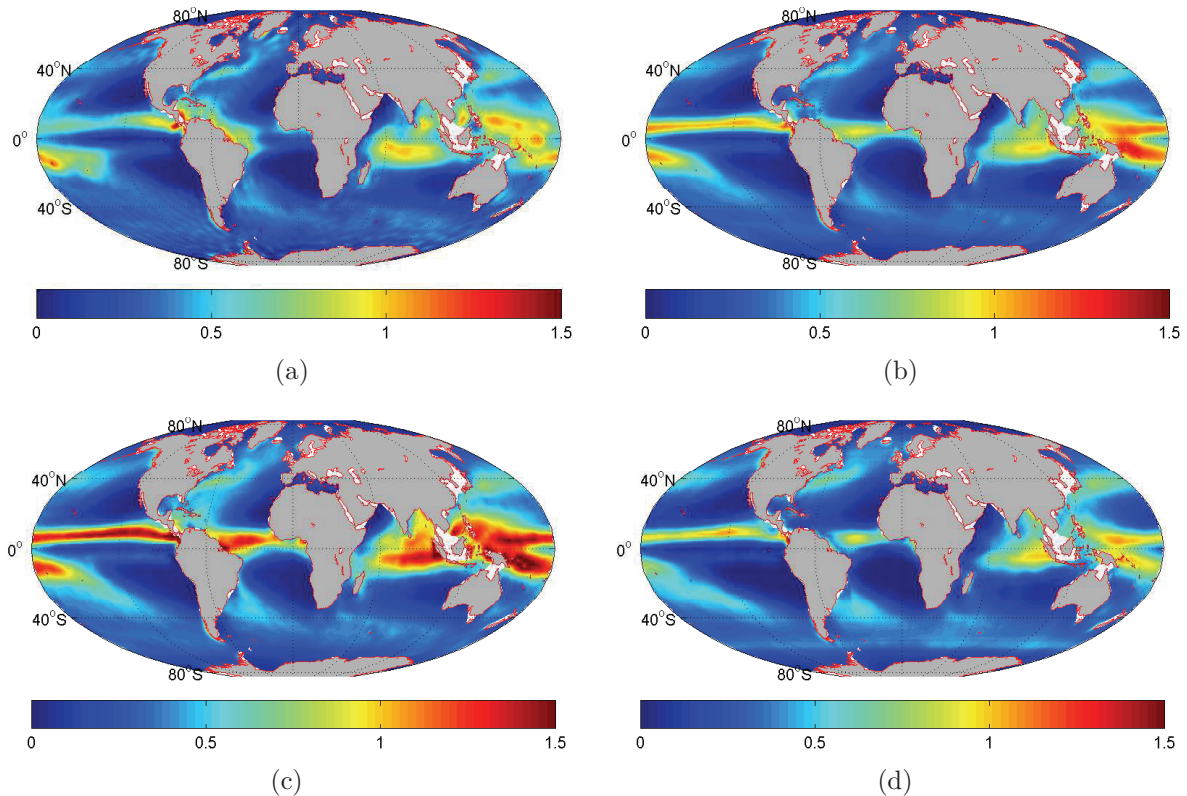


Figure 3.5: Ten year mean precipitation (1998 - 2007) of different data sets; (a): NCAR/NCEP reanalysis, (b): ERA Interim reanalysis, (c): ERA40 reanalysis (1998-2001) and operational ECMWF data (2002 -2007), (d): data from the Global Precipitation Climatology Project (GPCP). Units are in meter per year

consisting of measurements only. This data set is also interpolated to the model grid after missing values are filled, which naturally occur within a data set using only measurements and no model simulations (see Section 2.7.5). The ten year means of the different data sets and the GPCP data (1998 to 2007) show the spatial distribution of precipitation (Figure 3.5). The spatial distribution of precipitation of the ERA Interim reanalysis shows best fit to the GPCP data sets, especially in the equatorial region. The amount of precipitation is closer to the measurements of the GPCP data than the ERA40 reanalysis and the operational ECMWF data sets. Precipitation provided by NCAR/NCEP includes some artificial pattern mainly in the Southern Ocean originating from the spectral analysis during data processing at the data center. This leads to a slightly lower correlation of 0.82 to the GPCP data, compared to data sets provided by the ECMWF (Figure 3.6, left) having correlations of 0.92 for precipitation of ERA Interim reanalysis (Figure 3.6, middle) and

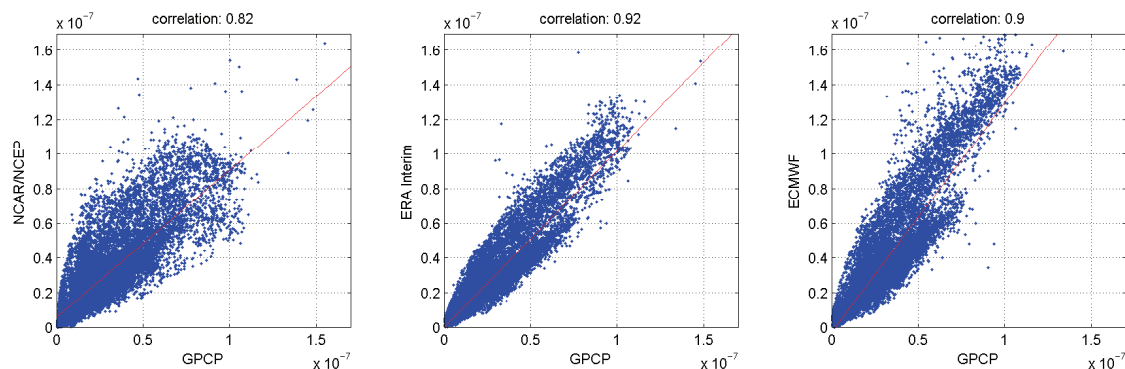


Figure 3.6: Correlation of ten year mean precipitation (1998-2007) from different data sets to GPCP; left: NCAR/NCEP Reanalysis, middle: ERA Interim Reanalysis, right: ERA40 reanalysis (1998-2001) and operational ECMWF data (2002-2007)

0.9 for precipitation provided by the ERA40 reanalysis/operational ECMWF data (Figure 3.6, right). All data sets show realistic geophysical patterns, whereas GPCP has lower precipitation rates in the tropical ocean especially compared to precipitation from the ERA40/operational ECMWF data reanalysis (Figure 3.7), causing the two clouds in their correlation.

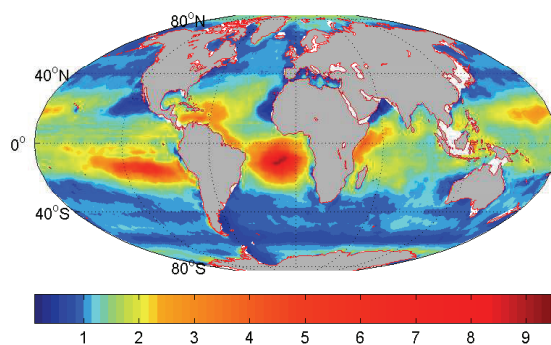


Figure 3.7: Ratio of ten year mean precipitation from GPCP and ECMWF (1998-2007); global mean: 1.4

### 3.3 Mass Balance in FESOM

The Boussinesq approximation, applied in FESOM, achieves conservation of volume, and a correction after Greatbatch, included into the model, conserves mass (Greatbatch, 1994;

Böning, 2009). The fresh water budget is closed by river runoff from the LSDM model, and precipitation and evaporation from NCAR/NCEP or the ECMWF weather centers are included as local volume flux to the reference model simulation. The different global fresh water fluxes (Figure 3.8, upper panel) and their sum (lower panel) show that the overall mass budget includes small long term trends.

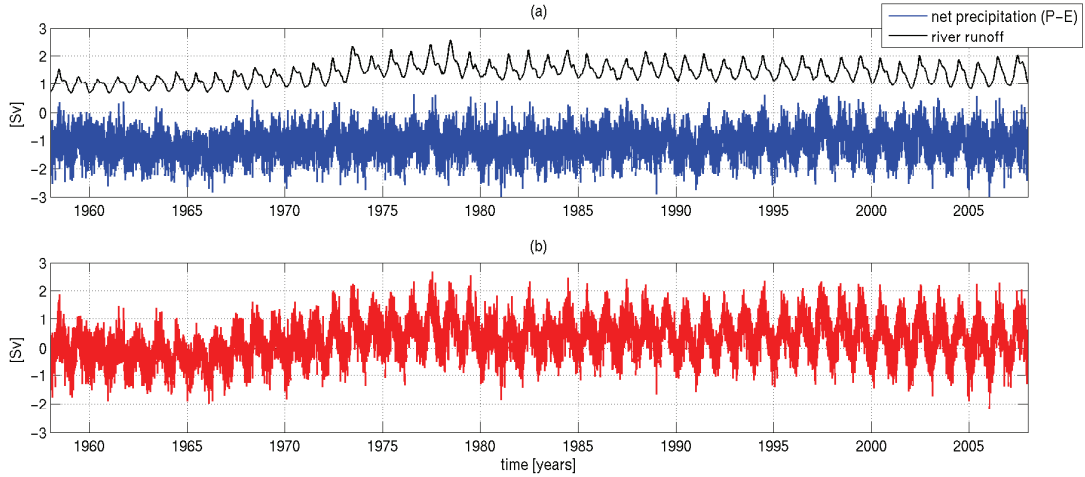


Figure 3.8: Global river runoff and net precipitation (a) and the total fresh water flux between atmosphere, ocean and land (b) in Sv

However, as already mentioned previously in Sections 2.7 and 3.2, the long term trends in the atmospheric data sets and the water mass exchanges between the continents and the ocean include high uncertainties. In addition, the small fresh water trends would lead to unrealistically strong trends in global mean ocean mass variations of FESOM. For these reasons, the global net freshwater flux has to be limited by realistic constraints. A two year running mean of the surface fluxes is scaled to be in equilibrium (Böning et al., 2008). Based on the assumption that river runoff is only poorly known it is scaled with a time dependent factor  $\alpha$ , which relates it to the net atmospheric flux (P-E) such that a global balance is achieved (Equation 3.1). This method, of course, does not allow to model long term trends of global mean ocean mass variation with FESOM<sup>1</sup>.

$$\overline{P}(t) - \overline{E}(t) + \alpha(t)\overline{R}(t) = 0 \quad (3.1)$$

where  $\overline{P}$  is the two 2 year running mean of precipitation,  $\overline{E}$  is the two year running mean evaporation,  $\alpha$  is scaling factor for river runoff, and  $\overline{R}$  is the two year running mean river

<sup>1</sup>The joint inversion described in Chapter 3.7 provides a mass correction term, which can be used to optimize the fresh water budget in the model, described in Section 3.7.2

runoff.

Alternatively, precipitation can be scaled when using ECMWF data sets within the model (Equation 3.2) instead of scaling the river runoff, because in comparison to measurements (GPCP data) precipitation of the different data sets provided by the ECMWF have higher long term trends in the global sum and overestimate precipitation rates in the equatorial region.

$$\alpha(t)\overline{P}(t) - \overline{E}(t) + \overline{R}(t) = 0 \quad (3.2)$$

Most data sets provided by the ECMWF, such as the ERA Interim reanalysis, are not available before 1989 and atmospheric data of the ERA40 reanalysis is used to spin up the model.

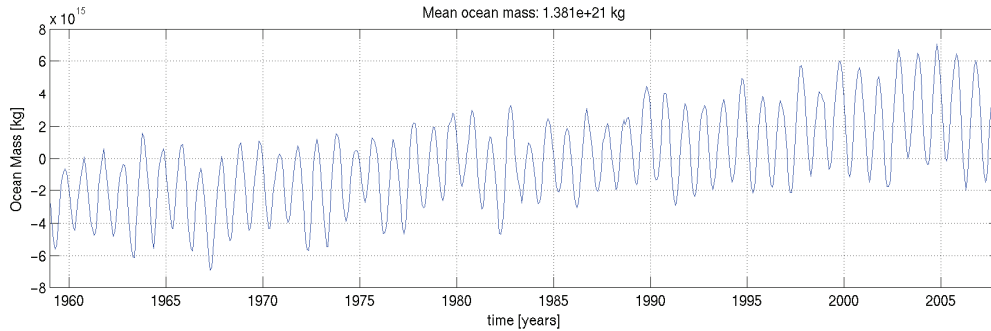


Figure 3.9: Variations of global mean ocean mass in kg

Global mean ocean mass of the reference model simulation, using data from LSDM model and the NCAR/NCEP reanalysis, is computed by subtracting the pressure of the atmosphere from ocean bottom pressure (in Pascal) and then dividing by the reference density of sea water  $\rho_w = 1027 \text{ kg/m}^3$  and the acceleration of gravity  $g = 9.806 \text{ m/s}^2$ . The mean global ocean mass is  $1.381 \cdot 10^{21}$  kg varying with an annual amplitude of about  $3 \cdot 10^{15}$  kg, which corresponds to approximately 9 mm equivalent water height (Figure 3.3).

Although the 2 year high pass filter has been applied, a positive mass trend of 0.3 mm/yr remains. This trend does not originate from the mass budget. If the heat exchange between atmosphere and ocean is set to zero, modeled global mean ocean bottom pressure can only be caused by mass variations. The pressure from the ocean bottom to the equipotential surface (geoid) is increasing due to cabelling, which occurs when two different water masses with same density but different temperature and salinity mix (Figure 3.10). The mixed water gets a higher density because of the non-linearity of the equation of state. It would continue to increase until a homogeneous ocean is reached. To conserve ocean mass, the

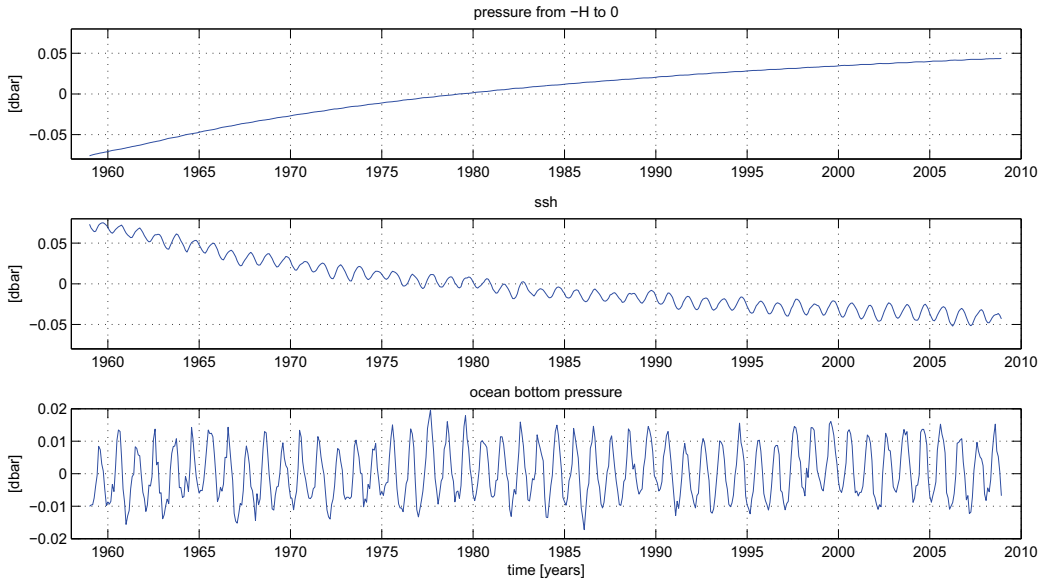


Figure 3.10: Variations in ocean bottom pressure anomalies, if the heat flux between the atmosphere and the ocean is set to zero. The upper panel shows the pressure from ocean bottom to the equipotential surface (geoid), the mid panel displays the sea surface height, and lower panel the ocean bottom pressure

correction after Greatbatch (Greatbatch, 1994; Böning, 2009) lowers the ocean volume by adjusting the sea surface height (see Section 2.2.2). The resulting global mean ocean bottom pressure includes no trend during the simulation period.

The trend in global ocean mass originates from numerical inconsistencies when computing  $\frac{\partial \eta}{\partial t}$  (temporal derivative of sea surface height) and  $\frac{\partial w}{\partial z}$  (vertical component of divergence). On one hand, small inconsistencies occur as  $\frac{\partial \eta}{\partial t}$  is computed at nodes and  $\frac{\partial w}{\partial z}$  element wise. On the other hand, both parameters need the same boundary conditions. When solving for  $w$ , it is slightly biased due to undetected inconsistent boundary conditions. This is not a strong issue when investigating sea surface height trends, but it poses a problem when solving for mass trends. To account for this, in the following analysis concerning ocean mass, only differences with respect to the reference model simulations will be investigated.

### 3.4 Weekly Ocean Bottom Pressure Anomalies

On the basis of the described mass balance ocean bottom pressure (OBP) anomalies are modeled with FESOM on weekly time scales. The period, which is investigated, starts on 5 January 2003, i.e. the first full GPS week in 2003, and ends in the last full GPS week

of 2008 (weeks from 1200 to 1511)<sup>2</sup>. OBP is computed through vertical integration of the water column by applying

$$p(\lambda, \phi, t) = \int_{-H}^0 \rho(\lambda, \phi, t, z)gdz + \int_0^{h(\lambda, \phi, t)} \rho_wgdz + p_a(\lambda, \phi, t) \quad (3.3)$$

where ocean depth is denoted as  $H$ ,  $h$  is the sea surface elevation,  $\rho$  the in-situ density, and  $p_a$  the atmospheric sea-level pressure (Böning et al., 2008).  $\lambda$  is the latitude and  $\phi$  the is longitude. Weekly anomalies are then computed by subtracting the multi-year mean OBP at each grid point.

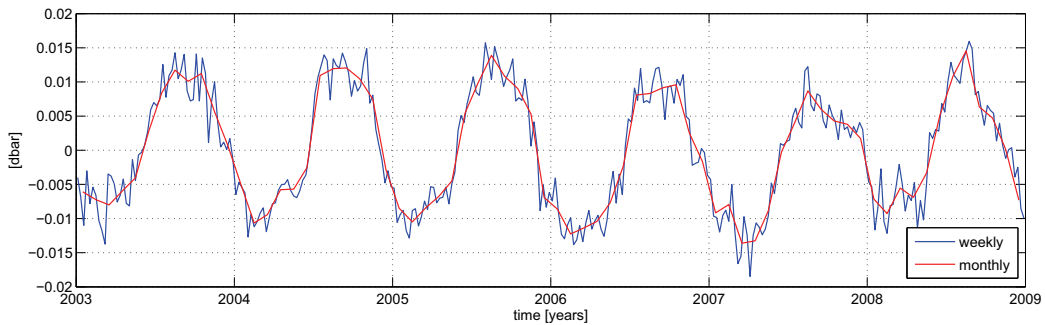


Figure 3.11: Global mean OBP variations modeled with FESOM (dbar)

The daily mean net precipitation (P-E) and variations in the global mean atmospheric pressure over the ocean introduce a short term variability in the global mean OBP. On monthly mean time series the short term variations are almost averaged out. The seasonal cycle in the global mean is induced by the net fresh water flux between land, ocean, and atmosphere. It has an amplitude of 11.2 mm equivalent water height and a phase of 244 (day of year). This is in good agreement with other studies (Blewitt and Clarke, 2003; Wu et al., 2006; Willis et al., 2008). More details on variations of global mean ocean mass are discussed in Rietbroek et al. (2009). Regionally weekly OBP variations can be separated into the contributions of ocean and atmosphere (Figure 3.12). The short term variability in the atmosphere is caused by the weather. To a large part, it is balanced by the inverse barometer effect leading to ocean mass anomalies of up to  $\pm 0.2$  dbar (atmospheric loading).

Comparing weekly mean OBP with monthly mean OBP anomalies (Figure 3.13), the amplitude of regional variations are about twice in the weekly solutions, whereas the geographical patterns remain the same. Strong variability appears mainly due to bottom topography as seen in the Southern Ocean, with a strong signal west of the Drake Passage.

<sup>2</sup>A GPS week corresponds to a time duration from Sunday through Saturday.

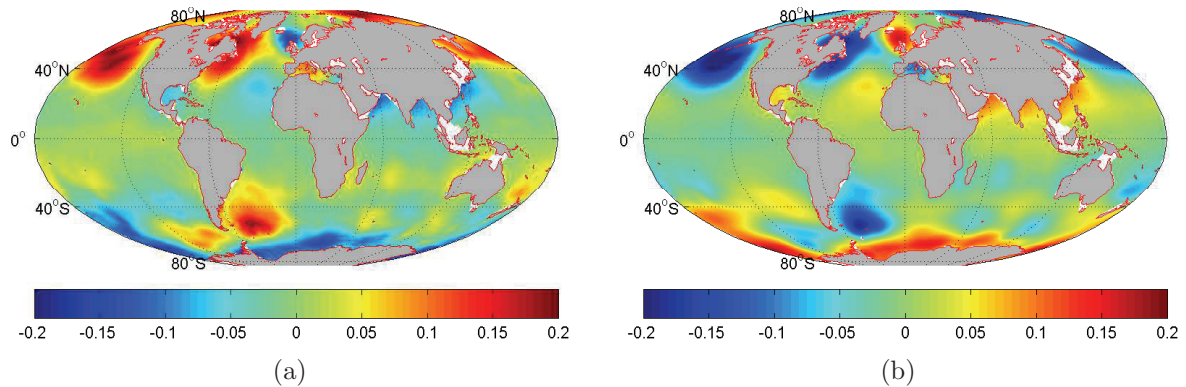


Figure 3.12: Weekly mean pressure of ocean (a) and atmosphere (b) of the first full GPS week in 2003 (week 1200) in dbar

Also semi-enclosed seas, such as the Hudson Bay or the Mediterranean Sea generally show high variability and are more sensitive to changes in the model configuration. Short term variations occur in the Arctic Ocean, which is generally homogeneously reacting to varying winds and atmospheric pressure fields. Also variability in ocean mass is high in regions of strong ocean currents, such as the Kuroshio, the Antarctic Circumpolar Current, or the Gulf Stream. In other regions in the open ocean, the variability appears to be rather moderate.

### 3.5 Error Estimation of Modeled Ocean Mass Variations

Error estimation is a crucial aspect when modeling OBP anomalies. Uncertainties of OBP are highly unknown. Among the errors of modeling OBP are those related to discretization. Further, model results generally suffer from uncertainties in the atmospheric forcing fields in particular from uncertainties in the mass fluxes used as model input. For example, the feature that long term trends may not be represented correctly in the data sets, used to define mass flux between atmosphere/ocean and land/ocean, directly affects the model results. Different model simulations are performed to investigate errors arising from spatial discretization as well as from the atmospheric forcing, which is the main driver of the ocean circulation.

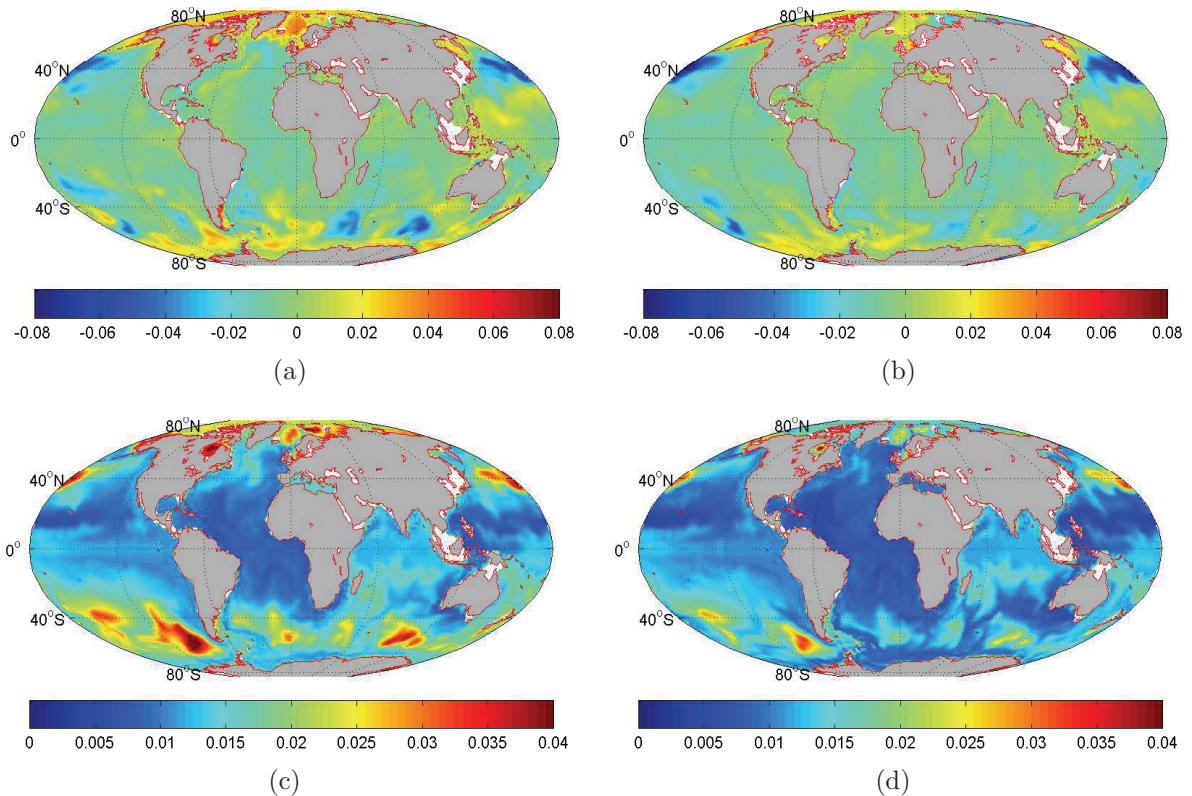


Figure 3.13: Monthly OBP and weekly OBP anomalies; (a): OBP anomalies of first full GPS week of year 2003 (week 1200) (b): OBP anomalies of January 2003 (c): Standard deviation of weekly mean OBP anomalies (d): Standard deviation of monthly mean OBP anomalies

### 3.5.1 Influence of Spatial Discretization

Modeled OBP is dependent on ocean bottom topography and on the spatial resolution, i.e. the size of the finite-elements. For example if the horizontal grid size is decreased, the model is able to represent small features like eddies, which are modifying ocean mass on small spatial scales.

To evaluate the influence of changed spatial resolution, a second model simulation has been performed using an alternative mesh including a refined grid structure in coastal regions. In addition, the grid has a modified topography. The difference between the OBP anomalies of the two experiments at the same location provides an estimate of the minimum error of the model, as they are only due to different numerical discretization. The main differences occur in the Southern Ocean and are related to the topographic features in this region. The first EOF of the difference (Figure 3.14a) shows an increased

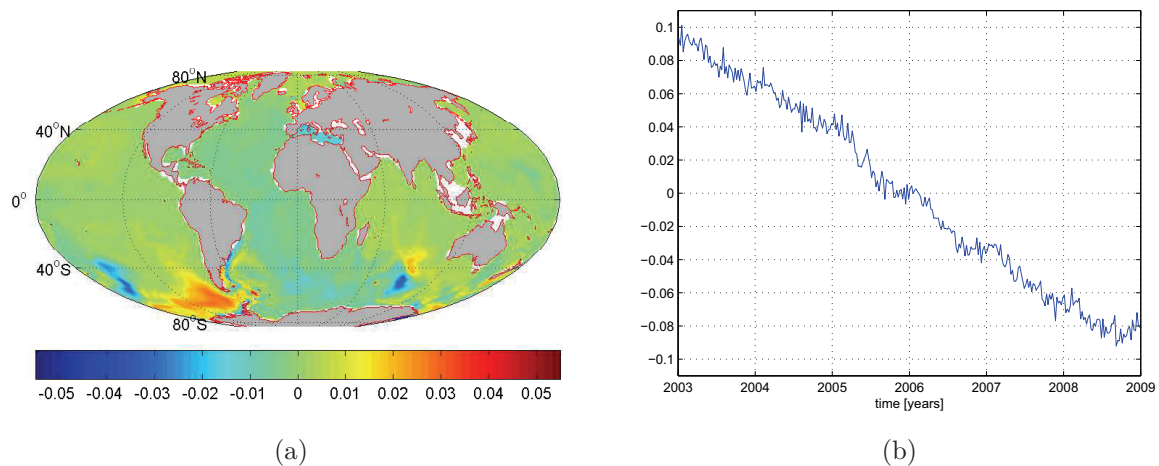


Figure 3.14: First EOF of the difference between OBP anomalies modeled with FESOM using different spatial discretization (a) and its principle component (b)

transport through the Drake Passage. Its principle component indicates a trend, related to the accelerating mass transport. It explains a variance of 46.6 percent (Figure 3.14b). The computed mass transport through the Drake Passage, simulated with the two model setups, range between 120 and 160 Sverdrups (Sv) with a slightly decreasing trend in the reference model simulation (Figure 3.15). The differences in mass transport amount up to 20 Sv in the last ten years.

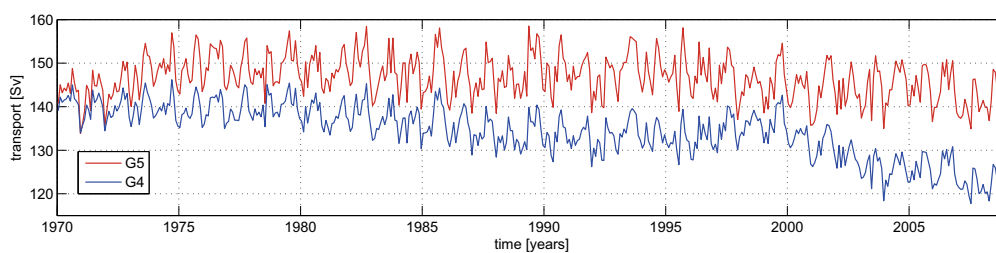


Figure 3.15: Volume transport through Drake Passage simulated with the reference model simulation (blue) and with an alternative grid (red)

The global mean OBP variations of the two model simulations are very similar (Figure 3.16, upper panel). Their difference has a very small range with a maximum of 1.1 mm, which can be neglected (Figure 3.16, lower panel). The difference between these model simulations would not lead to a realistic estimation of the error of modeled OBP, because the regional differences appear to be quite small. Only in the Southern Ocean, west of the Drake Passage more pronounced signals occur. For these reasons, the discretization error

does not provide reasonable error estimation, which could be used in the joint inversion (see Chapter 3.7).

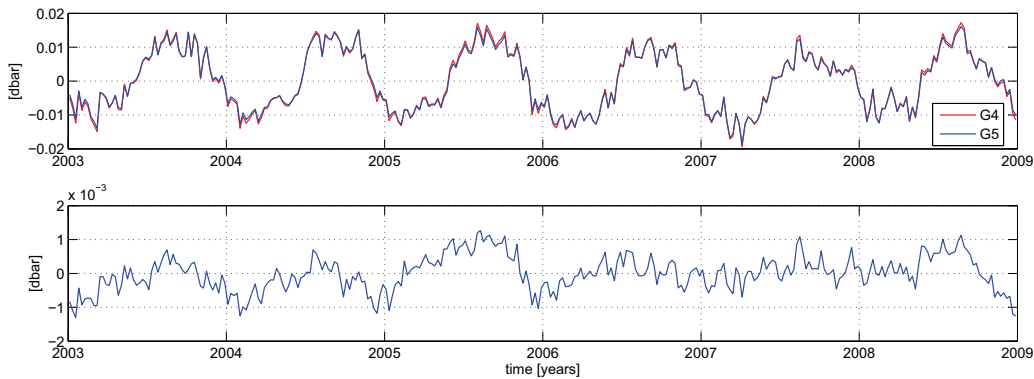


Figure 3.16: Global mean of modeled OBP using different spatial discretization; the upper shows both global mean ocean mass variations and lower panel their difference

### 3.5.2 FESOM and the Large Scale Geostrophic Model

Another possibility to estimate the error is to investigate OBP derived from an alternative model. Here, OBP anomalies from the large scale geostrophic model (LSG) are compared with OBP from the reference model simulation (FESOM), both applying the same ocean bottom topography.

The LSG model was originally developed to investigate climate change with time scales of thousands of years (Maier-Reimer and Mikolajewicz, 1991). After it has been combined with its adjoint, it has been used to simulate the ocean state (Wenzel and Schröter, 2002, 2007b). The simulations have a global configuration and a spatial discretization of  $1.5^\circ \times 1.5^\circ$  with 23 vertical layers. These layers vary in thickness from 20 m near the surface to 750 m near the ocean bottom. The LSG model conserves mass. Net freshwater fluxes are not separated into the individual contributions (precipitation, evaporation, and river runoff). OBP have been computed with the LSG model from January 1987 to December 2000 where measurements from the TOPEX/Poseidon and GEOSAT satellite missions and tide gauge records are assimilated.

For comparison with the LSG model results, monthly mean OBP anomalies of FESOM for the period from January 1991 to December 2000 are simulated. The resulting global mean OBP variations show significantly higher amplitude in the FESOM results as compared to the LSG model results (Figure 3.17). The phase of the seasonal cycle the FESOM

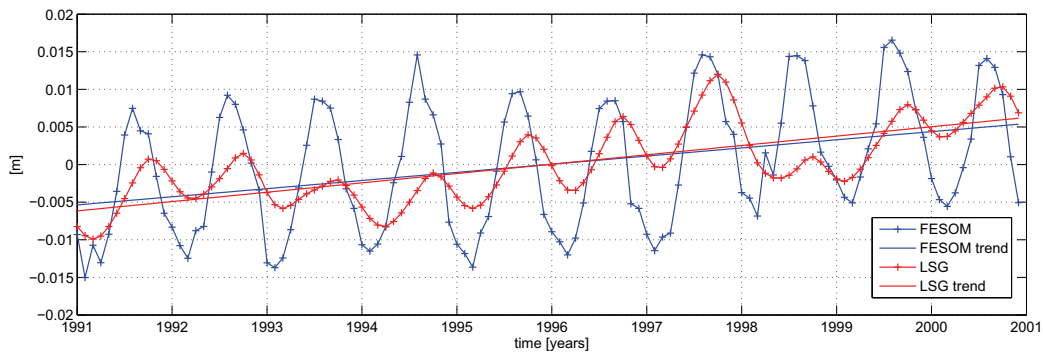


Figure 3.17: Global mean variations of modeled OBP anomalies simulated by FESOM and LSG in meter equivalent water height

results is slightly shifted compared to the phase of LSG model. The LSG model results contain a trend of 1.2 mm/yr, which is determined by the assimilation of measurements. Global mean OBP variations derived by FESOM shows a similar trend during this time period (1.1 mm/yr). Note, that this trend is not induced by the mass budget but results from the numerical inconsistencies when computing the temporal derivative of sea surface height and the vertical component of the divergence (described in Section 3.3).

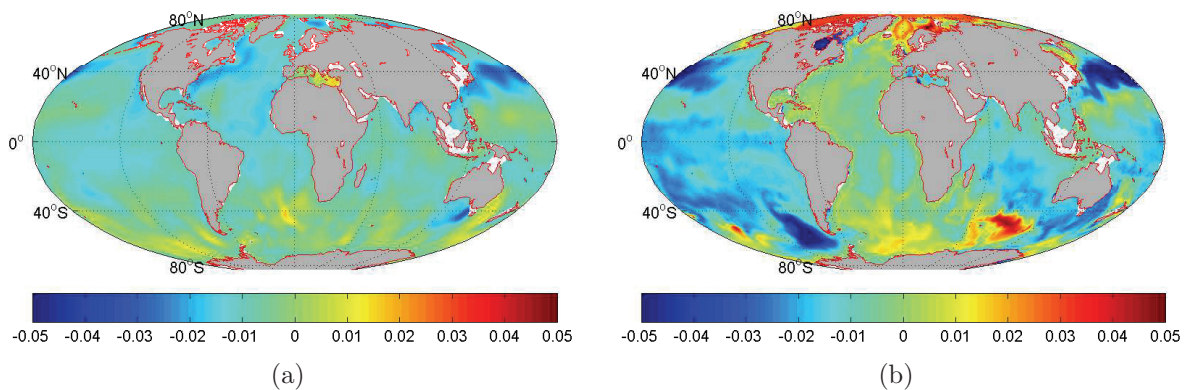


Figure 3.18: OBP anomalies of January 1991 derived with LSG (a) and FESOM (b) in dbar

Both model results show geophysical patterns originating from large scale currents, such as the Kuroshio or the Gulf Stream. In the polar regions, stronger variations in OBP are modeled with FESOM (Figure 3.18). In case of the LSG model, simulations suffer from low data availability for the assimilation process, as no altimetry measurements are provided for polar regions. When comparing regional trends of the time series of OBP

anomalies from FESOM and the LSG model, the values in the Atlantic Ocean and the Southern Ocean are mostly of opposite sign (Figure 3.19). For the Indian Ocean trends are similar. The same holds for the Mediterranean Sea. In the Pacific Ocean and in the Hudson Bay, almost no trend appears in the OBP anomalies derived from the LSG model, where FESOM exhibits a strong positive trend.

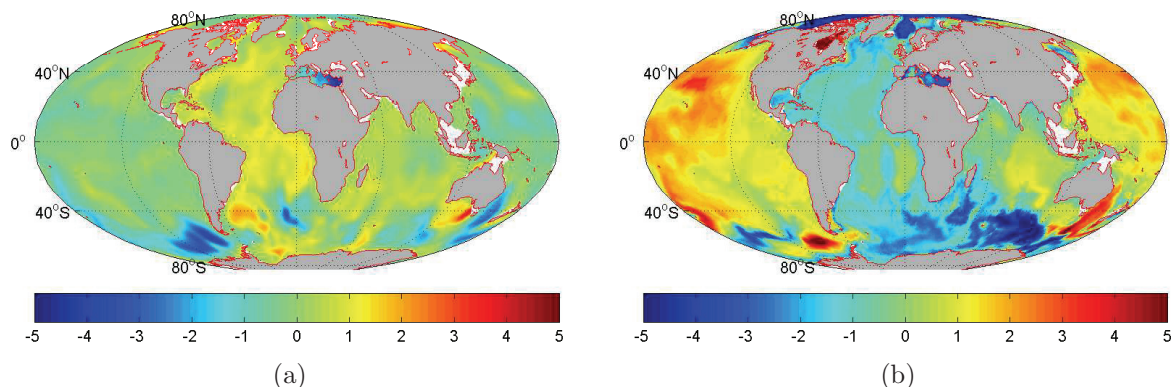


Figure 3.19: Regional trends of OBP anomalies (a) modeled with LSG and (b) modeled with FESOM in dbar

Generally, the amplitude of regional anomalies is much smaller in the LSG model than OBP in FESOM. If an error would be computed by taking differences, the anomalies modeled with FESOM would dominate and the error would mainly reflect its signals. Hence, the results are not used for the estimation of modeled OBP error.

### 3.5.3 Influence of Atmospheric Forcing

As already mentioned, the atmosphere is a driver of the ocean circulation and has a strong influence on the results of the model simulation. For this reason, the error of modeled OBP is estimated by comparing two model runs using different atmospheric forcing data sets, including different precipitation and evaporation fields. Instead of daily mean fields from the NCAR/NCEP reanalysis, used in the reference model simulation, the 6 hourly ERA40 reanalysis is used during spin up of a second model integration. The ERA Interim reanalysis, which also consists of 6 hourly data, is then used within FESOM from 1989 to 2008.

To analyze the influence of the two different atmospheric data sets, the two model runs have been performed for the period from 2003 to 2008. Major differences appear in the global mean ocean mass variations (Figure 3.20), whereas the seasonal cycles are almost

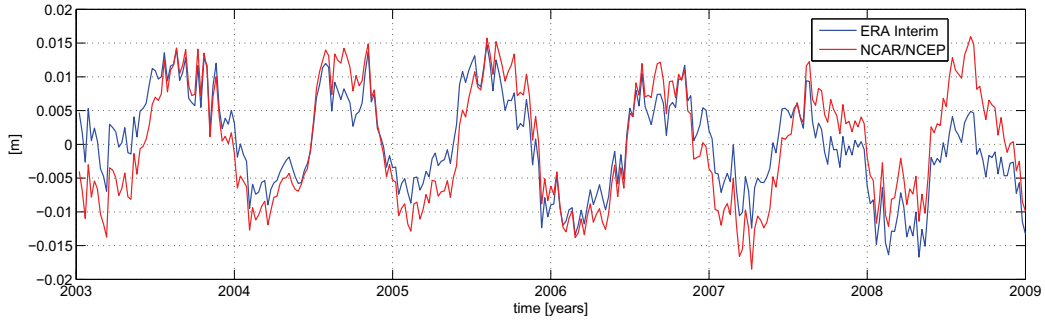


Figure 3.20: Global mean ocean mass variations in meter equivalent water height simulated using different atmospheric forcing.

in phase. The amplitude of the simulation using atmospheric parameters from the ERA Interim reanalysis is decreasing in the years 2007 and 2008 producing a slightly negative trend. Both time series show similar short term variations, caused by variations in mean mass of the atmosphere above the ocean.

$$\Delta p(\lambda, \phi) = \sqrt{\frac{1}{7} \sum_{d=1}^7 (\bar{p}_N^d(\lambda, \phi) - \bar{p}_E^d(\lambda, \phi))^2} \quad (3.4)$$

The weekly error of modeled OBP,  $\Delta p$ , is calculated by the weekly root mean square of the difference of daily mean OBP (equation 3.4).  $\bar{p}_N^d$  are daily mean OBP values modeled with forcing from the NCAR/NCEP reanalysis and  $\bar{p}_E^d$  are daily mean OBP values modeled with forcing from ERA-interim reanalysis.

The mean estimated error of modeled OBP is 0.04 m per  $1.5^\circ \times 1.5^\circ$  grid cell. The error maps show similar patterns for all weeks, varying in order of magnitude of mm. Major variations of the error occur in the Southern Ocean and in regions of shallow topography, which are not well connected to the open ocean, such as the Mediterranean Sea and the Hudson Bay, where OBP reacts very sensitive to changes in the forcing. The error for week 1200 (the first full GPS week in January 2003) ranges between 0.003 m in the ocean near the equator and 0.31 m in the Weddell and Ross Seas (Figure 3.21a). An error of about 0.1 m is found in the Southern Ocean west of the Drake Passage, which originates from differences in the wind fields. The Arctic Ocean also appears to be sensitive to perturbation in forcing fields (Brunnabend et al., 2010).

The root mean square of the differences between the two model runs indicates higher variability of the differences in the Southern Ocean because of topographic features and sensitivity of the strong currents of the Antarctic Circumpolar Current (Figure 3.21b).

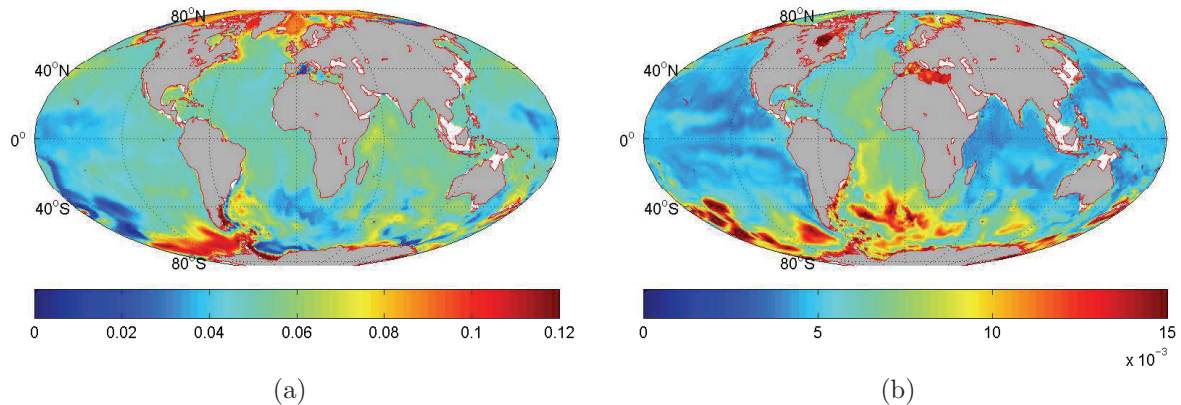


Figure 3.21: Estimated error of modeled OBP of first full GPS week in 2003 (week 1200) (a). For comparison, the standard deviation of OBP error in the period 2003-2008 is shown in panel (b).

The error of modeled OBP is validated in Chapter 3.8.3.

## 3.6 Gravity Recovery and Climate Experiment

Instead of modeling OBP, measurements from the Gravity Recovery and Climate Experiment (GRACE) can be used to estimate time-variable ocean mass on a global scale. In general, GRACE is measuring gravity variations of the Earth (Tapley et al., 2004; Bettadpur, 2007). These are caused by mass variations in the atmosphere and ocean, in land hydrology, in ice sheets and glaciers, and in the solid earth, for example due to plate tectonics. The system consists of two satellites in a nearly circular low Earth orbit (LEO) following each other with a distance varying between 200 km and 300 km. They fly in a nearly polar orbit with an inclination of  $89^\circ$  and an altitude of about 500 km. Their positions, velocity and the precise time are measured with the GPS system (appendix B).

The GRACE satellites fly with respect to the center of mass and measure the gravity of the Earth by computing variations in the distance between them. For example, if the first satellite gets closer to a region with higher density (e.g. a mountain), it will be attracted more than the second satellite as this is still farther away from this region. The increased distance between the satellites is measured by a microwave ranging system, both satellites have on-board. When the second satellite is also reaching the area of higher density the distance between the satellite become smaller again. If both satellites have the same distance to this region, the distance is minimum. It increases again, when the

Table 3.1: GRACE Solutions

|        |   |
|--------|---|
| GAA    | vertically integrated atmosphere from the background model (tide free mean atmosphere)  |
| GAB    | vertically integrated ocean from the background model (tide free mean ocean)  |
| GAC    | vertically integrated atmosphere over land and above ocean regions vertically integrated atmosphere and ocean from the background model (GAA + GAB) |
| GAD    | OMCT mean   |
| GSM    | Estimate of the gravity field for an epoch (residuals derived from GRACE)   |
| GACGSM | Combination of GAC and GSM which represent mean ocean mass variations   |
| GADGSM | Combination of GAD and GSM which represent mean ocean mass variations   |

first satellite is flying away from this region. After both satellites have passed this region and are far enough away, the distance between the satellites is the same as before they arrived at the radius of influence. Also non-gravitational forces are acting on the satellites, like air drag, solar radiation pressure, or attitude control activator impulses, which may influence the distance between the satellites. Hence, accelerometers are carried measuring surface force acceleration. Star cameras are measuring the attitude of the satellites and are responsible for the correct interpretation accelerometer measurements.

Although different GRACE gravity field solutions are made available by the four major research organizations, during this study, only solutions based on the GFZ RL4 processing are used. The solution consists of different products, whose content can be recognized by a special identifier (Table 3.1). Geo-potential estimates (G) are represented in spherical harmonics (SH) coefficients and can be converted to monthly mean OBP by equation 3.5 (Wahr and Molenaar, 1998) (Böning et al., 2008).

$$P_g = \frac{ag\rho_E}{3} \sum_{l=2}^{30} \sum_{m=0}^l \frac{2l+1}{1+k_l} \tilde{P}_{lm}(\sin\theta) [C'_{lm} \cos(m\Phi) + S'_{lm} \sin(m\Phi)] \quad (3.5)$$

where  $a$  is the radius of the Earth,  $\rho_E$  is the mean density of the Earth, and  $g$  the constant gravity acceleration. The spherical harmonics coefficients of degree  $l$  and order  $m$  are  $C'_{lm}$  and  $S'_{lm}$ .  $\tilde{P}_{lm}$  is defined as the fully normalized Legendre functions and  $k_l$  is the load love number of degree  $l$ , which describes the deformation of the Earth surface due to loading.

Products from the background model (A) are averaged over a specific time period. To determine OBP from GRACE measurements (S), the background model GAC or GAD has to be added to the GRACE estimate (GSM). Almost all GRACE solutions have to be filtered, because of aliasing effects, causing unrealistic meridional patterns (Seo et al., 2008). In this study, a two dimensional Gauss filter is applied (Wahr and Molenaar, 1998). The numerical ocean model for circulation and tides (OMCT) was chosen as background model for GRACE processing and the FES2004 tide model provides tide estimates that

are used for tidal correction of the GRACE products.

Note that K-band measurements from GRACE are not useful to resolve geocenter motion (SH degree 1 coefficients). This motion results from mass redistribution in the atmosphere, ocean and land. It is defined as the variations of the Earth's center of mass with respect to Earth's center of figure (CF). The two GRACE satellites fly with respect to center of mass (in the CM reference frame), which is defined as center of the solid Earth and the surface loads. It is stationary with respect to the GRACE orbits in inertial space (Blewitt, 2003). The reference frame CF instead is characterized by the geometric shape of the Earth (Rietbroek et al., 2009) and plays an important role in the analysis of GPS-networks or VLBI. It can be approximated by the CE reference frame (center of mass of the solid Earth). Compared to the CM frame, the CE frame cannot change its center, if redistributed mass causes deformations of the solid Earth (Blewitt, 2003).

Because of tidal aliasing the  $C_{20}$  coefficient can also not be well determined by GRACE (Chen and Wilson, 2008; Chen et al., 2008). This leads to some uncertainties, which for example can be solved by combining different data sets, as performed in the joint inversion. This issue is investigated in a related study (Rietbroek et al., 2009).

GRACE estimates with an increased temporal resolution to weekly time scales are provided by the GFZ Potsdam (Dahle et al., 2008). It is characterized by a decrease in spatial resolution as fewer measurements are available for the reduced averaging period. Another limiting factor is the orbit configuration. To achieve a maximum solution space of  $30 \times 30^3$ , a ground track analysis has been performed, based on predicted orbits of GRACE A and on the maximal spacing of ground tracks at degree 35N latitude (Dahle et al., 2008). The background models and standards are identical to GFZ RL04 monthly solutions. Currently the time series are provided for 306 estimates for weeks 1177 to 1489 (August 2002 to July 2008), with seven weeks missing due to erroneous GRACE L1B data (Dahle et al., 2008).

The background models GAA and GAB (Figure 3.22a, and 3.22b) show similar patterns as modeled with FESOM (Figure 3.12b, 3.12a), resulting from the fact that atmospheric pressure is causing the main structure of ocean mass redistribution and both models use pressure fields provided by the weather forecast centers ECMWF and NCEP. If the pressure of atmosphere and ocean is added, the sum can mostly be described by the inverse barometer effect. The remaining ocean signal is dominated by wind driven ocean circulation and large scale ocean waves.

The global mean OBP of both background model products are similar (Figure 3.23, black and blue lines in upper panel) and show a lower amplitude than seen in the FESOM

---

<sup>3</sup>These maximum of SH degree and order is best suited for the inversion, described in Section 3.7

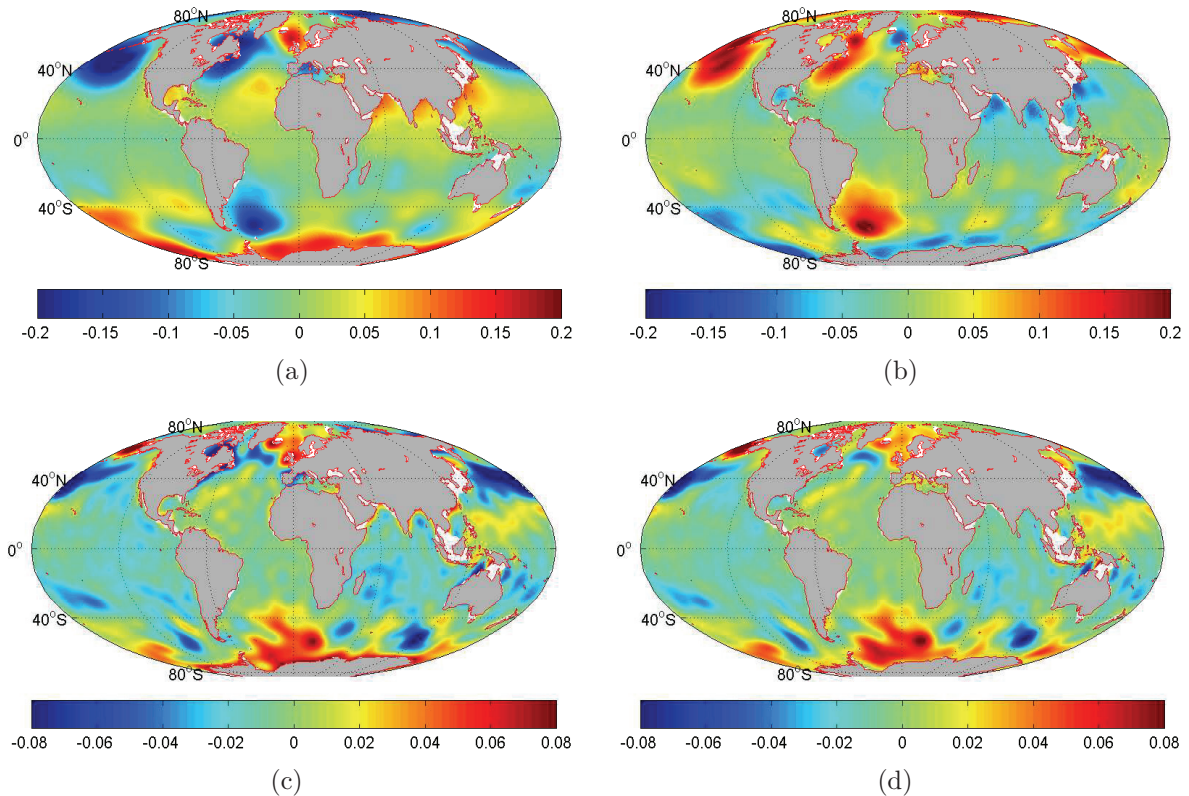


Figure 3.22: Weekly GRACE background models of the first full GPS week in 2003 (week 1200) in meter e.w.h. (a) the atmosphere product GAA (b) the ocean product GAB (c) GAC, which is the sum of Atmosphere (GAA) and Ocean (GAB) (d) GAD, which is the OMCT mean.

results (red). Also a phase shift is apparent, which disappears, when the GSM product is added to GAC and GAD (Figure 3.23, lower panel). The amplitudes are comparable. Compared to the GRACE estimates, the phase of of ocean mass variations from FESOM is better than in GAC. The amplitude in the background model is closer to the GRACE estimates.

OBP anomalies simulated with the background models (GAC and GAD) strongly correlate with OBP anomalies derived by FESOM (Figure 3.24a and 3.24b). Correlations higher than 0.6 appear mostly in the open ocean and a level of around 0.5 is found in the Arctic Ocean. Highest correlations are visible in the Indian ocean. Low correlations occur in the Mid Atlantic Ocean. Near coastlines the correlation decreases, for example near the coasts in the Amazon Delta or in the Indonesian region.

The weekly GRACE estimates, used for comparisons, are filtered with a Gauss filter

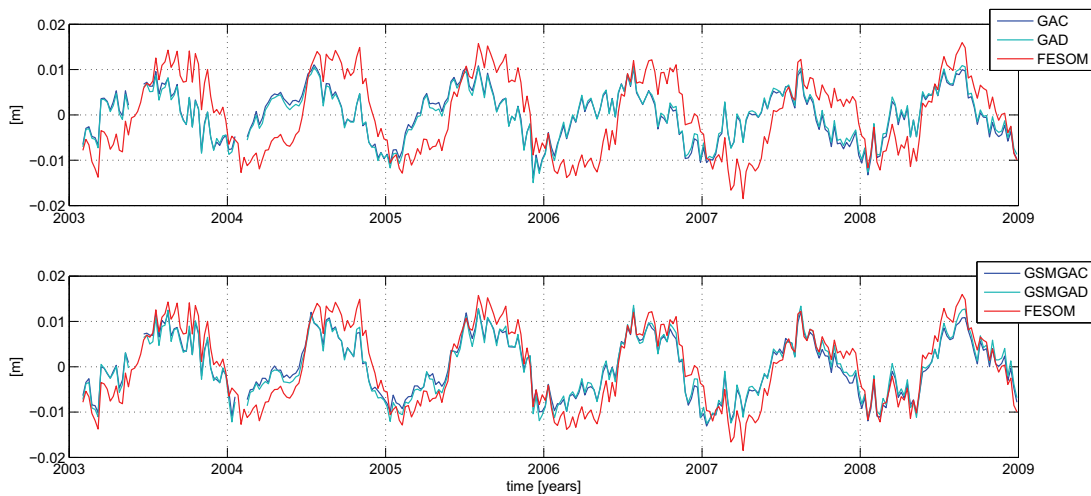


Figure 3.23: Global mean ocean mass variations derived with GRACE in meter equivalent water height.

to minimize aliasing artifacts. An averaging radius of 750 km is chosen as these solutions show best correlation with in-situ measurements (see Section 3.8.1). The GRACE products show less correlation with FESOM, compared with the correlation between FESOM and the background models (Figure 3.24c and 3.24d). Best correlation with values over 0.6 appear in the Arctic Ocean. Due to the filter, strong negative correlations occur in regions near the coasts as strong land hydrology signals are mixed with ocean signals, as seen for example in the Amazonian region (leakage effects).

The strong negative correlations found between the GRACE solutions and the FESOM results are much less visible between GRACE estimates and their background models (Figure 3.24e and 3.24f). Generally, GRACE estimates deviate more from their background models than from FESOM. Both background model products show low correlations to GRACE measurements in the Arctic Ocean and in the North Atlantic. In the Southern Hemisphere the correlation is higher, compared to the correlation between the GRACE estimates and FESOM. Near the Antarctic coast, the correlation between the GRACE estimates and the background model GAC is high, surrounded by a thin line of lower correlation. This feature probably results from the mass patterns over land, which are taken into account here. The correlation of the GRACE estimates and the background model GAD does not display them.

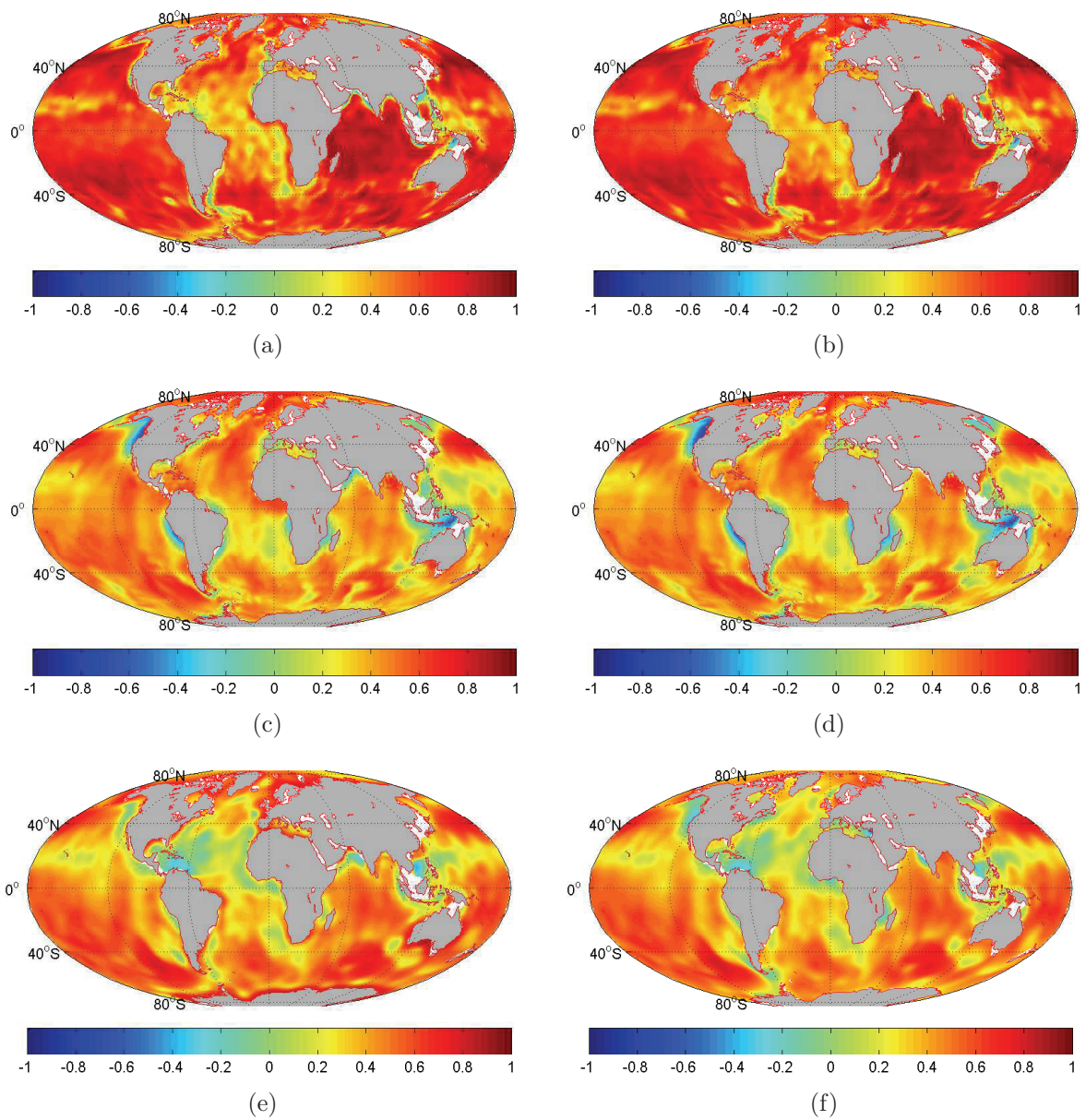


Figure 3.24: Correlation of OBP of GRACE Products and FESOM (degree and order up to 30); (a): GAC and FESOM, (b): GAD and FESOM, (c): GSMGAC and FESOM, (d): GSMGAD and FESOM, (e): Correlation of GAC and GSMGAC, and (f): Correlation of GAD and GSMGAD; for products including GSM a 750 km Gauss filter is applied

### 3.7 Joint Inversion

Although GRACE data can be used to measure ocean mass redistribution on a global scale, measurements suffer from the limited capability to measure geocenter motion, as only the GPS tracking of the two GRACE satellites can be used to for this issue. Also aliasing, leakage effects, and the limitations in spatial and temporal resolution cause problems in the processing and interpretation of the data. Hence, different studies augment the GRACE measurements and combine multiple data types to overcome these problems. Wu et al. (2006) estimated global surface mass distributions up to degree and order 50 on monthly time scales by combining GRACE gravity data with GPS displacements and ocean bottom pressure derived from the Estimating Circulation and Climate of the Ocean (ECCO) model. This ocean circulation model assimilates altimetry data, and the spatially uniform error for modeled OBP was assumed to be 1.7 cm for monthly averaged  $1^\circ \times 1^\circ$  grid cells.

A similar inversion scheme has been set up (Rietbroek et al., 2009; Jansen et al., 2009a), which combines GRACE gravity data, GPS site displacements and OBP from the ECCO model to estimate spherical harmonics coefficients up to degree and order 30 including geocenter motion on monthly time scales. The error of modeled OBP has been assumed to be 5 cm, which corresponds to the error of the satellite altimetry measurements that are assimilated into the model. First experiments have also been performed using the Finite Element Sea-ice Ocean Model (FESOM; Timmermann et al. (2009)) of this study instead of applying the ECCO model (Rietbroek et al., 2009; Jansen et al., 2009b). The weekly combination has been performed up to degree and order 30 and uses weekly GPS solutions, weekly modeled OBP, and sub-monthly GRACE solutions. An uncorrelated error of 5 cm per block-averaged grid cell  $5^\circ \times 5^\circ$  has been assumed for modeled OBP on the weekly basis.

In a collaborative effort between the Alfred-Wegener-Institute Bremerhaven, the German Research Center for Geosciences in Potsdam and the University of Bonn a strategy for a joint inversion of time series of GPS site displacements, modeled OBP anomalies and GRACE gravity data has been developed to describe mass transport and mass redistribution of the ocean. This project is part of the priority program SPP1257 "Mass transport and mass distribution in the Earth system" of the German Science Foundation (DFG). The objectives of the project are improving the accuracy of GRACE, solving for geocenter motion and increasing temporal resolution. The joint inversion, is developed by Roelof Rietbroek (University of Bonn) and published in Rietbroek et al. (2009). It is performed in a least squares sense, where the design matrices of the inversion are set up in the representation of the spherical harmonics (SH). Then a least squares adjustment is performed for the

weekly normal system including full covariance of the GRACE and GPS data sets. The error of the modeled OBP is defined in the first stage as a diagonal covariance assuming an uncorrelated error of  $\sigma = 10$  cm for each grid cell. This corresponds to about 3 cm for an averaged grid cell of size  $5^\circ \times 5^\circ$ . The normal system of equations is solved at every time step (week) without considering temporal correlation. Results are load coefficients (Stokes) and residual reference frame parameters, which possibly effect the geometric observations (translation, rotation and scaling). The inversion also provides the geocenter motion and a mass correction term, which is used to improve the mass balance of the FESOM model.

The three different data sets that are used in the inversion are independent and complementary. GPS site displacements are responsible for the low degrees, as this data set is capable to resolve geocenter motion. GPS site displacements are described in Appendix B. GRACE gravity data is useful to solve for the mid degrees without geocenter motion as the two satellite are flying with respect to center of mass of the earth, described in Section 3.6. Weekly OBP anomalies, derived during this study, are used to derive ocean mass variations, which corresponds to high SH degrees.

### 3.7.1 Impacts of modeled OBP Error to the Inversion

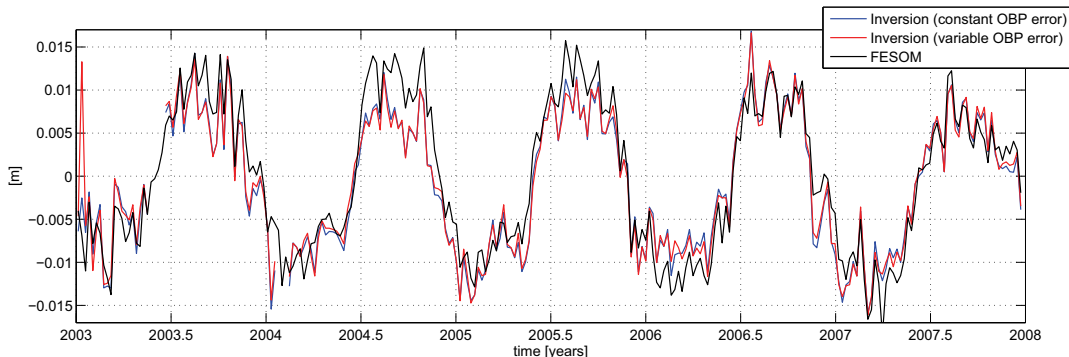


Figure 3.25: Weekly mean global ocean mass variations estimated by the joint inversion in meter equivalent water height

To improve the results, the error of modeled OBP estimated in Section 3.5.3 can be used in the inversion. This leads to a higher weighting of modeled OBP because the previous error is higher than that of the estimated variable error maps. Almost no differences in global mean ocean mass variations are seen using the alternative error estimation of modeled OBP (Figure 3.25). Generally, the inverse solutions show a smaller amplitude of the seasonal variations than the modeled OBP. FESOM simulates the phase of total ocean mass variations similarly to the GRACE solution, which also coincides well with

the inverse solution. The systematic difference occurring in the inverse solution, which includes the variable error of modeled OBP, at the beginning of year 2003, results from the problem of low GRACE data availability during this time period and the increased weighting of modeled OBP. This means that OBP modeled with FESOM might strongly influence the inverse solutions, if GRACE solutions are highly uncertain. As a consequence, in the following the first 4 weeks will not be considered further.

Both inverse solutions show the typical geophysical pattern in the weekly fields, showing reduced aliasing effects (Figure 3.26a and 3.26b). Hence, no filtering is applied for the following investigations. The variability strongly depends on the weighting of modeled OBP, especially in the polar regions, where less temporal variations are visible in the inverse solution using the variable error of modeled OBP (Figure 3.26c and 3.26d). This is caused by the generally less variable model results and its higher weighting in the inversion. The difference in the standard deviation of the inverse solutions and FESOM show that the inverse solution using the variable OBP error is closer to OBP derived with FESOM, especially in the Norwegian and Barents Sea, and in Southern Ocean (Figure 3.26e and 3.26f). The inverse solution still includes some stripes mainly visible in the Pacific Ocean. Also, the high differences at coastal regions occurring when using the constant error of modeled OBP in the inversion mostly remain, e.g. near the Antarctic and Greenland coasts.

### **3.7.2 Global Mass Correction derived from joint Inversion of GRACE gravity data, GPS site displacements, and modeled OBP**

The inversion of GRACE gravity data, GPS site displacements and modeled OBP provides a mass correction term for modeled OBP (Figure 3.27, upper panel). It is defined as a uniform layer of ocean mass, describing the difference of mean ocean mass derived from the inversion and the model simulation. The inversion calculations show that the correction term has zero mean and a standard deviation of 2.8 mm. It can be used to improve the fresh water budget of FESOM. The correction is performed by scaling precipitation with a factor  $\beta$  (equation 3.6). The precipitation rate is chosen as it allows a more global distribution of the mass correction term than for example river runoff. Furthermore, the global P is larger than the global R which implies that correcting P for the same total mass (per week) leads to a smaller relative correction (i.e.  $\beta$ ). The first derivative of the mass correction term is used as the inversion computes a bias for each week without correlation

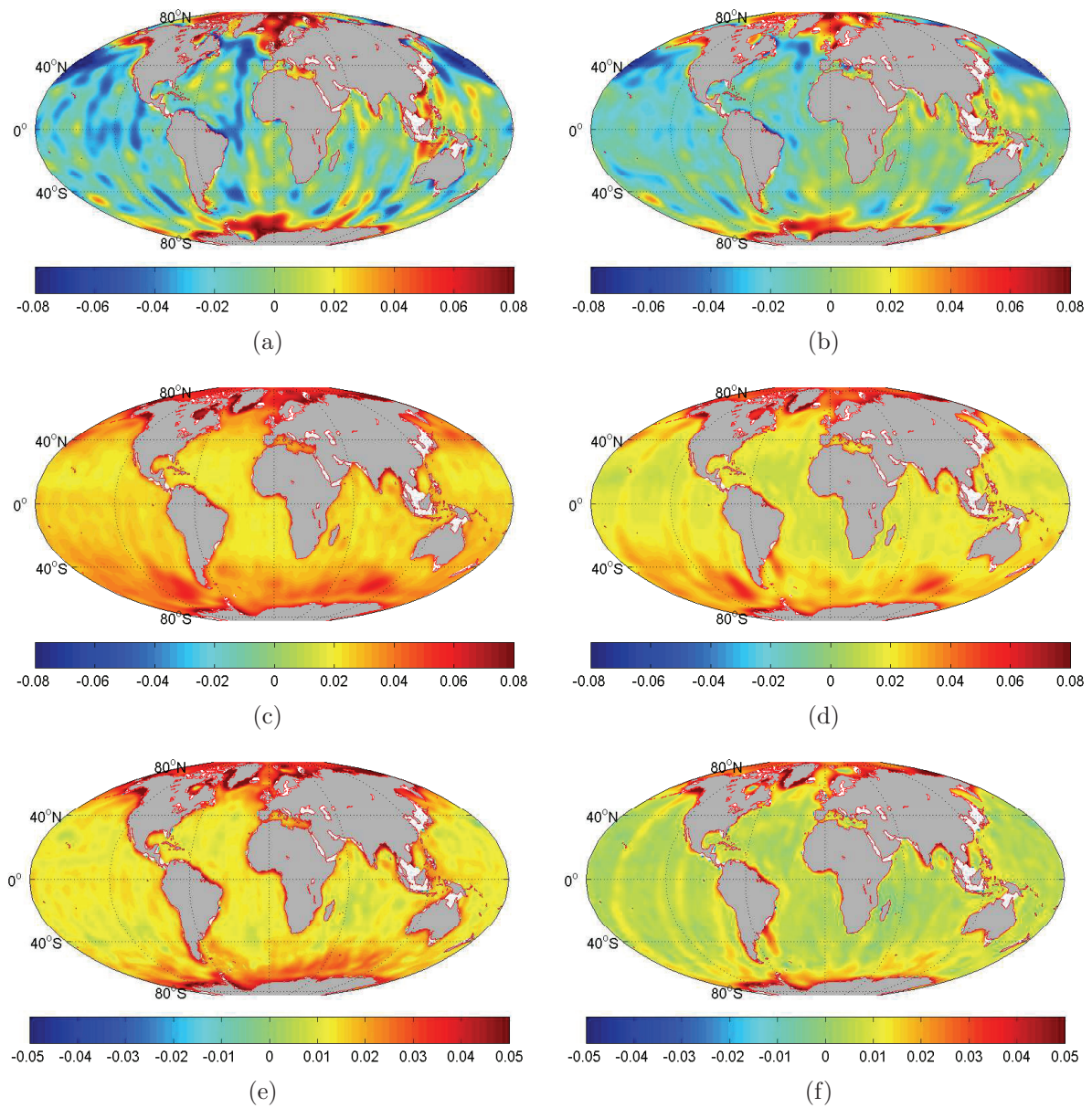


Figure 3.26: Inverse solutions in meter equivalent water height

- (a): Inverse solution using constant error of modeled OBP of first full GPS week in January 2003 (week 1200),
- (b): Inverse solution using variable error of modeled OBP of first full GPS week in January 2003 (week 1200),
- (c): Standard deviation of inverse solution using constant error of modeled OBP,
- (d): Standard deviation of inverse solution using variable error of modeled OBP,
- (e): Difference of STD of inverse solution using constant error of modeled OBP (c) and STD of modeled OBP,
- (f): Difference of STD of inverse solution using variable error of modeled OBP (d) and STD of modeled OBP

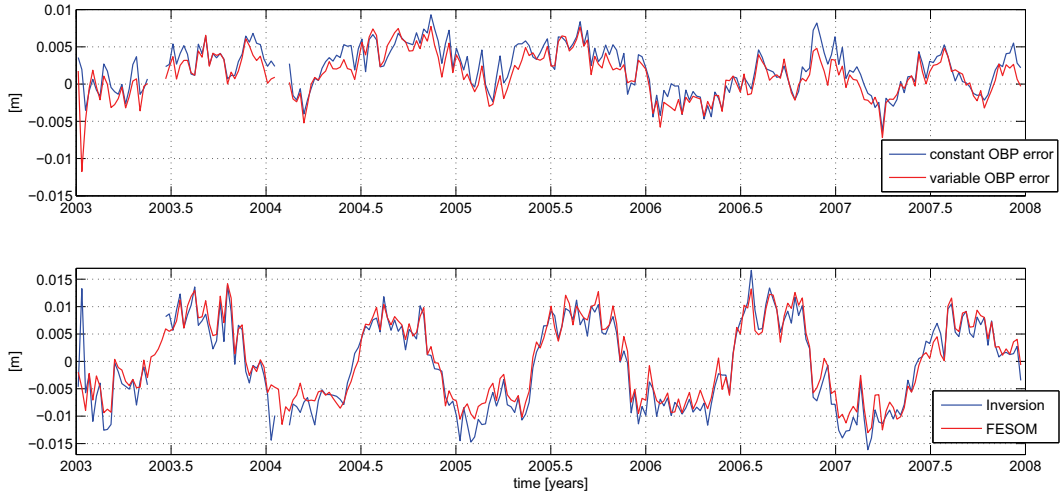


Figure 3.27: Ocean Mass Correction parameter (upper panel) and global mean ocean mass variations (lower panel), in equivalent water height.

with the neighboring weeks. The mass correction terms of the first four weeks of the inverse solution are not considered in the computation.

$$P^{new} = \beta P; \int P^{new} = \int P^{-\Delta M} d\Omega dt \quad (3.6)$$

The global precipitation is integrated over a week.  $\Delta M$  denotes the mass correction term. In the model the precipitation fields are multiplied with  $\beta$  and a subsequent model integration is performed.

Including the mass correction term as part of the model forcing reduces the amplitude of the simulated global ocean mass variation to values similar to those from the inversion (Figure 3.27, lower panel). Remaining differences between the two time series occur due to the truncation of the spherical harmonics at degree 30, causing the signal to be slightly blurred. Global mean ocean mass variations simulated by FESOM can be improved by introducing the mass correction term. Now it is possible to model global mean ocean mass with phase and amplitude similar to GRACE estimates. Also trends can be analyzed now if longer time series become available, as the mass budget is not only defined by the input parameters, but also refers to advanced ocean mass estimates, which mainly originate from GRACE and GPS measurements.

### 3.8 Ocean Bottom Pressure Recorders

About 152 time series at about 100 globally distributed locations from ocean bottom pressure recorders (OBPR) are available (Macrander et al., 2009). OBPR are deployed to estimate redistribution of mass in the ocean with a precision of up to 1 mm equivalent water height. OBPR measure the pressure at the ocean bottom, i.e. the pressure corresponding to ocean and atmosphere. The time period when measurements are taken differs at every location. OBPR are mainly deployed at locations with strong oceanographic interest. For example, ocean currents (e.g. in the Kuroshio extension) are investigated. Before the measurements can be used to compute weekly means, the time series have to be corrected for tides. To this end, results from the FES2004 tide model are subtracted from the OBPR measurements (Böning et al., 2008). It has to be mentioned that tide signals in OBPR measurements cannot be completely removed by subtracting estimates from the tide model. For instance, there are difficulties in separating the seasonal mass signal in OBPR from the seasonal tide signal. It may happen that the tide correction also reduces the seasonal mass signal. Also, time series have to be corrected for non-linear sensor drift by an exponential-linear fit function (least squares estimation) (Macrander et al., 2009). For this reason, OBPR measurements allow for investigations of short term variability but not for long term trends.

Time series of the inverse solutions, the modeled OBP and the weekly GRACE solutions (GSM+GAC) are compared with OBPR at three exemplary locations, one in the Southern Ocean and two in the North Atlantic (Figure 3.28). Generally the short term signal structure is best represented by FESOM, whereas seasonal variations, which are not well modeled in the FESOM results, are captured in the GRACE solutions. The inverse solutions using the estimated variable error of modeled OBP best represent the temporal mass signal measured with OBPR. This does not hold for the Arctic Ocean (see Figure 3.32b). At this location, the mass signal of the inverse solution (including the variable error) is much less correlated to OBPR than the signals of GRACE measurements and modeled OBP. Here, the inversion solution is not optimal, which indicates that there is still some potential of improvement, e.g. of the weighting scheme of the inversion.

When comparing OBP of the model simulations including the optimized fresh water budget with uncorrected model estimates, the regional influence of the mass correction term (see Chapter 3.7.2) is mostly limited up to a change in correlation of 0.05 (Table 3.2 and 3.3). The difference between the variance ratio is very small and can be neglected. This is expected, as the mass correction term is defined to be uniform over the globe and is not due to a change ocean circulation. The time sequence of the OBPR signals can be

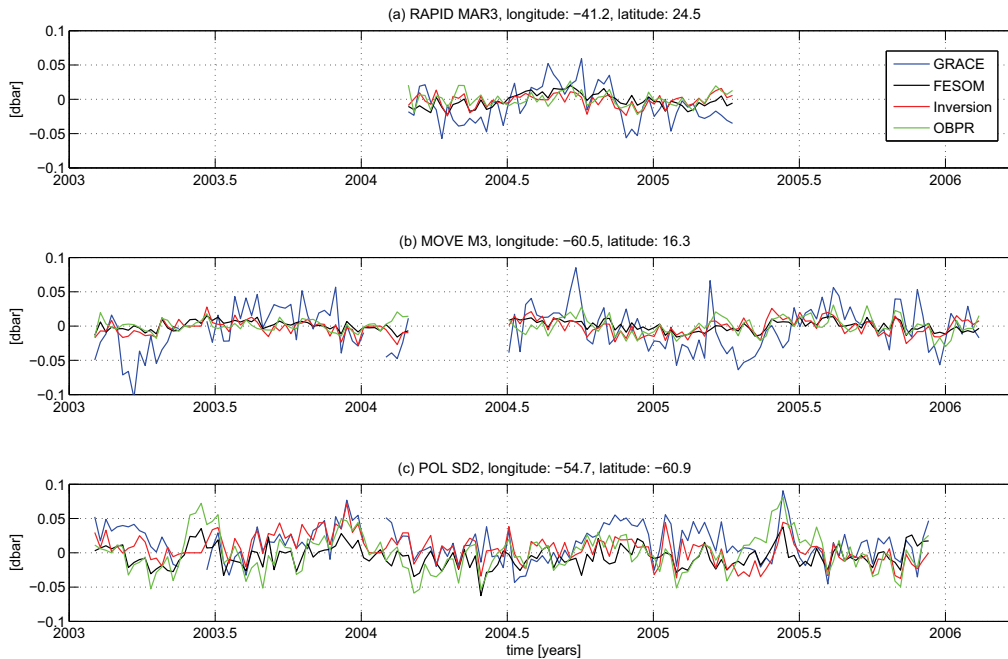


Figure 3.28: Comparison of ocean bottom pressure time series with OBPR at specific locations; (upper panel): RAPID MAR3 (24.5N 41.2W); (mid panel): MOVE M3 (16.3N 60.5W); (lower panel): POL SD2 (60.9S 54.7W).

represented well, e.g. at the location POL SD2 (South Drake Passage), AWI F8 (Fram Strait), and AWI ANT13a (ACC region). However, the short term and seasonal variability is not optimally described at many locations in both model simulations as seen at location 'AWI F8'. This is especially the case for the Kuroshio region where the variability of modeled OBP generally represents about 7% to 15 % of the variability of the OBPR measurements. For a complete list of all time series please refer to Appendix C to F.

### 3.8.1 Correlation with OBPR

The correlation between the different data sets and OBPR are highly dependent on the region (Figure 3.29a and 3.29b). This holds for the different GRACE solutions as well as for the FESOM model results, simulated with and without the mass correction term. For example, modeled ocean mass variations correlate well in regions like the Arctic Ocean. In other regions, (e.g. at the Kuroshio Current) the correlation between FESOM and OBPR is even higher than between the inverse solutions and OBPR. This is mainly due to the fact that in these regions weekly GRACE solutions (750 km Gauss filter applied) have lower correlation. This is partly due to the issue of solving the SH degree 1 and 2 coefficients

with GRACE only solutions. On the other hand FESOM cannot model the full variability, which is seen in the OBPR time series. Looking at the variance ratio  $R$ ,

$$R = \frac{\text{variance}(obp)}{\text{variance}(obpr)} \quad (3.7)$$

the signal of FESOM mostly represents only 0.2 to 0.5 times the variability in the long term signal of OBPR. Table 3.2 shows an overview of the correlations and regressions of all time series and OBPR that are longer than 25 weeks. The cell is shaded if the correlation is significant on a 95% confidence level. A dense pattern of OBPR is deployed in the Kuroshio Current (see Table 3.3).

Correlations between OBPR and the different data sets are depicted in Figure 3.29. If the correlation is significant at a location (on a 95% confidence level), the position is marked with a bold black circle. The correlation between OBPR and the model simulations forced by the reanalysis NCAR/NCEP (Figure 3.29a) and the ERA Interim (Figure 3.29b) are computed for the time series of the investigated period (year: 2003 to 2007). In general the correlations of both model simulations and OBPR are very similar, mainly resulting from the similar wind fields used. Only in a few regions like the mid Atlantic Ocean they differ slightly (up to 0.1). Most correlations are significant and appear to be between 0.5 and 0.9, only at few a locations the correlation is lower than 0.4. The correlation of modeled OBP using different model grids show similar correlations because small differences between the two model simulations are located mainly in the Southern Ocean west of the Drake Passage, where no OBPR were deployed (Figure 3.29c). If the fresh water budget is optimized by introducing the mass correction term into the mass budget of FESOM, correlation remains almost unchanged (Figure 3.29d). This has been expected, since the mass correction term influences the global mass budget, but not regional mass variations.

GRACE results show generally a good correlation with OBPR (Figure 3.29e and 3.29f). The Gauss filter influences the correlation, which appears to be high at most locations when an averaging radius (Wahr and Molenaar, 1998) of 750 km is chosen. Only at a few locations the correlation becomes smaller. Comparing the correlation between GRACE and OBPR with the correlation of modeled OBP and OBPR, the correlation of modeled OBP is much higher (about 0.2) in the Kuroshio region, in the South Drake Passage and in the Atlantic Ocean east of the Caribbean Sea (e.g. the array of the Meridional Overturning Variability Experiment (MOVE)). Both estimates show high correlations to OBPR in the Arctic Ocean and in the Southern Ocean, near the Kerguelen Islands, and low correlations at the Azores and the North Drake Passage. Correlations of GRACE and OBPR are higher than FESOM and OBPR in the Fram Strait and in the North Pacific, with a few exceptions

Table 3.2: OBPR Correlation with modeled OBP from the different model simulations (reference simulation, simulation using alternative atmospheric forcing, and including the optimized mass budget), weekly GRACE solutions, and the two inverse solutions. Corr denotes the correlation coefficient and R the variance ratio. If a correlation is significant on a 95 % confidence level, the cell is shaded

| Station ID  | FESOM<br>NCEP |       | FESOM<br>ERA Interim |       | FESOM<br>corrected |       | GRACE<br>weekly |       | Inversion |       | Inversion<br>(incl. err. OBP) |       |
|-------------|---------------|-------|----------------------|-------|--------------------|-------|-----------------|-------|-----------|-------|-------------------------------|-------|
|             | Corr          | R     | Corr                 | R     | Corr               | R     | Corr            | R     | Corr      | R     | Corr                          | R     |
| ANT11       | 0.62          | 0.47  | 0.62                 | 0.59  | 0.61               | 0.47  | 0.56            | 0.61  | 0.52      | 0.52  | 0.59                          | 0.40  |
| ANT13a      | 0.77          | 1.00  | 0.76                 | 1.40  | 0.76               | 1.00  | 0.67            | 1.20  | 0.66      | 0.94  | 0.74                          | 0.77  |
| ANT3        | -0.039        | 0.005 | -0.09                | 0.004 | 0.049              | 0.004 | 0.11            | 0.036 | 0.32      | 0.016 | 0.17                          | 0.008 |
| ANT5        | 0.32          | 0.081 | 0.21                 | 0.055 | 0.34               | 0.078 | 0.37            | 0.55  | 0.37      | 0.28  | 0.39                          | 0.16  |
| ANT537      | 0.40          | 0.14  | 0.27                 | 0.14  | 0.42               | 0.15  | 0.46            | 0.91  | 0.50      | 0.46  | 0.51                          | 0.28  |
| ANT7        | 0.69          | 0.21  | 0.63                 | 0.25  | 0.68               | 0.21  | 0.64            | 0.91  | 0.57      | 0.53  | 0.67                          | 0.34  |
| ANT9        | 0.62          | 0.36  | 0.55                 | 0.45  | 0.61               | 0.36  | 0.59            | 1.10  | 0.58      | 0.79  | 0.70                          | 0.57  |
| APL_ABPR_1  | 0.71          | 0.16  | 0.73                 | 0.19  | 0.69               | 0.15  | 0.73            | 1.00  | 0.51      | 0.97  | 0.55                          | 0.82  |
| APL_ABPR_3  | 0.73          | 0.23  | 0.74                 | 0.30  | 0.75               | 0.20  | 0.59            | 1.00  | 0.44      | 1.00  | 0.47                          | 0.89  |
| AWI_F2      | 0.57          | 0.22  | 0.57                 | 0.22  | 0.57               | 0.20  | 0.73            | 1.20  | 0.67      | 1.00  | 0.70                          | 0.76  |
| AWI_F4      | 0.68          | 0.21  | 0.68                 | 0.21  | 0.67               | 0.20  | 0.78            | 1.20  | 0.71      | 1.00  | 0.71                          | 0.77  |
| AWI_F5      | 0.68          | 0.16  | 0.66                 | 0.16  | 0.65               | 0.15  | 0.80            | 0.90  | 0.71      | 0.73  | 0.68                          | 0.55  |
| AWI_F6      | 0.58          | 0.17  | 0.58                 | 0.18  | 0.58               | 0.16  | 0.71            | 0.90  | 0.62      | 0.76  | 0.63                          | 0.60  |
| AWI_F7      | 0.63          | 0.12  | 0.63                 | 0.13  | 0.60               | 0.12  | 0.79            | 0.72  | 0.68      | 0.58  | 0.68                          | 0.45  |
| AWI_F8      | 0.64          | 0.14  | 0.62                 | 0.15  | 0.63               | 0.13  | 0.73            | 0.78  | 0.63      | 0.64  | 0.64                          | 0.51  |
| CNES_AMS    | 0.54          | 0.22  | 0.53                 | 0.28  | 0.52               | 0.22  | 0.55            | 0.36  | 0.41      | 0.29  | 0.46                          | 0.20  |
| CNES_CRO    | 0.58          | 0.27  | 0.57                 | 0.29  | 0.61               | 0.26  | 0.54            | 0.69  | 0.40      | 0.41  | 0.54                          | 0.23  |
| MOVE_M2.5   | 0.48          | 0.29  | 0.55                 | 0.26  | 0.48               | 0.22  | 0.078           | 4.30  | 0.18      | 0.81  | 0.20                          | 0.62  |
| MOVE_M3     | 0.55          | 0.43  | 0.50                 | 0.43  | 0.54               | 0.34  | 0.25            | 7.50  | 0.39      | 1.20  | 0.41                          | 0.97  |
| MOVE_M1     | 0.46          | 0.28  | 0.50                 | 0.26  | 0.61               | 0.24  | -0.065          | 5.30  | 0.15      | 0.98  | 0.44                          | 0.63  |
| MOVE_M1.5   | 0.19          | 0.18  | 0.21                 | 0.14  | 0.26               | 0.16  | 0.26            | 2.10  | 0.20      | 0.46  | 0.092                         | 0.28  |
| MOVE_M6     | 0.35          | 0.36  | 0.50                 | 0.28  | 0.43               | 0.3   | 0.17            | 4.50  | 0.45      | 0.90  | 0.49                          | 0.56  |
| MOVE_M2     | 0.43          | 0.11  | 0.55                 | 0.089 | 0.33               | 0.10  | -0.004          | 1.80  | 0.26      | 0.41  | 0.26                          | 0.29  |
| DART_d125   | 0.52          | 0.60  | 0.51                 | 0.48  | 0.56               | 0.48  | 0.34            | 4.50  | 0.43      | 1.80  | 0.49                          | 1.50  |
| DART_d157   | 0.12          | 0.088 | 0.14                 | 0.073 | 0.13               | 0.069 | 0.53            | 0.46  | 0.44      | 0.36  | 0.43                          | 0.18  |
| DART_d171   | 0.72          | 0.56  | 0.72                 | 0.63  | 0.74               | 0.52  | 0.63            | 0.78  | 0.57      | 0.66  | 0.64                          | 0.43  |
| DART_46402  | 0.26          | 0.12  | 0.37                 | 0.12  | 0.30               | 0.11  | 0.48            | 0.50  | 0.34      | 0.37  | 0.41                          | 0.20  |
| DART_46403  | 0.29          | 0.083 | 0.35                 | 0.067 | 0.31               | 0.063 | 0.33            | 0.57  | 0.27      | 0.46  | 0.34                          | 0.23  |
| DART_46404  | 0.30          | 0.37  | 0.43                 | 0.22  | 0.33               | 0.29  | 0.18            | 1.90  | -0.003    | 1.40  | 0.18                          | 0.83  |
| DART_46405  | 0.52          | 0.38  | 0.58                 | 0.30  | 0.59               | 0.28  | 0.14            | 1.80  | 0.30      | 0.72  | 0.45                          | 0.35  |
| DART_51407  | 0.29          | 0.16  | 0.33                 | 0.18  | 0.30               | 0.15  | -0.12           | 1.90  | -0.12     | 0.20  | 0.004                         | 0.17  |
| POL_IO1     | 0.66          | 0.29  | 0.66                 | 0.31  | 0.64               | 0.26  | 0.50            | 0.83  | 0.54      | 0.72  | 0.58                          | 0.45  |
| POL_IO2     | 0.65          | 0.26  | 0.56                 | 0.28  | 0.60               | 0.23  | 0.47            | 0.82  | 0.40      | 0.79  | 0.55                          | 0.52  |
| POL_ND2     | 0.26          | 0.018 | 0.30                 | 0.013 | 0.30               | 0.013 | -0.008          | 0.06  | 0.14      | 0.053 | 0.18                          | 0.035 |
| POL_SD2     | 0.70          | 0.36  | 0.65                 | 0.63  | 0.66               | 0.36  | 0.40            | 0.96  | 0.34      | 0.76  | 0.39                          | 0.57  |
| POL_MYRTLE  | 0.70          | 0.37  | 0.80                 | 0.39  | 0.75               | 0.32  | 0.35            | 1.50  | 0.33      | 0.61  | 0.45                          | 0.42  |
| POL_SHAGEX1 | 0.33          | 0.11  | 0.35                 | 0.11  | 0.28               | 0.085 | 0.34            | 0.36  | 0.26      | 0.31  | 0.20                          | 0.17  |
| POL_SHAGEX2 | 0.56          | 0.073 | 0.54                 | 0.053 | 0.58               | 0.056 | -0.003          | 0.31  | 0.24      | 0.25  | 0.48                          | 0.16  |
| RAPID_MAR1  | 0.48          | 0.43  | 0.49                 | 0.28  | 0.53               | 0.32  | 0.039           | 6.10  | 0.17      | 1.80  | 0.35                          | 0.89  |
| RAPID_MAR2  | 0.56          | 0.55  | 0.55                 | 0.35  | 0.61               | 0.41  | 0.085           | 7.70  | 0.25      | 2.30  | 0.46                          | 1.10  |
| RAPID_MAR3  | 0.44          | 0.91  | 0.53                 | 0.50  | 0.52               | 0.63  | 0.23            | 6.10  | 0.45      | 1.30  | 0.55                          | 0.80  |
| RAPID_MAR4  | 0.54          | 0.85  | 0.59                 | 0.47  | 0.60               | 0.59  | 0.32            | 5.70  | 0.49      | 1.20  | 0.60                          | 0.75  |
| RAPID_EB1   | 0.23          | 0.41  | 0.28                 | 0.19  | 0.27               | 0.26  | 0.18            | 2.40  | 0.21      | 0.70  | 0.30                          | 0.35  |
| RAPID_EB3   | 0.71          | 0.43  | 0.67                 | 0.28  | 0.69               | 0.25  | 0.35            | 3.30  | 0.066     | 1.70  | 0.10                          | 1.40  |
| RAPID_EBH1  | 0.43          | 0.63  | 0.48                 | 0.35  | 0.49               | 0.38  | 0.26            | 4.00  | 0.052     | 1.70  | 0.10                          | 1.30  |
| RAPID_EBH2  | 0.43          | 0.66  | 0.47                 | 0.38  | 0.48               | 0.41  | 0.21            | 5.00  | -0.022    | 2.80  | 0.01                          | 2.20  |
| RAPID_EBH3  | -0.026        | 0.43  | 0.13                 | 0.24  | 0.095              | 0.26  | 0.14            | 3.20  | -0.028    | 1.80  | 0.046                         | 1.40  |
| RAPID_EBH4  | 0.18          | 0.45  | 0.21                 | 0.26  | 0.24               | 0.28  | 0.098           | 3.40  | -0.015    | 1.90  | 0.021                         | 1.50  |
| RAPID_EBH5  | 0.26          | 0.20  | 0.12                 | 0.11  | 0.16               | 0.12  | 0.22            | 1.50  | 0.062     | 0.84  | 0.053                         | 0.65  |

Table 3.3: Correlations at the Kuroshio (KESS) array with modeled OBP from the different model simulations (reference simulation, simulation using alternative atmospheric forcing, and including the optimized mass budget), weekly GRACE solutions, and the two inverse solutions. Corr denotes the correlation coefficient and R the variance ratio. If a correlation is significant on a 95 % confidence level, the cell is shaded

| Station ID      | FESOM<br>NCEP |       | FESOM<br>ERA Interim |       | FESOM<br>corrected |       | GRACE<br>weekly |       | Inversion |       | Inversion<br>(incl. err. OBP) |       |
|-----------------|---------------|-------|----------------------|-------|--------------------|-------|-----------------|-------|-----------|-------|-------------------------------|-------|
|                 | Corr          | R     | Corr                 | R     | Corr               | R     | Corr            | R     | Corr      | R     | Corr                          | R     |
| <i>KESS_A2b</i> | 0.54          | 0.17  | 0.53                 | 0.19  | 0.56               | 0.15  | 0.23            | 0.20  | 0.50      | 0.14  | 0.56                          | 0.10  |
| <i>KESS_B1b</i> | 0.56          | 0.14  | 0.55                 | 0.14  | 0.60               | 0.11  | 0.46            | 0.20  | 0.57      | 0.18  | 0.65                          | 0.13  |
| <i>KESS_B2b</i> | 0.68          | 0.25  | 0.67                 | 0.27  | 0.73               | 0.22  | 0.45            | 0.24  | 0.54      | 0.20  | 0.64                          | 0.14  |
| <i>KESS_B3b</i> | 0.39          | 0.17  | 0.41                 | 0.18  | 0.43               | 0.15  | 0.32            | 0.19  | 0.26      | 0.15  | 0.29                          | 0.10  |
| <i>KESS_B4b</i> | 0.49          | 0.17  | 0.48                 | 0.16  | 0.52               | 0.15  | 0.25            | 0.17  | 0.34      | 0.14  | 0.43                          | 0.11  |
| <i>KESS_B5b</i> | 0.55          | 0.12  | 0.56                 | 0.12  | 0.57               | 0.11  | 0.32            | 0.12  | 0.38      | 0.096 | 0.47                          | 0.074 |
| <i>KESS_C1b</i> | 0.67          | 0.16  | 0.68                 | 0.14  | 0.67               | 0.13  | 0.45            | 0.27  | 0.53      | 0.26  | 0.65                          | 0.18  |
| <i>KESS_C2b</i> | 0.50          | 0.08  | 0.49                 | 0.075 | 0.51               | 0.063 | 0.27            | 0.11  | 0.52      | 0.11  | 0.54                          | 0.083 |
| <i>KESS_C3b</i> | 0.44          | 0.09  | 0.43                 | 0.10  | 0.50               | 0.08  | 0.23            | 0.10  | 0.36      | 0.081 | 0.45                          | 0.058 |
| <i>KESS_C4b</i> | 0.53          | 0.10  | 0.54                 | 0.11  | 0.57               | 0.086 | 0.30            | 0.11  | 0.32      | 0.08  | 0.44                          | 0.059 |
| <i>KESS_C5b</i> | 0.21          | 0.074 | 0.23                 | 0.077 | 0.25               | 0.061 | 0.11            | 0.12  | 0.12      | 0.08  | 0.13                          | 0.056 |
| <i>KESS_C6b</i> | 0.56          | 0.092 | 0.55                 | 0.094 | 0.58               | 0.083 | 0.21            | 0.13  | 0.43      | 0.084 | 0.56                          | 0.062 |
| <i>KESS_D1b</i> | 0.73          | 0.15  | 0.76                 | 0.14  | 0.70               | 0.12  | 0.39            | 0.38  | 0.51      | 0.34  | 0.60                          | 0.25  |
| <i>KESS_D2b</i> | 0.65          | 0.15  | 0.67                 | 0.15  | 0.67               | 0.12  | 0.41            | 0.18  | 0.46      | 0.14  | 0.55                          | 0.10  |
| <i>KESS_D3b</i> | 0.49          | 0.10  | 0.49                 | 0.12  | 0.54               | 0.095 | 0.36            | 0.15  | 0.40      | 0.088 | 0.45                          | 0.062 |
| <i>KESS_D4b</i> | 0.40          | 0.071 | 0.40                 | 0.075 | 0.44               | 0.063 | 0.21            | 0.095 | 0.30      | 0.071 | 0.36                          | 0.053 |
| <i>KESS_D5b</i> | 0.38          | 0.058 | 0.44                 | 0.058 | 0.39               | 0.051 | 0.13            | 0.071 | 0.20      | 0.05  | 0.22                          | 0.041 |
| <i>KESS_D6b</i> | 0.51          | 0.089 | 0.53                 | 0.09  | 0.51               | 0.079 | 0.10            | 0.11  | 0.30      | 0.079 | 0.36                          | 0.062 |
| <i>KESS_E1b</i> | 0.40          | 0.18  | 0.45                 | 0.18  | 0.42               | 0.14  | 0.27            | 0.45  | 0.29      | 0.38  | 0.38                          | 0.28  |
| <i>KESS_E2b</i> | 0.62          | 0.13  | 0.64                 | 0.13  | 0.61               | 0.11  | 0.37            | 0.17  | 0.45      | 0.14  | 0.47                          | 0.10  |
| <i>KESS_E3b</i> | 0.48          | 0.096 | 0.48                 | 0.099 | 0.49               | 0.081 | 0.30            | 0.13  | 0.39      | 0.11  | 0.39                          | 0.08  |
| <i>KESS_E4b</i> | 0.44          | 0.077 | 0.43                 | 0.082 | 0.46               | 0.068 | 0.17            | 0.10  | 0.38      | 0.079 | 0.43                          | 0.059 |
| <i>KESS_E5b</i> | 0.11          | 0.062 | 0.17                 | 0.063 | 0.10               | 0.053 | 0.027           | 0.075 | -0.058    | 0.056 | 0.11                          | 0.044 |
| <i>KESS_E6b</i> | 0.49          | 0.094 | 0.51                 | 0.095 | 0.47               | 0.083 | 0.17            | 0.12  | 0.34      | 0.083 | 0.36                          | 0.066 |
| <i>KESS_E7b</i> | 0.52          | 0.11  | 0.53                 | 0.11  | 0.51               | 0.097 | 0.20            | 0.17  | 0.35      | 0.10  | 0.43                          | 0.082 |
| <i>KESS_F1b</i> | 0.50          | 0.10  | 0.54                 | 0.10  | 0.51               | 0.079 | 0.15            | 0.20  | 0.32      | 0.18  | 0.34                          | 0.14  |
| <i>KESS_F2b</i> | 0.42          | 0.11  | 0.45                 | 0.11  | 0.44               | 0.094 | 0.35            | 0.14  | 0.33      | 0.11  | 0.31                          | 0.08  |
| <i>KESS_F3b</i> | 0.34          | 0.10  | 0.34                 | 0.11  | 0.35               | 0.089 | 0.076           | 0.16  | 0.17      | 0.11  | 0.21                          | 0.089 |
| <i>KESS_F4b</i> | 0.30          | 0.086 | 0.31                 | 0.09  | 0.30               | 0.074 | 0.11            | 0.10  | 0.23      | 0.082 | 0.32                          | 0.064 |
| <i>KESS_F5b</i> | 0.31          | 0.089 | 0.32                 | 0.094 | 0.27               | 0.08  | 0.18            | 0.15  | 0.33      | 0.094 | 0.29                          | 0.076 |
| <i>KESS_F6b</i> | 0.42          | 0.072 | 0.42                 | 0.076 | 0.38               | 0.064 | 0.35            | 0.12  | 0.42      | 0.081 | 0.43                          | 0.064 |
| <i>KESS_G1b</i> | 0.72          | 0.12  | 0.70                 | 0.12  | 0.71               | 0.098 | 0.23            | 0.17  | 0.50      | 0.12  | 0.55                          | 0.093 |
| <i>KESS_G2b</i> | 0.69          | 0.12  | 0.68                 | 0.12  | 0.68               | 0.099 | 0.16            | 0.17  | 0.39      | 0.13  | 0.44                          | 0.095 |
| <i>KESS_G3b</i> | 0.053         | 0.12  | 0.049                | 0.13  | 0.031              | 0.10  | -0.078          | 0.15  | 0.009     | 0.12  | 0.071                         | 0.094 |
| <i>KESS_G4b</i> | 0.31          | 0.14  | 0.31                 | 0.14  | 0.27               | 0.12  | 0.036           | 0.17  | 0.15      | 0.13  | 0.23                          | 0.11  |
| <i>KESS_G5b</i> | 0.39          | 0.073 | 0.41                 | 0.077 | 0.33               | 0.064 | 0.29            | 0.11  | 0.27      | 0.07  | 0.32                          | 0.058 |
| <i>KESS_G6b</i> | 0.31          | 0.27  | 0.35                 | 0.29  | 0.31               | 0.24  | 0.088           | 0.40  | 0.30      | 0.26  | 0.29                          | 0.22  |
| <i>KESS_H2b</i> | 0.68          | 0.096 | 0.67                 | 0.098 | 0.65               | 0.083 | 0.081           | 0.17  | 0.42      | 0.11  | 0.49                          | 0.088 |
| <i>KESS_H3b</i> | 0.58          | 0.16  | 0.59                 | 0.16  | 0.53               | 0.14  | 0.25            | 0.26  | 0.24      | 0.18  | 0.31                          | 0.15  |
| <i>KESS_H4b</i> | 0.098         | 0.13  | 0.13                 | 0.14  | 0.068              | 0.11  | 0.088           | 0.20  | 0.076     | 0.14  | 0.12                          | 0.12  |
| <i>KESS_H5b</i> | 0.34          | 0.085 | 0.39                 | 0.09  | 0.27               | 0.077 | 0.18            | 0.17  | 0.17      | 0.096 | 0.15                          | 0.084 |
| <i>KESS_H6b</i> | 0.38          | 0.17  | 0.39                 | 0.19  | 0.35               | 0.15  | 0.19            | 0.32  | 0.26      | 0.20  | 0.24                          | 0.16  |
| <i>KESS_I1b</i> | 0.52          | 0.25  | 0.55                 | 0.26  | 0.51               | 0.21  | 0.23            | 0.45  | 0.31      | 0.24  | 0.34                          | 0.20  |
| <i>KESS_N1b</i> | 0.65          | 0.21  | 0.65                 | 0.23  | 0.67               | 0.18  | 0.39            | 0.24  | 0.50      | 0.17  | 0.61                          | 0.12  |
| <i>KESS_S1b</i> | 0.70          | 0.29  | 0.73                 | 0.31  | 0.70               | 0.24  | 0.38            | 0.60  | 0.39      | 0.32  | 0.48                          | 0.25  |
| <i>KESS_S2b</i> | 0.40          | 0.41  | 0.43                 | 0.43  | 0.43               | 0.33  | 0.36            | 0.88  | 0.34      | 0.49  | 0.38                          | 0.40  |

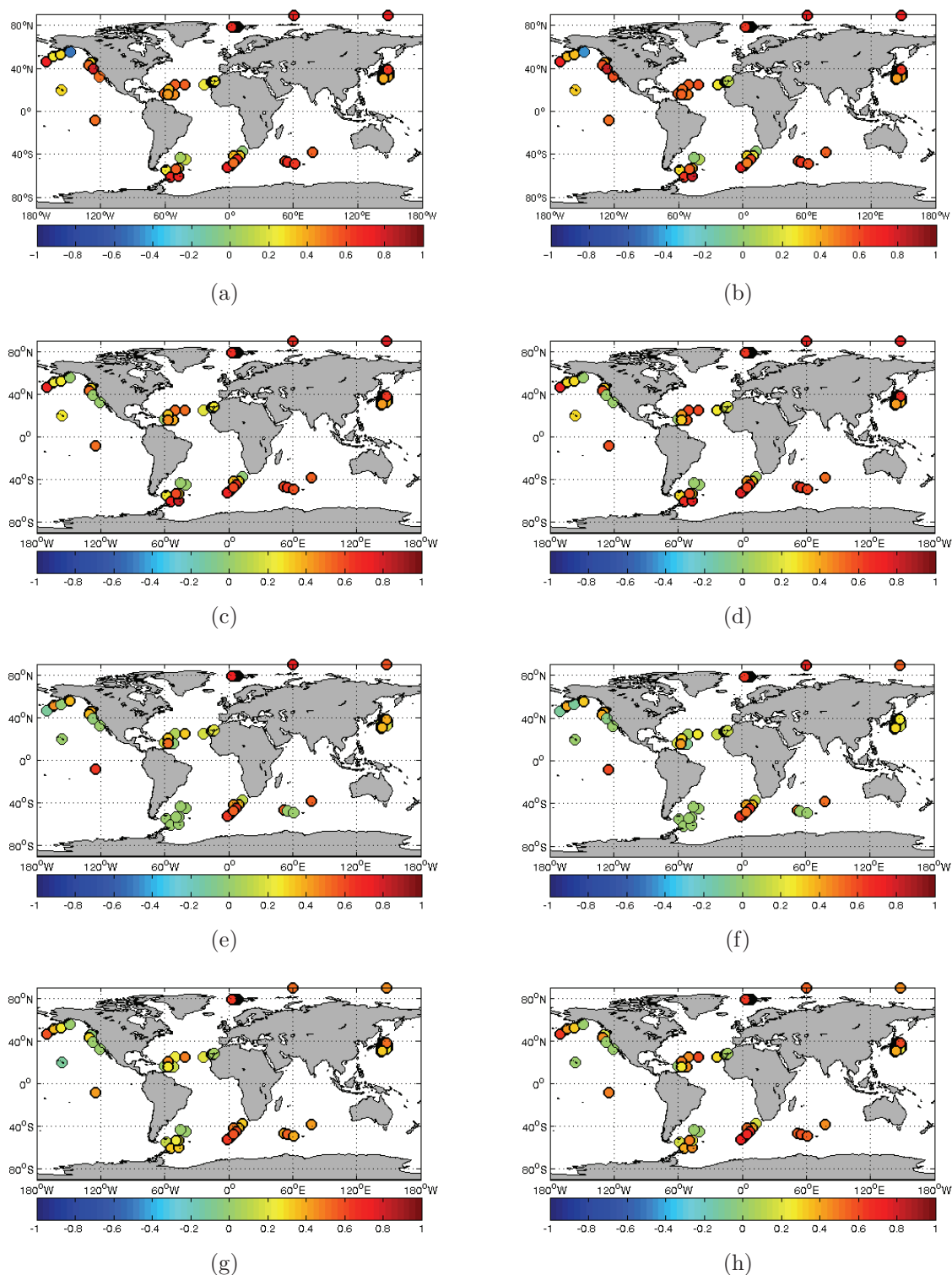


Figure 3.29: Correlation of OBPR with (a) FESOM using NCAR/NCEP reanalysis as atmospheric forcing, (b) FESOM using ERA Interim reanalysis as atmospheric forcing, (c) FESOM using an alternative spatial discretization, (d) FESOM including optimized fresh water budget, (e) GRACE GSMGAC solution filtered with 750 km Gauss filter, and (f) GRACE GSMGAD solution filtered with 750 km Gauss filter, (g) Inverse solution using assumed constant OBP error, (h) Inverse solution using space and time variable error of modeled OBP

(Brunnabend et al., 2010).

The representation of mass signals is improved by combing different data sets as described in Chapter 3.7 (Figure 3.29g). This is especially true for the MOVE array (Atlantic Ocean east of the Caribbean Sea), where GRACE only solutions have low correlation to OBPR (Kanzow et al., 2005). Further increased correlation of the inversion results is achieved when introducing the variable error of modeled OBP in the inversion. However, correlation of the inverse solutions and OBPR measurements depends on the weighting of the individual data sets. If one data set has a low weight, because the data set includes high uncertainties, some of the signals from this data set may be damped during the inversion.

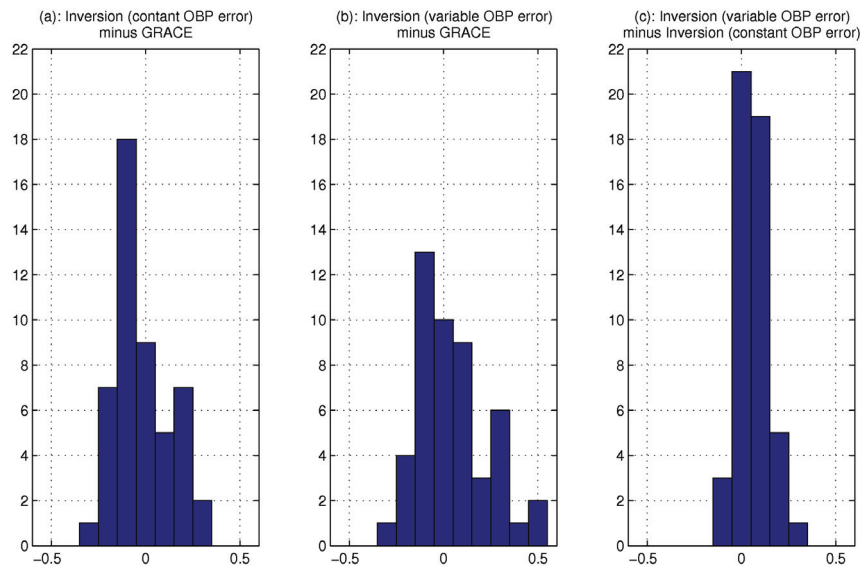


Figure 3.30: Histogram of the differences between correlations with OBPR measurements and (a): Inversion (constant OBP error applied) and weekly GRACE (750 km Gauss filter applied), (b): Inversion (variable OBP error applied) and weekly GRACE (750 km Gauss filter applied), as well as (c): Inversion (variable OBP error applied) and Inversion (constant OBP error applied)

The influence of the weighting on the combinations of different data sets is also visible in Figure 3.30 (Brunnabend et al., 2010). Even with a constant error of modeled OBP, the inverse solution shows at many positions a higher correlation with OBPR measurements than the GRACE-only solutions. At some positions, however, the correlation decreases, e.g. south of Africa crossing the ACC. This is largely cured when the estimated error of modeled OBP is applied. Compared to GRACE data, the correlation to OBPR data is increased by up to 0.5. Compared to the inversion with the constant model error applied, the correlation to OBPR increased in almost all cases, only at three positions it gets smaller.

Because of the large number of deployments, the OBPR measurements in the Kuroshio Current region are not included here. Figure 3.30 clearly demonstrates that the inverse results improve the OBP estimate over a GRACE only solution (a,b). The improvement is much more pronounced, when variable OBP error is taken into account (c).

### 3.8.2 OBPR for Regional Mean Mass Variations

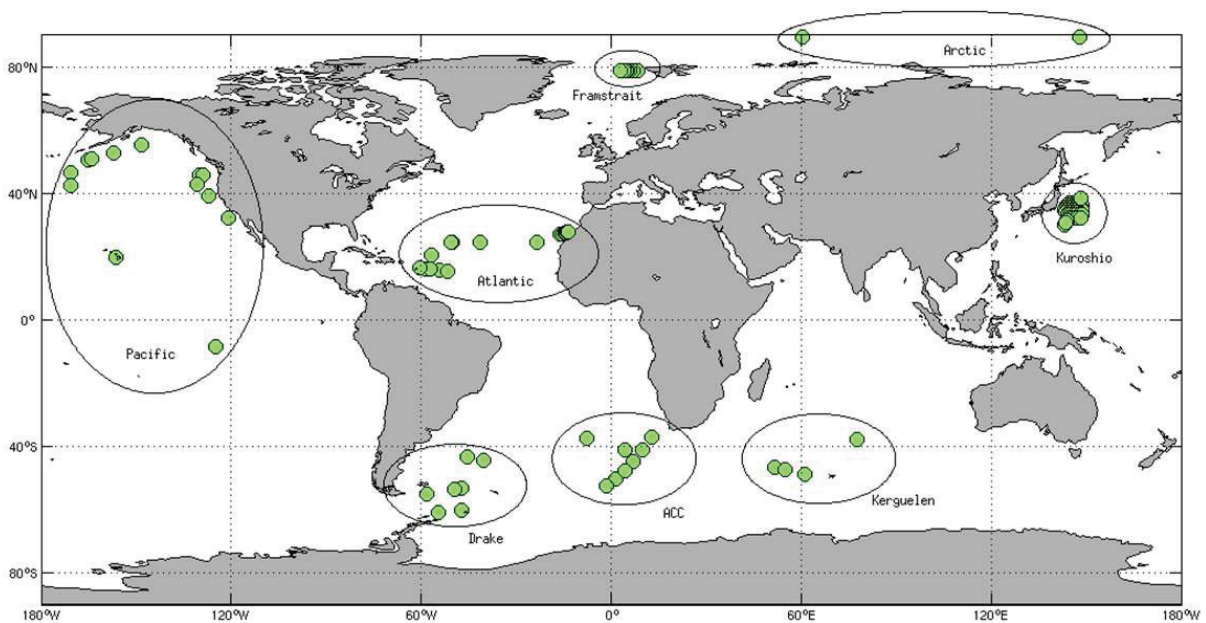


Figure 3.31: Locations of OBPR (grouped by regions)

One disadvantage of OBPR is that they are point measurements and represent OBP at a specific location. GRACE analysis and inverse solutions are more accurate on larger scales. By averaging over a set of OBPRs in a region an estimate of regional mass variations can be approximated. It will be tested if a comparison on a regional basis improves the fit between the two data sets. OBPR mean mass variations of a specified region depend on the location. In the following OBPR recorders are grouped in eight different regions, Arctic, Fram Strait, Pacific, Atlantic, Drake Passage, ACC, Kerguelen, and Kuroshio (Figure 3.31). Their respective mean is compared with regional mean mass variations from FESOM, GRACE estimates and the inverse solution (variable error of modeled OBP applied). For every week all available measurements are considered. If a measurement at a location is not existing, this location not considered for the particular week.

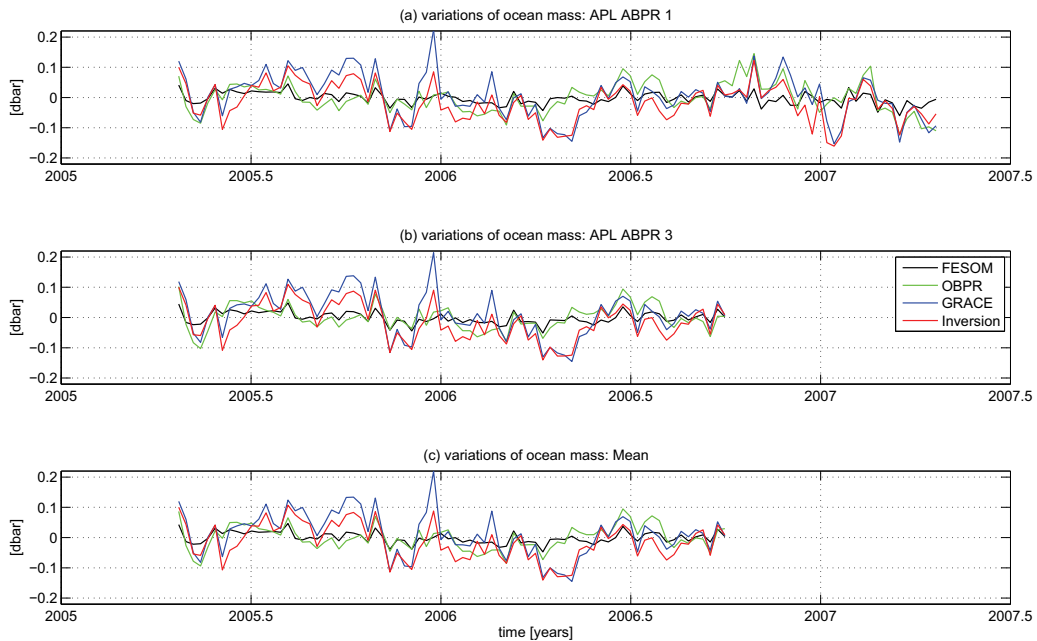


Figure 3.32: Ocean bottom pressure time series of North Polar Region; (upper panel): Station ABPR1 (89.2543N 60.3597E) (mid panel): Station ABPR3 (89.2475N 148.1257E) (lower panel): mean of station ABPR1 and ABPR3, during the time both time series are available

### Arctic Region

Two OBPR time series are provided by Morison et al. (2007) with positions near the North Pole. Here, the inverse solution using the variable error of model OBP best represents the regional mass variations (Figure 3.32), only the seasonal cycle from GRACE measurements, is not described in OBPR. The capability of FESOM to model OBP in this region has some limitations due to the problem of singularity at the North Pole. In the present model version, this issue is solved by inserting a small island. Hence, ocean circulation might not be as well represented as in other regions. However, FESOM still shows good agreement with OBPR measurements, especially in the short term structure.

The two measurements, the inversion and FESOM, well correlate with the mean ocean mass variations of the Arctic Ocean above  $80^{\circ}\text{N}$  latitude, which are derived from GRACE (Figure 3.33). FESOM results show lower amplitudes compared to the other data sets, but similarly correlate to OBPR as GRACE (about 0.7). Regional mean ocean mass variations of the inverse solutions show correlations with OBPRs of 0.8, including a good representation of seasonal variations of the mass signal, which is also the case for the GRACE solutions. Also the short term structure is well defined, except for some short

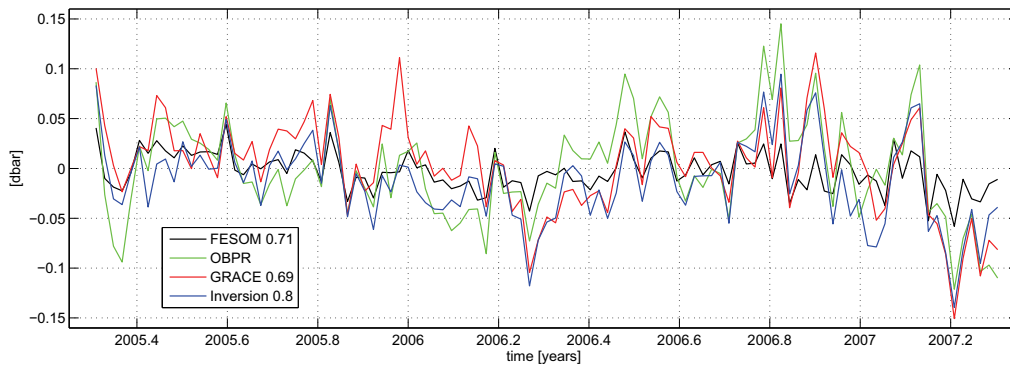


Figure 3.33: Ocean bottom pressure variations in the Arctic Ocean

time periods like in spring 2005.

## Kuroshio

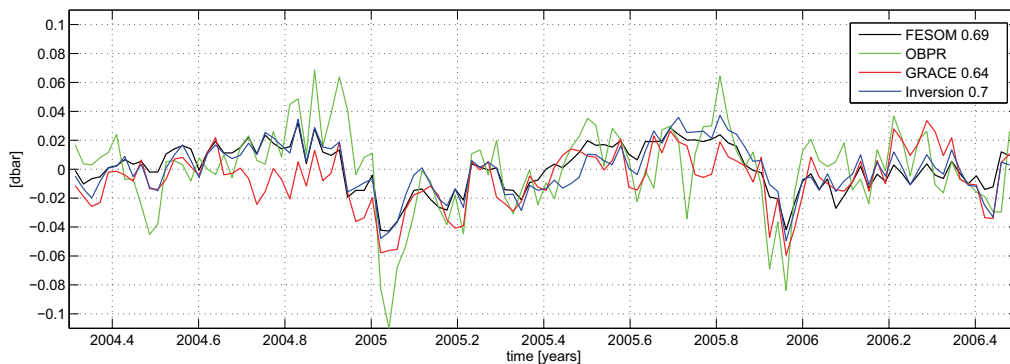


Figure 3.34: Mean ocean bottom pressure variations at the Kuroshio current

The Kuroshio is a surface current located in the North West Pacific east of Japan. In this region an array, which consists of 46 OBPR have been deployed from 2004 to 2006 (Park et al., 2008). The mean mass signal of the OBPR measurements in this region are compared with regional mean mass variations of the different data sets ( $30^\circ \leq \text{latitude} \leq 50^\circ$  and  $130^\circ \leq \text{longitude} \leq 175^\circ$ ). The inverse solution shows best correlation with OBPR, closely followed by modeled OBP and GRACE estimates. Short term variations are also well described in all data sets. They depict the yearly signal of mass variations, with slightly underestimated amplitude (Figure 3.34).

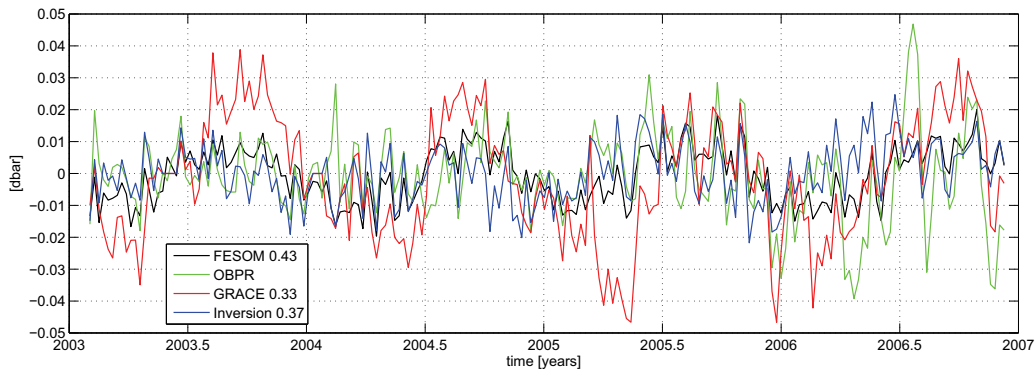


Figure 3.35: Mean ocean bottom pressure variations in the Mid Atlantic Ocean

### Mid Atlantic Ocean

In the equatorial Atlantic Ocean two arrays (MOVE and RAPID) are deployed. The MOVE array (Kanzow et al., 2005) is located East of the Caribbean Sea, whereas the RAPID array spans the whole width of the equatorial Atlantic Ocean. The region investigated here, is defined as  $0^\circ \leq \text{latitude} \leq 40^\circ$  and  $-75^\circ \leq \text{longitude} \leq 0^\circ$ . The correlations of OBPR and the regional means of the different data sets are quite low (Figure 3.35). All estimates are following the seasonal cycle, where the amplitude is somewhat overestimated in the GRACE solutions. This was also seen previously in the comparison of the point estimates with OBPR from the MOVE array.

### Fram Strait

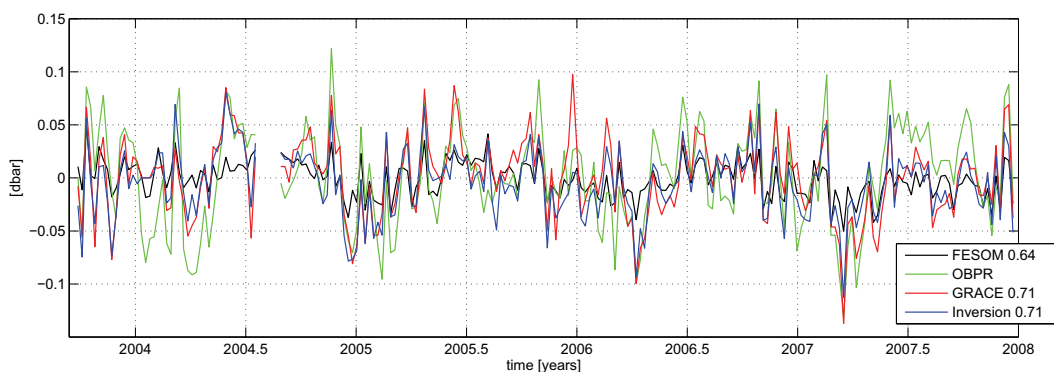


Figure 3.36: Mean ocean bottom pressure variations in the Fram Strait

The Fram Strait is located between Spitsbergen and Greenland. It denotes the passage between the Arctic Ocean and the Norwegian and Greenland Seas. The mean of all OBPR

at Fram Strait and the mean of all corresponding OBP derived by the different methods are computed for the region of  $60^\circ \leq \text{latitude} \leq 87^\circ$  and  $-20^\circ \leq \text{longitude} \leq 20^\circ$  (Figure 3.36). Mean mass variation from GRACE and the inverse solutions correlate well with mean OBPR measurements with values over 0.7 in the Fram Strait region. The correlation of regional mean OBP of FESOM and OBPR measurements is a bit lower but still above 0.6 as the short term structure is well described. On the other hand, modeled mass variations cannot represent the variability of mean ocean mass in this region as good as GRACE or the inverse solution can do.

### Antarctic Circumpolar Current

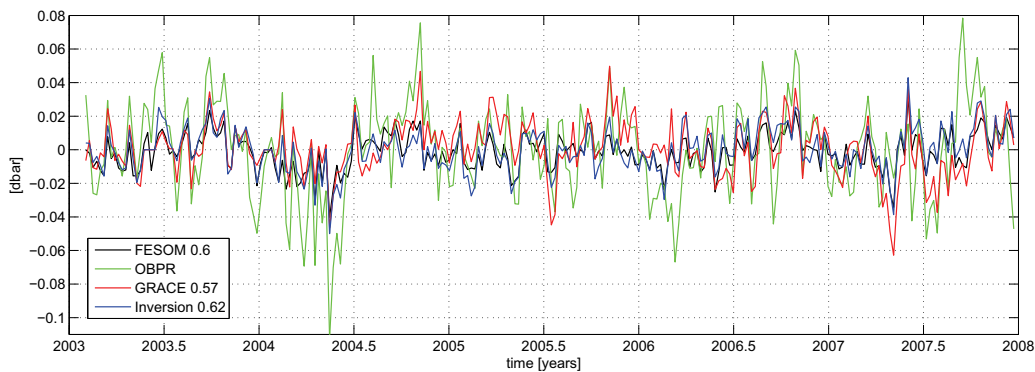


Figure 3.37: Mean ocean bottom pressure variations in the ACC (South Atlantic)

The mean of all OBPR in the ACC in the South Atlantic and the mean of all corresponding OBP derived by the different methods are computed for the region south of Africa  $-60^\circ \leq \text{latitude} \leq -30^\circ$  and  $-30^\circ \leq \text{longitude} \leq 35^\circ$  (Figure 3.37). OBPR measurements at location AWLANT\_3 are not taken into account, as they show very strong short term fluctuations, which are known to be related to much smaller scales of the Agulhas Retroflexion. Regional mean mass variations of FESOM and the inversion are estimated with a correlation higher than 0.6. The correlation between GRACE estimates and OBPR is slightly lower (0.57). The representation of the variability of the mass signal is underestimated in all data sets, compared to OBPR measurements. The short term structure in the signal of OBPR can be identified in all data sets.

### Kerguelen

The Kerguelen islands are a sub-Antarctic group of islands and are located in the Southern Indian Ocean with a distance of 2000 km to Antarctica and 4000 km to Australia. Near

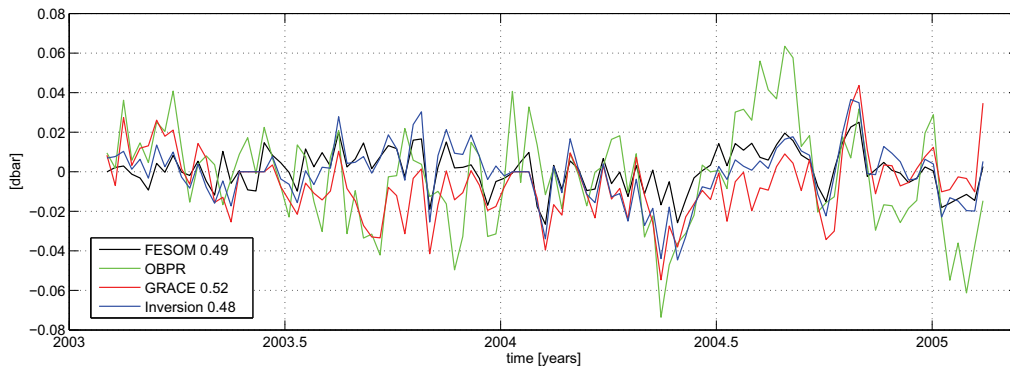


Figure 3.38: Mean ocean bottom pressure variations near Kerguelen Islands

the Kerguelen Islands four OBPR were deployed from beginning of year 2003 to beginning of year 2005 (Rietbroek et al., 2006). All regional mean mass estimates have similar correlation of about 0.5 with OBPR (region:  $-60^\circ \leq \text{latitude} \leq -30^\circ$  and  $30^\circ \leq \text{longitude} \leq 100^\circ$ ). The short term structure of the mass signal in OBPR is well represented in all data sets (Figure 3.38). Low frequency mass variations are not as well described as in other regions. For example, in the second half of year 2003 only GRACE measurements follow the OBPRs, while the inverse solution is mostly following the model results. Since the second half of 2004 no data set describes the variability of the mass signal from OBPR.

### Drake Passage

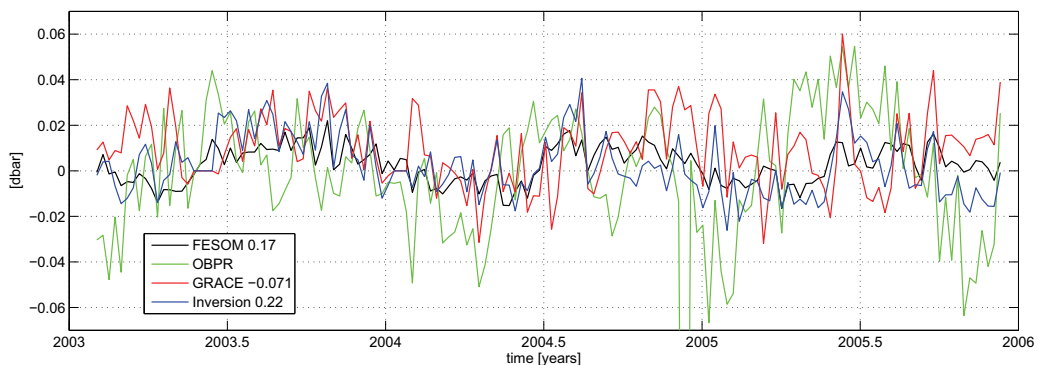


Figure 3.39: Mean ocean bottom pressure variations in the Drake Passage

Drake Passage, the 800 km wide strait between the Cape Horn (South America) and the Antarctic Peninsula, is part of the Southern Ocean and connects the Pacific and the Atlantic Ocean. The ACC is the only current, which flows zonally around the globe, after

the Drake Passage opened some 40 million years ago. Regional mean mass variations are computed for  $-65^\circ \leq \text{latitude} \leq -40^\circ$  and  $-70^\circ \leq \text{longitude} \leq -30^\circ$ . Although there are good correlations between point estimates of the data sets and OBPR measurements available, OBPR measurements deployed in the Drake Passage cannot represent mean mass variations of larger areas (Figure 3.39). There is almost no correlation between the data sets and OBPR. Only the seasonal signal with underestimated amplitude and a small phase shift is captured.

### Pacific

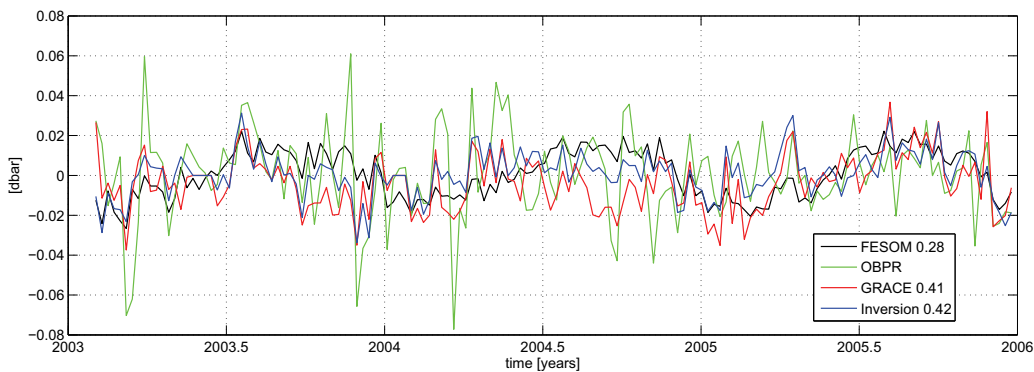


Figure 3.40: Mean ocean bottom pressure variations in the North Pacific

In the North Pacific mean mass variations are computed for the area  $30^\circ \leq \text{latitude} \leq 70^\circ$  and  $-180^\circ \leq \text{longitude} \leq -100^\circ$ , where most OBPR are deployed for the Tsunami Early Warning System. The two deployments south of  $30^\circ$  latitude, which are defined to be in the Pacific group, are not considered in the calculation of the mean, as their locations are too remote from the other OBPR. It would be necessary to massively enlarge the area of investigation to a size, where the OBPR measurements are not able to depict the mass variations (Figure 3.40). For the Pacific region the correlation is already quite low for modeled OBP, where the short term fluctuations are strongly underestimated. The GRACE and inverse solutions are a bit higher correlated with OBPR (about 0.4). The seasonal cycle is well defined in all data sets.

### 3.8.3 Validation of modeled OBP error

Modeled OBP from FESOM directly influences the inverse calculation. The estimated error of the FESOM result has an indirect influence as it is used in the weighting scheme

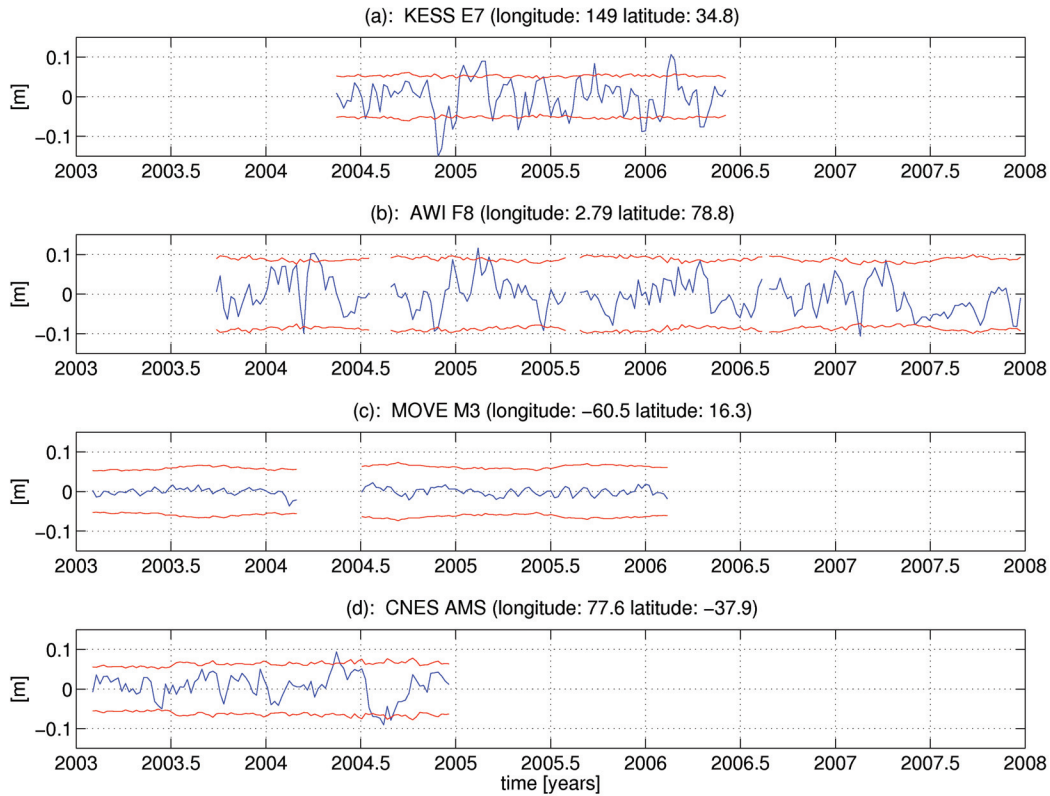


Figure 3.41: Comparison of modeled OBP error (red) with the true error, i.e. the difference between modeled OBP and OBPR measurements (blue) for locations (a): KESS E7 (Kuroshio), (b): AWI F8 (Fram Strait), MOVE M3 (Atlantic Ocean, east of the Caribbean Sea), and CNES AMS (near New Amsterdam, about  $10^\circ$  north-east of the Kerguelen Islands)

of the Normal equations. In the previous chapters OBPRs were used to test the modeled OBP. Now the error estimate, which varies in space and time, is tested with the in situ data. A measure for the real error at these locations can be estimated when computing the difference between modeled OBP and the measurements. Comparing these errors with the perturbation-based error estimate (Chapter 3.5.3) reveals that they have similar magnitude (Figure 3.41). The difference is mostly located within the estimated error boundaries. At some positions the error is overestimated, for example in the Mid Atlantic Ocean. Variability of the model OBP error estimate is small. The difference sometimes exceeds the error estimate for a short time period, because of the stronger fluctuations of the short term signals in the OBPR measurements. At least 84 % of the data remains within the estimated error bounds (Brunnabend et al., 2010). In a Gaussian error distribution less measurements would lie within one standard deviation, which shows our error estimate is

conservative.

### 3.9 Conclusion

OBP anomalies modeled with FESOM capture the geophysical patterns of the global ocean, whereas the modeled mass budget directly depends on the fresh water budget. This leads to a direct transfer of uncertainties in the input variables to the modeled global mean ocean mass variations.

On the basis of different atmospheric forcing fields, weekly error maps of modeled OBP were derived, as atmospheric parameters such as wind, temperature and net precipitation influences the state of the ocean. The estimated error has impacts on the joint inversion of GRACE gravity, GPS site displacements and modeled OBP. Variable OBP error estimates lead to a higher weighting of modeled OBP in the inverse calculations. The increased trust in the FESOM bottom pressure appears to be justified because the inverse results significantly improve. This holds true especially for the MOVE array in the equatorial Atlantic Ocean, where the correlation between OBPR and GRACE measurements is quite low. Correlation is improved by introducing modeled OBP into the inversion since FESOM well simulates ocean mass change in this region. FESOM is well suited to represent large-scale ocean mass variation on weekly time scales, while the seasonal variability of ocean mass is better captured by GRACE. The comparison between inverse solutions and the model results shows that simulated weekly global mean ocean mass variations have similar phase, only the modeled amplitude is slightly overestimated. This can be improved by introducing the mass correction term from the inversion into the model, e.g. as a scaling to precipitation.

The mean of OBPR measurements in defined regions can represent mean ocean mass variations of this regions, depending on the amount of deployments available and the size of the region. Also the complexity of the different currents is influencing this capability. For example, in the Arctic Ocean the regional mass is varying with the entire basin and a few OBPR deployments can represent regional mean mass variations. This is not possible e.g. at the Drake Passage, although FESOM results and the inverse solutions show good correlations with most OBPR time series in this region.

Finally, OBP modeled with FESOM shows high correlations with the background model GAC and GAD used in the GRACE processing (GFZ RL4 solutions). In the Arctic Ocean the correlation is lower. But as FESOM results show better correlation to the GRACE solutions here (GSMGAC and GSMGAD) than the background model, OBP derived with

the FESOM model better represents ocean mass variations in these regions. This is also true for the North Atlantic Ocean. On the other hand, FESOM results show strong negative correlation with the GRACE solutions in several coastal regions, where the background models correlate better.

## Chapter 4

# Sea Surface Topography and Steric Sea Level

In ocean modeling, sea level is generally simulated with respect to a geopotential surface. This so called geoid is a surface of equal gravitational potential energy and would coincide with the average ocean surface, if it would not move. The dynamic sea surface topography has its origins in hydrodynamic processes and amounts to magnitudes on the order of  $\pm 1$ -2 m. Globally, the fresh water balance leads to deviations, but also the steric components. They change global sea level through variations of the temperature (thermsteric) and salinity (halosteric).

Different studies suggested an increased sea level rise since the early 1990s due to thermal expansion (Levitus et al., 2005; Wenzel and Schröter, 2007b,a; Bindoff et al., 2007). Lombard et al. (2005) analyzed thermal expansion from 1950 to 1998 using data from Levitus et al. (2000) and Ishii et al. (2003). They found significant differences in the global mean estimated for the period 1990 to 1998: The Levitus-based estimate leads to an increase of  $0.47 \pm 0.44$  mm/year, whereas the Ishii-based estimate amounts to  $1.41 \pm 0.49$  mm/year. They explained the difference as being caused from problems with the XBT (Expandable Bathy-Thermographs) depth correction and the inhomogeneous data during the computation of the Ishii data set. However, they found a closer estimate for thermsteric contributions in the layers of the upper 500 m for the period of 1950 to 1990, which amount to  $0.11 \pm 0.04$  mm/year for the Ishii-based estimate and  $0.19 \pm 0.06$  mm/year for the Levitus-based estimate. In addition, they identified in the Ishii-based estimate regional patterns of thermal expansion, which relate to the major oscillations such as the Southern Annular Mode (SAM), the El Niño Southern Oscillation (ENSO), the North Atlantic Oscillation (NAO), or the Pacific Decadal Oscillation (PDO).

Thermal expansion is dependent on the variability of the heat content in the ocean. The world ocean database is used to estimate annual changes in heat content for the upper 300 m and 700 m for the period of 1955 to 1998 by Levitus et al. (2005). Also pentadal estimates for the upper 3000 m are provided. An increase in heat content of  $14.5 \cdot 10^{22}$  J ( $0.33 \cdot 10^{22}$  J/year for the 44 years) is found. This corresponds to an increase in mean temperature of  $0.037^\circ\text{C}$ . Ishii et al. (2006) suggested linear trends of global mean thermosteric sea level of  $0.31 \pm 0.07$  mm/yr and halosteric sea level of  $0.04 \pm 0.01$  mm/yr, which are derived for the upper 700 m of the area between latitudes  $60^\circ\text{S}$  and  $60^\circ\text{N}$ . In the IPCC 4th Assessment Report estimated steric sea level rise has been  $1.6 \pm 0.25$  mm/yr for the years 1993 to 2003. For the period 2003 to 2008 Cazenave et al. (2008) suggested a reduced trend in steric sea level rise of  $0.3 \pm 0.15$  mm/year. In that study steric sea level change was computed by taking the difference of altimetry measurements, which measures full sea surface topography, and mass estimates derived from the GRACE mission.

In the following, different contributions of modeled heat exchange are described. The sum of these contributions induces a loss in ocean heat, which results in a unrealistic decrease of global mean sea level. For this reason, net heat flux is corrected, before investigating modeled sea surface topography and steric height variations. Spatial patterns of modeled steric height anomalies are identified in steric estimates derived from satellite altimetry and GRACE measurements following the approach of Cazenave et al. (2008). Alternatively, the inverse solutions (Chapter 3.7) are subtracted from the altimetry measurements for comparisons with modeled steric height variations.

## 4.1 Modeled Surface Heat Flux

Ocean heat change is a consequence of heat exchange between ocean and atmosphere and internal heat transports. The heat exchange at the ocean surface is due to latent heat flux, sensible heat flux, in-coming and out-going long wave radiation and short wave radiation. Note, that in FESOM the heat exchange between atmosphere and ocean, and atmosphere and sea-ice is computed separately (Parkinson and Washington, 1979).

Latent heat flux is the heat, which cools of the ocean during evaporation (Figure 4.1a and 4.2a). It mainly depends on the wind speed and the specific humidity. Evaporation is higher with dry air and strong winds and lower if winds are weak and the air is almost saturated (relative humidity near 100%). Also the state of the ocean surface influences the latent heat flux. If the ocean is ice covered, less evaporation occurs than from the open water. Global average latent heat flux is about  $-80$  W/m<sup>2</sup> (loss for the ocean).

Sensible heat flux is defined as the heat, which is carried out of the ocean by turbulent fluxes (Figure 4.1b and 4.2b). It depends on surface wind speed and the temperature gradient at the ocean surface. If winds are strong and the temperature difference is high, the sensible heat flux is large. Its global average amounts to about  $+24 \text{ W/m}^2$  (gain for the ocean), i.e. it is generally smaller than the latent heat flux.

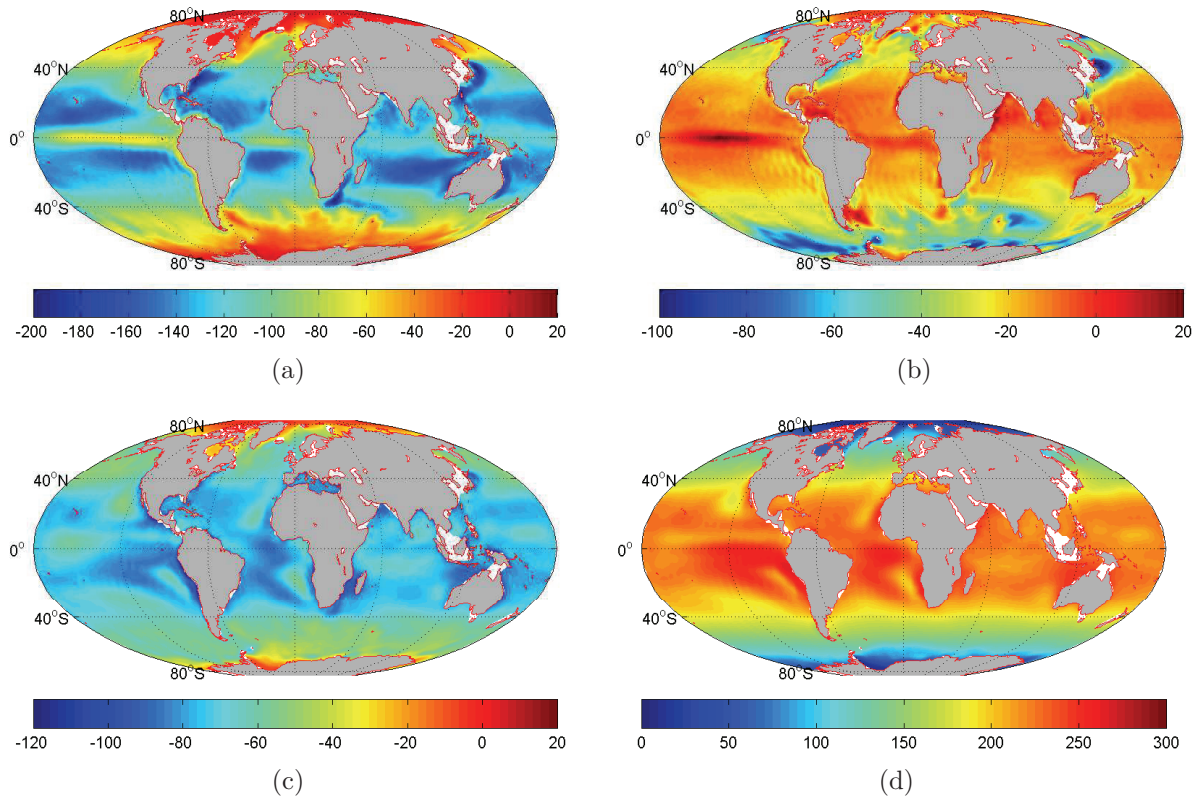


Figure 4.1: Modeled ten year mean surface heat fluxes in  $\text{W/m}^2$  for the open ocean; (a): latent heat flux, (b): sensible heat flux, (c): net long wave radiation, and (d): net shortwave radiation

The incoming and outgoing long wave radiation at the ocean surface is depicted as net infrared radiation flux in Figures 4.1c and 4.2c. It depends on the cloud cover, as long wave radiation of ocean water mostly radiates at wavelengths (near  $10 \mu\text{m}$ ), which are absorbed by clouds and water vapor in the atmosphere and radiated back. Here, the height (temperature) of clouds as well as their thickness (optical depth) is important. In case of water vapor, dryer air lets more long wave radiation escape to space than more humid air. Additional radiation is absorbed in the atmosphere in other spectral bands. For example, in the band ranging from  $3.5 \mu\text{m}$  to  $4.0 \mu\text{m}$   $\text{CO}_2$  absorbs long wave radiation. Also the ocean surface temperature and the state of the ocean surface influence long wave

radiation. If the temperature is higher, stronger radiation occurs. Ten year mean net long wave radiation amount to about  $-65 \text{ W/m}^2$  (loss for the ocean) in global average.

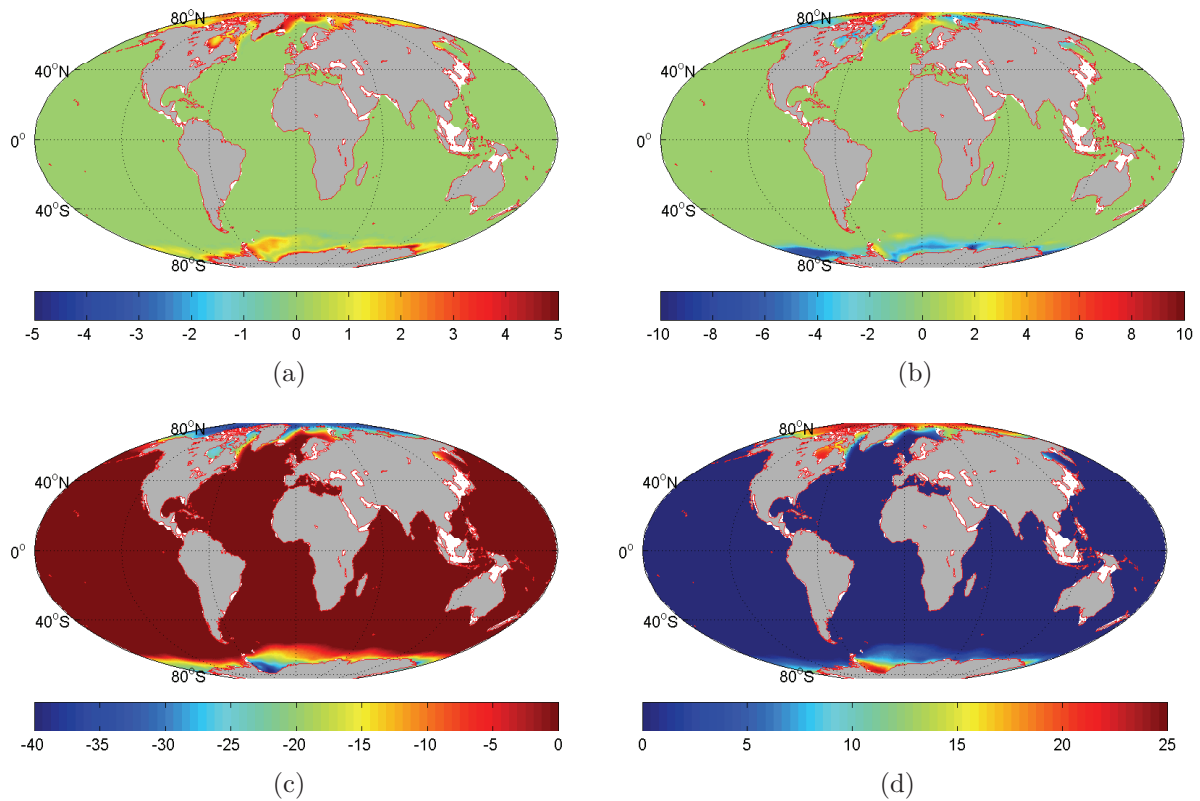


Figure 4.2: Modeled ten year mean surface heat fluxes in  $\text{W/m}^2$  for the ice covered ocean; (a): latent heat flux, (b): sensible heat flux, (c): net long wave radiation, and (d): net shortwave radiation

The shortwave radiation (solar energy flux), also called insolation, is partly absorbed by the ocean (Figure 4.1d and 4.2d). The absorbed energy is dependent on the angle between sun and horizon, which defines the cross-sectional area of the ocean surface absorbing the heat. The angle varies with the seasons, which are also influencing insolation by the varying length of the day (also depended on latitude). Global average short wave radiation amounts to values between  $+145 \text{ W/m}^2$  and  $+180 \text{ W/m}^2$  (gain for the ocean) with maximum values in the equatorial regions.

The full surface heat fluxes depend on the ocean state and are modeled with bulk formulas described in Chapter 2.4 (Parkinson and Washington, 1979). Comparing the net heat flux (sum of all heat fluxes) modeled with FESOM and provided by the NCAR/NCEP reanalysis similar patterns are apparent (Figure 4.3). But also significant differences occur, especially in the North Atlantic, in the regions of the Gulf stream, the Labrador current and

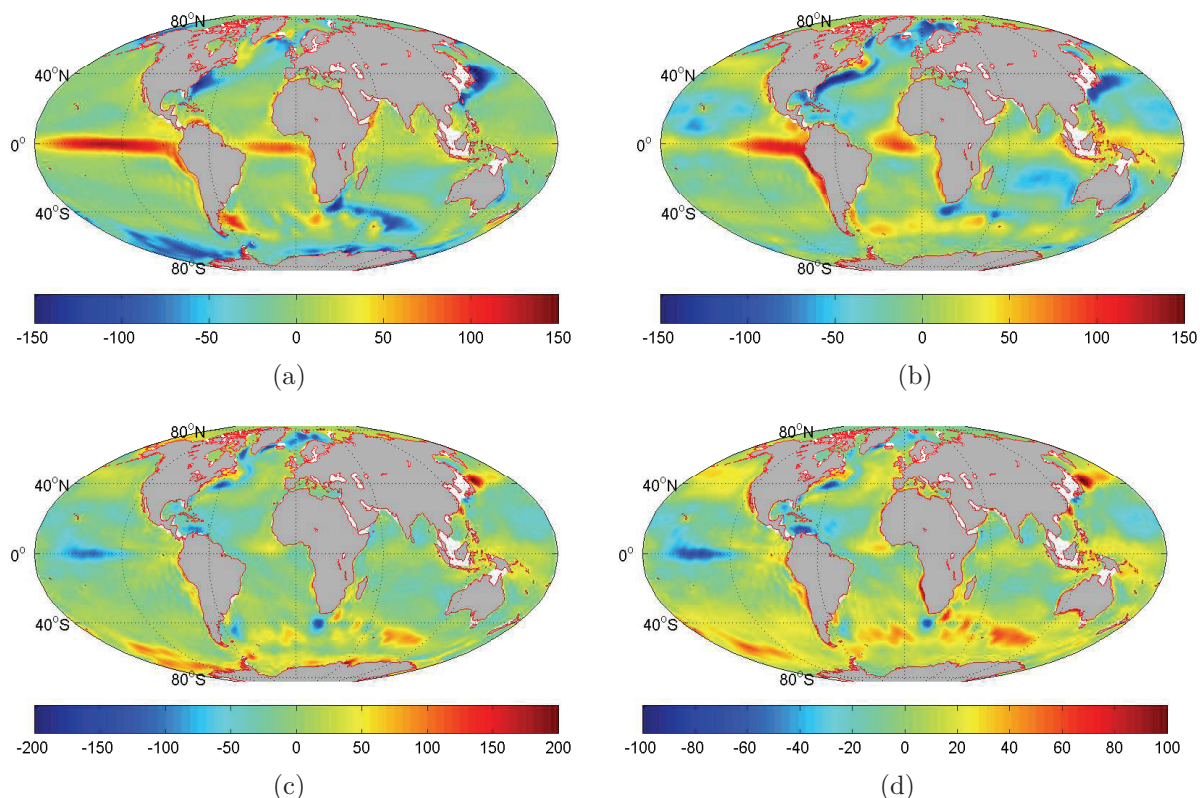


Figure 4.3: Ten year mean net heat flux in  $\text{W}/\text{m}^2$ , (a) modeled with FESOM and (b) from the NCAR/NCEP reanalysis, interpolated to the FESOM grid. (c) being their difference and (d) the difference in mean latent heat flux

Barents Sea. Here, the 10 year mean net heat flux from the NCAR/NCEP reanalysis shows loss in heat of about  $200 \text{ W}/\text{m}^2$  higher than modeled with FESOM. Also the equatorial Pacific mean net heat loss difference of about  $40 \text{ W}/\text{m}^2$  compared to the NCAR/NCEP reanalysis is found. Modeled net heat is mostly similar to atmospheric reanalysis but it includes a higher heat loss in the Southern Ocean west of the Drake Passage (about  $80 \text{ W}/\text{m}^2$ ) and West of Japan where the Kuroshio Current and Oyashio Current join (about  $200 \text{ W}/\text{m}^2$ ). The differences originate from all contributions, not from a single one only, although mean latent heat flux best represents the structure of the differences. Within the ten year period the global mean net heat flux of FESOM is about  $6 \text{ W}/\text{m}^2$  lower than global mean net heat flux from the NCAR/NCEP reanalysis. This leads to an unrealistic loss of heat. Thermosteric contraction then induces a decrease of the modeled sea level.

## 4.2 Surface Heat Flux Correction

Instead of calculating net heat fluxes in FESOM, data sets from weather prediction centers (e.g. NCEP or ECMWF) can be used in the model as varying boundary conditions. Although it appears to be more consistent to use predefined data sets a disadvantage results in the fact that the multi-year mean of heat flux averaged over the ocean is not required to be balanced. The analysis must only be balanced on a decadal average within a few  $W/m^2$  (Taylor et al., 1999)<sup>1</sup>. The multi-year mean of the NCAR/NCEP reanalysis amounts to  $-5.8 W/m^2$  (Sterwart, 2008). This yields a heat loss on inter-annual time scales, influencing the thermosteric sea level. In addition, analyzed ice surface temperature appears to be too high yielding a drastic decrease of sea ice in the first years of the simulation until no sea ice is left after about 4 years. For this reason FESOM uses bulk Formula to obtain heat fluxes instead of taking reanalyzed flux fields.

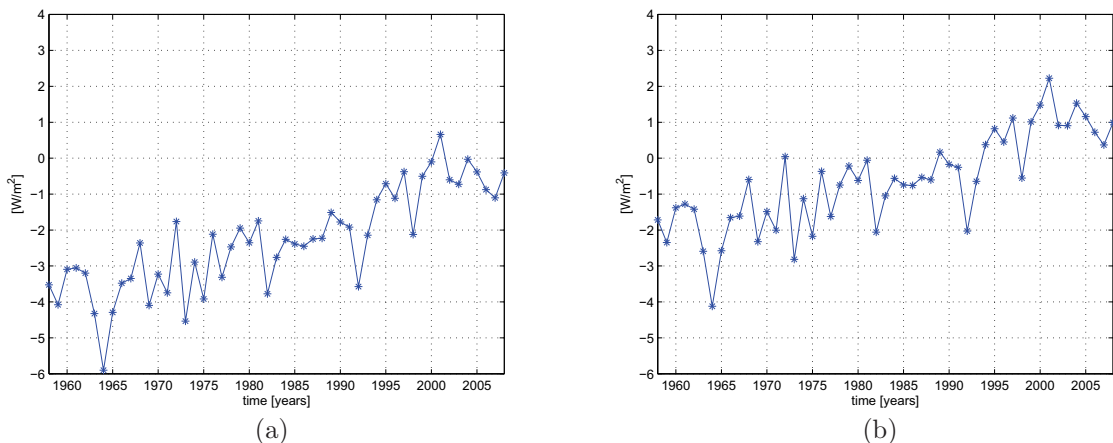


Figure 4.4: Global yearly mean net heat flux computed with original bulk formulas (a) and with the offset included (b)

Similar to the heat budget of the NCAR/NCEP reanalysis the modeled heat budget is negative. A negative feedback takes place which lowers ocean surface temperatures and outgoing long-wave radiation. The surface heat budget slowly adjusts and balances (i.e. is zero). The adjustment is shown in Figure 4.4. The lowered sea surface temperature and the loss of volume due to thermosteric contraction are not acceptable and an alternative way to balance the surface heat fluxes is sought. To this end we add sufficient heat to balance the global average for the period 1975 to 2008 at zero. The necessary correction

<sup>1</sup>Heat flux of  $10 W/m^2$  into the ocean leads to an increase of temperature of  $0.15^\circ C$  if add in the upper 500 m (Taylor et al., 1999)

amounts to  $1.65 \text{ W/m}^2$ . However, it is dangerous to add this correction uniformly as sea ice reacts to changed heat fluxes very sensitively. As a consequence heat is added only in an equatorial band with a structure of unity for  $-25^\circ < \text{latitude} < 25^\circ$  and a smooth transition to zero at  $35^\circ$  in the shape of a tangent hyperbolic (Figure 4.5).

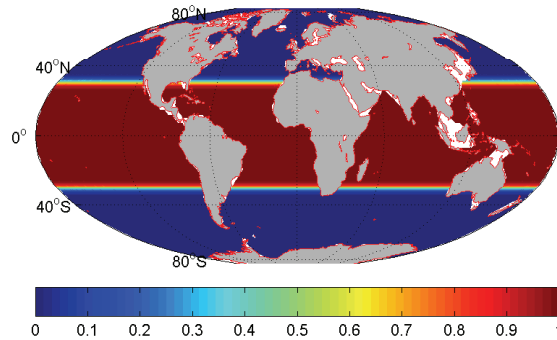


Figure 4.5: Tangent hyperbolic function used to correct modeled net heat flux

After the net heat flux has been corrected, it is introduced in a second model integration as an additional forcing parameter.

### 4.3 Modeled Sea Surface Topography

Sea surface topography, also called dynamic topography, can be used to analyze the transport of heat in the ocean from equatorial to polar regions. On long time-scales it is mainly influenced by the global mass and heat balance of the ocean. The surface topography is an expression of the ocean circulation, i.e. the location of currents and their seasonal and inter-annual variability. Sea level is higher at locations with warm water as density is lower. The state of the subsurface water is equally important. After the net heat flux is corrected, modeled sea surface topography are more realistic in regions of subtropical gyres. Previously, these patterns have been underestimated (Figure 4.6).

Modeled sea surface topography, corrected for atmospheric pressure, maps the major ocean currents (Figure 4.7). Due to the Coriolis force, in the Northern Hemisphere clockwise rotation of currents exist at high sea surfaces (e.g. at the subtropical gyre in the North Atlantic) and a counter-clockwise rotation at low sea surfaces (e.g. at the sub-polar gyre in the North Atlantic). In the Southern Hemisphere, it is the other way around. Clockwise rotation of currents occur at low sea surfaces (e.g. at the ACC) and a counter-clockwise rotation at high sea surfaces (e.g. at the south pacific gyre)

Four different mean dynamic topographies, derived from GRACE, altimetry and in-situ

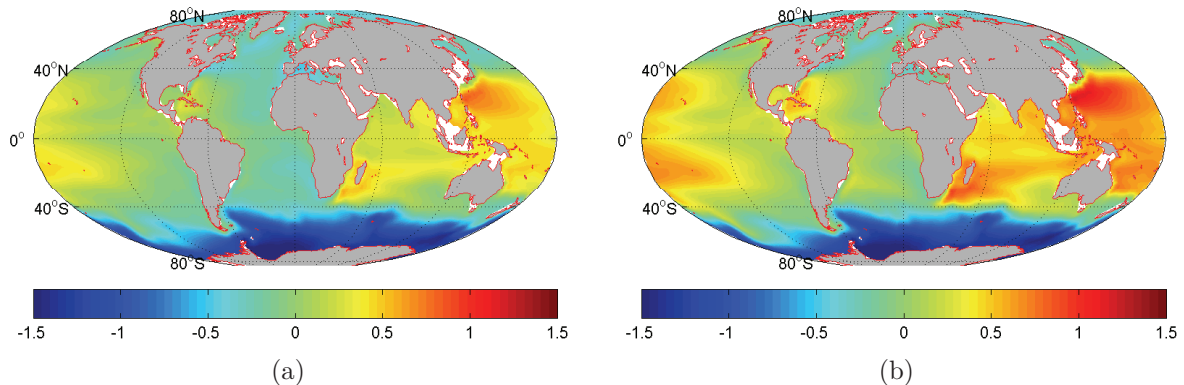


Figure 4.6: Mean sea surface topography of year 2007 (in meter) simulated by using the original bulk formulas (a) and by introducing the offset to the modeled net heat flux (b)

Table 4.1: Mean Dynamic Topography

| Product        | Period    | Resolution | Source  | Correlation with FESOM |
|----------------|-----------|------------|---|------------------------|
| DNSCMSS08      | 1993-2004 | 1°         | (Vianna and Menezes, 2010)<br>(EGM08 (Pavlis et al., 2008)) | 0.95                   |
| MDOT060401     | 1992-2002 | 1/2°       | (P.Niiler et al., 2003; Maximenko and Niiler, 2005)         | 0.96                   |
| RIO5           | 1993-1999 | 1/2°       | (Rio and Hernandez, 2004; Rio et al., 2005)                 | 0.97                   |
| MDT_CNES_CLS09 | 1993-1999 | 1/4°       | (Rio et al., 2009, 2010)                                    | 0.97                   |

measurements are compared with the mean dynamic topography simulated with FESOM (Figure 4.8, Table 4.1). To produce the data sets, which have different resolution, to be comparable to modeled sea surface topography, they are interpolated onto the model grid. In addition, modeled sea surface topography is averaged over the corresponding averaging periods of the individual data sets. Compared to the FESOM results, mean dynamic topography derived from measurements shows more detailed structures. The model simulation has a smoother structure, whereas the global patterns, which originate from the major currents, are similar. Generally, modeled sea surface topography shows correlations above 0.95 to the mean topography derived from measurements.

The main difference to all data sets is caused by a global offset. For example, the RIO05 data set shows a strong positive offset, resulting in sea surface heights over 2.5 m in the equatorial regions. This is much reduced in a later development (CNES-CLS09). Differences to all four data sets occur in the North Atlantic, around Greenland, where modeled sea surface topography is too high (Figure 4.9). This is caused by the fact that the model is not losing enough heat in this region in comparison to the NCAR/NCEP reanalysis (Figure 4.3). In the Canadian Basin (Arctic Ocean) the sea surface topography

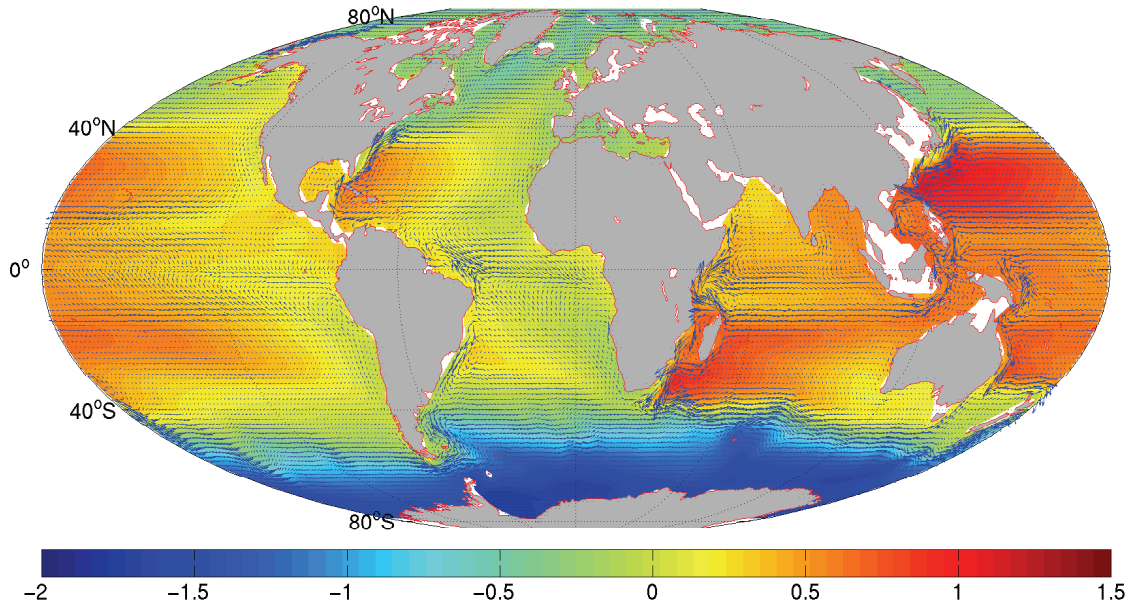


Figure 4.7: Modeled mean dynamic topography in meter and mean horizontal velocity at 50 m depth (1993-2008)

induces highest negative difference to the FESOM results. Also variations in the difference occur in the ACC, which are caused by strong variations in volume transport and the sensitivity of the model in this region. Some portion also originates from uncertainties in modeled heat flux exchange between ocean and atmosphere. However, there might also be higher uncertainties in the polar regions in the measured data sets as high accuracy altimetry measurements are not available for latitudes higher than  $\pm 66^\circ$ .

## 4.4 Variations in Sea Level

After the heat flux correction has been applied the unrealistic negative trend in sea level change is eliminated (Figure 4.4). The global mean sea level shows only a slight increase by about 0.7 mm/yr in the first decades. The trend amounts to about 3.1 mm/yr for the period from 1993 to 2003, which is slightly overestimated compared to studies from (Bindoff et al., 2007; Cazenave and Nerem, 2004) Note, sea level contributions of melt water from glaciers, ice caps, and continental ice sheets, are not included, here. For the years 2003 to 2008 a reduced trend in sea level of about 2 mm/yr is simulated. The reduction in trend has also been observed by Cazenave et al. (2008) (ARGO-based study).

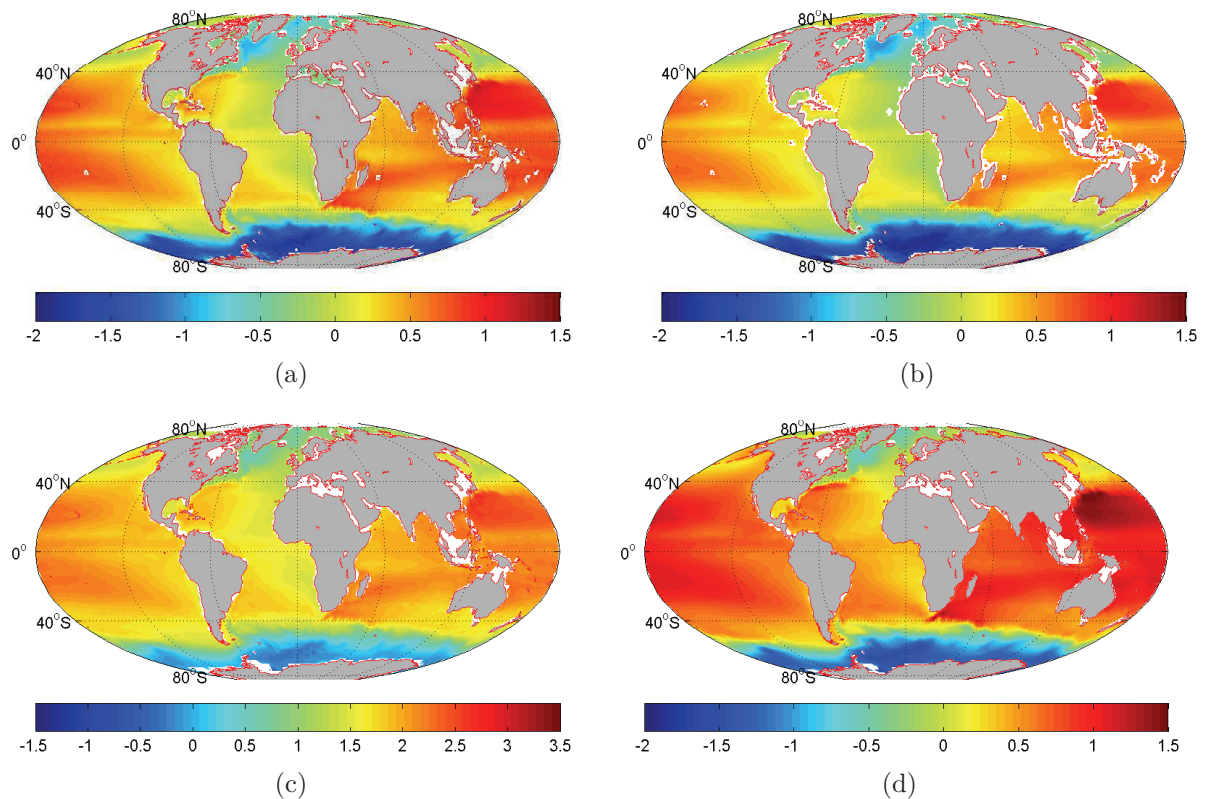


Figure 4.8: Mean dynamic topography in meter provided by (a) (Vianna and Menezes, 2010), (b) (P.Niiler et al., 2003; Maximenko and Niiler, 2005), (c) (Rio and Hernandez, 2004; Rio et al., 2005), and (d) (Rio et al., 2009, 2010)

In this study the trend in sea level is reduced to about 2.5 mm/yr. However, modeled global mean sea level shows much more realistic trends than without the heat flux correction.

Regionally, sea surface topography is not only varying due to continuous changes of ocean circulation but can also change by events such as the Pacific Decadal Oscillation (PDO), which is a pattern of warm and cold surface waters oscillating on decadal time scales. A cold phase of the PDO is observed in the trend of yearly mean sea surface topography derived for the period from 1993 to 2008 (Figure 4.11). In this phase warm water reaching from the north to the south of the west Pacific enclose a large area of cold water (with a wedge pattern) in the eastern Pacific, where sea surface height decreases as a consequence. In a warm phase it is the other way around.

Another reason for variations in sea surface topography is the El Niño-Southern Oscillation (ENSO). The El Niño event is a perturbation of the system between atmosphere and ocean. It is located in the equatorial Pacific Ocean and appears about every few years in the months around December. Under normal conditions, the south east trade winds are

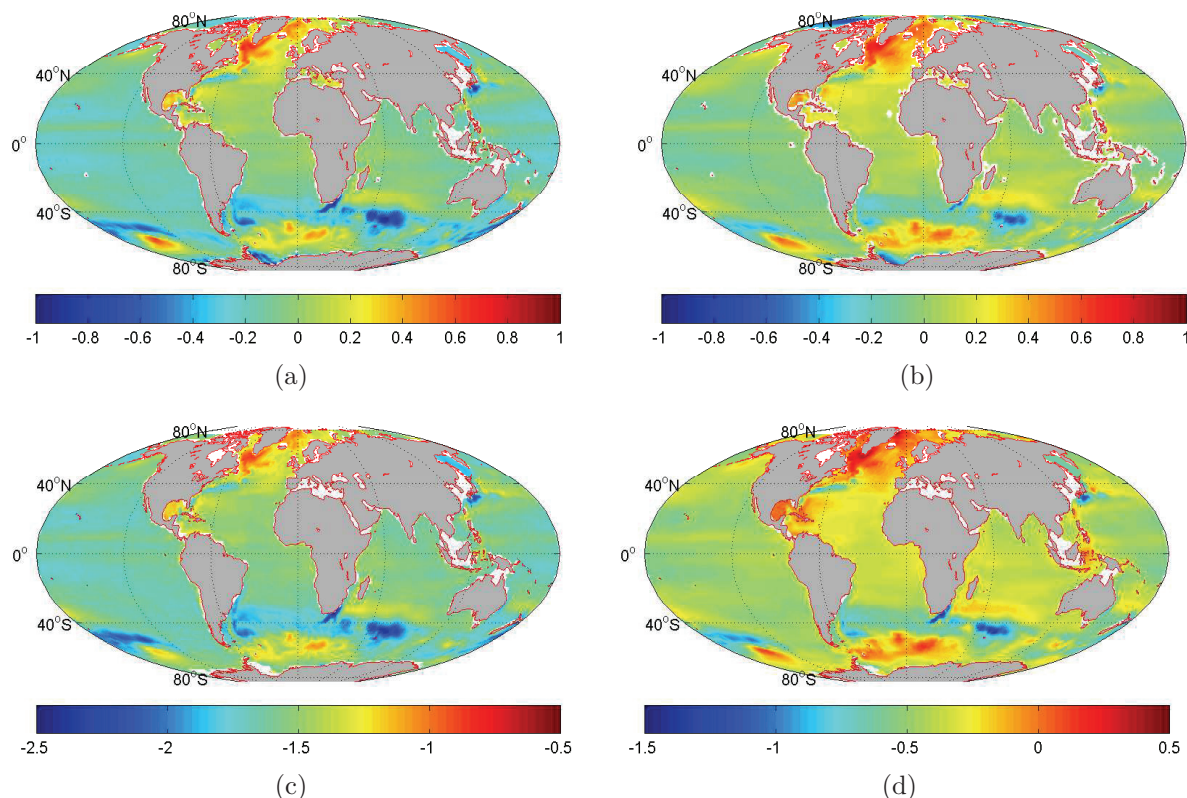


Figure 4.9: Difference of mean dynamic topography (in meter) simulated with FESOM and provided by (a) (Vianna and Menezes, 2010), (b) (P.Niiler et al., 2003; Maximenko and Niiler, 2005), (c) (Rio and Hernandez, 2004; Rio et al., 2005), and (d) (Rio et al., 2009, 2010)

driving the ocean currents. The winds are dependent on the difference between the subtropical high pressure field above the eastern south Pacific, including mostly dry and cold air and the Indonesian low pressure field. When the El Niño event develops the Indonesian low, where normally warm and moist air rises producing high precipitation rates, becomes weaker and shifts to the central Pacific. In addition, the high pressure field in the south Pacific becomes lower. The pressure difference gets smaller weakening the trade winds. Caused by this happenings, the slope in sea surface and therefore also the thermocline gets flattened out, inducing some of the warm mixed-layer water to flow eastward as Kelvin waves. At the coast of the eastern Pacific, these are separated to north and southward coastal Kelvin waves<sup>2</sup>. For example, the El Niño, which occurred in 1997/98 started to develop in April 1997 (Figure 4.12b), where some volume of warm water started to move to the eastern Pacific. When it reached the coast of Ecuador and Peru it splits up and

<sup>2</sup>Parts of them are reflected as Rossby waves.

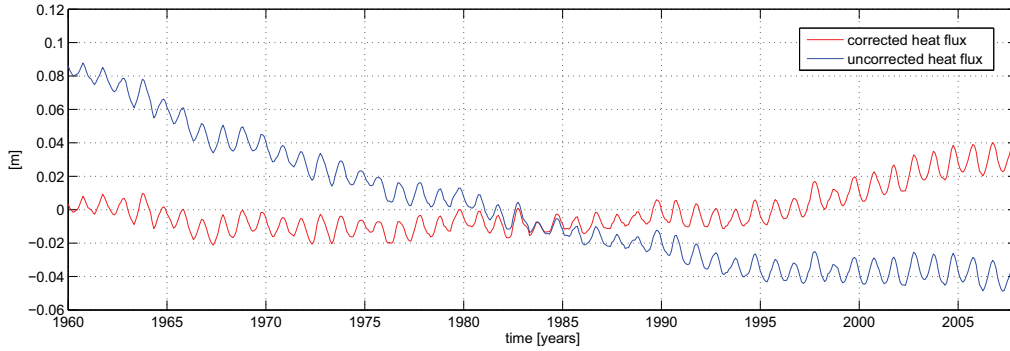


Figure 4.10: Variations of global mean sea level in meter from 1960 to 2008

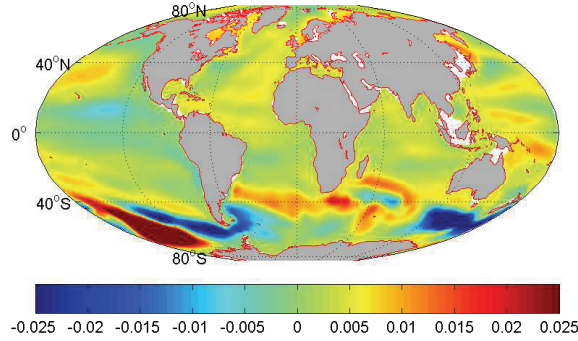


Figure 4.11: Trends of regional sea level change for the period from 1993 to 2008 in meter per year

flows north and southwards in the coastal regions (Figure 4.12c). A second Kelvin wave arrived at the American coast in January 1998 (Figure 4.12d).

## 4.5 Modeled Steric Height Variations

Steric height anomalies are computed with the Seawater Library (Morgan, 1994) from the year 2003 to 2007 using modeled results of salinity, temperature and pressure. The steric height

$$sh(S, T, P) = \frac{1}{g} \int_{-H}^0 \alpha(S, T, P) \quad (4.1)$$

is defined as the integral of the specific volume anomaly  $\alpha$

$$\alpha(S, T, P) = \frac{1}{\rho(S, T, P)} - \frac{1}{\rho(35, 0, P)}$$

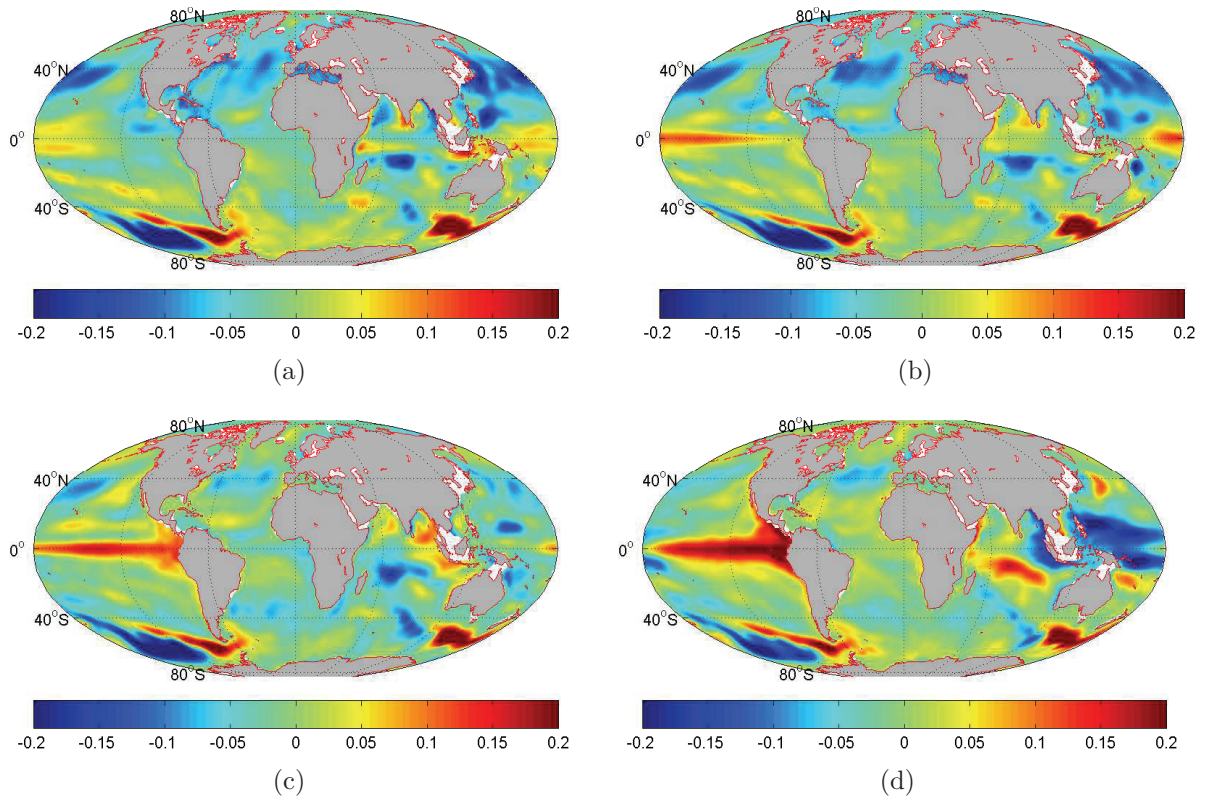


Figure 4.12: Development of the El Niño-Southern Oscillation in 1997-98 modeled by the monthly mean anomalies (in meter) of sea surface topography (1993-2008); (a): January 1997, (b): April 1997, (c): July 1997, and (d) January 1998

extending from the sea surface to the ocean bottom divided by  $g$  ( $9.806 \text{ m/s}^2$ ), where  $\rho$  is ocean density. To achieve steric height anomalies, the multi-year mean is then subtracted at every grid point, similar to the computation of the OBP anomalies.

Strong variations in global and regional sea level arise from ocean density changes, dependent on variations in temperature and salinity (expansion and contraction of the water column). Modeled global mean steric height variations show a clear seasonal signal with highest values in January and lowest in July. It has an amplitude of about 3 mm and includes a trend of about 0.4 mm/yr in the first decades. Between the years 1993 and 2003 the trend increased to about 2.5 mm/yr, and a decreased positive trend of about 2.0 mm/yr between 2003 and 2008.

Regional oscillations of steric sea level between the Northern and Southern Hemisphere are observed in weekly steric sea level variations (Figure 4.14). For example, in March 2005 steric height anomaly is higher than average in the Southern Hemisphere by up to 0.1 m whereas in the Northern Hemisphere steric height variations are up to 0.1 m lower

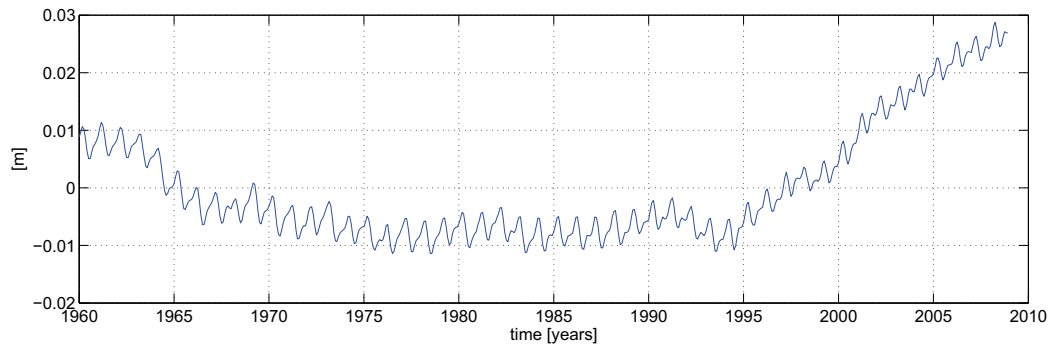


Figure 4.13: Monthly variations of modeled global steric sea level in meter from 1960 to 2008

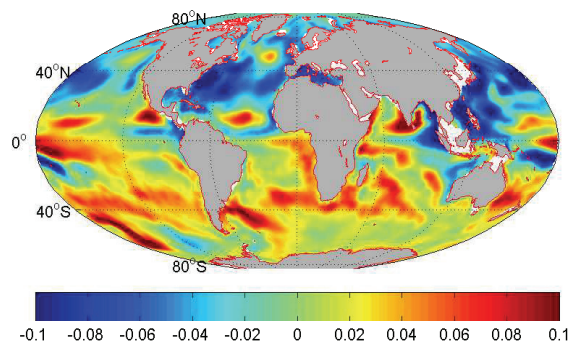


Figure 4.14: Modeled steric height anomalies for March 2005 (week 1314; three weeks running mean)

than multi-year mean. This is caused by the seasonally varying heat and fresh water fluxes at the sea surface. Regional steric variations on smaller spatial scales are produced by horizontal and vertical water movements, arising from variations in the wind fields or by movements of eddies or fronts.

## 4.6 Satellite Altimetry

An effective system to estimate sea level variations on global and regional scales is satellite altimetry. Additional satellite systems are needed to compute variations in sea level from altimetry measurements with respect to the geopotential surface. The geoid can be derived from the GRACE mission. Other applications are analysis of ocean tides, estimation of the variability of ocean currents, waves and eddies, or estimation of the dynamics and the mass balance of ice sheets.

Satellite altimetry measures the distance between the satellite and the ocean surface by sending a short  $\mu$ -wave pulse to the ocean surface (Figure 4.15). The signal travels

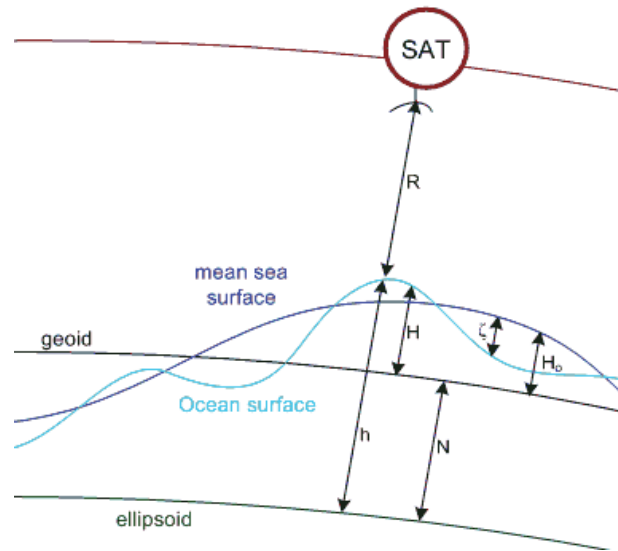


Figure 4.15: Diagram of how satellite altimetry measures sea surface topography

through the atmosphere and is reflected at the surface. The satellite receives the signal after it traveled through the atmosphere for a second time. The measured distance  $R$

$$R = c \frac{t}{2} - \tilde{R} \quad (4.2)$$

is computed by the travel time  $t$  and the speed of light  $c$  (speed of the signal). The travel time is divided by 2 as the signal travels twice the distance from the satellite to the ocean surface. In addition, the measurements have to be corrected for inaccuracies in the range  $\tilde{R}$  originating from instruments, the atmosphere and variations in the ocean state. For example, using radar altimetry sea surface roughness is a source of error in the return signal as the signal (spherical wave) is reflected earlier at the crest of a wave (at shortest distance) than at its trough (at longest distance). As a result, the return signal is extended and the travel time increases. A correction of the erratic signal can be achieved for example by averaging over several return pulses. This method would decrease along track resolution as the satellite is moving while the return pulses are received. After computation of the distance the height of the satellite is used to compute the sea surface height, which is the distance from the ocean surface to the ellipsoid. Sea surface topography is then computed by subtracting the geoid height from the sea surface height. The geoid height deviates from the ellipsoid by about -100 m to +80 m ( $\pm 30$  m). The resulting difference of the geoid and the sea surface topography amount to  $\pm 2m$ . There are additional anomalies from the static ocean topography, called sea level anomalies, resulting e.g. from waves,

tides, eddies, or atmospheric loading.

To minimize systematic errors in the orbits, a cross over adjustment is generally performed. Here, the sea surface height at locations where ascending and descending satellite tracks are overlapping (crossover point) are subtracted from each other. This can be done when there is only little time difference between the 2 measurements. There are two different types of crossovers defined. The first one is called "Single-Mission-Crossovers" where only 1 satellite mission is considered. But as there are more than one satellite mission available for the different applications, generally "Multi-Mission-Crossovers" can be used, which include a minimum of two satellite altimetry system in the cross over adjustment. Cross over points can be approximated analytically using e.g. Kepler elements. Cross-over analysis also allows for quantifying the time variable part in the signal as  $H_o$  and  $N$  can be eliminated.

Satellites of altimetry missions normally fly at an altitude of 800 km to 1000 km, because at lower altitude the air drag would strongly increase, which would decrease the mission life time, and the satellites are not flying higher, because the signal strength is decreasing with increasing altitude as  $\frac{1}{(2R)^2}$ .

## 4.7 Multi-Mission Altimetry Measurements

Multi-mission altimetry measurements (including cross over adjustment) are used to compute the sea surface topography and are provided on a weekly time scale for the period 2003 to 2007 by the Deutsches Geodätisches Forschungsinstitut (DGFI) München (Bosch and Savcenko, 2008; Albertella et al., 2008). Measurements are interpolated to the grid of FESOM with a spatial resolution of  $1.5^\circ$ . For every grid point a linearly weighted mean has been computed from all measurements within the radius of influence of  $1^\circ$ . Another issue occurs as weekly solutions don't include the full repeat cycle of the altimetry satellites, which result in small data gaps. They are filled by nearest neighbor interpolation.

The resulting mean sea surface topography for the years 2003 to 2007 (Figure 4.16) shows patterns similar to the simulated sea surface topography (Figure 4.7), including the decrease in height in the region of the sub-polar gyre in the North Atlantic. Also the patterns of increased sea level at the subtropical gyres and of decreased sea level in the Southern Ocean can be identified. The standard deviation of geodetic observations identifies strongest variations mainly in region of the Gulf Stream in the North Atlantic, the Kuroshio, the Agulhas Current south of Africa, and in the Malvinas current south-east of South America. These currents have strong and variable flows, including eddies and

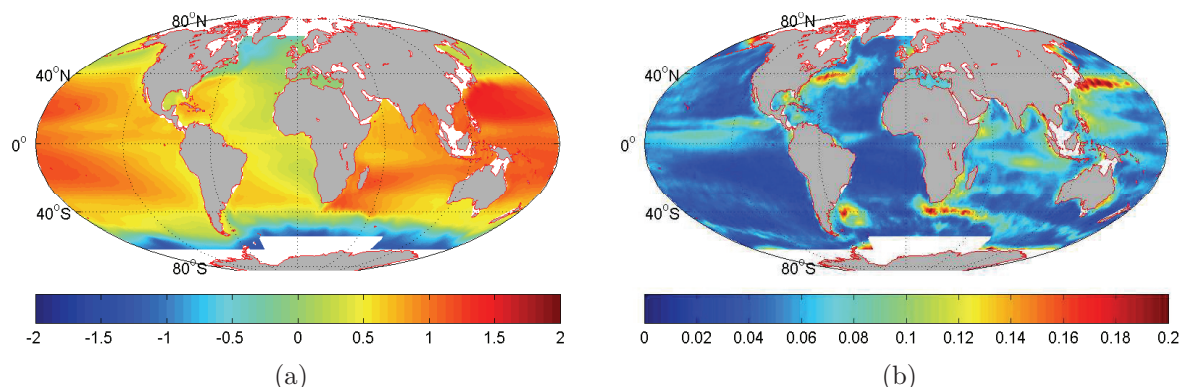


Figure 4.16: Mean sea surface topography derived from weekly altimetry measurements (a) and its standard deviation (b) in meter (2003 - 2007)

meanders.

## 4.8 Identification of Modeled Steric Height Changes in Altimetry

Steric variations of the ocean are used to analyze density changes. The geodetic measurements of steric change reflects the difference of the observed volume change and the volume change associated with mass change. To estimate the ocean surface topography altimetry measurements from multi missions are used. Mass changes are derived from the GRACE gravity mission and the joint inversion. Here, only the lowest order terms of the geoid change are considered because of the degree and order ( $30 \times 30$ ) of the weekly GRACE and inverse solutions. To minimize systematic errors, GRACE solutions are again smoothed with a Gaussian filter using the averaging radius of 750 km. The inverse solution is not filtered. Measurements are smoothed with a 3 weeks running mean to reduce noise (not applied in computing the global means).

Similar patterns can be identified when comparing modeled steric height with steric height derived from GRACE estimates (Figure 4.17a). The pattern of the seasonal oscillation between the two hemispheres is also observed. Small structures, e.g. in the equatorial regions or in the North Atlantic are visible. Steric height variations computed with GRACE estimates show good correlations with modeled steric height variations, with values mostly between 0.5 and 0.6 (Figure 4.17b). In the Southern Ocean correlation is very low for two reasons. First, less altimetry measurements are available in these latitudes and the FESOM model shows strong sensitivity in this region. A negative correlation occurs at the

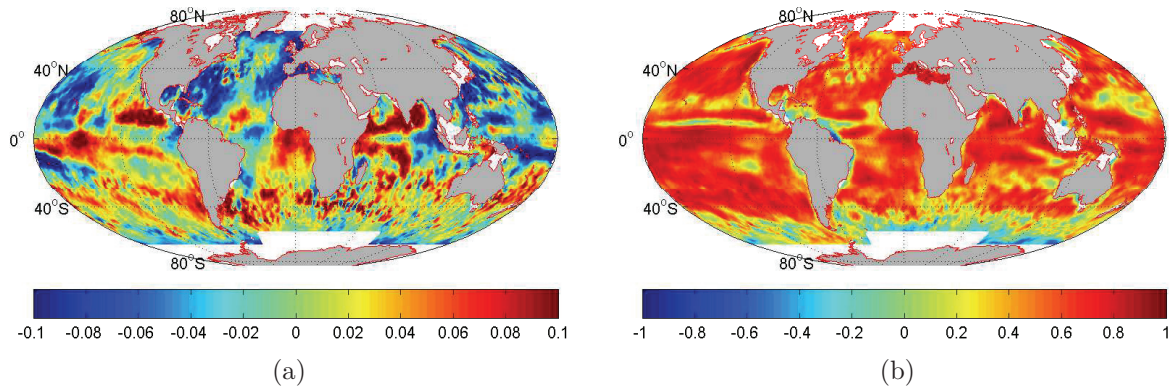


Figure 4.17: Weekly steric height anomalies (3 weeks running mean applied) derived by subtracting GRACE solutions from weekly altimetry measurements for March 2005 (week 1314) (a), correlation of geodetic and modeled steric height anomalies for 2003 - 2007 (b)

north-east coast of South America possibly caused by differences in the runoff from the Amazonian River or leakage effects from land hydrology. Note, that the correlation might be affected by applying the Gauss filter and by the uncertainties arising from the issue of the low degree spherical harmonics coefficients of the weekly GRACE solutions (described in Section 3.6).

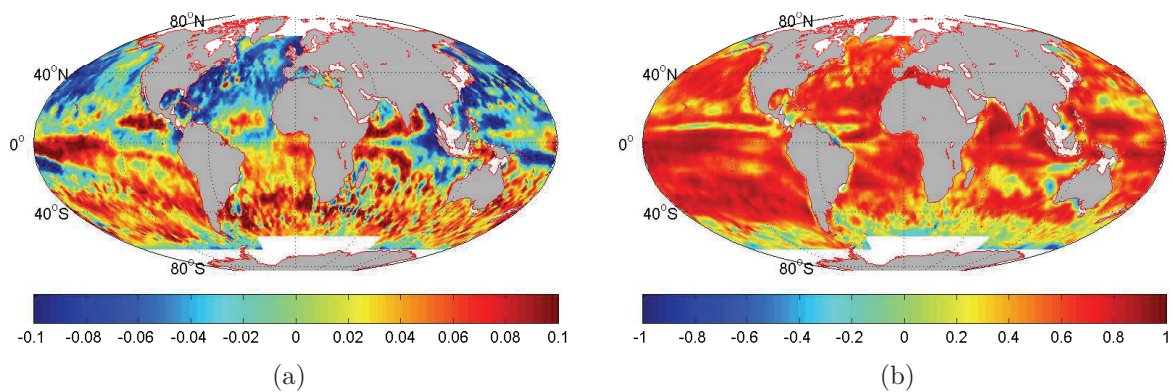


Figure 4.18: Weekly steric height anomalies (3 weeks running mean applied) for March 2005 (week 1314) derived by subtracting ocean mass variations of the inversion from weekly altimetry measurements (a), as well as its correlation to modeled steric height anomalies (2003-2007) (b)

When computing steric height variations using the inverse solution, the oscillation between the hemispheres is more pronounced compared to using GRACE estimates (Figure 4.18a), but local patterns remain very similar. Correlation with the modeled steric height anomalies is improved to range mostly between 0.6 and 0.7. The improvement is caused by

the availability of the low degree spherical harmonics coefficients and because no filtering is applied to the mass variations.

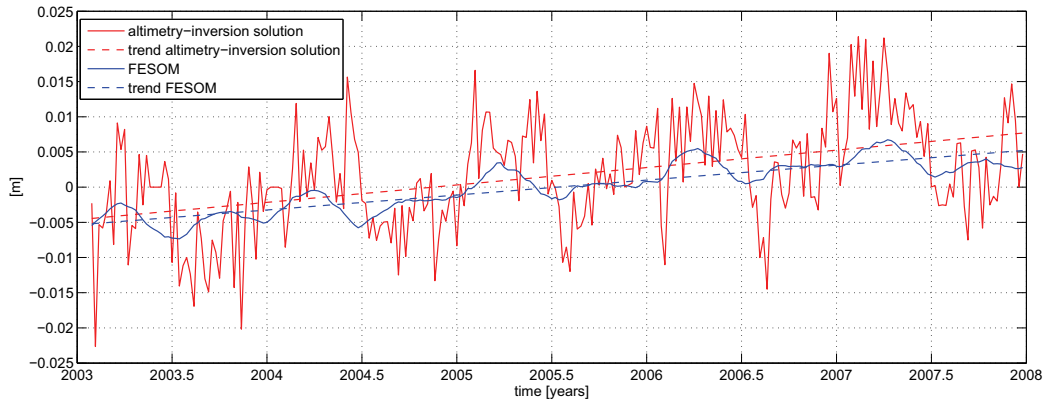


Figure 4.19: Weekly global mean steric height variations derived by taking the difference of altimetry measurements and the inversion solution, and modeled with FESOM.

The trend of weekly global mean steric sea level variations of FESOM amounts to about 2 mm/yr for the years 2003 to 2007. Measured estimates of global mean steric height variations, computed by subtracting the mass variations of the inversion from altimetry measurements show a trend of about 2.4 mm/yr. Both trends are overestimated by about 1 to 2 mm/yr compared to other studies (Cazenave et al., 2008; Leuliette and Miller, 2009). On the other hand they are consistent with studies by Wenzel and Schröter (2007b). The phases of both solutions show similar values, only the amplitude differs. Compared to the modeled steric height variations, the geodetic observations show about a doubled amplitude, including strong short term fluctuations, not visible in the model solution.

## 4.9 Conclusion

Variations in sea surface topography are caused by steric and eustatic parameters. Eustatic sea level changes corresponds to changes in the mass of the ocean, through fresh water inflow. Changes in ocean temperature and salinity are the steric components. They are transported in the ocean by currents, which are associated with sea surface topography. Global mean sea level change modeled with FESOM includes a trend of about 3.1 mm/yr for the period from 1993 to 2003. Compared to other studies (Wenzel and Schröter, 2007b; Bindoff et al., 2007; Cazenave et al., 2008) it is slightly overestimated since eustatic sea level change due to glaciers, ice caps, and continental ice sheets, are not considered in the model experiment.

During the first decades of the simulation steric sea level shows a trend of about 0.4 mm/yr, which well coincides with Bindoff et al. (2007). For the period between the years 1993 and 2003, the overestimated trend in sea level change results from the trend in modeled steric sea level rise of about 2.5 mm/yr, which well agrees with the geodetic observations implying a trend of 2.4 mm/yr for this period. This results confirms the results of the study of Wenzel and Schröter (2007b), who estimated steric sea level rise of 2.47 mm/yr. However, other studies implies lower trends of about 1.6 mm/yr (Bindoff et al., 2007; Cazenave et al., 2008). A decreased positive trend of about 1.8 mm/yr between 2003 and 2008 is modeled.

Regionally modeled steric height anomalies show similar spatial structures compared to geodetic observations. This indicates that FESOM is able to realistically simulate spatial distributions of temperature and salinity in the ocean. Here, the correlations appear to be higher when computing observed steric height variations by subtracting the inverse solution from altimetry measurements.

# Chapter 5

## Sea Level Change due to Ice Sheet Melting

During the last decades global mean sea level has risen due to global warming (Church et al., 2001). The increase in mean temperature results in thermal expansion of the ocean, which is the major contributor to sea level change (about 60%) (Bindoff et al., 2007). Another strong contribution arises from mass change in the ocean due to melting of glaciers, ice caps, and ice sheets in Greenland and West Antarctica (Lemke et al., 2007).

The fresh water inflow around the coasts of the two major ice sheets strongly influences the state of the ocean. Global sea level is rising due to the additional mass. Density variations in turn change the sea level locally due to the freshening of the regional ocean. The reaction of the ocean to fresh water anomalies caused by Greenland ice sheet melting under different boundary conditions is investigated by Gerdes et al. (2006). Their Modular Ocean Model (MOM) simulations featured reduced overturning and gyre circulation in the North Atlantic. Stammer (2008) investigated salinity and temperature variations, and the response of the sea surface height (SSH) of the ocean to ice sheet melting in Greenland and Antarctica using the MIT ocean general circulation model. He found a depression of SSH located in the center of the sub-polar North Atlantic and the western subtropical North Atlantic, associated with colder water masses. Also a reduced meridional overturning circulation (MOC) in the North Atlantic was found. In the Southern Ocean, the fresh water inflow is mainly from the West Antarctic Ice Sheet. It strengthens the MOC in the southern hemisphere after 30 years. A study by Marsh et al. (2009) forced an eddy-permitting ocean model, based on NEMO (Nucleus for European Modeling of the Ocean), with fresh water inflow at the Greenland coast from 1991 to 2000. They found only slight impacts in large scale ocean circulation, whereas sea level is changing west of Greenland,

mainly in the Baffin Bay.

During this study, the influence of melting of the Antarctic and Greenland ice sheets on the sea level is investigated. Theoretical melting scenarios are introduced into the FESOM model to derive sea level change. The following scenarios are studied: Fresh water inflow of 100 Gt/yr has been added at the coast of West Antarctica, to analyze its response to the global ocean. At the Greenland coast, four different amounts of fresh water inflow have been applied (100, 200, 500, and 1000 Gt/yr), to investigate the impacts of different amounts of fresh water inflow on sea level. In an additional experiment, daily melt rates are computed to investigate the influence of seasonal variability of ice sheet melting to the sea level. The self gravitational effects are analyzed here, which account for less attraction to the Greenland Ice Sheet (GIS), as mass is reduced due to melting. Additionally, the resulting change in potential of the deformed Earth causes small changes in sea level. These effects are modeled by applying Green's functions and maps of melting rates, created from melt extent data (Abdalati and Steffen, 2001; Abdalati, 2009).

## 5.1 Definition of Ice sheets

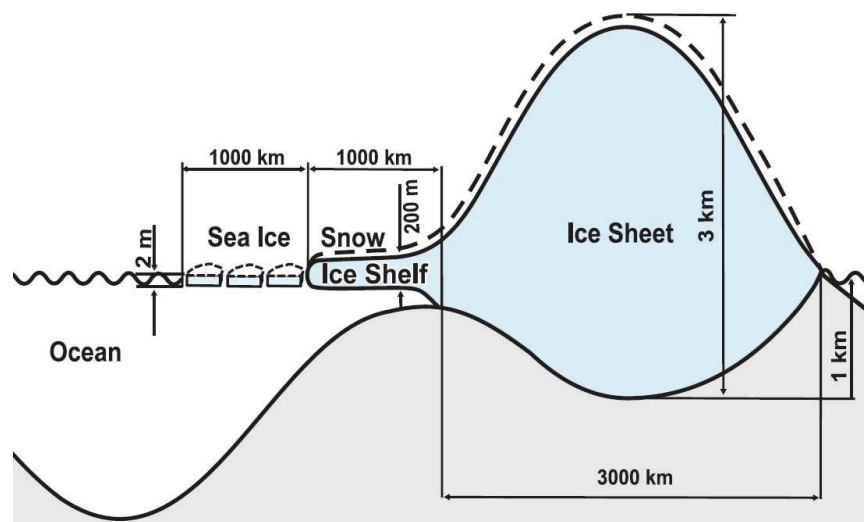


Figure 5.1: Definition of ice sheets (Lemke et al., 2007)

The cryosphere on the Earth is separated into glaciers and ice caps, ice sheets, ice shelves, sea ice, and frozen ground, and ice on rivers and lakes. A glacier is defined as large body of ice, which has its origins on land and flows due to gravity. On time scales between years and centuries, glaciers increase their mass by precipitation in form of snow,

whereas mass is lost through melting and sublimation. They can be found in mountain areas world wide, but in tropical regions they occur only on top of high mountains, like the Kilimanjaro. However, most ice is stored within the two larger ice sheets in Greenland and Antarctica.

Ice sheets (Figure 5.1) are generally located on land and are larger than 50,000 square kilometers. They are defined as glacier ice, also covering large areas around them. Today, there are two major ice sheets, the Antarctic ice sheet and the Greenland ice sheet, which are the major storage of fresh water on Earth. In the Antarctic new ice is entering the ice sheet via snow, which is compressed to glacier ice. This is transported via ice streams to the coast. Here, the ice sheet is passing the grounding line feeding floating ice shelves, which may melt or be the origin of icebergs, via calving. Generally, if the ice mass loss to the sea and the snow fall on top of the ice sheet is balanced, no change in global mean sea level would occur. However, regional steric variations might occur due to the redistribution of fresh water.

In comparison to ice shelves, sea ice is generated by freezing of ocean water. Due to the salt in the ocean, water is freezing if the temperature becomes lower than about  $-1.7^{\circ}\text{C}$ . During the sea ice formation, salt is expelled from the sea ice, which becomes less saline. Variations of sea ice have no influence on the global mean sea level as it floats on top of the ocean water. The higher volume of sea ice compared to the salty ocean water, is compensated by its lower density.

## 5.2 Loading and Self Attraction

Variations of mass in the ocean deform the shape of the Earth. This effect is separated into loading (ocean floor deformation due to mass loads above) and self attraction. Also changes of continental ice masses e.g. in Greenland influence the regional sea level, which correspond to the gravitational effects. Sea level change due to global isostatic adjustment (GIA) is not considered in the following.

Loading and self attraction do not change global mean sea level, but influence sea level regionally. For example, the mass of the Greenland ice sheet is attracting water, which results in a higher sea level near the coast of Greenland. Also the attracted water has a mass, which again is attracting additional water masses (self attraction). The mass loss induces a deformation of the ocean bottom, decreasing sea level (relative to the ocean bottom). If the Greenland ice sheet loses mass, the ocean water is less attracted to the ice causing a decrease of sea level near to the ice loss. A slight sea level rise in more distant

regions occurs. Also the ocean bottom is lifted up due to the reduced load.

Loading and self attraction effects are computed during the calculation of ocean tides (Farrell, 1972; Francis and Mazzega, 1990), using load Love numbers. They are first defined by Love (1909), Love (1911), describing the elasticity of the Earth. The load Love numbers define the deformation of the Earth due to loading in radial direction. Also, the horizontal displacement due to loading is described. This effect is very small and is normally neglected. The gravitational effect due to variations of surface mass are defined by  $1 + k'_n$  (Equation 5.2) and is called self attraction (or gravitational effect).

The self attraction effect of ocean mass redistribution is introduced into the model at each time step, using Green's functions (Farrell, 1972). It has only small influence as the mass of the water inflow is redistributed through waves within days. The effect is almost averaged out when computing weekly or monthly means. The loading effect is not visible in the model because it computes sea level change with respect to the geoid. Hence, the loading effect is not taken into account in FESOM. However, the indirect effect, i.e. change in the gravity field arising from the Earth's deformation to load changes leads to small changes in regional sea level. This gravitational effect due to Greenland ice sheet melting yields a geocentric load as seen from altimetry measurements. It is computed in the same way as self attraction. It is computed during postprocessing, which is possible as it does not change the ocean circulation.

A convolution integral calculates the sea level redistribution  $I$  due to the gravitational attraction in equivalent water height for a location  $(\phi, \lambda)$  (Equation 5.1; Francis and Mazzega (1990)). The point-wise integration is used, as it is most accurate according to a study of Schrama (2004), disregarding the high computational costs.

$$I(\phi, \lambda) = \rho_w \sum_{i=0}^N G_k(\alpha_i) F_i(\phi', \lambda') dS_i \quad (5.1)$$

$F_i(\phi', \lambda')$  is the change of the water level at location  $(\phi', \lambda')$ , where  $\phi$  is latitude and  $\lambda$  is longitude. The surface area is  $dS_i$  and  $N$  the number of oceanic elements of the model. The distribution of the Greenland ice sheet melt is derived from estimates of daily melt extent (Abdalati and Steffen, 2001; Abdalati, 2009). The mass loss  $F_i(\phi', \lambda')$  is converted to equivalent water height before performing the convolution. The Green's function  $G_k$  is defined as

$$G_k(\alpha) = \frac{a}{M_e} \sum_{n=0}^{\infty} (1 + k'_n) P_n(\cos(\alpha)) \quad (5.2)$$

with

$$P_n(x) = \frac{1}{2^n n!} \frac{d^n}{dx^n} (x^2 - 1)^n \quad (5.3)$$

and  $\alpha$  being the spherical distance between  $\phi, \lambda$  and  $\phi', \lambda'$ . It is calculated from

$$\cos \alpha = \sin \phi \sin \phi' + \cos \phi \cos \phi' \cos (\lambda - \lambda')$$

where the mean radius of the Earth is denoted as  $a$ , the total mass of the Earth is  $M_e$ , and  $P_n$  is the associate Legendre polynomial. The sum  $1 + k'_1$  accounts for the direct gravitational effect of the change mass (denoted by 1) and the load Love number  $k'_n$  accounts for the gravitational effects due to the deformation of the Earth (Blewitt, 2003).

### 5.3 Melting of the Antarctic Ice sheet

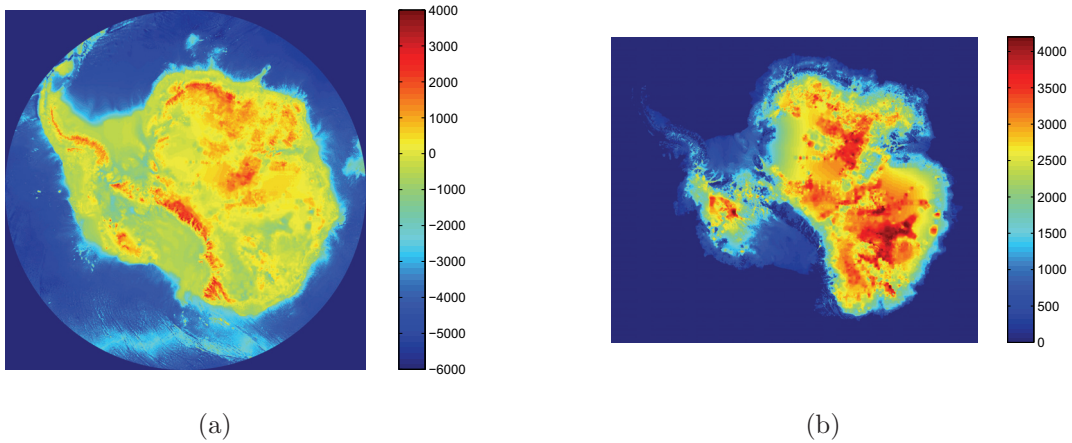


Figure 5.2: Antarctic ice sheet (a) and bedrock (b) elevation in meter (Lythe et al., 2000)

The ice sheet on the Antarctic continent is the biggest ice sheet on Earth. Its volume amounts  $30 \cdot 10^6 \text{ km}^3$  on an area of about 14 million  $\text{km}^2$ . The ice sheet covers about 98% of the Antarctic continent with a maximum thickness of around 4 km. Sea level would be about 57 m higher than today, if it would melt entirely (Lemke et al., 2007). The Antarctic ice sheet is geographically separated into two parts, the West Antarctic Ice Sheet (WAIS) and the East Antarctic Ice Sheet (EAIS), which rests on land mass (Figure 5.2, Lythe et al. (2000)). In large regions the mass of the ice sheets depresses the bedrock

Table 5.1: Antarctic Ice Mass Balance

| Study                     | Time Period       | Mass Loss   | Datasets   |
|---------------------------|-------------------|---|--|
| Chen et al. (2009)        | 04/2002 - 01/2009 | $-190 \pm 77$ Gt/yr                                   | GRACE measurements   |
| Gunter et al. (2009)      | 07/2002 - 03/2005 | $-84$ to $-103$ Gt/yr                                 | GRACE and ICESat measurements                                      |
| Rignot et al. (2008)      | 1996, 2000, 2006  | $-12 \pm 91$ , $-106 \pm 60$ ,<br>$-196 \pm 92$ Gt/yr | satellite interferometric<br>synthetic-aperture radar observations |
| Velicogna and Wahr (2006) | 2002 - 2005       | $-152 \pm 80$ km <sup>3</sup> /yr                     | GRACE measurements   |
| Velicogna (2009)          | 04/2002 - 02/2009 | $-143 \pm 73$ Gt/yr                                   | GRACE measurements   |
| Wingham et al. (2006)     | 1992 - 2003       | $+27 \pm 29$ Gt/yr                                    | satellite radar altimetry  |
| Wu et al. (2010)          | 2002 - 2008       | $-99 \pm 59$ Gt/yr                                    | GRACE measurements (GIA corrected)                                 |
| Zwally et al. (2005)      | 1992 - 2002       | $-31 \pm 12$ Gt/yr                                    | Satellite radar altimetry data from<br>ERS-1 and ERS-2             |

to elevations near or below sea level. The bedrock below the WAIS extends to over 2500 m below sea level. It would be uplifted to higher elevation if ice mass would be lost, as the load would be reduced. The EAIS remains almost constant in the interior of the continent in today's climate. Only at the coastal regions small variations in ice mass occur (Gunter et al., 2009). Melting occurs at the WAIS, which is described in recent studies (Table 5.1), estimating a mass loss of around 100 Gt/yr. For example, a loss of  $143 \pm 73$  Gt/yr of Antarctic ice mass had been observed between April 2002 and February 2009 by Velicogna (2009) using time-variable gravity measurements from GRACE. Gunter et al. (2009) compared mass variations in Antarctica derived from the GRACE and ICESat missions. Both data sets show similar ice mass loss of about 100 Gt/yr, mainly located at the WAIS. This coincides well with a study of Rignot et al. (2008), showing a similar ice mass loss in the Antarctic in the year 2000 using interferometric synthetic-aperture radar data from different remote sensing satellite missions. During the whole period of investigation (1996 to 2006) they found an accelerating ice mass loss from 78 Gt in 1996 to 153 Gt in 2006.

In the present study, an experiment is performed to investigate how much the global and regional sea level increases if 100 Gt/yr of the WAIS is molten. Hence, the mass loss is converted to a continuous volume flux, which is distributed along the coast of the WAIS (Figure 5.4). Including the additional fresh water inflow, a model simulation is performed for 48 years. Sea level change is computed by taking differences to a reference model simulation.

Global sea level change amounts to about 0.3 mm/yr, slightly varying due to additional steric effects. In the first years, relative sea level mainly changes near the source of the fresh water in the West Antarctic (Figure 5.3). After about 15 years density variations reach the Antarctic Circumpolar Current (ACC) and start to be transported around the Southern Ocean. The ACC acts like a wall, which the fresh water passes very slowly. For this reason,

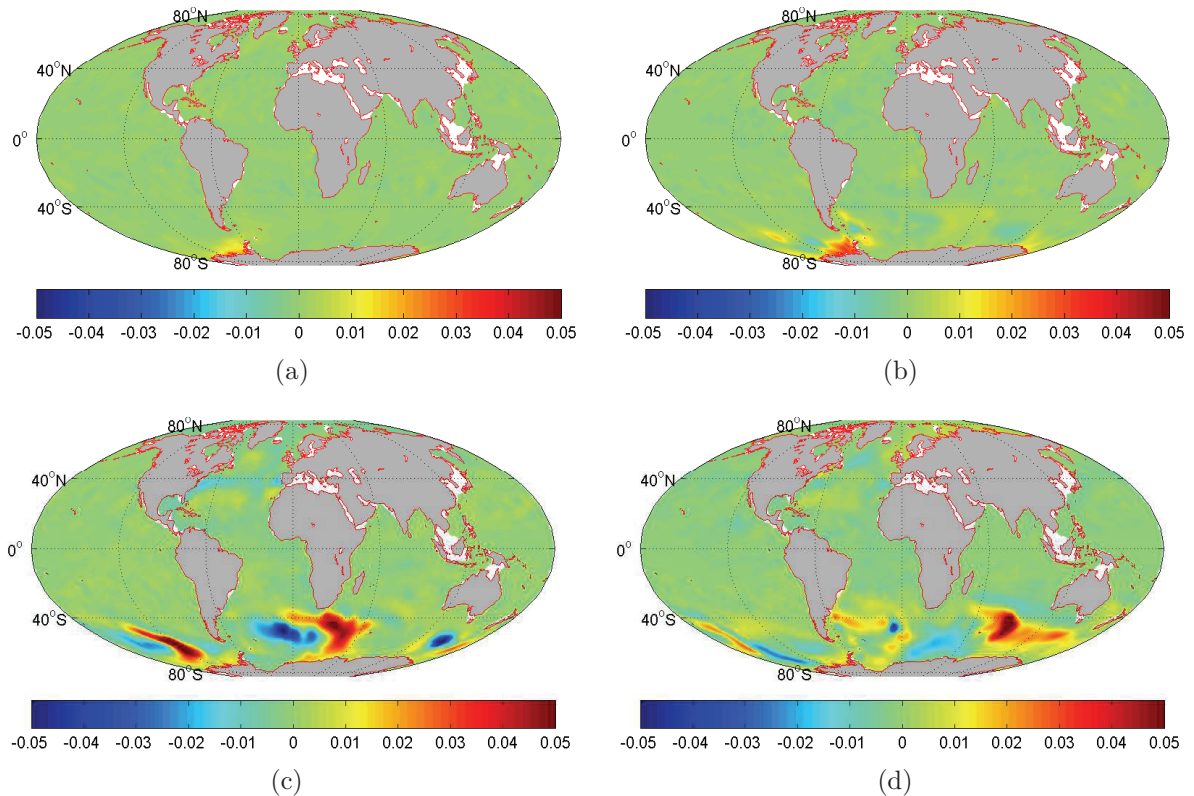


Figure 5.3: Relative sea level change due to 100 Gt/yr West Antarctic ice sheet melting after (a) 5, (b) 15, (c) 35, and (d) 48 years

sea level change is mostly limited to latitudes poleward of  $30^{\circ}\text{S}$ . The response is confined to the Southern Ocean. The quadrupole-like patterns of positive and negative change in the Southern Ocean resemble patterns of high variability in locally excited circulations.

Temperature variations are advected by the ACC and distributed over the whole Southern Ocean, mainly occurring at depths between 100 m and 500 m. After 48 years, similar patterns as in the relative sea level change are visible. At the surface no specific structures of temperature change can be identified, as sea surface temperatures are dominated by atmospheric forcing. Also an increase in temperature occurs in the North Atlantic reaching from the Sargasso Sea to Barents Sea. East and West of this narrow band the temperature decreases, mainly at the east coast of Canada and west of Strait of Gibraltar. This leads to small variations in sea level that occur in the North Atlantic after some decades, as the volume transport to the North within the intermediate water is slightly modified.

Salinity changes, which are occurring in the upper 200 m of the water column, are localized at the coast of the WAIS and are slowly transported by the ACC to the Atlantic

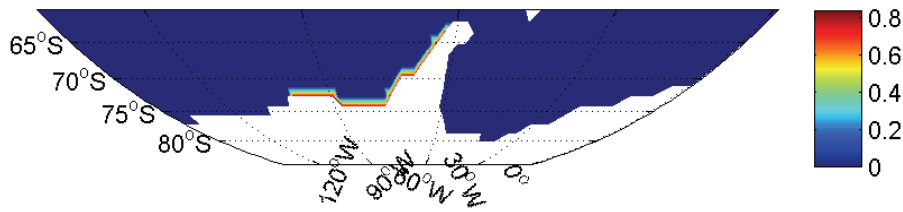


Figure 5.4: Continuous fresh water inflow in m/yr, due to melting of the West Antarctic ice sheet (100 Gt/yr)

basin of the Southern Ocean after 48 years of model integration. Its maximum is located at the surface around 40°S between Rio de la Plata (South America) and South Africa.

## 5.4 Mass Variations of the Greenland Ice Sheet

Besides the Antarctic ice sheet, a large ice sheet is located on Greenland. It extends over an area of  $1.7 \cdot 10^6 \text{ km}^2$ , which covers about 82 % of Greenland. Its volume amounts to  $2.8 \cdot 10^6 \text{ km}^3$  and is on average about 2.3 km thick. In central Greenland the ice sheet can reach a thickness of more than 3 km (Figure 5.6) (Bamber et al., 2001a,b). The mass of the ice sheet results in a depression of the bedrock mainly lying near sea level. In some region the bedrock topography is lying more than 100 m below sea level, mainly in the interior of Greenland. No ice is reaching the Greenland coast without obstruction by mountains, resulting in the lack of large ice shelves. However, strong calving of icebergs occur where glaciers reach the sea. Due to its location the GIS is strongly influenced by global warming. In the recent past Greenland is melting below an altitude of 2000 m. Above 2000 m the ice mass is almost balanced or slightly thinning (Luthcke et al., 2006; Shepherd and Wingham, 2007; Wouters et al., 2008). If no ice would remain on Greenland global sea level would rise by about 7 m (Lemke et al., 2007).

Due to present day melting, several studies were undertaken to investigate the GIS characteristics using either in-situ or satellite measurements, or models (Table 5.2). For example, ice mass loss of  $101 \pm 16 \text{ Gt/yr}$  in Greenland between 2003 and 2005 was derived by Luthcke et al. (2006). GRACE measurements indicate a mass loss of 155 Gt/yr at elevations lower than 2000 m and a gain of ice mass at higher elevations, including a strong seasonal cycle at lower elevations. Wouters et al. (2008) estimated ice mass loss of  $179 \pm 26 \text{ Gt/yr}$  in Greenland between 2003 and 2007, including a negative mass balance above 2000 m in 2007. A loss of Greenland ice mass had been estimated during April 2002

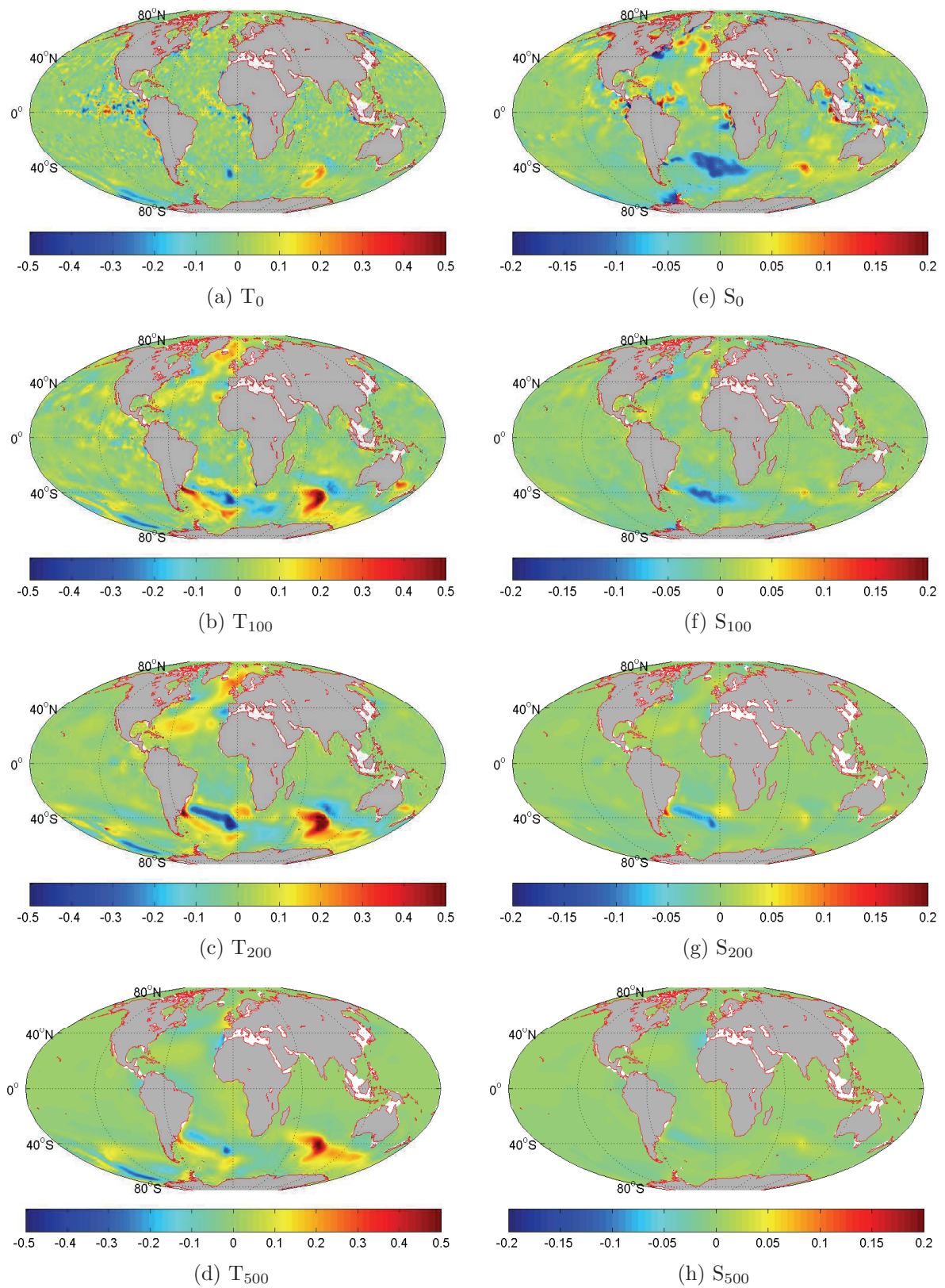


Figure 5.5: Difference of temperature ( $^{\circ}\text{C}$ ) and salinity (psu) at different depth after 48 years if 100 Gt/yr of West Antarctic ice is released into the ocean (with respect to a reference simulation without additional melt water input).

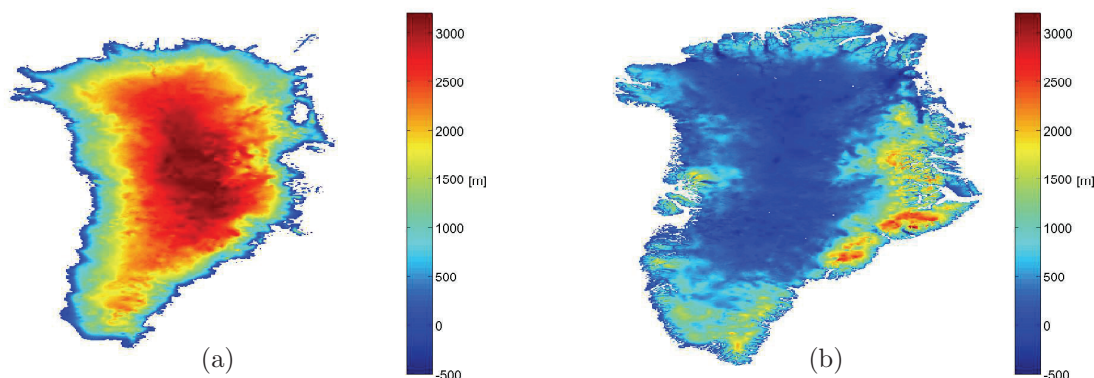


Figure 5.6: Greenland ice sheet (a) and bedrock (b) elevation in meter; (Bamber et al., 2001a,b)

and February 2009 by Velicogna (2009) using time-variable gravity measurements from GRACE. They found a mass loss of the GIS of 137 Gt/yr between 2002 and 2003, and of 286 Gt/yr between 2007 and 2009.

#### 5.4.1 Constant Melt Rates

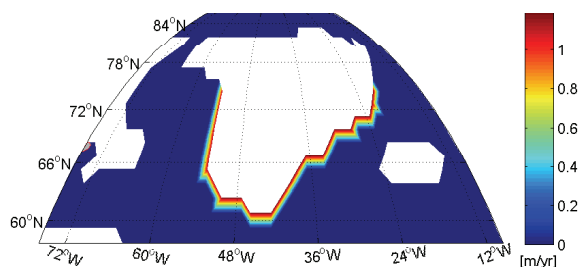


Figure 5.7: Continuous fresh water inflow in m/yr due to Greenland ice sheet melting (200 Gt/yr).

Four simulations have been performed with different mass losses at the Greenland coasts to investigate the oceanic response. The mass losses of 100 Gt/yr and 200 Gt/yr span the range of observational studies (e.g. Rignot et al. (2008), Wouters et al. (2008), or Velicogna (2009)). Furthermore, two extreme cases were tested, adding 500 Gt/yr, and 1000 Gt/yr of melt into the ocean. They describe scenarios when mass loss of the Greenland ice sheet would drastically increase. The continuous fresh water flux, which is added to the model is evenly distributed along the coast of Greenland south of 75°N (Figure 5.7). The simulations are performed for 48 years, starting in 1960. Sea level change is computed by

Table 5.2: Greenland Ice Mass Balance

| Study                        | Time Period                            | Mass Loss  | Data sets   |
|------------------------------|--|--|---|
| Box et al. (2004)            | 1991 - 2000                            | $-78 \text{ km}^3/\text{yr}$   | Polar MM5 model and in-situ measurements  |
| van den Broeke et al. (2009) | 2003 - 2008                            | $-237 \pm 20 \text{ Gt}/\text{yr}$   | GRACE measurements and Regional Atmospheric Climate Model (RACMO2/GR)                 |
| Chen et al. (2006)           | 04/2002 - 11/2005                      | $-239 \pm 23 \text{ km}^3/\text{yr}$   | GRACE measurements  |
| Hanna et al. (2005)          | 1961 - 1990<br>1998 - 2003             | $+22 \pm 51 \text{ km}^3/\text{yr}$<br>$-36 \pm 59 \text{ km}^3/\text{yr}$             | meteorological ECMWF data, surface melt water runoff/retention model and in-situ data |
| Luthcke et al. (2006)        | 2002 - 2005                            | $-113 \pm 17 \text{ Gt}/\text{yr}$   | GRACE measurements  |
| Ramillen et al. (2006)       | 07/2002 - 03/2005                      | $-129 \pm 15 \text{ km}^3/\text{yr}$   | GRACE measurements (10-day GRGSEIGEN-GL04 solutions)                                  |
| Thomas et al. (2006)         | 04/1993 - 09/1998<br>09/1998 - 12/2004 | $-4 \text{ to } 50 \text{ Gt}/\text{yr}$<br>$-57 \text{ to } 105 \text{ Gt}/\text{yr}$ | Laser altimeter measurements  |
| Velicogna and Wahr (2005)    | 2002 - 2004                            | $-82 \pm 28 \text{ km}^3/\text{yr}$  | GRACE measurements  |
| Velicogna (2009)             | 04/2002 - 02/2009                      | $-230 \pm 33 \text{ Gt}/\text{yr}$   | GRACE measurements  |
| Wouters et al. (2008)        | 02/2003 - 01/2008                      | $-179 \pm 25 \text{ Gt}/\text{yr}$   | GRACE measurements  |
| Wu et al. (2010)             | 2002 - 2008                            | $-161 \pm 35 \text{ Gt}/\text{yr}$   | GRACE measurements (GIA corrected)  |
| Zwally et al. (2005)         | 1992 - 2002                            | $+11 \pm 3 \text{ Gt}/\text{yr}$   | Satellite radar altimetry data from ERS-1 and ERS-2                                   |

taking the difference of monthly mean sea level simulated with the additional fresh water inflow and a reference model simulation.

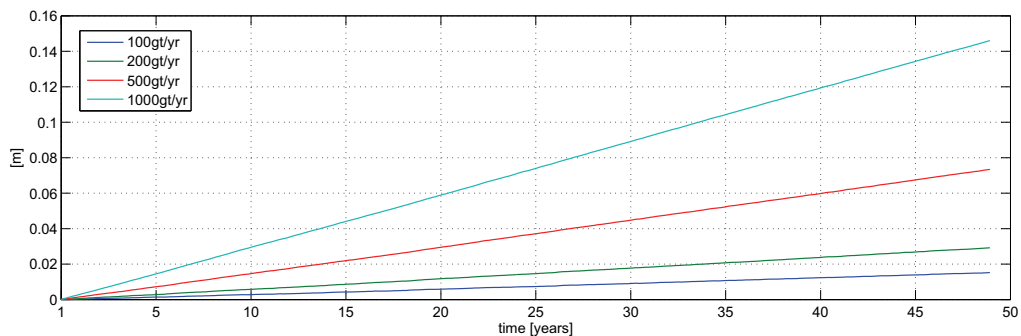


Figure 5.8: Response of global mean sea level to melting of the Greenland ice sheet (GIS) for continuous melt during 48 years

Global mean sea level is rising if the Greenland ice sheet is melting (Figure 5.8a). Its amount is given by the amount of ice mass change and the geometry of the ocean. Global mean sea level rises by about  $0.3 \text{ mm}/\text{yr}$  if  $100 \text{ Gt}/\text{yr}$  of land ice mass flow as additional fresh water into the ocean, proportionally increasing with the amount of fresh water. This finding coincides with many other studies e.g. from Hanna et al. (2005), Luthcke et al. (2006), van den Broeke et al. (2009).

Figure 5.9 depicts the relative sea level change after 5, 15, 35, and 48 years of model integration, if  $200 \text{ Gt}/\text{yr}$  of melt water is released into the ocean along the coast of Greenland. During the first years the relative sea level increases near the coast of Greenland

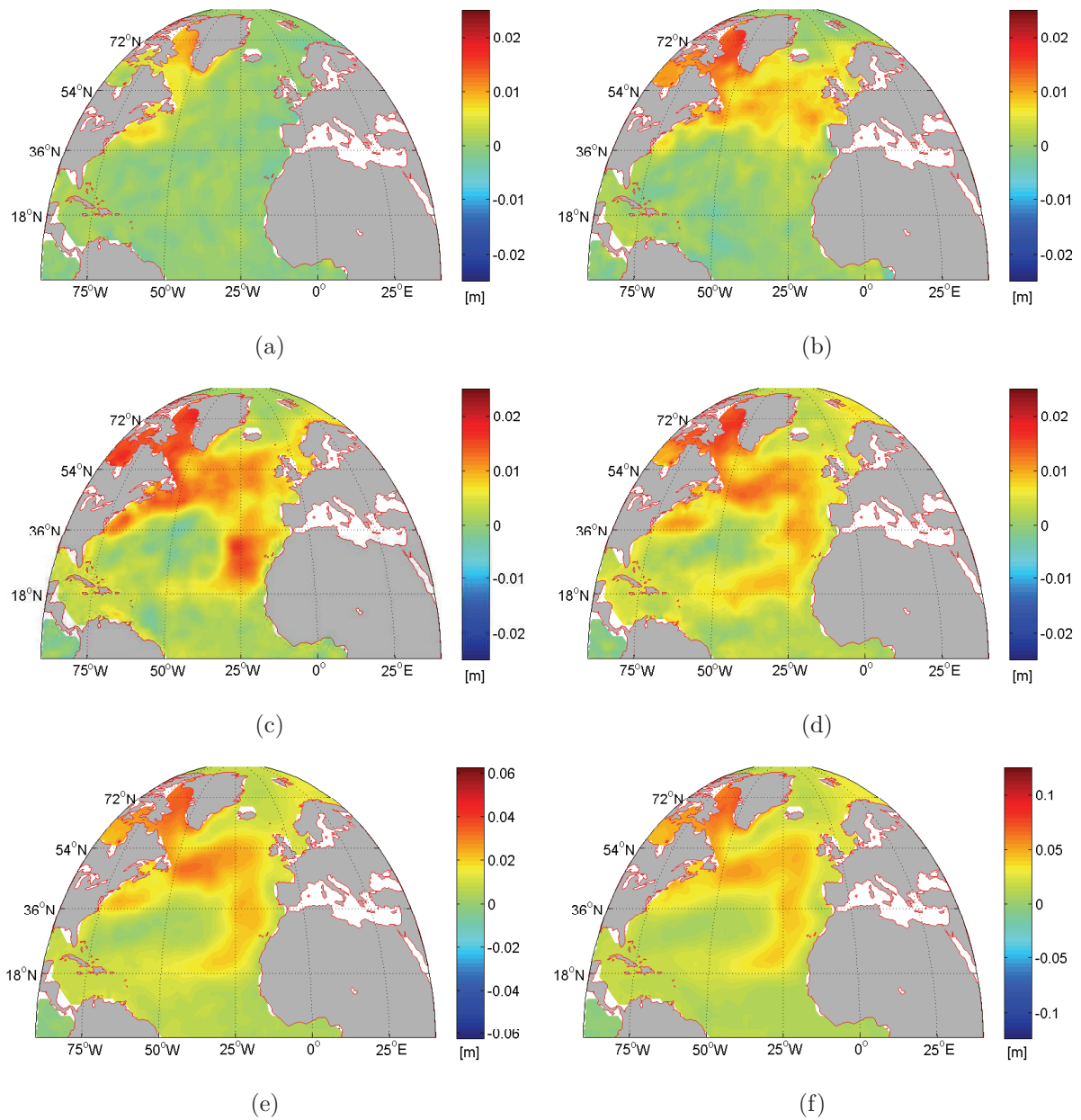


Figure 5.9: Relative sea level change in meter if 200 Gt/yr of the Greenland ice sheet is melting, after (a) 5 years, (b) 15 years, (c) 35 years, and (d) 48 years. Relative sea level change for increased inflow of 500 and 1000 Gt/yr is shown in panels (e) and (f), respectively, after 48 years. Note the change in color scale, which is scaled according to the source strengths.

mainly in the Labrador Sea and the Baffin Bay. After about five years, sea level change enters the North Atlantic near the east coast of Canada via the Labrador Current. In the next ten years it slowly follows the North Atlantic Drift, reaching Europe after about one decade. From there, the change is following the subtropical gyre to the equatorial region of the Atlantic Ocean while another filament is entering the Arctic Ocean along the Eastern coast. After 48 years sea level reaches the entire North Atlantic, whereas the center of the subtropical gyre is not affected, also suggested by Gerdes et al. (2006). The sensitivity experiment using different melting scenarios around Greenland show similar structures and time evolutions in regional sea level (Figure 5.9d-f). Mainly the amplitude varies with the amount of fresh water inflow.

The pattern of the deviation in relative sea level mostly results from salinity changes due to the fresh water input (Figure 5.4.1). The structure of the variations in temperature and salinity in the North Atlantic Ocean at 100 m depth is very similar to the modeled sea level change, shown in Figure (5.9). The surface salinity decrease originates from the additional fresh water, which stays in the upper 200 m above the saltier ocean water, and is following ocean surface currents. Sea surface temperature does not show a specific structure, as it is dominated by unchanged atmospheric forcing.

In Baffin Bay, the sea surface salinity is reduced by about 0.2 psu due to the additional fresh water. The corresponding reduced surface density causes an increase in stability of the near-surface water column. This reduces vertical mixing in the top ocean layers and less heat exchange between colder water on top and warmer sub-surface water occurs, leading to reduced erosion of the temperature maximum around 450 m depth. A slight warming in the depth interval between 100 and 1000 m occurs. Also salinity exchange is decreased in the top 500 m, leading to an increased salinity around 200 m depth.

No melt water is transported to the South Atlantic west of Namibia by surface circulation. Hence, there is no significant change of surface water properties. But the reduced upwelling of cold, fresh water induces a warming and increased salinity of subsurface water around the 200 m level. In the North Atlantic, more fresh water is found at the surface, reducing sea surface salinity by about 0.1 psu. The reduced surface density increases the stability of the near-surface water column. The vertical mixing in the top ocean layers is reduced and less heat is exchanged between warmer water on top and colder sub-surface water. The ocean is warming by 0.1 °C at 100 m level, cooling by 0.01-0.05 °C at depths between 200 and 1200 m.

After several decades, global mean sea level rise amounts to 0.028 m after 48 years with a local maximum due to density change of 0.04 m at the coast of Nova Scotia (Canada). The density change will lead to an increase in the sea level at the European and North

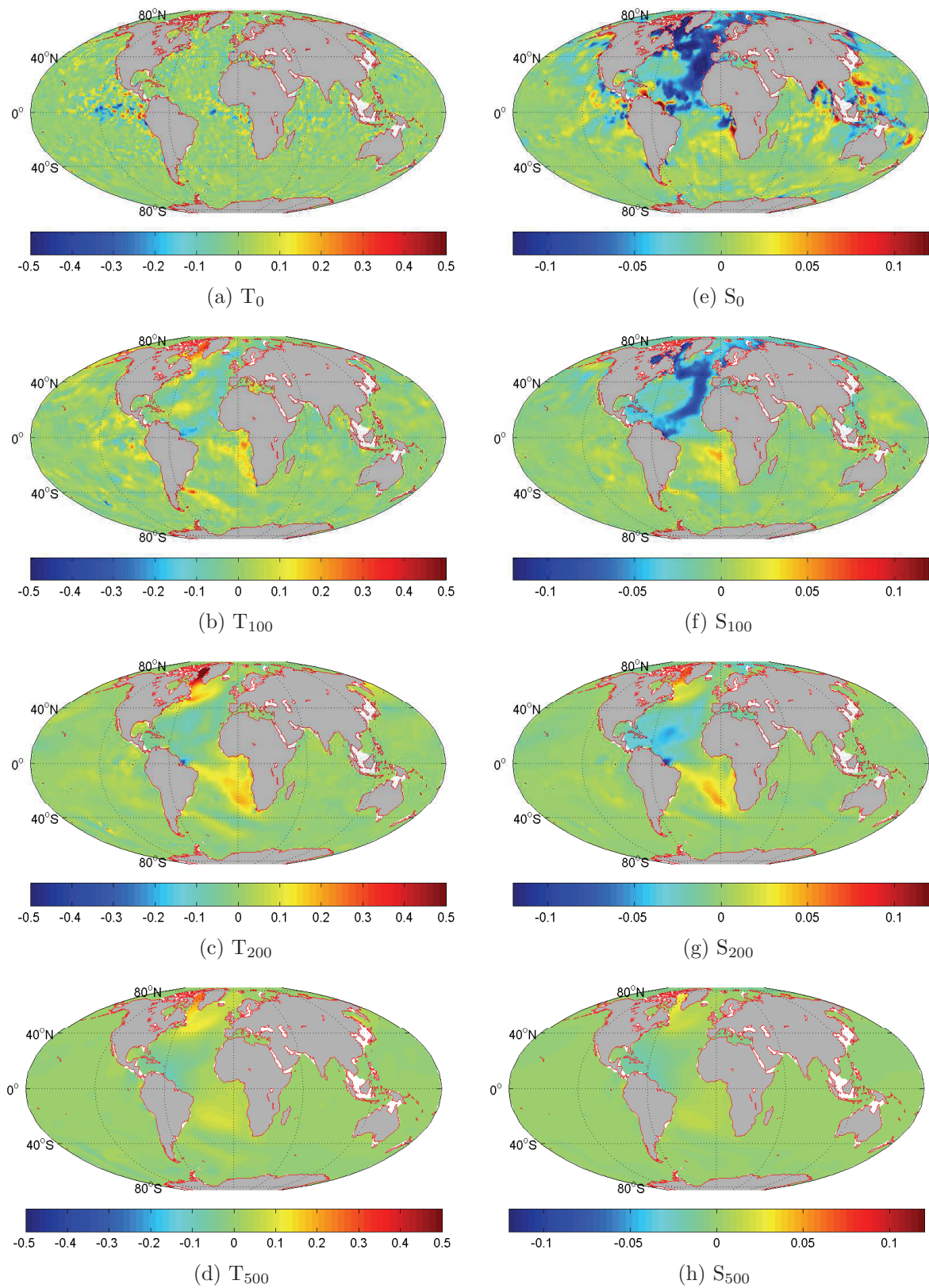


Figure 5.10: Difference of temperature ( $^{\circ}\text{C}$ ) and salinity (psu) at different depths after 48 years if 200 Gt/yr of Greenland ice is released into the ocean (with respect to a reference simulation without additional melt water input).

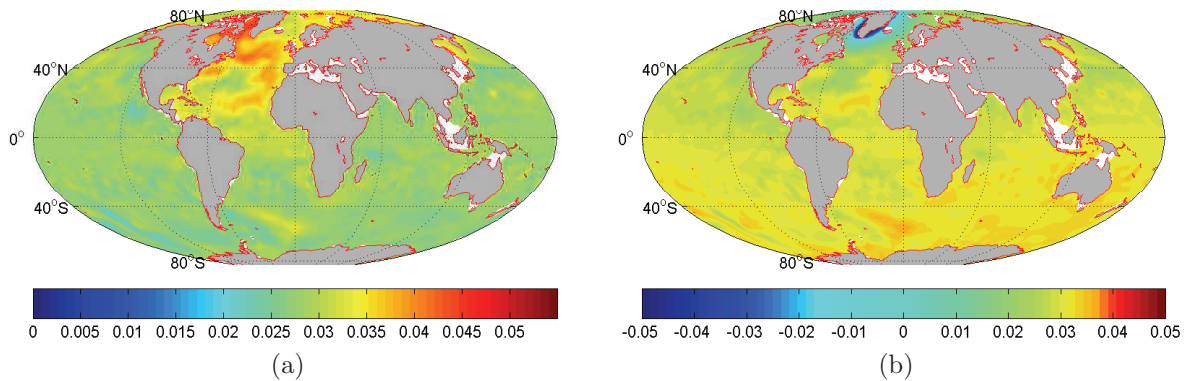


Figure 5.11: Regional sea level change in meter resulting from Greenland ice sheet melting of 200 Gt/yr after 48 years; (a): Relative sea level change including regional and global mean sea level change and (b) total change, after adding the gravitational effect due to Greenland ice mass loss

American coast (Figure 5.11). The sea level around Greenland is falling by 0.14 m, as the reduced gravitational attraction leads to stronger decrease in sea level than the increase due to the additional melt water near the origin of mass loss. Note, that the gravitational effect will also cause an additional increase in sea level at greater distances. Generally, the gravitational attraction does not change global mean sea level and its global mean over the ocean is therefore zero.

#### 5.4.2 Sea Level Evolution in Coastal Regions

As previously described, variations in sea level are dependent on the amount as well as on the location of ice sheet melt. This leads to local changes in sea level at different coastal regions, not identical to the global trend. Sea level evolution, with respect to a reference model simulation is depicted in Figure 5.12a at three locations if the Greenland ice sheet is continuously melting at a rate of 200 Gt/yr. Compared to the global mean, small variations in local sea level change occur at the coast of Maine (USA), the Dutch coast in the North Sea, and the south-east coast of Greenland, induced by the non-linearity of the oceanic response. Locally sea level rise appears to be above the average due to the changes in density caused by the freshening in the surface waters. When adding the gravitational effect, the sea level at the coast of south east Greenland strongly decreases as after a few years the gravitational effect, which is not changing its spatial pattern, becomes higher than the regional trend given by the additional ocean volume (Figure 5.12b). At the two other locations only a slight decrease occurs, as in these regions there is only a small

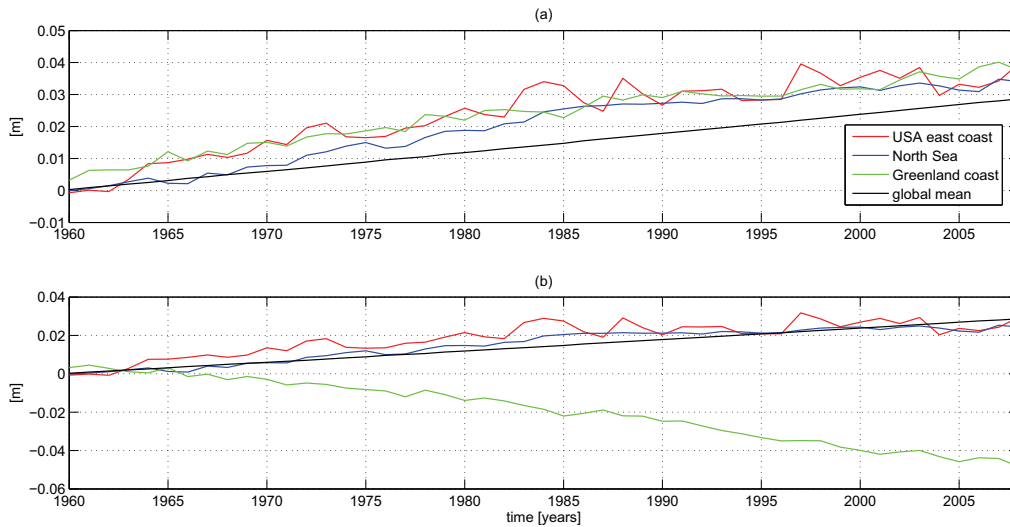


Figure 5.12: Local sea level change, due to fresh water inflow at the Greenland coast, corresponding to 200 Gt/yr (a) without and (b) with the gravitational effects

influence of the gravitational effect.

Comparing the total change in the sea level at the coast in the North Sea, including different continuous melt rates, variations are mainly caused by the additional volume (Figure 5.13). The non-linear signal is identified as steric variations, mostly caused by freshening in the upper ocean layers. It reaches the North Sea after about one decade and does not necessarily increase with the amount of melt water (non-linear ocean response). For example, it may happen, that for a period of time steric height may increase stronger if the ice mass loss correspond to 100 Gt/yr than to 200 Gt/yr, as observed after 42 years of model integration. After 48 years of model integration, the small gravitational effect in this region amounts to about 1 cm decrease of sea level if 200 Gt/yr of ice is molten. If 1000 Gt/yr is molten, the gravitational effect amount to about 5 cm. This leads to a fall in total sea level as the gravitational effect becomes more dominant than the steric effects.

### 5.4.3 Varying Melt Rates

In an additional experiment the influence of seasonal melt signals on the sea level is investigated. Here, a time series of regional melt rates has been created to investigate the influence of seasonal variations in the water inflow. In this experiment ice sheet melting of 161 Gt/yr in Greenland has been assumed for the years 2003 to 2007, according to Wu et al. (2010). The distribution of the ice mass loss is approximated by using the maps of daily melt extent, defined on a  $25 \text{ km} \times 25 \text{ km}$  grid (Abdalati and Steffen, 2001;

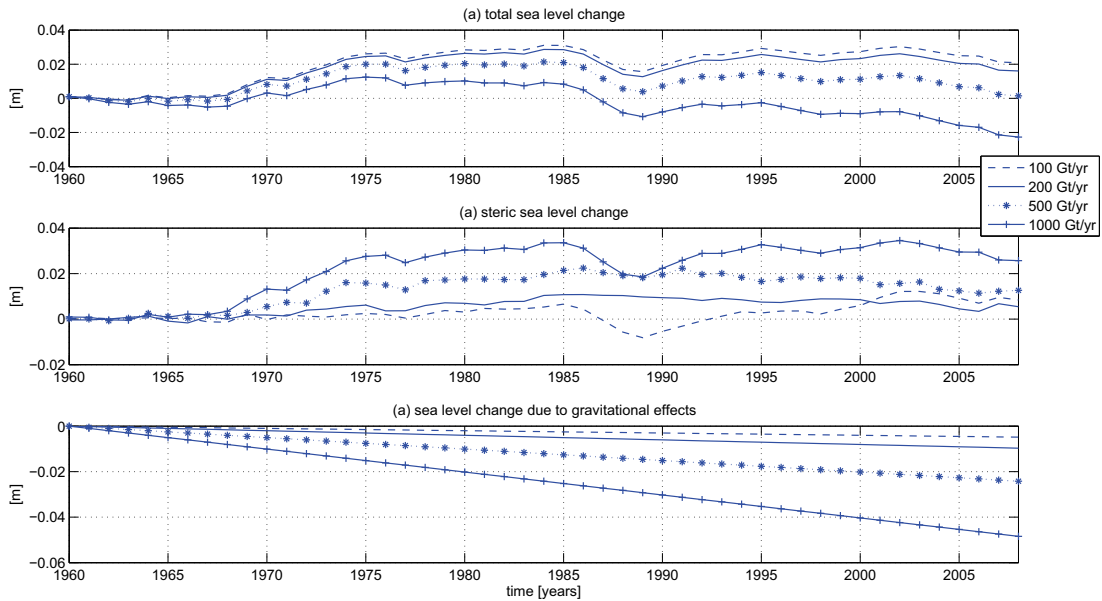


Figure 5.13: Local sea level change at the coast of the North Sea (a), including the regional steric effects due to fresh water inflow at the Greenland coast (b) and the gravitational effect due to the reduced Greenland ice mass (c)

Abdalati, 2009)<sup>1</sup>. The total ice melt of five years is equally distributed to all melting days of the time period. All melting days are weighted with their respective melting areas. This results in melt rates between 133 Gt/yr in 2003 and 207 Gt/yr in 2007. Figure 5.14a depicts the total melt of the year 2007 in equivalent water height. The map of year 2007 indicates strong melting in the coastal regions of Greenland, which have elevations lower than 2000 m. In the south also large melt regions in the interior of Greenland occur. Strong melting appears in small regional near the north east and north west coast of Greenland, inducing a major difference to the experiments using continuous melt water inflow. Previously, no fresh water inflow was included into the model at locations north of 75°N latitude. Now, a more realistic pattern of the fresh water flux is found (Figure 5.14b).

In Greenland, the ice sheet melting generally is not continuous over time but varies with the seasons. It occurs mainly in the summer months between July and September (Figure 5.15) with a maximum daily melt rate in summer. Weekly sea level variations are analyzed from 2003 to 2007 after the daily fresh water inflow fields are included into the model. The model results are compared with simulated sea level variations, where continuous fresh

<sup>1</sup>Annual Greenland ice mass loss extent is measured by passive microwave satellites from year 1979 to 2007 ((Abdalati and Steffen, 2001; Abdalati, 2009)). The data describes the regional distribution of surface melt in Greenland.

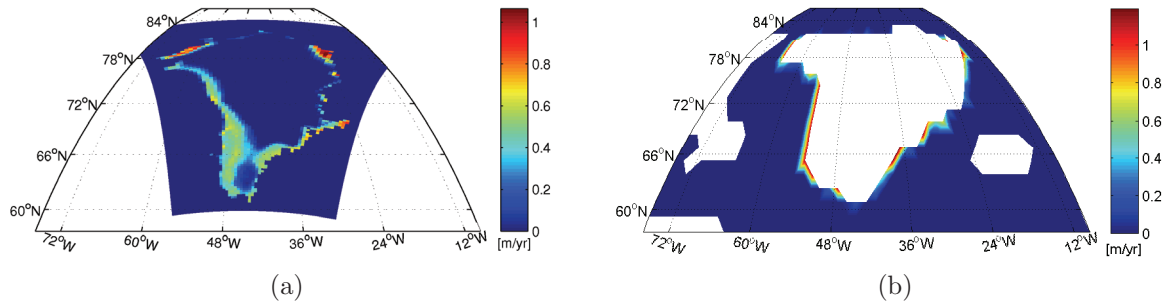


Figure 5.14: The sum of Greenland ice sheet melting of 2007 (a) and the corresponding water inflow (b) in equivalent water height (in total 207 Gt)

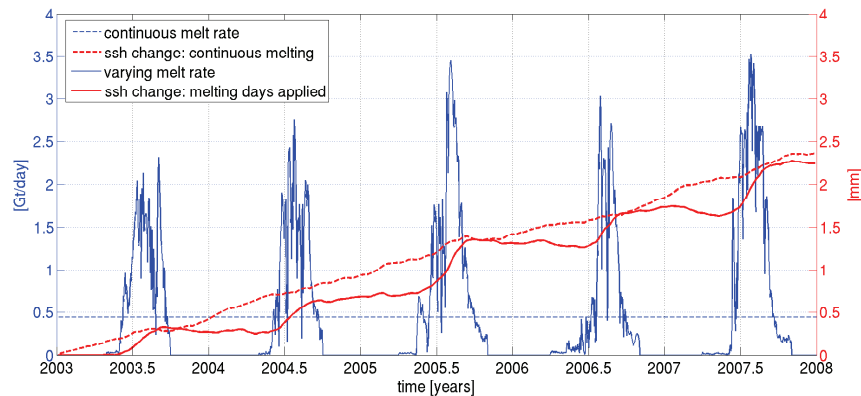


Figure 5.15: Response of global mean sea level to continuous and varying melt rates of the Greenland (GIS) after 5 years (in total 805 Gt of ice melt)

water inflow of 161 Gt/yr is evenly distributed over the Greenland coastal nodes south of  $75^{\circ}\text{N}$  latitude, similar to the first set of experiments. Compared to a continuous melting rate, a clear seasonal variability of global mean sea level is modeled, if daily varying fresh water inflow is added. Here, strong increase in global mean sea level occurs in the summer months, whereas in winter the sea level stays constant, as no melting is present. During winter and spring, also a slight decrease in sea level can happen, because small steric effects occur due to the additional fresh water, which changes global mean sea level by about one order of magnitude less than by the additional mass. This steric effect originates from changed exchange of heat between atmosphere and ocean (Figure 5.16). However, no specific location can be identified, where heat flux is changing. In the mean, the heat flux change appears to be random and generated by internal variability.

The structure of relative sea level change after five years is similar to the simulation

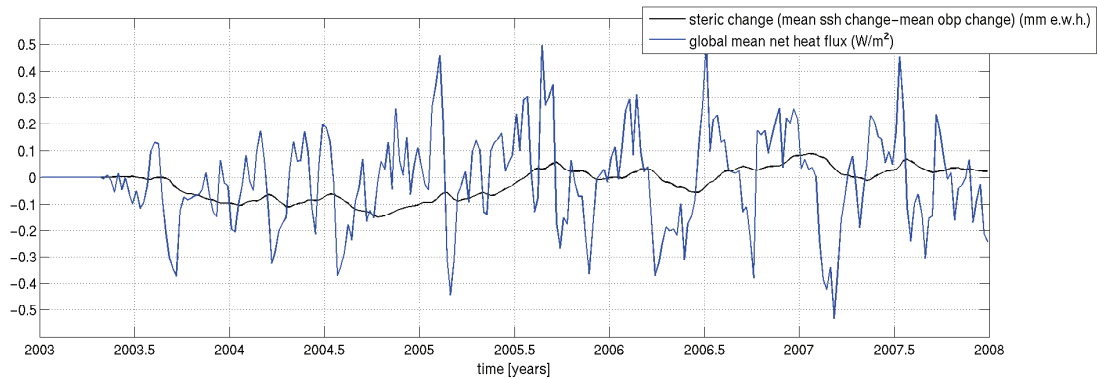


Figure 5.16: Comparison of steric height variations in meter equivalent water height and surface net heat flux in  $\text{W}/\text{m}^2$

using continuous melting rates of  $161 \text{ Gt}/\text{yr}$  (Figure 5.17). Also sea level increases mainly west of Greenland, but in this case, sea level rise mostly remains in the Baffin Bay, less affecting the Labrador Sea. Adding the global mean sea level change of about  $0.46 \text{ mm}/\text{yr}$  (varying with the seasons and the amount of melting days of a year), yields a rise in sea level at the east coast of Greenland and in the Labrador Sea.

The sum of all contributions (regional and global mean sea level change, and sea level change due to the gravitational effect) are depicted in Figure 5.17d. Only slight sea level rise occurs at the east coast of Greenland and in the Labrador Sea. An increased sea level in the Baffin Bay remains. In addition, sea level stays almost constant in the Norwegian and Barents Sea, caused by the reduced gravitational attraction of the ice sheet. Due to the gravitational effect, ocean water is less attracted and sea level is falling near the Greenland coast by about  $6 \text{ mm}$  and in large regions of the Arctic Ocean by about  $0.8 \text{ mm}$  after five years (Figure 5.18). The sea level slightly rises up to  $0.5 \text{ mm}$  further away with a maximum in the Southern Ocean.

## 5.5 Conclusion

Global mean sea level is confirmed to rise by about  $0.3 \text{ mm}/\text{yr}$  if  $100 \text{ Gt}/\text{yr}$  is melting, proportionally increasing with the amount of ice sheet melting. Steric effects lead to small additional variations in sea level. They are about one order of magnitude smaller than the direct effect due to the addition of water mass.

Relative sea level change due to WAIS melting is limited to the Southern Ocean, because density changes cross the ACC only very slowly. Impacts on the ocean due to fresh water inflow at the Greenland coasts are not regionally limited and can be distributed over

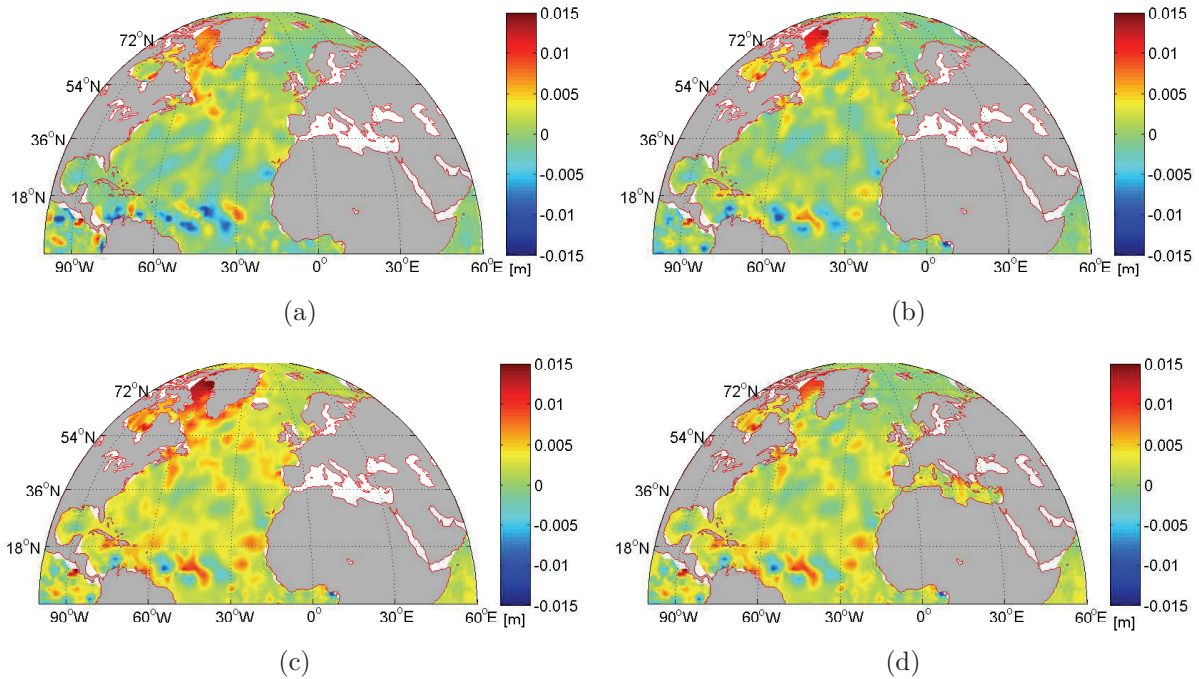


Figure 5.17: Relative sea level resulting from Greenland Ice Sheet melting of 161 Gt/yr after 5 years (2003-2008), (a) with continuous melting equally distributed at coastal nodes below 75°N latitude, and (b) distributed according to melting days, (c) distributed according to melting days plus global mean sea level change, and (d): the total sea level change including regional and global mean sea level change and the gravitational effect related to Greenland ice sheet melting

the whole ocean. The patterns of steric sea level change are following the currents and are mainly originating from changes in temperature and salinity in the upper 200 m. The decrease in Greenland ice mass also reduces its gravitational attraction, leading to a sea level decrease near the Greenland coast, but also to a slight increase further away. Seasonal variations in ice sheet melting in Greenland influences sea level change in the North Atlantic, mainly near the source of melting. After five years, sea level change is more restricted to Baffin Bay and less rising in the Labrador Sea, compared to the case of continuous melting.

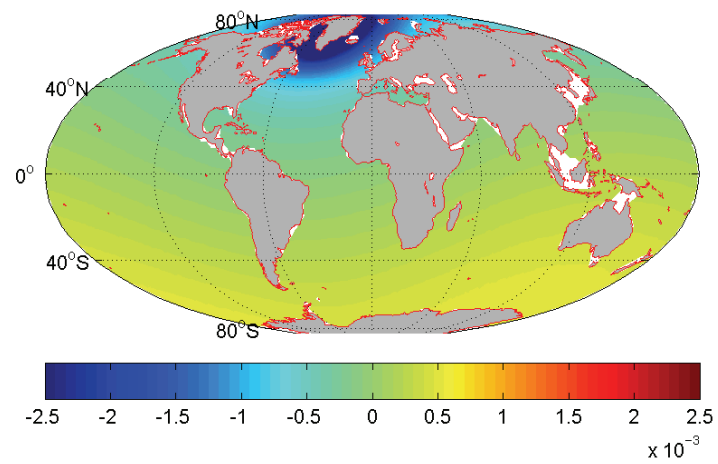


Figure 5.18: Relative sea level change in meter due to the gravitational effect of Greenland Ice Sheet melting of 805 Gt, corresponding to 2.35 mm mean sea level equivalent

# Chapter 6

## Summary and Outlook

The present study investigates the major contributions of sea level change for the last fifty years, with special interest in the recent past (2003 to 2007). The major aim was to investigate the separation of eustatic and steric change. Since the beginning of the GRACE mission it has become possible to measure mass changes. In conjunction with observations of ocean volume from space altimetry the steric contributions can be estimated indirectly. We study ocean mass variations on weekly time scales, which are derived from the mass conserving finite element sea-ice ocean model (FESOM, Timmermann et al. (2009); Böning et al. (2008)). In the reference model simulation, the daily mean fresh water input from land to ocean was provided by the LSDM model (Dill, 2008). The fresh water flux between atmosphere and ocean is provided by the NCAR/NCEP reanalysis (Kalnay et al., 1996). The global sum of all contributions is not balanced. A correction is performed to achieve a realistic mass budget (Böning, 2009). The fresh water budget needs to be filtered with a 2-year high pass filter to achieve realistic long term behavior of global variations in ocean mass. All weekly solutions show realistic geophysical patterns and a realistic seasonal cycle in global mean ocean mass variations (Figure 6.1a). Their phase is similar to GRACE estimates, but the amplitudes are overestimated.

Changing atmospheric conditions directly results in ocean mass redistribution. In this study, the error of modeled OBP has been estimated by computing weekly standard deviations of daily mean differences of ocean bottom pressure (OBP) from two model simulations using different atmospheric forcing from NCAR/NCEP and ECMWF (S.M.Uppala et al., 2005; Simmons et al., 2006; Berrisford et al., 2009). The resulting weekly error maps show high errors in regions of strong signals, e.g. in the Southern Ocean west of the Drake Passage. Patterns vary only slightly over time.

Among others, Böning (2009) successfully validated regional variations modeled OBP

and GRACE estimates on monthly time scales. On weekly time scales, validation of modeled OBP variations has been performed by comparison with GRACE and in-situ measurements from ocean bottom pressure recorders (OBPR).

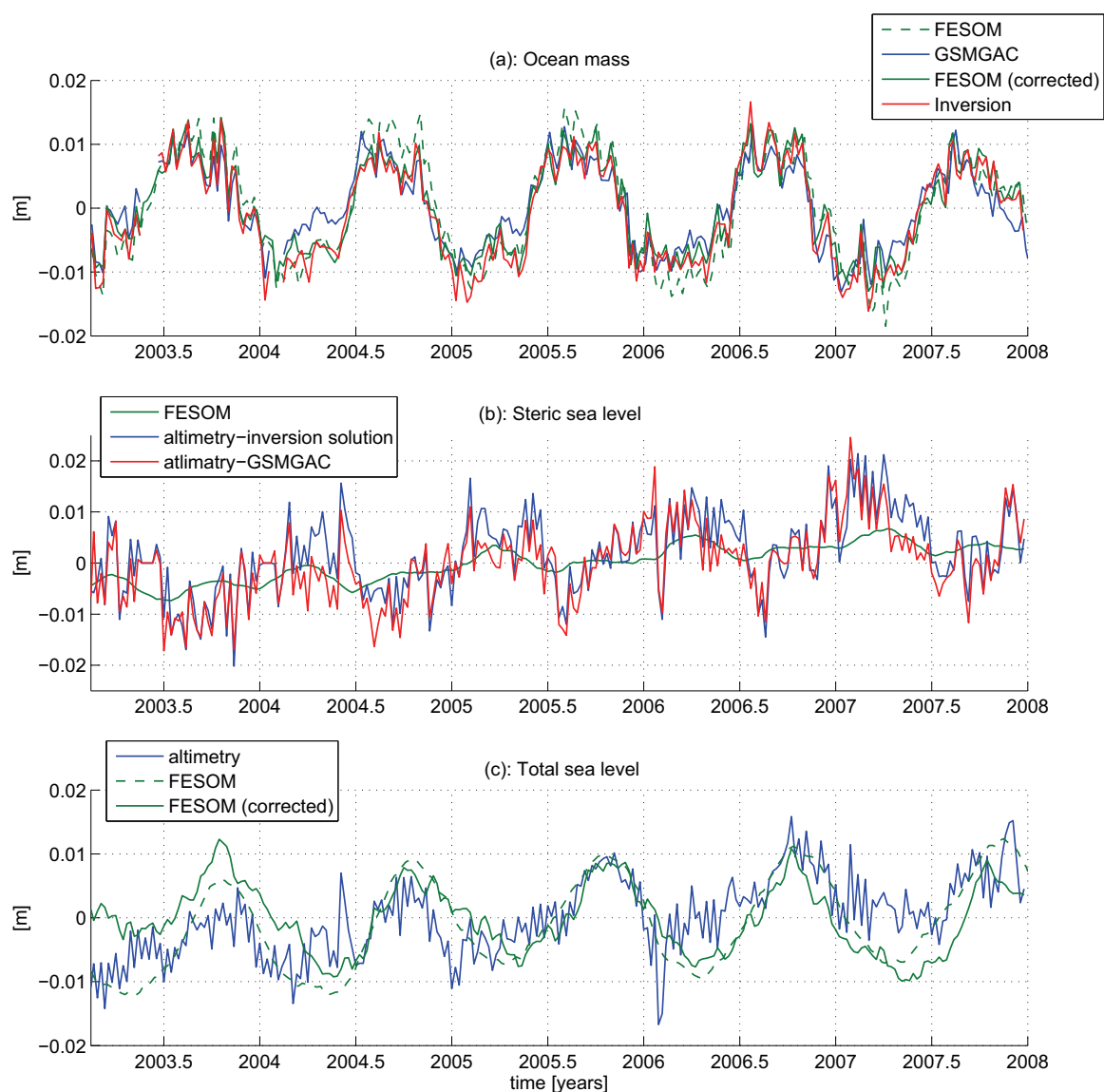


Figure 6.1: Global mean sea level in meter; (a) ocean mass, (b) steric sea level, and (c) total sea level

FESOM model results show significant high correlations to OBPR and the weekly GRACE solutions. Correlations in high latitudes of up to 0.7 are confirmed. However, limited by the low spatial resolution of  $1.5^\circ$ , model results cannot represent the full variability of ocean mass redistribution measured with OBPR. This variability can be represented by

GRACE estimates, which also show high correlation to OBPR measurements. GRACE estimates suffer from the filtering needed to account for aliasing effects. In addition, uncertainties arise from missing degree-1 spherical harmonic coefficients (geocenter motion) and the erroneous (2,0) coefficient (oblateness of the Earth). These issues can be resolved by combining modeled OBP, GPS site displacements and GRACE estimates in a joint inversion (Rietbroek et al., 2009). The inverse solution merges the small scale structures of modeled OBP, which originate from ocean circulation and the variability from the GRACE estimates. It best represents the time series from OBPR. Especially the spurious GRACE signals in the equatorial Atlantic are strongly improved.

The inverse solution strongly depends on the weighting of the individual input variables, which are defined by their error estimates. Replacing a constant error for modeled OBP by an estimated variable error of modeled OBP in the joint inversion improves the results, compared to OBPR measurements.

The inversion provides a mass correction term, which allows for modeling a more accurate description of global mass in the model. It improves the fresh water balance, which is used in a second model integration. This reduces the amplitude of modeled global mean ocean mass variations to values similar to global mean ocean mass variations derived from GRACE data and the inverse solution.

A second major contribution to sea level change arises from temperature and salinity variations in the ocean. These steric variations change ocean volume through expansion and contraction. To achieve realistic sea level changes in the model, the net heat flux between atmosphere and ocean has been tuned with an offset to reduce the unrealistic heat loss of the ocean implicit in the atmospheric reanalysis. The resulting global mean sea level rise between 1960 and 2008 appears to be realistic compared to other studies, although in the last decades it might be less reliable, as no melt water of ice sheets and glaciered regions is included in this experiment.

Spatial patterns of modeled steric height variations are identified in steric anomalies derived from geodetic observations. Especially the seasonal oscillation between the hemispheres is clearly visible. Ocean mass variations estimated by the joint inversion of GRACE gravity data, GPS site displacements and modeled OBP improves the geodetic steric height observations (Bosch and Savcenko, 2008; Albertella et al., 2008). The correlation with modeled steric height variations increased compared to steric height measurements derived with GRACE and altimetry data. Modeled global mean steric height variations are slightly overestimated since the 1990's, but still remaining in a realistic range, as most studies investigate steric height variations only down to a specific depth. Here modeled steric effects include the whole water column. Especially in the recent past, steric sea level rise shows a

reduced trend, which is similar to the trend of the geodetic observations (Figure 6.1b).

In the recent past, modeled global mean variations in total sea level shows realistic amplitude and phase, compared to altimetry measurements (Figure 6.1c). The sea surface topography is associated with variations of the ocean circulation. It correlates well with the mean dynamic topography derived in different studies. Regular oscillations, which are mostly induced by atmosphere conditions, like the El Niño-Southern Oscillation (ENSO) or the Pacific Decadal Oscillation (PDO), can be identified.

During the last decade, several studies investigated the mass loss of the Greenland and West Antarctic Ice Sheet. The melt water flows into the ocean and increases the eustatic sea level by about 0.3 mm/yr if 100 Gt/yr of mass is lost. To investigate the oceanic response to the additional melt water, different amounts of fresh water have been added as additional volume flux along the coast of Greenland. Results are compared to a reference model simulation and confirm the magnitude of global mean sea level rise, estimated by other studies. The additional volume is distributed over the ocean within days, as barotropic waves are generated. In these perturbation experiments global sea level rises due to the additional water mass, a small portion of global mean sea level change originates from varying heat exchange between ocean and atmosphere, which cannot be related to a specific region. This effect is at least one order of magnitude smaller than the sea level change caused by the mass of the melt water inflow. It can be attributed to the non-linear nature of oceanic processes and may be regarded as a measure of uncertainty.

Locally, the fresh water inflow changes ocean density near the source of the melt water and radiates as baroclinic waves dependent on the seasonal character of the melt water inflow. In case of Greenland Ice Sheet melting, density changes mainly in the Labrador Sea and Baffin Bay during the first years. After some decades density variations are distributed through ocean currents farther away mainly showing patterns identified in salinity variations at 100 m depth. After the density change reaches the coastal regions of east Canada, it follows the North Atlantic Drift to the European continent. Then it separates in one filament flowing into the Arctic Ocean and another one following the subtropical gyres to the equatorial North Atlantic. The density in the center of the subtropical gyre is not affected. However, in the Labrador Sea a more stable water column is modeled, leading to reduced vertical mixing. Additional local variations in sea level appear by the decreased gravitational attraction corresponding to the reduced ice sheet mass. Gravitational change is computed in post processing using maps of local melt extent and Green's functions. The effect reduces sea level near the source of mass loss, while farther away it slightly increases. Global mean sea level is not affected by the change in gravitational attraction.

In addition to melting of the ice sheet in Greenland, mass loss of the West Antarctic Ice Sheet has been observed by different studies, whereas the East Antarctic Ice Sheet remains almost constant. An experiment with 100 Gt/yr of melt water flux from the West Antarctic Ice Sheet into the ocean shows similar behavior in global mean sea level. Main differences occur in density variations, which are limited to the Southern Ocean as the ACC acts as a barrier, which steric variations can pass only very slowly. Additionally temperature variations show a quadripol-like pattern, resulting from the sensitivity of the model in this region. These patterns are known from the calculation of error estimates.

## Outlook

This study evaluates the capability of current ocean models to simulate sea level variations without assimilation of geodetic observations. It gives an indication on how much the major contributions modify global and regional sea level. The main focus lies on the computation and analysis of spatial and temporal variability, including trends of short time periods (< 10 years). These cannot necessarily be extended into a long term trend, as variations of one year can strongly contribute and change these trends. Therefore, longer time series from measurements have to be developed to be able to analyze trends in the recent past. This is especially true for measured ocean mass variations, as the modeled global mean ocean mass variations are corrected using GRACE estimates. In addition, further investigations are needed to solve the issue of the artificial trend caused by the numerical inconsistencies described in Section 3.3.

Global mean ocean mass variations of the recent past can be modeled with realistic phase and amplitude and is further improved by optimizing the fresh water budget of the model using the mass correction term of the inverse solutions. Its short term variations are similar to GRACE estimates and the inverse solution, because they are induced by variations of the total mass of the atmosphere above the ocean, which are provided by data sets from NCEP and ECMWF. The interesting fact that global ocean mass derived from GRACE does not show a trend that can be assigned to uncertainties in GIA estimates. Hence, the different contributions of eustatic sea level have to be investigated in detail to identify consistent quantities of the different contributions of the ocean mass budget. Precipitation and evaporation rates, derived by the weather forecast centers show realistic estimates, but include uncertainties especially in the global sum. Also, different ongoing studies investigate the land hydrology including the surface runoff to the ocean, whose results are most promising, but normally don't include runoff from ice melting. Hence, the question arises about the change in the mass budget of the ice sheets and glaciers.

In-situ measurements from OBPR can be used for validation of modeled OBP. They generally include mass variations originating from tides, which are not modeled with FESOM. Time series of OBPR are corrected for tides using the FES2004 tide model, but not all tide signals can be removed. Although most of the remaining tide signal is eliminated when weekly means are computed, further investigations, especially under usage of alternative tide models, are needed to find the optimal tide correction.

The fast barotropic response of the ocean remains on the same time scales as other waves in response to atmospheric pressure change. It is also difficult to differentiate the seasonal melt signal from the regular seasonal signal. The long term signals originating from currents are persistent enough to be measured by tide gauges, altimetry and salinity measurements. In ongoing studies such as in the project "Fingerprints of ice melting in geodetic GRACE and ocean models" (FIGO), within in the framework of the DFG priority program "Mass transport and Mass distribution in System Earth" time varying estimates from measurement systems like GRACE or ICESat will be added as forcing into ocean modeling to achieve time dependent forcing, including the seasonal cycle. Beside estimates from the Greenland and Antarctic ice sheets, also estimates from land glaciers in different regions like Alaska, Patagonia or the Himalayas will be considered. In future investigations, the grid will be refined at regions of interest, such as the Labrador Sea to study the influence of the additional fresh water on properties of this region.

Long term influence on ocean circulation due to ice sheet melting can be investigated on decadal time scales. This includes estimation of present and future variations of salinity changes caused by the additional fresh water, of regional heat content including the exchange of heat between atmosphere and ocean, and of changes in the ocean surface fluxes within different climate scenarios. In addition, variations in the deep water formation in the Weddell, Labrador and Greenland Seas as well as the convection and stratification in these regions should be investigated. This is in particular important for the North Atlantic. If deep water production changes in the future, it will have strong impacts on the temperature in Europe. For this reason, the influence of Greenland Ice Sheet melting on the meridional overturning circulation (MOC) transports should be investigated including sensitivity experiments. Here, a refined grid is needed in the North Atlantic, which can then also be used to analyze influences on major ocean currents like the Gulf Stream, its extension, and on coastal currents.

The identification of modeled sea level change in measurements produced by tide gauges is important for the validation of the model results. Therefore, time series of sea level change need to be analyzed at their positions. Time series at special positions in the open ocean like the center of the Subtropical Gyre can be compared with altimetry measure-

ments. However, modeled sea level change only considers dynamic changes. The geometric effects like loading or GIA have to be accounted for during comparison. In addition, it has to be investigated if modeled variations in salinity and ocean currents are localized enough to be able to be detected in oceanic measurements like from ARGO floats or satellite missions dedicated to measure sea surface salinity.

# Bibliography

- Abdalati, W. (2009). Greenland ice sheet melt characteristics derived from passive microwave data: 1979-2007. *Boulder, Colorado USA: National Snow and Ice Data Center*. Digital media.
- Abdalati, W. and Steffen, K. (2001). Greenland ice sheet melt extent: 1979-1999. *Journal of Geophysical Research (Atmospheres)*, 106. doi:10.1029/2001JD900181.
- Adler, R. F., Huffman, G. J., Chang, A., Ferraro, R., Xie, P., Janowiak, J., Rudolf, B., Schneider, U., Curtis, S., Bolvin, D., Gruber, A., Susskind, J., Arkin, P., and Nelkin, E. (2003). The version 2 global precipitation climatology project (gpcp) monthly precipitation analysis (1979-present). *J. Hydrometeor.*, 4:36–50.
- Albertella, A., R. Savcenko, W. B., and Rummel, R. (2008). Dynamic ocean topography - the geodetic approach. *DGFI/IAPG Report 82, Deutsches Geodtisches Forschungsinstitut (DGFI), Mnchen*.
- Antonov, J. I., Levitus, S., and Boyer, T. P. (2002). Steric sea level variations during 1957-1994: Importance of salinity. *Journal of Geophysical Research*, 107. 8013, doi:10.1029/2001JC000964.
- Antonov, J. I., Levitus, S., and Boyer, T. P. (2005). Thermosteric sea level rise, 1955-2003. *Geophysical Research Letters*, 32. L12602, doi:10.1029/2005GL023112.
- Ao, C. O., Meehan, T. K., Hajj, G. A., and Mannucci, A. J. (2003). Lower troposphere refractivity bias in gps occultation retrievals. *Journal of Geophysical Research*, 108. 4577 doi:10.1029/2002JD003216.
- Bamber, J., Layberry, R., and Gogenini, S. (2001a). A new ice thickness and bed data set for the greenland ice sheet 1: Measurement, data reduction, and errors. *Journal of Geophysical Research*, 106. doi:10.1029/2001JD900054.
- Bamber, J., Layberry, R., and Gogenini, S. (2001b). A new ice thickness and bed data set for the greenland ice sheet 2: Relationship between dynamics and basal topography. *Journal of Geophysical Research*, 106. doi:10.1029/2001JD900053.

- Beckmann, A., Hellmer, H. H., and Timmermann, R. (1999). A numerical model of the weddell sea: large scale circulation and water mass distribution. *Journal of Geophysical Research*, 104:23375–23391.
- Berrisford, P., Dee, D., Fielding, K., Fuentes, M., Kallberg, P., Kobayashi, S., and Uppala, S. (2009). The era-interim archive. *ERA Report Series, ECMWF*.
- Bettadpur, S. (2007). Gravity recovery and climate experiment. *Level-2 Gravity Field Product User Handbook*. <ftp://podaac.jpl.nasa.gov/pub/grace/doc/L2UserHandbookv2.3.pdf>.
- Bindoff, N. L., Willebrand, J., Artale, V., A, C., Gregory, J., Gulev, S., Hanawa, K., Qur, C. L., Levitus, S., Nojiri, Y., Shum, C. K., Talley, L. D., and Unnikrishnan, A. (2007). Observations: Oceanic climate change and sea level. In Solomon, S., Qin, D., Manning, M., Chen, Z., Marquis, M., Averyt, K. B., Tignor, M., and Miller, H. L., editors, *The Scientific Basis, Contribution of Working Group I to the Fourth Assessment Report of the Intergovernmental Panel on Climate Change*. Cambridge University Press, Cambridge, New York.
- Blewitt, G. (2003). Self-consistency in reference frames, geocenter definition, and surface loading of the solid earth. *Journal of Geophysical Research*, 108. 2103 doi:10.1029/2002JB002082.
- Blewitt, G. and Clarke, P. (2003). Inversion of the earth’s changing shape to weigh sea level in static equilibrium with surface mass redistribution. *Journal of Geophysical Research*, 108. 2311 doi:10.1029/2002JB002290.
- Böning, C. (2009). *Validation of ocean mass variability derived from the Gravity Recovery and Climate Experiment - Studies utilizing in-situ observations and results from a Finite Element Sea-ice Ocean Model*. Dissertation, University of Bremen, Bremen, Germany.
- Böning, C., Timmermann, R., Macrandner, A., and Schröter, J. (2008). A pattern-filtering method for the determination of ocean bottom pressure anomalies from grace solutions. *Geophysical Research Letters*, 35. doi: L18611 10.1029/2008GL034974.
- Bosch, W. and Savcenko, R. (2008). On estimating the dynamic ocean topography - a profile approach. *Proceedings of GCEO08*. (submitted).
- Box, J., Bromwich, D. H., and Bai, L.-S. (2004). Greenland ice sheet surface mass balance 1991-2000: Application of polar mm5 mesoscale model and in situ data. *Journal of Geophysical Research*, 109. doi:10.1029/2003JD004451.
- Brunnabend, S.-E., Rietbroek, R., Timmermann, R., Schröter, J., and Kusche, J. (2010). Improving grace analysis by modelling ocean bottom pressure uncertainty. *Journal of Geophysical Research*. (submitted).

- Cazenave, A., Dominh, K., Guinehut, S., Berthier, E., Llovel, W., Ramillien, G., Ablain, M., and Larnicol, G. (2008). Sea level budget over 2003-2008: A reevaluation from grace space gravimetry, satellite altimetry and argo. *Global Planetary Change*. doi: 10.1016/j.gloplach.2008.10.004, in press.
- Cazenave, A. and Nerem, R. S. (2004). Present day sea level change: observations and cause. *Rev. Geophys.*, 42. RG 3001 doi: 10.1029/2003RG000139.
- Chambers, D. P. (2006). Evaluation of new grace time-variable gravity data over the ocean. *Geophysical Research Letters*, 33:17603.
- Chambers, D. P., Wahr, J., and Nerem, R. S. (2004). Preliminary observations of global ocean mass variations with grace. *Geophysical Research Letters*, 31(13).
- Chen, J. L. and Wilson, C. R. (2008). Low degree gravity changes from grace, earth rotation, geophysical models, and satellite laser ranging. *Journal of Geophysical Research (Solid Earth)*, 113. 6402, doi:10.1029/2007JB005397.
- Chen, J. L., Wilson, C. R., Blankenship, D., and Tapley, B. (2009). Accelerated antarctic ice loss from satellite gravity measurements. *Nature Geoscience*, 2:859–862. doi:10.1038/NNGEO694.
- Chen, J. L., Wilson, C. R., and Seo, K.-W. (2008). S2 tide aliasing in grace time-variable gravity solutions. *Journal of Geodesy*. doi:10.1007/s00190-008-0282-1.
- Chen, J. L., Wilson, C. R., and Tapley, B. (2006). Satellite gravity measurements confirm accelerated melting of greenland ice sheet. *Science*, 313:1958–1960. doi:10.1126/science.1129007.
- Church, J. A., Gregory, J. M., Huybrechts, P., Kuhn, M., Lambeck, K., Nhuan, M. T., Qin, D., and Woodworth, P. L. (2001). Changes in sea level. In Houghton, J. T., Ding, Y., Griggs, D. J., Noguera, M., der Linden, P. J. V., Dai, X., Maskell, K., and Johnson, C. A., editors, *The Scientific Basis, Contribution of Working Group I to the Third Assessment Report of the Intergovernmental Panel on Climate Change*, pages 639–694. Cambridge University Press, Cambridge, New York.
- Church, J. A., Rosemich, D., Dominhues, C. M., Willis, J. K., White, N. J., Gilson, J. E., Stammer, D., Köhl, A., Chambers, D. P., Landerer, F. W., Marotzke, J., Gregory, J. M., Suzuki, T., Cazenave, A., and Traon, P.-Y. L. (2010). Ocean temperature and salinity contributions to global and regional sea-level change. In Church, J. A., Woodworth, P. L., Aarup, T., and Wilson, W. S., editors, *Understanding Sea-Level Rise and Variability*, pages 143–176. Wiley-Blackwell, UK.
- Connolley, W., Gregory, J., Hunke, E., and McLaren, A. (2004). On the consistent scaling of terms in the sea-ice dynamics equation. *Journal Phys. Ocean.*, 34. 17761780.

- Dahle, C., Flechtner, F., Kusche, J., and Rietbroek, R. (2008). Gfz eigen-grace05s (rl04) weekly gravity field time series. *Proceedings of the 2008 GRACE Science Team Meeting*. San Francisco, December 12./13.2008, <http://www.csr.utexas.edu/grace/GSTM>.
- Danilov, S., Kivman, G., and Schröter, J. (2004). A finite-element ocean model: principles and evaluation. *Ocean Modelling*, 6:125–150. doi:10.1016/S1463-5003(02)00063-X.
- Danilov, S., Kivman, G., and Schröter, J. (2005). Evaluation of an eddy-permitting finite-element ocean model in the north atlantic. *Ocean Modelling*, 10:35–49. doi:10.1016/j.ocemod.2004.07.006.
- Danilov, S. and Yakovlev, N. (2003). A finite element ice model.
- Dee, D., Uppala, S., Kobayashi, S., Healy, S., and Poli, P. (2008). Re-analysis applications of gps radio occultation measurements. *European Centre for Medium-range Weather Forecasts, Shinfield Park, Reading, RG2 9AX, UK*. [http://dss.ucar.edu/datasets/ds627.0/docs/IFS\\_documentation/](http://dss.ucar.edu/datasets/ds627.0/docs/IFS_documentation/).
- Dill, R. (2008). Hydrological model lsdm for operational earth rotation and gravity field variations. *Scientific Technical Report; 08/09*. Helmholtz-Zentrum Potsdam Deutsches GeoForschungsZentrum, 37, doi: 10.2312/GFZ.b103-08095.
- ECWMF (1995). The description of the ecmwf/wcrp level iii-a. *Global Atmospheric Data Archive*.
- Farrell, W. E. (1972). Deformation of the earth by surface loads. *Reviews of Geophysics and Space Physics*, 10:761–797.
- Fischer, H. (1995). Vergleichende untersuchungen eines optimierten dynamisch-thermodynamischen meereismodells mit beobachtungen in weddelmeer. *Berichte zur Polarforschung*, 166. Alfred-Wegener-Institut, Bremerhaven, Germany.
- Francis, O. and Mazzega, P. (1990). Global charts of ocean tide loading effects. *Journal of Geophysical Research*, 95:11,411–11,424.
- Galerkin, B. G. (1915). Rods and plates: Series occurring in various questions concerning the elastic equilibrium of rods and plates. *Vestnik Inzhenerov i Tekhnikov*, 19:897–908. Petrograd, Russia.
- Gates, W. L. and Nelson, A. (1975a). A new (revised) tabulation of the scripps topography on a 1 degree global grid. part i: Terrain heights. *Tech. Report R12761ARPA*. The Rand Corporation, Santa Monica, CA.
- Gates, W. L. and Nelson, A. (1975b). A new (revised) tabulation of the scripps topography on a 1 degree global grid. part ii: Ocean depths. *Tech. Report R12771ARPA*. The Rand Corporation, Santa Monica, CA.

- Gent, P. R. and McWilliams, J. C. (1990). Isopycnal mixing in ocean circulation models. *Journal of Physical Oceanography*, 20:150–155.
- Gent, P. R., Willebrand, J., McDougall, T. J., and McWilliams, J. C. (1995). Parameterizing eddy-induced tracer transports in ocean circulation models. *Journal of Physical Oceanography*, 24:1365.
- Gerdes, R., Hurlin, W., and Griffies, S. M. (2006). Sensitivity of a global ocean model to increased run-off from greenland. *Ocean Modelling*, 12. doi: 10.1016/j.ocemod.2005.08.003.
- Greatbatch, R. J. (1994). A note on the representation of steric sea level in models that conserve volume rather than mass. *Journal of Geophysical Research*, 99:12767–12771.
- Griffies, S. M. (2004). Fundamentals of ocean circulation models. *Princeton University Press, Princeton, USA*, page 496 pp.
- Gunter, B., Urban, T., Riva, R., Helsen, M., Harpold, R., Poole, S., Nagel, P., Schutz, B., and Tapley, B. (2009). A comparison of coincident grace and icesat data over antarctica. *Journal of Geodesy*, 34:1051–1060. doi: 10.1007/s00190-009-0323-4.
- Hagemann, S., Arpe, K., and Bengtsson, L. (2005). Validation of the hydrological cycle of era-40. *ERA-40 Project Report Series, ECMWF*. <http://www.ecmwf.int/publications/library/do/references/list/192>.
- Hagemann, S. and Duemenil, L. (1998a). Documentation for the hydrological discharge model. *Technical Report, Max Plank Institute for Meteorology, Hamburg*. ISSN 0940-9327.
- Hagemann, S. and Duemenil, L. (1998b). A parametrization of the lateral waterflow for the global scale. *Climate Dynamics*, 14:17–31.
- Hanna, E., Huybrechts, P., Janssens, I., Cappelen, J., Steffen, K., and Stephens, A. (2005). Runoff and mass balance of the greenland ice sheet: 1958-2003. *Journal of Geophysical Research*, 110. D13108, doi: 10.1029/2004JD005641.
- Healy, S. B. and Thepaut, J.-N. (2006). Assimilation experiments with champ gps radio occultation measurements. *Q. J. R. Meteorol. Soc.*, 132. doi: 10.1256/qj.04.182.
- Hibler III, W. D. (1979). A dynamic thermodynamic sea ice model. *Journal Physical Oceanography*, 9:815–846.
- Huffman, G. J., Adler, R. F., Morrissey, M., Bolvin, D. T., Curtis, S., Joyce, R., McGavock, B., and Susskind, J. (2001). Global precipitation at one-degree daily resolution from multi-satellite observations. *J. Hydrometeorol.*, pages 36–50.
- Huffman, G. J. and Bolvin, D. T. (2009). Gpcp one-degree daily precipitation data set documentation. *Laboratory for Atmospheres, NASA Goddard Space Flight Center and Science Systems and Applications, Inc.*

- Ilk, K., Flury, J., Rummel, R., Schwintzer, P., Bosch, W., Haas, C., Schröter, J., Stammer, D., Zahel, W., Miller, H., Dietrich, R., Huybrechts, P., Schmeling, H., Wolf, D., Götze, H., Riegger, J., Bardossy, A., Güntner, A., and Gruber, T. (2005). Mass transport and mass distribution in the earth system - contribution of the new generation of satellite gravity and altimetry missions to geosciences. *GOCE Projektbro, TU Munchen und GFZ Potsdam*,. <http://www.massentransporte.de/index.php?id=33>.
- Ishii, M., Kimoto, M., and Kaci, M. (2003). Historical ocean subsurface temperature analysis with error estimates. *Monthly Weather Rev.*, 131:51–73.
- Ishii, M., Kimoto, M., Sakamoto, K., and Iwasaki, S.-I. (2006). Steric sea level changes estimated from historical ocean subsurface temperature and salinity analysis. *Journal of Oceanography*, 62:155–170.
- Jansen, M. J. F., Gunter, B. C., and Kusche, J. (2009a). The impact of grace, gps, and obp data on estimates of global mass redistribution. *Geophys. J. Int.*, 177. doi: 10.1111/j.1365-246X.2008.04031.x.
- Jansen, M. J. F., Gunter, B. C., Rietbroek, R., Dahle, C., Kusche, J., Flechtner, F., Brunnabend, S.-E., and Schröter, J. (2009b). Estimating sub-monthly global mass transport signals using grace, gps, obp data sets. In *Proc. of the IAG International Symposium on Gravity, Geoid and Earth Observation (GGEO2008)*, volume 177. Chania, Crete, June 23-27, 2008.
- Kalnay, E., Kanamitsu, M., Kistler, R., Collins, W., Deaven, D., Gandin, L., Iredell, M., Saha, S., White, G., Woollen, J., Zhu, Y., Chelliah, M., Ebisuzaki, W., Higgins, W., Janowiak, J., Mo, K., Ropelewski, C., Wang, J., Leetmaa, A., Reynolds, R., Jenne, R., and Joseph, D. (1996). The ncep/ncar 40-year reanalysis project. *Bull. Amer. Met. Soc.*, 77:437–471.
- Kanzow, T., Flechtner, F., and R. Schmidt, A. C., Schwintzer, P., and Send, U. (2005). Seasonal variation of ocean bottom pressure derived from gravity recovery and climate experiment (grace): Local validation and global patterns. *Journal of Geophysical Research*, 110. C09001 doi: 10.1029/2004JC002772.
- Koenig-Langlo, G. and Augstein, E. (1994). Parametrization of the downward longwave radiation at the earth's surface in polar regions. *Meteorologische Zeitschrift*, 3:343–347.
- Kusche, J. (2007). Approximate decorrelation and non-isotropic smoothing of time-variable grace-type gravity field models. *Journal of Geodesy*, 81:733–749. doi:10.1007/s00190-007-0143-3.
- Laevastu, T. (1960). Factors affecting the temperature of the surface layer of the sea. *Comment. Phys. Math.*, 25.

- Lemke, P., Owens, W. B., and III, W. D. H. (1990). A coupled sea ice - mixed layer - pycnocline model for the weddell sea. *Journal of Geophysical Research*, 95:9513–9525.
- Lemke, P., Ren, J., Alley, R. B., Allison, I., Carrasco, J., Flato, G., Fujii, Y., Kaser, G., Mote, P., Thomas, R. H., and Zhang, T. (2007). Observations: Changes in snow, ice and frozen ground. In Solomon, S., Qin, D., M. Manning, Z. C., Marquis, M., Averyt, K. B., Tignor, M., and Miller, H. L., editors, *Climate Change 2007: The Physical Science Basis. Contribution of Working Group I to the Fourth Assessment Report of the Intergovernmental Panel on Climate Change*. Cambridge University Press, Cambridge, New York.
- Leuliette, E. and Miller, L. (2009). Closing the sea level rise budget with altimetry argo and grace. *Geophysical Research Letters*, 36. doi: L04608 10.1029/2008GL036010.
- Levitus, S., Antonov, J. I., and Boyer, T. P. (2005). Warming of the world ocean, 1995-2003. *Geophysical Research Letters*, 32. doi: L02604 10.1029/2004GL021592.
- Levitus, S., Stephens, C. M., Antonov, J. I., and Boyer, T. P. (2000). Yearly and year-season upper ocean temperature anomaly fields, 1948-1998. *U.S. Gov. Printing Office, Washington, DC*, page 23.
- Lombard, A., Cazenave, A., Traon, P.-Y. L., and Ishii, M. (2005). Contribution of thermal expansion to present-day sea-level change revisited. *ScienceDirect, Elsevier B.V.*, 47:1–16. doi: 10.1016/j.gloplacha.2004.11.016.
- Love, A. E. H. (1909). The yielding of the earth to disturbing forces. *Proceedings of Royal Society*, 82:73–88. doi:10.1098/rspa.1909.0008.
- Love, A. E. H. (1911). *Some Problems of Geodynamics*. Cambridge University Press, Cambridge. <http://digital.library.cornell.edu/>.
- Luthcke, S. B., Zwally, H. J., Abdalati, W., Rowlands, D. D., Ray, R. D., Nerem, R. S., Lemoine, F., McCarthy, J. J., and Chinn, D. S. (2006). Recent greenland ice mass loss by drainage system from satellite gravity observations. *Science*, 314:1286–1289. doi: 10.1126/science.1130776.
- Lythe, M. B., Vaughan, D. G., and the BEDMAP Consortium (2000). Bedmap - bed topography of the antarctic. *Cambridge, United Kingdom: British Antarctic Survey*. Digital Media, available at [http://www.antarctica.ac.uk/bas\\_research/data/access/bedmap/](http://www.antarctica.ac.uk/bas_research/data/access/bedmap/).
- Macrander, A., Böning, C., Boebel, O., and Schröter, J. (2009). Grace, validation by in-situ data of ocean bottom pressure. *in preparation*.
- Maier-Reimer, E. and Mikolajewicz, U. (1991). The hamburg large scale geostrophic ocean general circulation model (cycle 1). *Technical Report, 2, Deutsches Klimarechenzentrum, Hamburg*. <http://hdl.handle.net/10068/256030>.

- Marsh, R., Desbruyeres, D., Bamer, J. L., Cuevas, B. A., Coward, A. C., and Aksenov, Y. (2009). Short-term impacts of enhanced greenland freshwater fluxes in an eddy-permitting ocean model. *Ocean Science Discussions*, 6:2911–2937. [www.ocean-sci-discuss.net/6/2911/2009/](http://www.ocean-sci-discuss.net/6/2911/2009/).
- Maximenko, N. A. and Niiler, P. (2005). Hybrid decade-mean global sea level with mesoscale resolution. In Saxena, N., editor, *Recent Advances in Marine Science and Technology*, pages 55–59. Honolulu: PACON International.
- Maykut, G. A. (1977). Estimates of regional heat and mass balance of the ice cover. *A Symposium on Sea Ice Processes and Models*, 1:65–74. University of Washington, Seattle.
- Millero, F. J. (1978). Freezing point of sea water. in: Eighth report of the joint panel of oceanographic tables and standards. *UNESCO Technical Papers in Marine Science*, 28:29–31.
- Mitrovica, J. X., Latychev, K., and Tamisiea, M. E. (2007). Time variable gravity: Glacial isostatic adjustment. *Treatise of Geophysics*, (e.d. T. Herring), 3:197–211.
- Mitrovica, J. X., Tamisiea, M. E., Davis, J. L., and Milne, G. A. (2001). Recent mass balance of polar ice sheets inferred from patterns of global sea-level change. *Nature*, 409:1026–1029.
- Morgan, P. P. (1994). Seawater, a library of matlab<sup>®</sup> computational routines for the properties of sea water, version 1.2. *CSIRO Marine Laboratories, Report 222*. 29pp.
- Morison, J., Wahr, J., Kwok, R., and Peralta-Ferriz, C. (2007). Recent trends in arctic ocean mass distribution revealed by grace. *Geophysical Research Letters*, 34. doi: 10.1029/2006GL029016.
- Morison, J. H., McPhee, M. G., and Maykut, G. A. (1987). Boundary layer, upper ocean and ice observations in the greenland sea marginal ice zone. *Journal of Geophysical Research*, 92:6987–7011.
- Murray, F. W. (1967). On the computation of saturation vapor pressure. *Journal of Applied Meteorology*, 6:203–204.
- Owens, W. B. and Lemke, P. (1990). Sensitivity studies with a sea ice-mixed layer-pycnocline model in the weddell sea. *Journal of Geophysical Research*, 95:9527–9538.
- Pacanowski, R. and Philander, S. G. H. (1981). Parameterization of vertical mixing in numerical models of the tropical oceans. *Journal Phys. Oceanogr.*, 11:1443–1451.
- Park, J., Watt, D., Donohue, K., and Jayne, S. (2008). A comparison of in situ bottom pressure array measurements with grace estimates in the kuroshio extension. *Geophysical Research letters*, 35. L17601 doi: 10.1029/2008GL034778.

- Parkinson, C. L. and Washington, W. M. (1979). A large-scale numerical model of sea ice. *Journal of Geophysical Research*, 84:311–337.
- Pavlis, N. K., Holmes, S. A., Kenyon, S. C., and Factor, J. K. (2008). An earth gravitational model to degree 2160. *EGM2008, paper presented at EGU General Assembly 2008, Vienna, 13–18 April*.
- P.Niiler, P., Maximenko, N. A., and McWilliams, J. C. (2003). Dynamically balanced absolute sea level of the global ocean derived from near-surface velocity observations. *Geophysical Research Letters*, 30. 2164, doi:10.1029/2003GL018628.
- Ramillen, G., Lombard, A., Cazenave, A., Ivins, E. R., Llubes, M., Ramy, F., and Biancale, R. (2006). Interannual variations of the mass balance of the antarctica and greenland ice sheets from grace. *Global and Planetary Change*, 53:198–208.
- Redi, M. (1982). Oceanic isopycnal mixing by coordinate rotation. *Journal of Physical Oceanography*, 12:1154–1158.
- Rietbroek, R., Kusche, J., Dahle, C., Flechtner, F., Brunnabend, S.-E., Schröter, J., and Timmermann, R. (2009). Changes in total ocean mass derived from grace, gps, and ocean modelling with weekly resolution. *Journal of Geophysical Research*, (submitted).
- Rietbroek, R., LeGrand, P., Wouters, B., Lemoine, J.-M., Ramillien, G., and Hughes, C. W. (2006). Comparison of in situ bottom pressure data with grace gravity in the crozet-kerguelen region. *Geophysical Research Letters*, 33. doi:10.1029/2006GL027452.
- Rignot, E., Bamber, J. L., van den Broeke, M. R., Li, C. D. Y., van de Berg, W. J., and Meijgaard, E. V. (2008). Recent antarctic ice mass loss from radar interferometry and regional climate modelling. *Nature geoscience*, 1. doi:10.1038/geo102.
- Rio, M.-H., Faugere, Y., Schaeffer, P., Moreaux, G., Bourgoigne, S., Lemoine, J.-M., Bronner, E., and Picot, N. (2010). The new cnes cls09 global mean dynamic topography computed from the combination of grace data, altimetry and insitu measurements. *Oral presentation ESA's Living Planet Symposium*. June 2010.
- Rio, M.-H. and Hernandez, F. (2004). A mean dynamic topography computed over the world ocean from altimetry, in-situ measurements and a geoid model. *Journal of Geophysical Research*, 109. C12032 doi:10.1029/2003JC002226.
- Rio, M.-H., Lemoine, P. S. J.-M., and Hernandez, F. (2005). Estimation of the ocean mean dynamic topography through the combination of altimetric data, in-situ measurements and grace geoid: From global to regional studies. *Proceedings of the GOCINA international workshop, Luxembourg*.
- Rio, M.-H., Schaeffer, P., Moreaux, G., Lemoine, J.-M., and Bronner, E. (2009). A new mean dynamic topography computed over the global ocean from grace data, altimetry

- and in-situ measurements. *Poster communication at OceanObs09 symposium*. 21-25 September 2009, Venice.
- Rollenhagen, K. (2008). *Data Assimilation in a Regional Finite Element Sea-Ice Model for the Arctic - Application of the Singular Evolutive Interpolated Kalman Filter*. Dissertation, University of Bremen, Bremen, Germany.
- Schrama, E. J. O. (2004). Three algorithms for the computation of tidal loading and their numerical accuracy. *Journal of Geodesy*. accepted.
- Seo, K.-W., Wilson, C. R., Chen, J., and Waliser, D. E. (2008). Grace's spatial aliasing error. *Geophys. J. Int.*, 172:41–48.
- Shepherd, A. and Wingham, D. (2007). Recent sea-level contributions of the antarctic and greenland ice sheets. *Science*, 315:1529–1532.
- Simmons, A., Uppala, S., Dee, D., and Kobayashi, S. (2006). Era-interim: New ecmwf reanalysis products from 1989 onwards. *ECMWF Newsletter*, 110. [http://www.ecmwf.int/publications/newsletters/pdf/110\\_rev.pdf](http://www.ecmwf.int/publications/newsletters/pdf/110_rev.pdf).
- S.M.Uppala, Kallberg, P., Simmons, A., Andrae, U., da Costa Bechtold, V., Fiorino, M., Gibson, J., Haseler, J., Hernandez, A., Kelly, G., Li, X., Onogi, K., Saarinen, S., Sokka, N., Allan, R., Andersson, E., Arpe, K., Balmaseda, M., Beljaars, A., van de Berg, L., Bidlot, J., Bormann, N., Caires, S., Chevallier, F., Dethof, A., Dragosavac, M., Fisher, M., Fuentes, M., Hagemann, S., Holm, E., Hoskins, B., Lsaksen, L., Janssen, P., Jenne, R., McNally, A., Mahfouf, J.-F., Morcrette, J.-J., Rayner, N., Saunders, R., Simon, P., Sterl, A., Trenberth, K., Untch, A., Vasiljevic, D., Viterbo, P., and Woollen, J. (2005). The era-40 re-analysis. *Quart. J. R. Meteorol. Soc.*, 131:2961–3012. doi: 10.1256/qj.04.176.
- Stammer, D. (2008). Response of the global ocean to greenland and antarctic ice melting. *Journal of Geophysical Research*, 113. C06022, doi: 10.1029/2006JC004079.
- Sterwart, R. H. (2008). *Introduction to Physical Oceanography*. Department of Oceanography, Texas A and M University. URL: [http://oceanworld.tamu.edu/resources/ocng\\_textbook/contents.html](http://oceanworld.tamu.edu/resources/ocng_textbook/contents.html).
- Tapley, B., Bettadpur, S., Watkins, M., and Reigber, C. (2004). The gravity recovery and climate experiment: Mission overview and early results. *Geophysical Research Letters*, 31. L09607 doi:10.1029/2004GL019920.
- Taylor, P., Bradley, E. F., Fairall, C. W., Legler, D., Schulz, J., Weller, R. A., and White, G. H. (1999). Surface fluxes and surface reference sites. *The Ocean Observing System for Climate - Oceanobs 99*. St Raphael, 25-27 October.

- Thomas, R., Frederick, E., Krabill, W., Manizade, S., and Martin, C. (2006). Progressive increase in ice loss from greenland. *Geophysical Research Letters*, 33. L10503, doi: 10.1029/2006GL026075.
- Timmermann, R. and Beckmann, A. (2004). Parametrization of vertical mixing in the weddell sea. *Ocean Modelling*, 6:83–100.
- Timmermann, R., Beckmann, A., and Hellmer, H. H. (2002). Simulation of ice-ocean dynamics in the weddell sea. part 1: model configuration validation. *Journal of Geophysical Research*, 107. doi: 10.1029/2000JC000741.
- Timmermann, R., Danilov, S., Schröter, J., Böning, C., Sidorenko, D., and Rollenhagen, K. (2009). Ocean circulation and sea ice distribution in a finite-element global sea ice - ocean model. *Ocean Modelling*, 27:114–129. doi: 10.1016/j.ocemod.2008.10.009.
- van den Broeke, M., Bamber, J., Ettema, J., Rignot, E., Schrama, E., van de Berg, W. J., van Meijgaard, E., Velicogna, I., and Wouters, B. (2009). Partitioning recent greenland mas loss. *Science*, 326. doi:10.1126/science.1178176.
- Velicogna, I. (2009). Increasing rates of ice mass loss from the greenland and antarctic ice sheets revealed by grace. *Geophysical Research Letters*, 36. L19503, doi: 10.1029/2009GL040222.
- Velicogna, I. and Wahr, J. (2005). Greenland mass balance from grace. *Geophysical Research Letters*, 32. L18505, doi: 10.1029/2005GL023955.
- Velicogna, I. and Wahr, J. (2006). Measurements of time-variable gravity show mass loss in antarctica. *Science*, 311:1754 – 1756.
- Vianna, M. L. and Menezes, V. V. (2010). Mean mesoscale global ocean currents from geodetic pre-goce mdts with a synthesis of the north pacific circulation. *Journal of Geophysical Research*, 115. C02016, doi:10.1029/2009JC005494.
- Wahr, J. and Molenaar, M. (1998). Time variability of the earth’s gravity field: Hydrological and oceanic effects and their possible detection using grace. *Journal of Geophysical Research*, 103(B12):30,205–30,229.
- Walter, C. (2008). *Simulationen hydrologischer Massenvariationen und deren Einfluss auf die Erdrotation*. Dissertation, Technical University of Dresden, Dresden, Germany. URL: <http://nbn-resolving.de/urn:nbn:de:bsz:14-ds-1205946097808-36130>.
- Wang, Q. (2007). *The finite element ocean model and its aspect of vertical discretization*. Dissertation, University of Bremen, Bremen, Germany. <http://nbn-resolving.de/urn:nbn:de:gbv:46-diss000108304>.

- Wenzel, M. and Schröter, J. (2002). Assimilation of topex/poseidon data in a global ocean model: differences in 1955-1996. *Pergamon, Elsevier Science Ltd.*, 568. PII: S1474-7065(02)00086-4.
- Wenzel, M. and Schröter, J. (2007a). The global ocean mass budget in 1993-2003 estimated from sea level change. *American Meteorological Society*. doi: 10.1175/JPO3007.1.
- Wenzel, M. and Schröter, J. (2007b). Understanding measured sea level rise by data assimilation. *Proceedings, ESA Workshop: 15 years of progress in radar altimetry*.
- Willis, J., Chambers, D. P., and Nerem, R. S. (2008). Assessing the globally averaged sea level budget on seasonal to interannual timescales. *Journal of Geophysical Research*, 113. C06015, doi:10.1029/2007JC004517.
- Willis, J., Roemmich, D., and Cornuelle, B. (2004). Interannual variability in upper ocean heat content, temperature, and thermosteric expansion on global scales. *Journal of Geophysical Research*, 109. C12036, doi:10.1029/2003JC002260.
- Wingham, D. J., Shepherd, A., Muir, A., and Marshall, G. (2006). Mass balance of the antarctic ice sheet. *Philosophical Transactions of the Royal Society*, 364:1627–1635.
- Wouters, B., Chambers, D., and Schrama, E. J. O. (2008). Grace observes small-scale mass loss in greenland. *Geophysical Research Letters*, 35. L20501, doi: 10.1029/2008GL034816.
- Wu, X., Heflin, M. B., Ivins, E. R., and Fukumori, I. (2006). Seasonal and interannual global surface mass variations from multisatellite geodetic data. *Journal of Geophysical Research*, 111. B09401, doi:10.1029/2005JB004100.
- Wu, X., Heflin, M. B., Schotman, H., Vermeersen, B. L. A., Dong, D., Gross, R. S., Ivins, E. R., Moore, A. W., and Owen, S. E. (2010). Simultaneous estimation of global present-day water transport and glacial isostatic adjustment. *Nature Geoscience*, 3:642–646. doi: 10.1038/NGEO938.
- Zillmann, J. W. (1972). A study of some aspects of the radiation and heat budgets of the southern hemisphere oceans. *Meteorological study*, 26. Bureau of Meteorology, Department of the interior, Canberra, Australia.
- Zwally, H. J., Giovinetto, M. B., Li, J., Cornejo, H. G., Beckley, M. A., Brenner, A. C., Saba, J. L., and Yi, D. (2005). Mass changes of the greenland and antarctic ice sheets and shelves and contributions to sea-level rise: 1992-2002. *Journal of Glaciology*, 51.

# Acknowledgement

This dissertation was developed at the Alfred Wegener institute for Polar and Marine Research. It was supported by the German Science Foundation (DFG) via the DFG priority program SPP1257 "Mass transport and mass distribution in the system Earth" under grant SCHR779/4-1. I would like to thank all project partners, Roelof Rietbroek, Prof. Dr.-Ing. Jürgen Kusche, Christoph Dahle, Dr.-Ing. Frank Flechtner, Matthias Fritsche and Prof. Dr.-Ing. Reinhard Dietrich for the great cooperation.

I would like to thank Prof. Dr. Peter Lemke and Prof. Dr.-Ing. Jürgen Kusche for their support and for reviewing this thesis.

I thank my advisor Jens Schröter for the opportunity to do work for my PhD in the field of physical oceanography and to attend various national and international conferences. I'm also very grateful for this scientific advice.

I wish to thank Ralph Timmermann for introducing me into the world of ocean modeling always supporting me during the last years. I thank you for the huge amount of time you spend on the inspiring discussions and on answering my question. I would like to thank Ralph Timmermann and Michael Schroeder for giving me the opportunity to participate in the Polarstern cruise ANT-XXVI/3 to West Antarctica.

Big thanks go to Carmen Böning for her support concerning ocean modeling and processing of GRACE and OBPR measurements.

All colleagues at AWI, I would like to thank for all the helping discussions and the pleasant work climate.

I would like to thank everyone who provided to me one of the several different data sets used. Without these data sets it would not have been possible to write this thesis. The data set NCEP/NCAR reanalysis was provided by the NOAA Climate Diagnostics Center, Boulder, USA, online at <http://www.cdc.noaa.gov>. ERA-40 and ERA Interim reanalyses were provided by the European Center for Medium-Range Weather Forecasts from their Web site at <http://data.ecmwf.int/data/>. ECMWF operational data was used by permission of ECMWF. Here, special thank go to Wolfgang Cohrs who helped me converting the operational data to an easier manageable data format. I would like to thank Prof. Maik Thomas and Herynk Dobslaw who provided the data sets precipitation, evaporation, and total cloud cover after we received the permission from the ECMWF. I would like to thank Keith Fielding from the ECMWF for his efforts to get this permission for us. GPCP One-Degree Daily Precipitation Data Set (1DD) were provided by the NASA/Goddard Space Flight Center's Laboratory for Atmospheres, which develops and

---

computes the 1DD as a contribution to the GEWEX Global Precipitation Climatology Project. The 1992-2002 mean ocean dynamic topography data has been obtained from Nikolai Maximenko (IPRC) and Peter Niiler (SIO). The mean dynamic topography (MDT) Rio05 was produced by CLS space Oceanography Division. The OBP anomalies from the LSG model were provided by Manfred Wenzel from AWI Bremerhaven. I would also like to thank Wolfgang Bosch and Roman Savcenko who provided weekly sea surface height (SSH) variation from multi mission altimetry measurements. I thank Andreas Macrander for make a huge collection of OBPR measurements available. The daily melt extent has been made available by Waleed Abdalati via the website of the National Snow and Ice Data Center (<http://nsidc.org/forms/nsidc-0218.html>) The Greenland 5 km Digital Elevation Model, Ice Thickness, and Bedrock Elevation Grids are provided by Jonathan Bamber via the website of the National Snow and Ice Data Center (<http://nsidc.org/data/nsidc-0092.html>)

Finally I would like to thank my brother, Ralf, my parents, Petra and Kurt, as well as my grandfather Otto. I'm very grateful for all your support on my way.



# Appendix

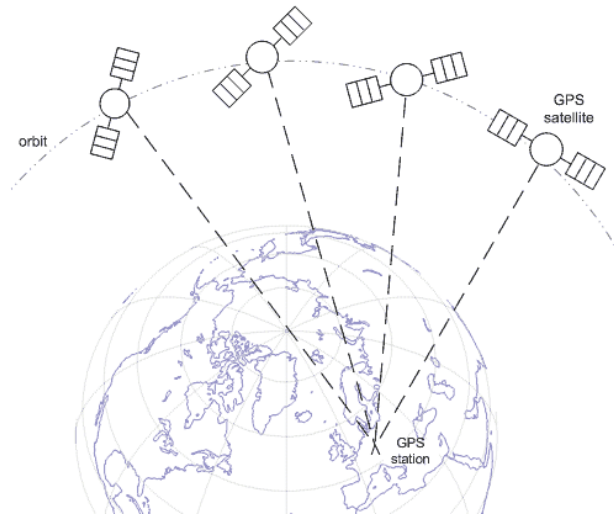
## A List of Acronyms

|       |   |
|-------|---|
| ACC   | Antarctic Circumpolar Current   |
| AIRS  | Atmospheric Infrared Sounders   |
| AWI   | Alfred-Wegener-Institut   |
| CF    | Center of Surface Figure  |
| CM    | Center of Mass of the Earth System  |
| DEM   | Digital Elevation Model   |
| DFG   | German Science Foundation (Deutsche Forschungsgemeinschaft)   |
| DWD   | Deutsche Wetterdienst   |
| EAIS  | East Antarctic Ice Sheet  |
| ECMWF | European Center for Medium-Range Weather Forecasts  |
| ENSO  | El Niño Southern Oscillation  |
| ERA40 | Reanalysis of the global atmosphere and surface conditions for 45-years                                 |
| FIGO  | Fingerprints of ice melting in geodetic GRACE and ocean models  |
| FE    | Finite Elements   |
| FESIM | Finite-Element-Sea-Ice-Model  |
| FEOM  | Finite-Element-Ocean-Model  |
| FESOM | Finite-Element-Sea-Ice-Ocean-Model  |
| GEO   | Geostationary Orbit   |
| GIS   | Greenland Ice Sheet   |
| GFZ   | German Research Center for Geosciences (Geoforschungszentrum Potsdam)                                   |
| GNSS  | Global Navigation Satellite System  |
| GPS   | Global Positioning System   |
| GPCC  | Global Precipitation Climatology Center   |
| GPCP  | Global Precipitation Climatology Project  |
| GRACE | Gravity Recovery and Climate Experiment   |
| HDM   | Hydrological Discharge Model  |
| IGS   | International GNSS Service  |
| LEO   | Low Earth Orbit   |
| LSA   | Loading and Self Attraction   |
| LSDM  | Land Surface Discharge Model  |
| JIGOG | Joint inversion of GPS site displacements, ocean bottom pressure models and GRACE global gravity models |
| LSG   | Large Scale Geostrophic   |
| MEO   | Medium Earth Orbit  |
| MDT   | Mean Dynamic Topography   |

---

|        |   |
|--------|---|
| NAO    | North Atlantic Oscillation                      |
| NCAR   | National Centers for Atmospheric Research       |
| NCEP   | National Centers for Environmental Prediction   |
| NetCDF | Network Common Data Form                        |
| NOAA   | National Oceanic and Atmospheric Administration |
| OBP    | Ocean Bottom Pressure                           |
| OBPR   | Ocean Bottom Pressure Recorders                 |
| OMCT   | Ocean Model for Circulation and Tides           |
| PDO    | Pacific Decadal Oscillation                     |
| RL04   | Release 04                                      |
| RMS    | Root Mean Square                                |
| SAM    | Southern Annular Mode                           |
| SLA    | Sea Level Anomalies                             |
| SMB    | Surface Mass Balance                            |
| SSH    | Sea Surface Height                              |
| SSM/I  | Special Sensor/Microwave Imager                 |
| SST    | Sea Surface Temperature                         |
| STD    | Standard Deviation                              |
| TIROS  | Television and Infrared Observation Satellite   |
| TVOS   | TIROS Operational Vertical Sounders             |
| WAIS   | West Antarctic Ice Sheet                        |
| WOA    | World Ocean Atlas                               |
| WCRP   | World Climate Research Program                  |
| XBT    | Expandable Bathy Thermographs                   |

## B Global Positioning System



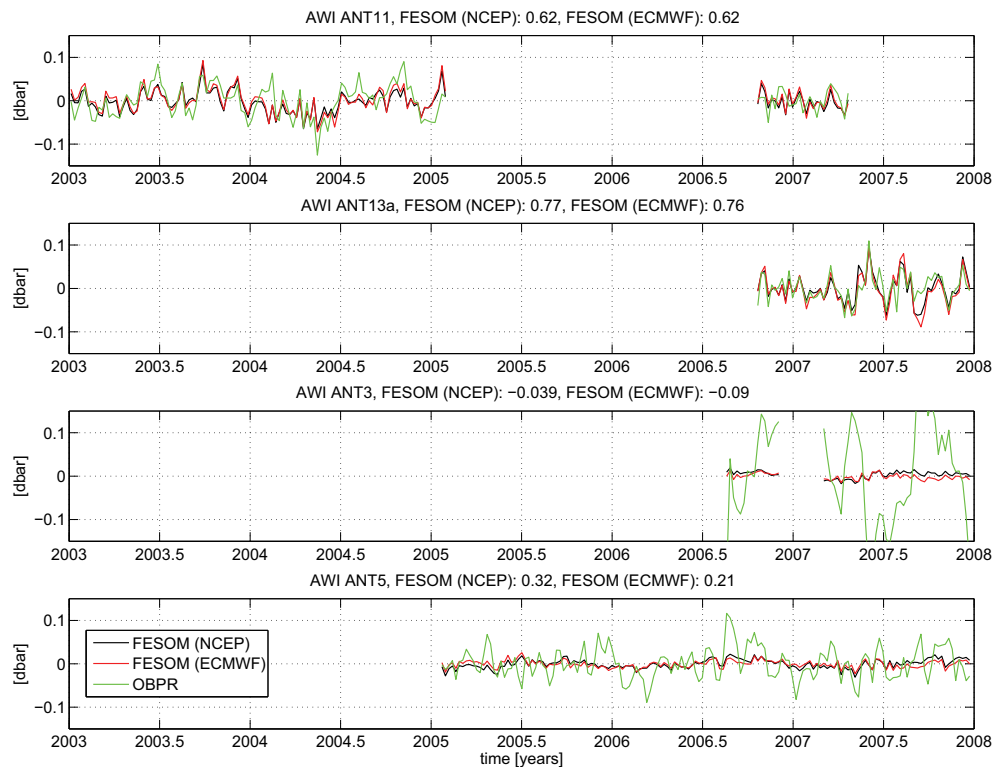
Global Positioning System

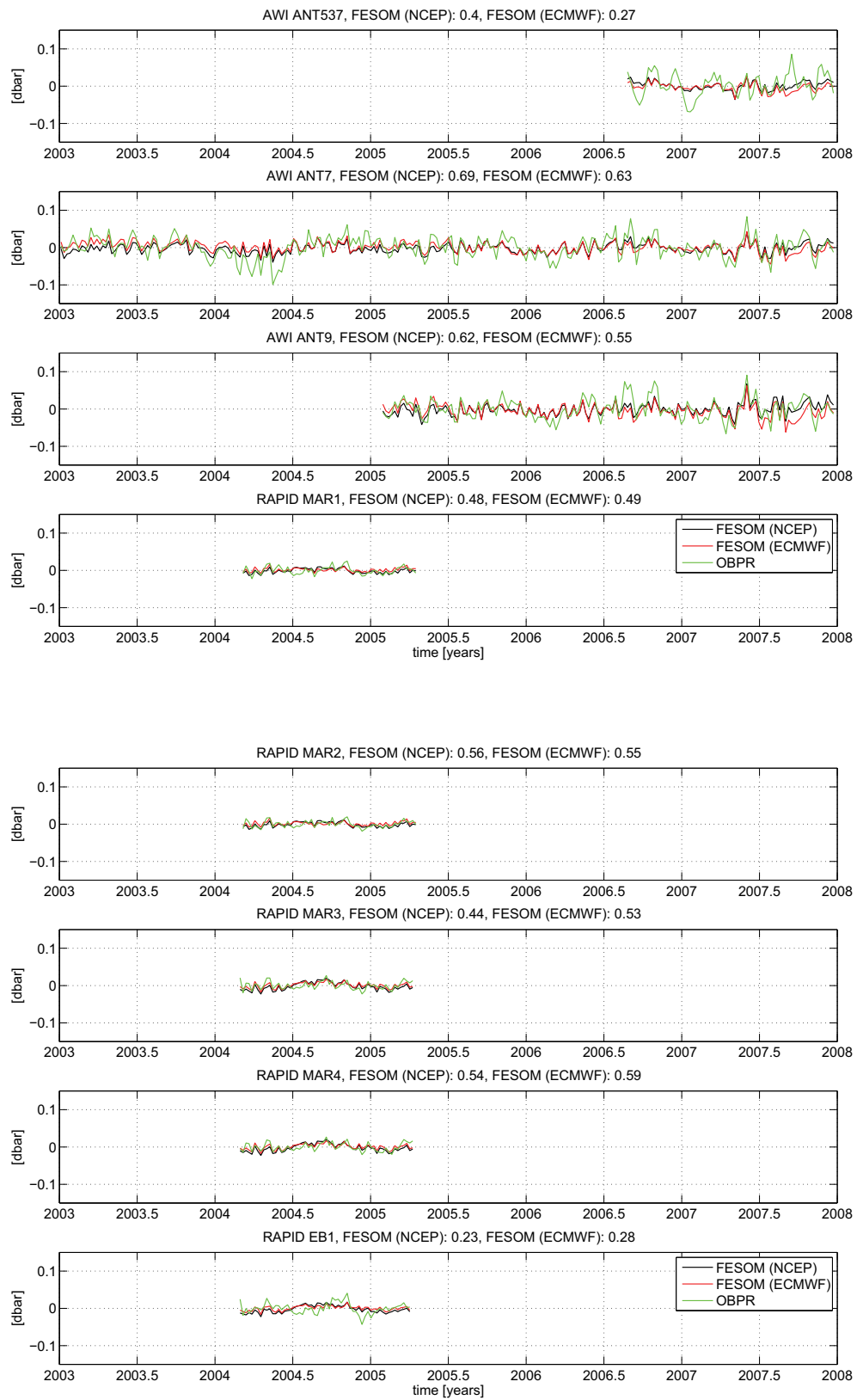
The Global Positioning System (GPS) is a Global Navigation Satellite System (GNSS). Although it is primarily designed for navigation purposes, it is also useful for many geodetic sciences, such as meteorological science, plate tectonics, or to forecast volcanic eruptions. This is mainly the case since with different positioning strategies the accuracy can be improved from meters to a few centimeters. The space segment includes 24 Satellites that are flying on a Medium Earth Orbit (MEO) with an altitude of about 20,000 kilometer. The 6 different orbits are nearly circular and are separated along the equator by 60 degrees. The inclination is 55 degrees with a revolution time a 11h58m (half a sidereal day). A minimum four satellites are needed to estimate the position of a GPS station on the ground in 3D.

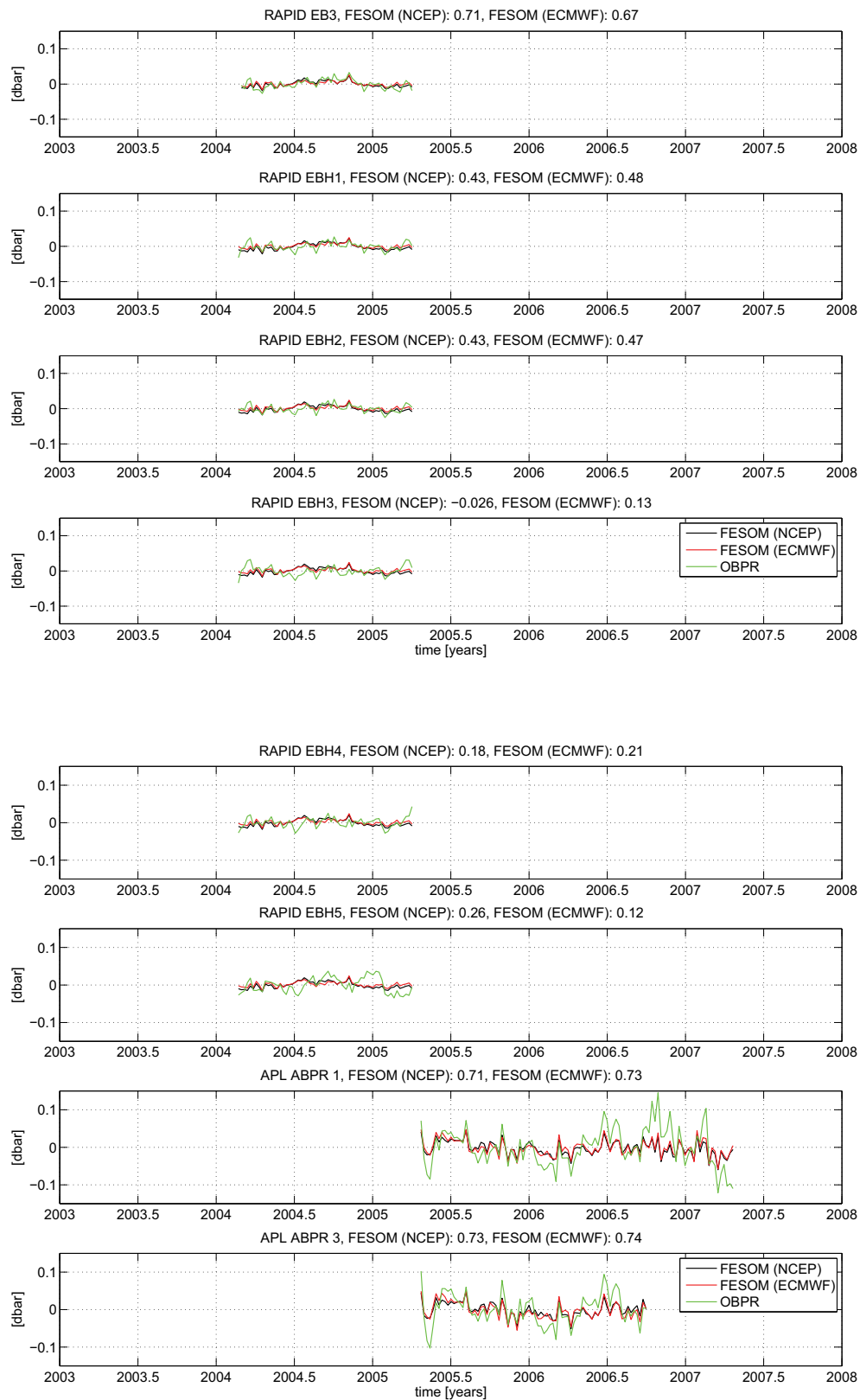
Site displacements computed from the Global Positioning System (GPS) are included in the inversion because they allow the estimation of low degree surface loadings as well as the detection of geocenter motion (detection of degree 1 deformation). Note, the estimates of the  $z$  component (height) is generally worse as no satellite is visible below 0 degree. Therefore, weekly IGS network solutions from 150 - 200 stations have been used for a global coverage. For example if inverting GPS site displacements alone, the global solution becomes ill-posed. Then it has to be stabilized over the ocean. A disadvantage of this data set is the contamination by (post) seismic effects, plate motion, or Postglacial rebound (PGR), for example.

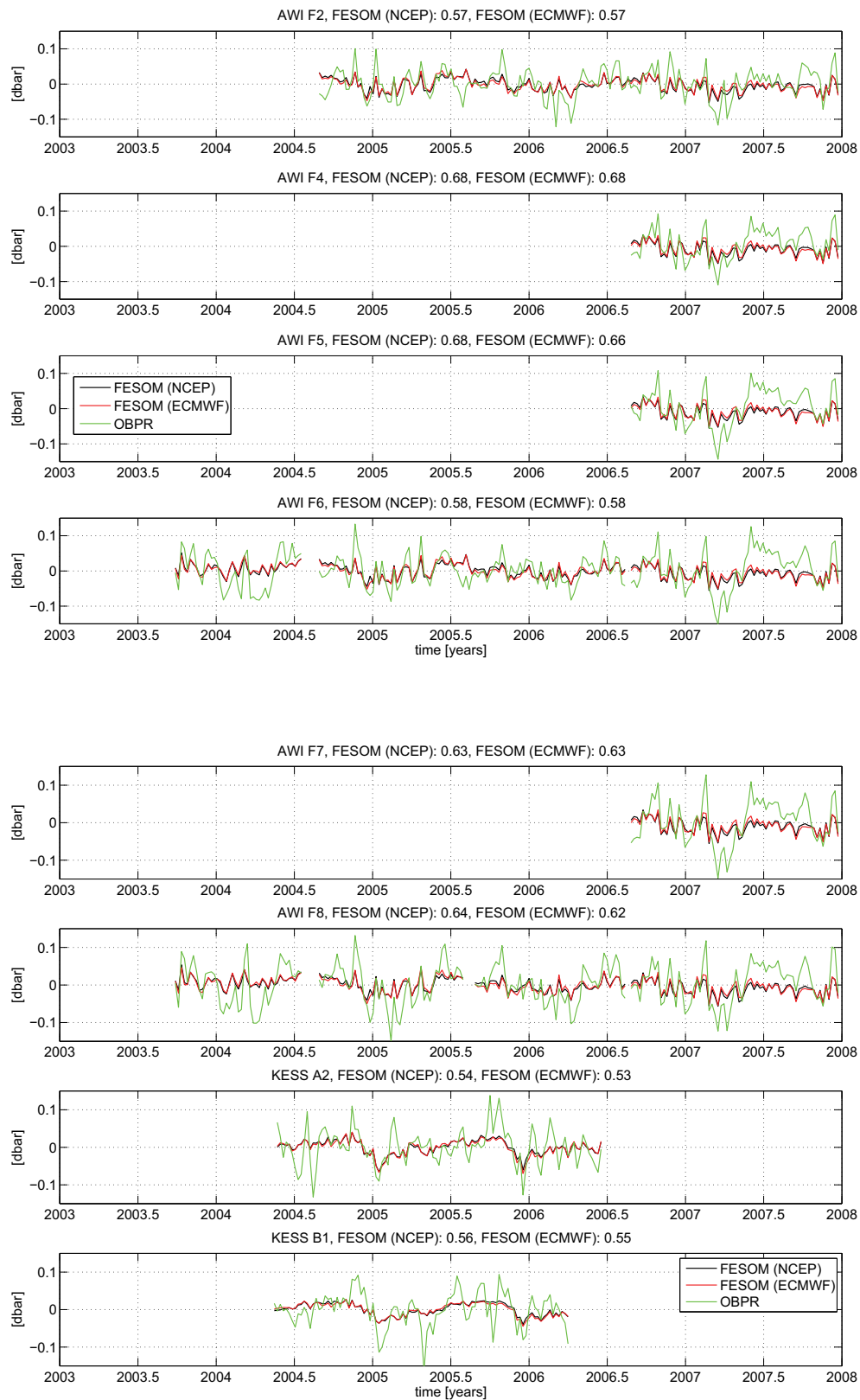
## C Comparison of OBPR and FESOM Timeseries

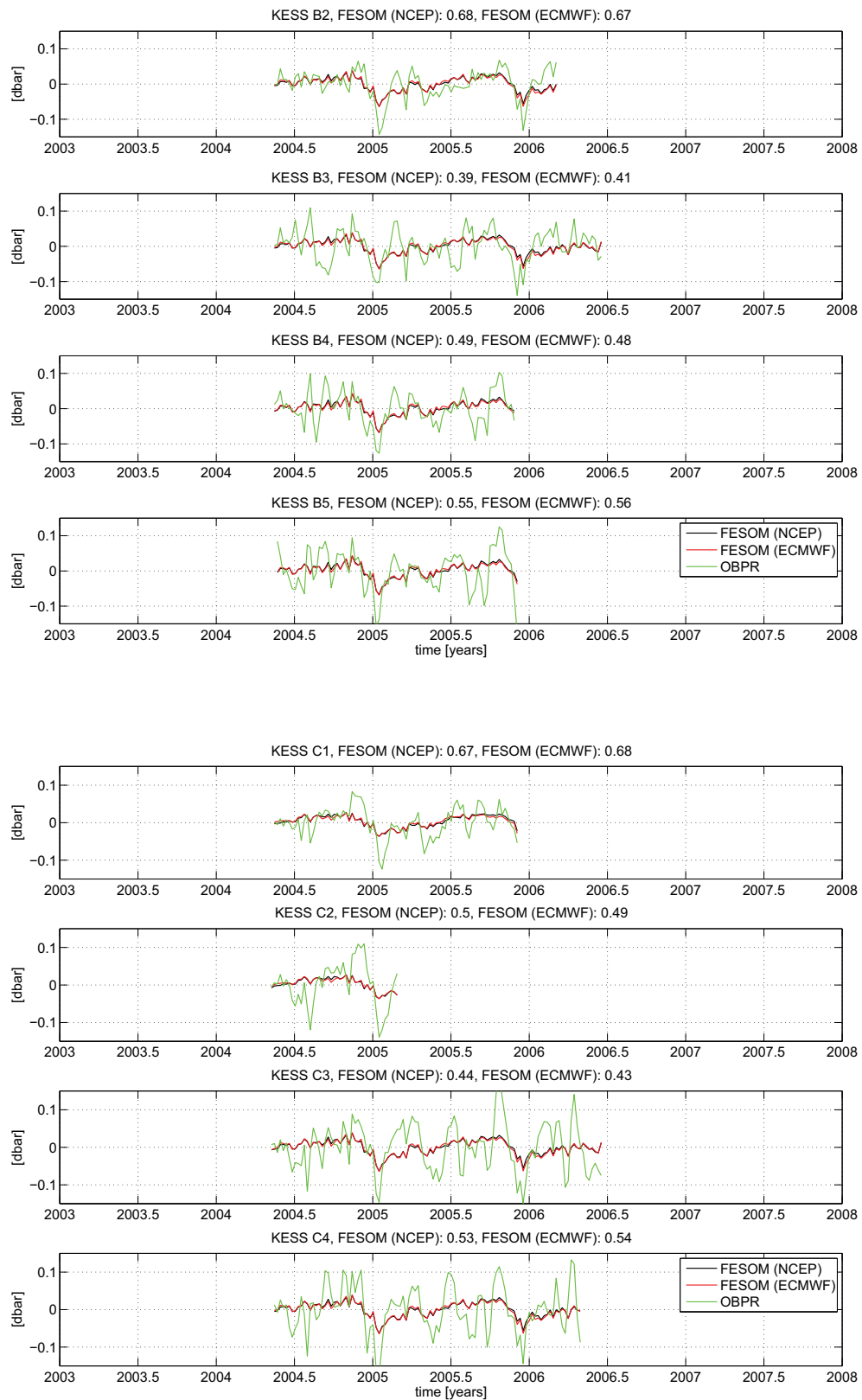
In the following all OBPR time series, which are longer than 20 weeks, are compared with time series of two FESOM simulations using different atmospheric forcing. In the title the location and the correlation of the two model simulations and OBPR are shown. For inter-comparison, the time series and correlation are computed for the time period of the inversion (2003 to 2007).

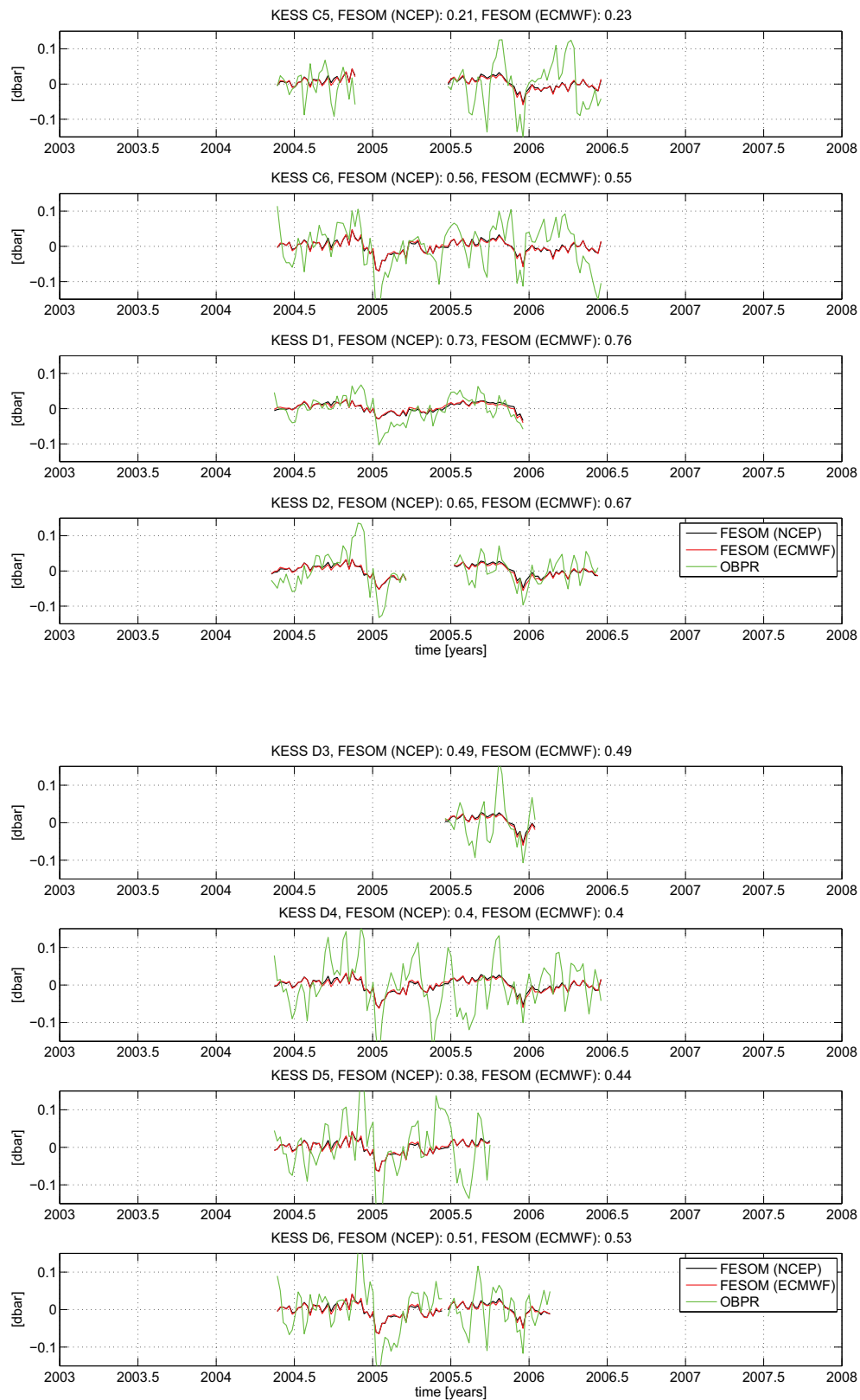


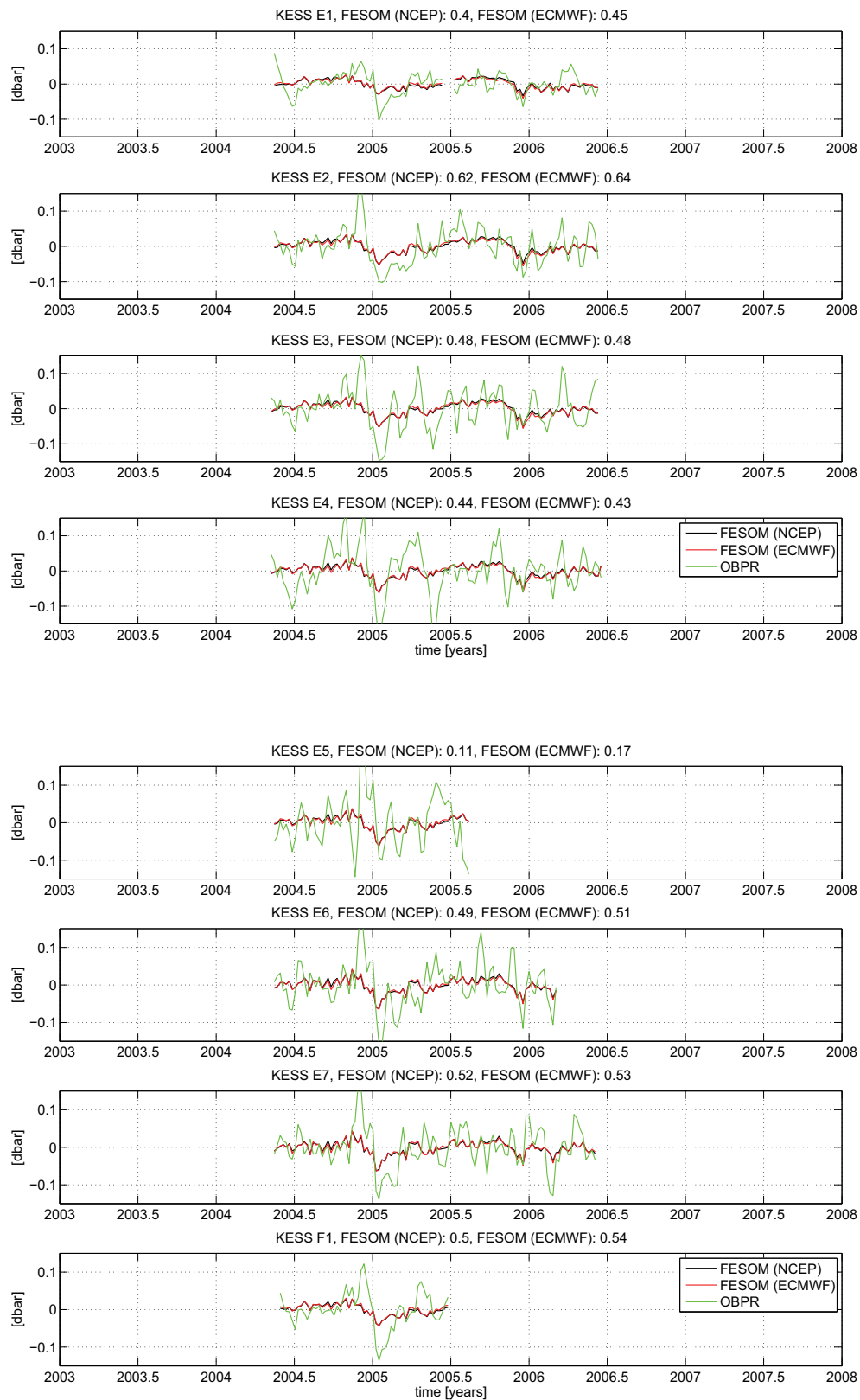


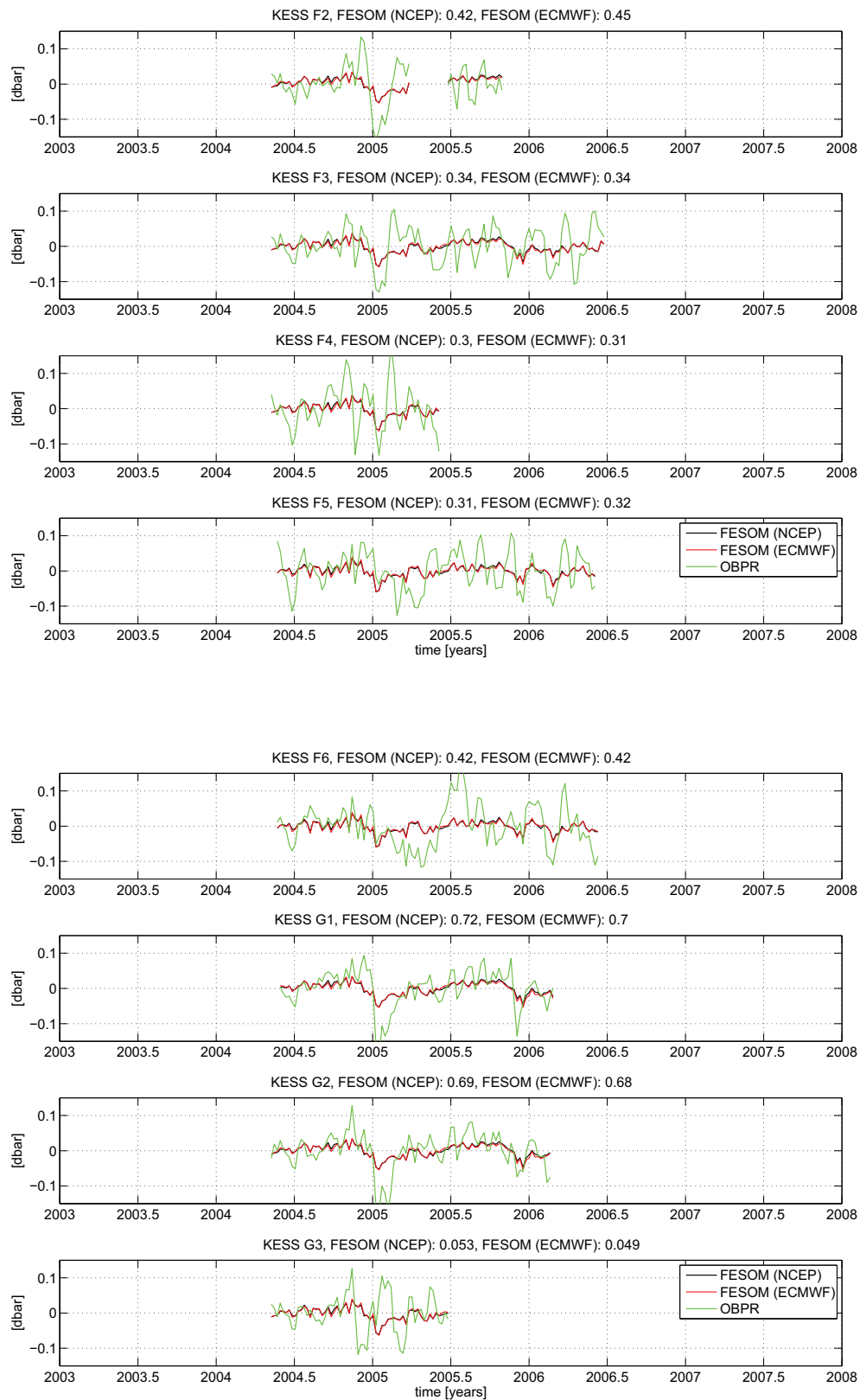


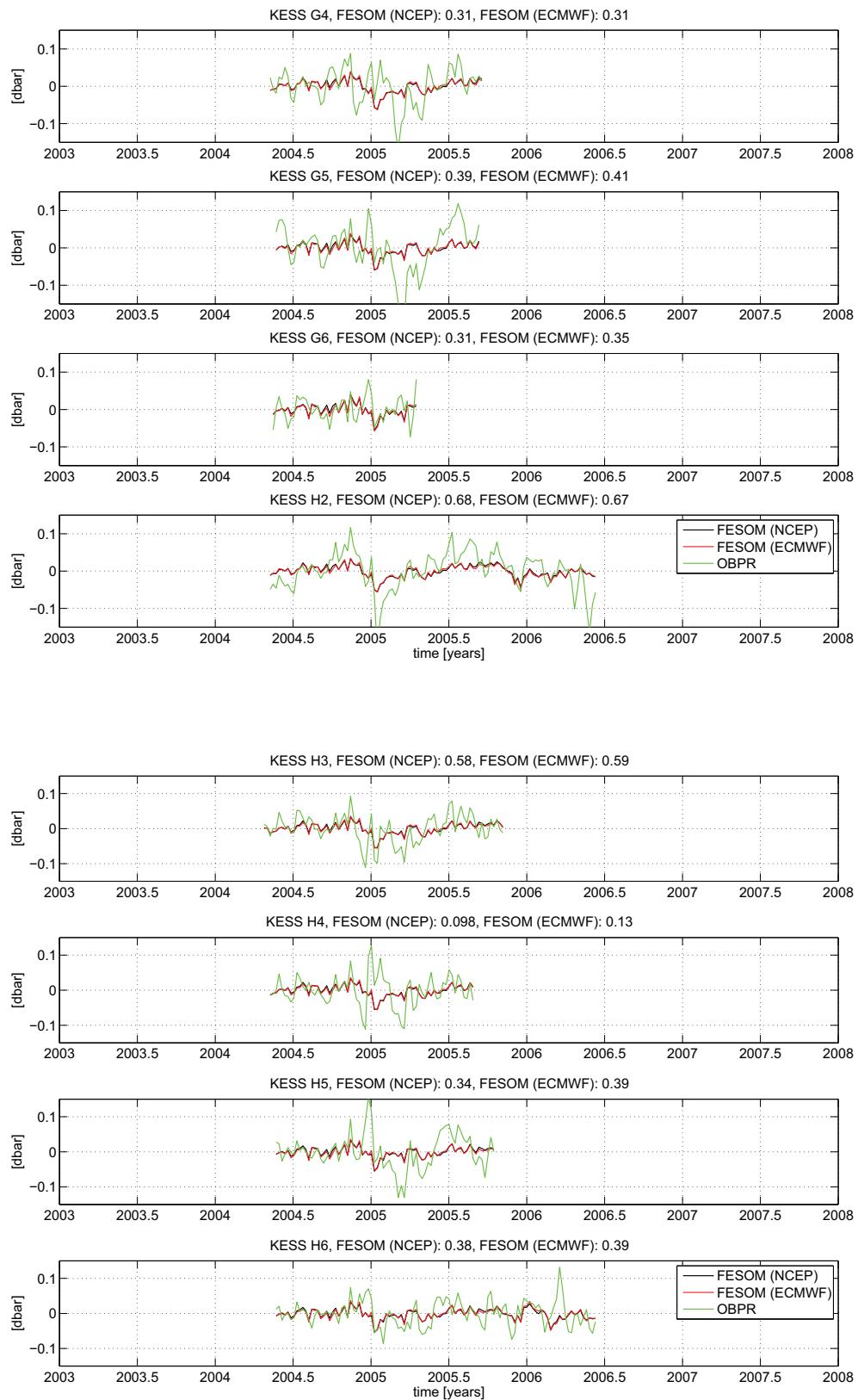


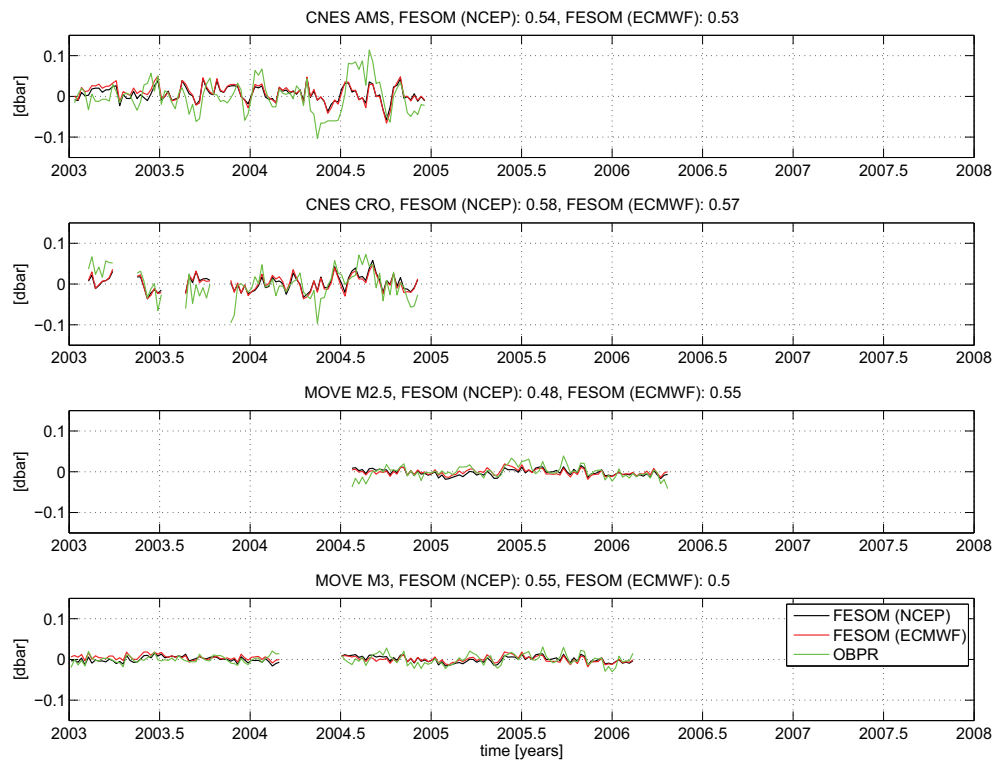
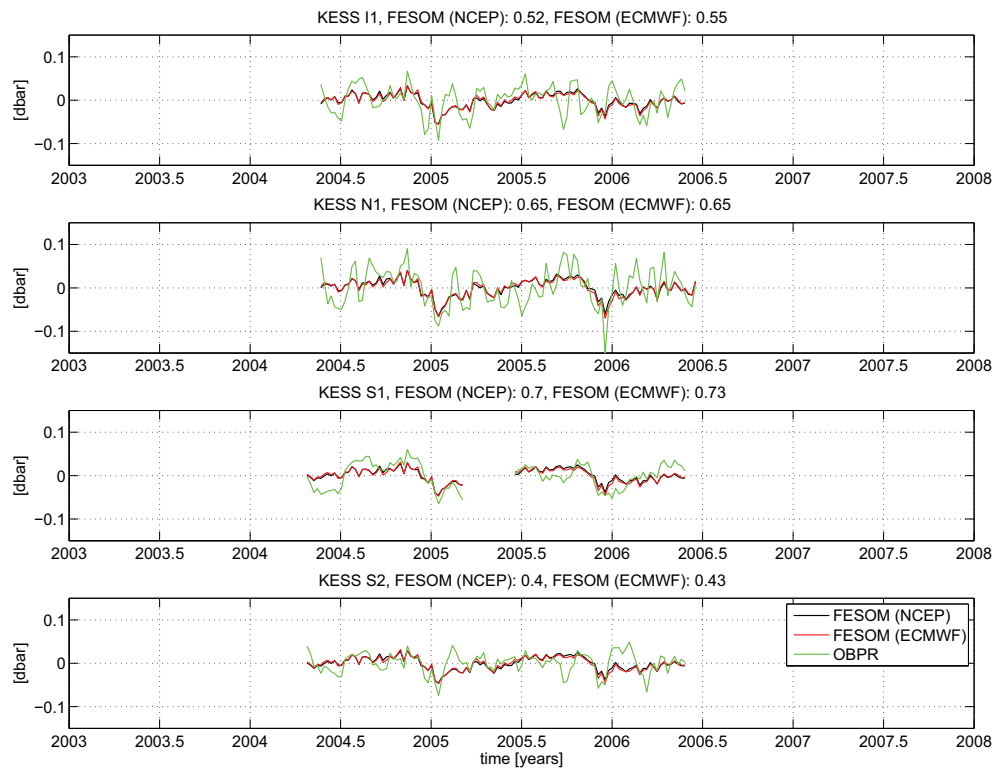


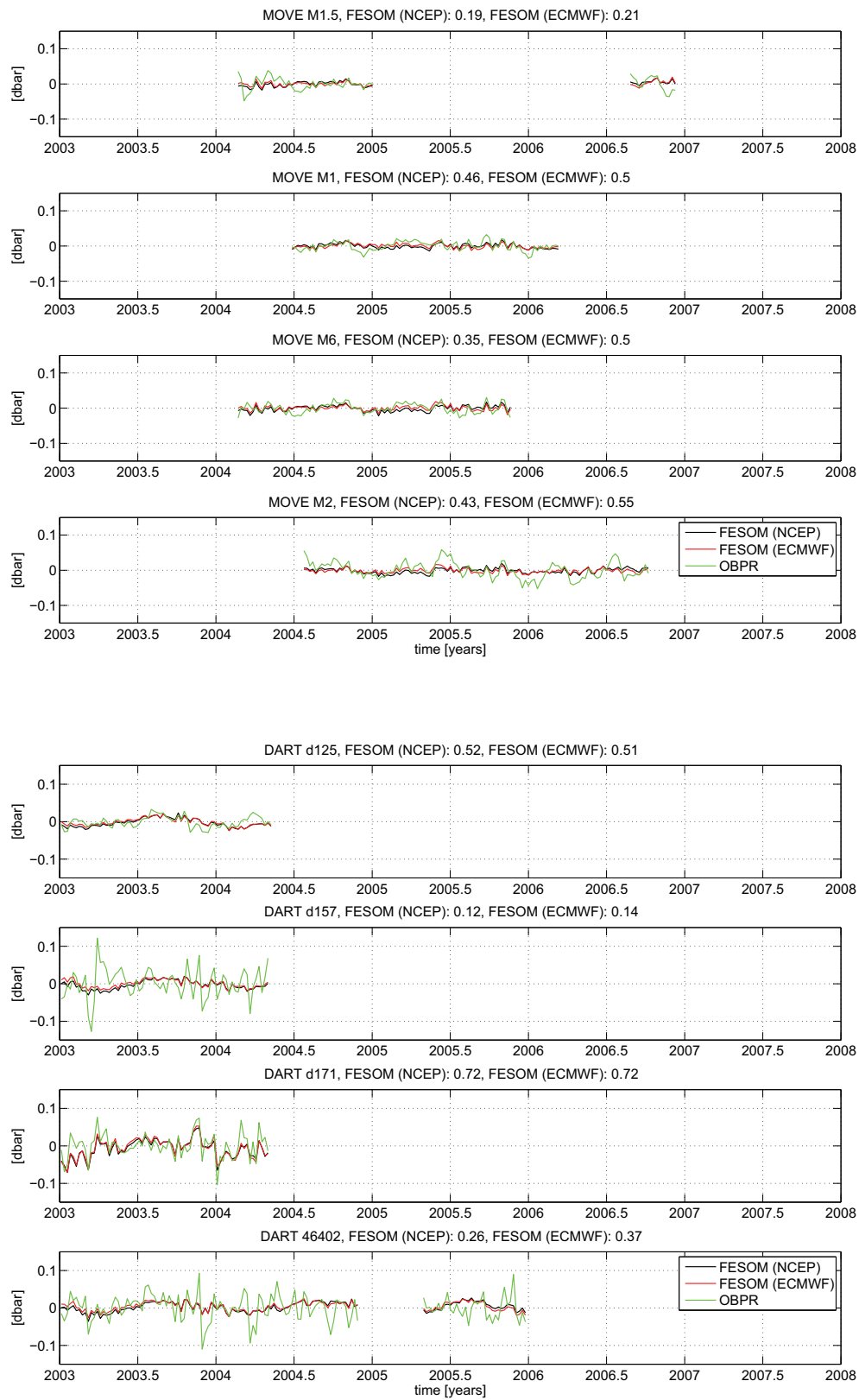


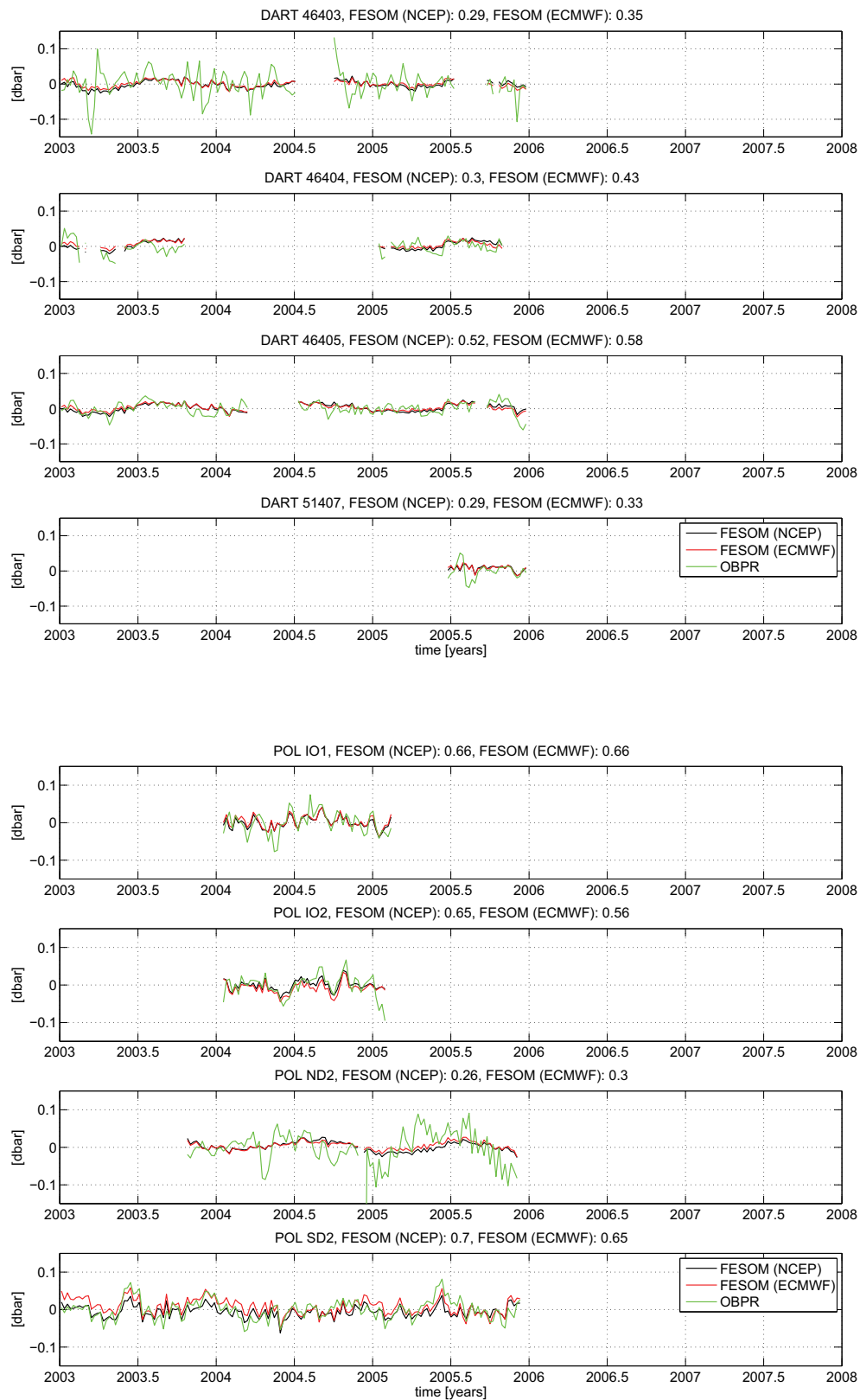


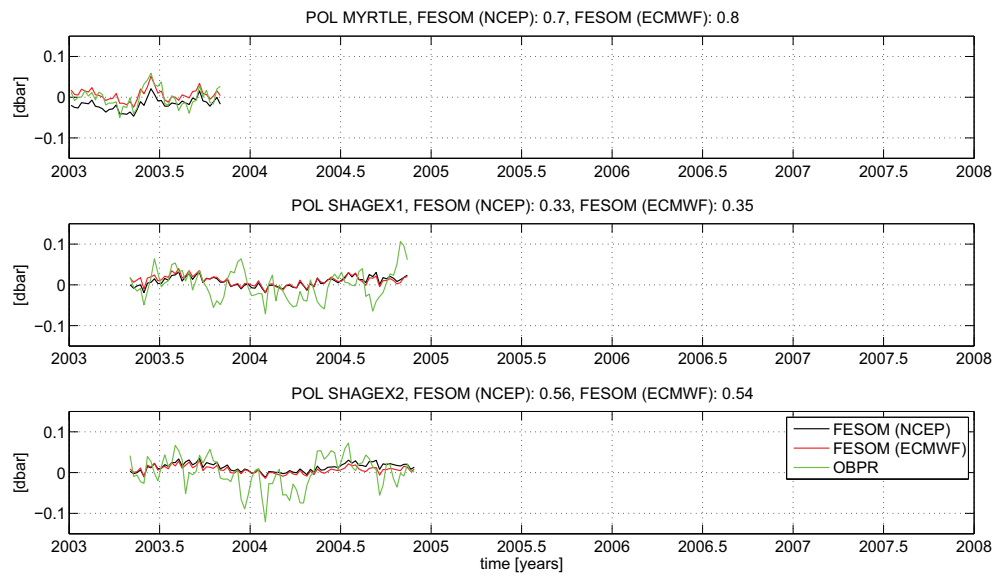






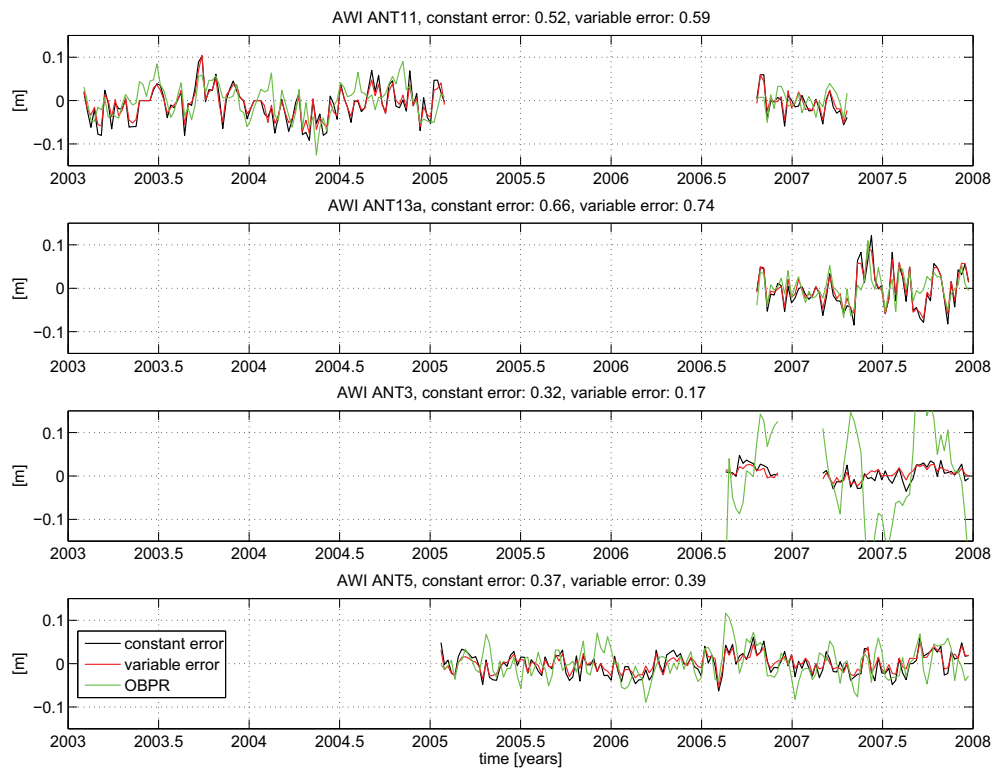




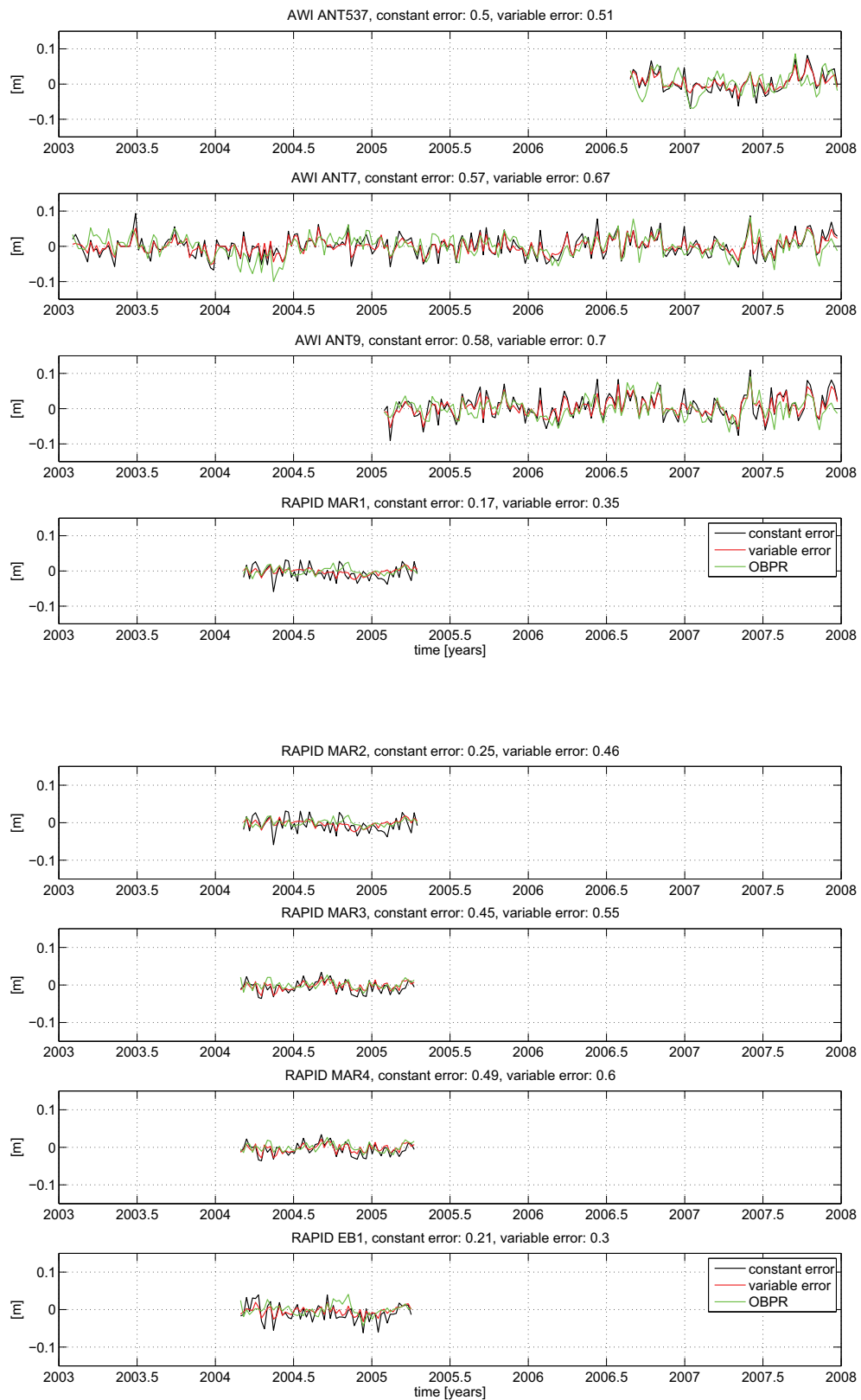


## D Comparison of time series from OBPR and Inverse Solutions

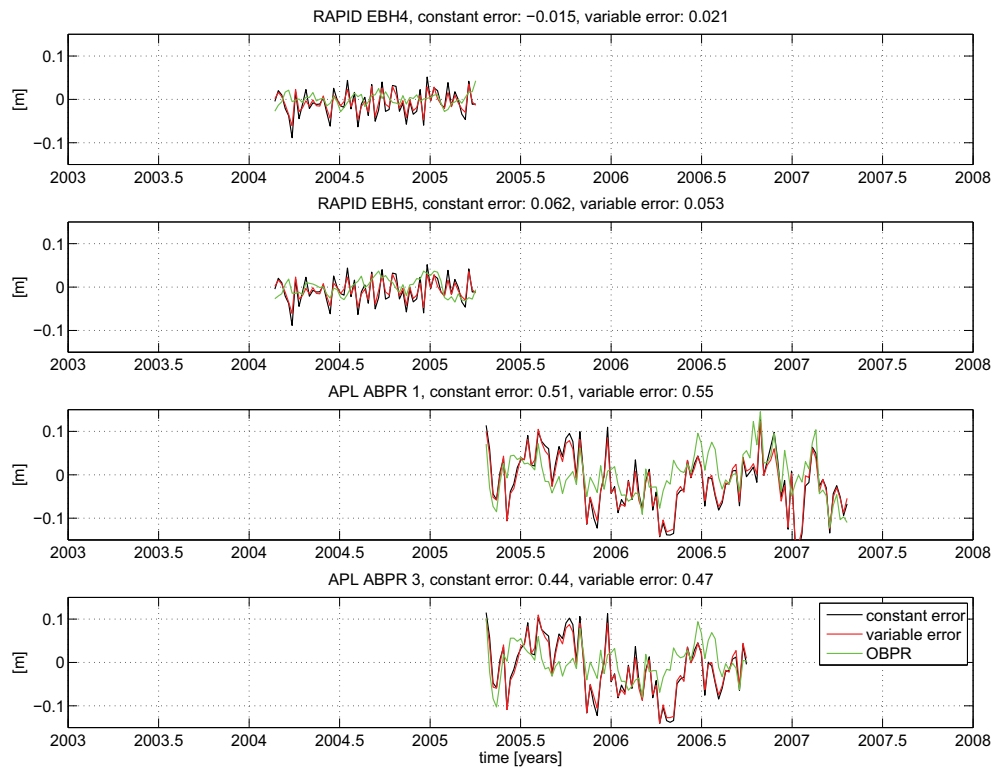
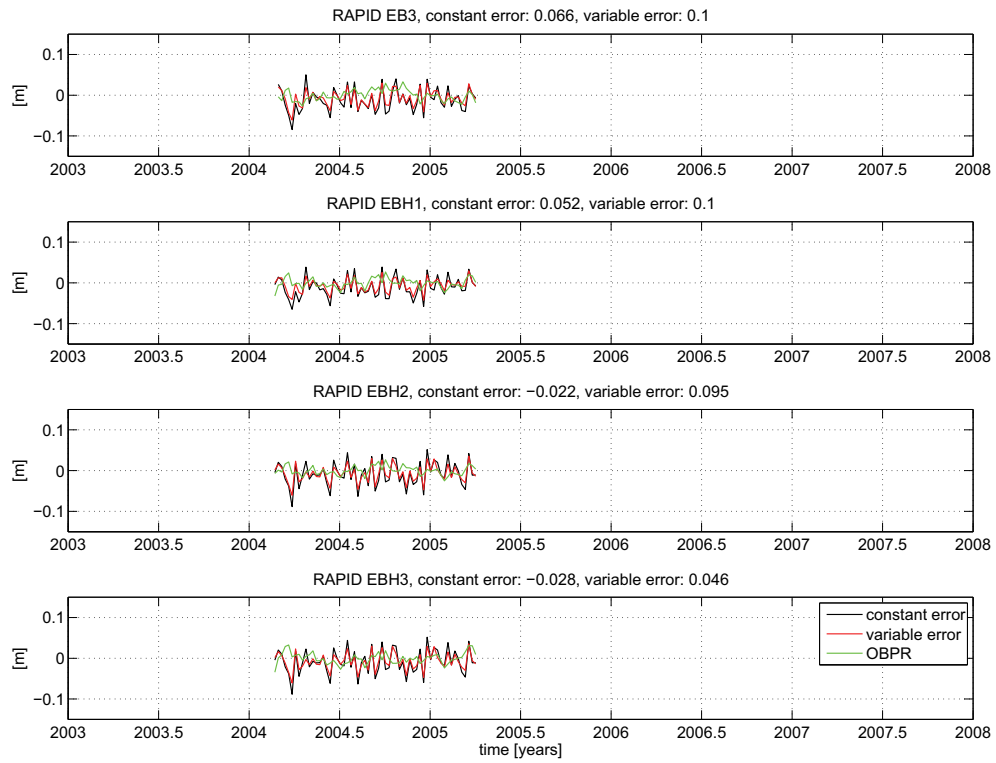
In the following all OBPR time series, which are longer than 20 weeks, are compared with time series of the two inverse solutions. The first inversion uses a constant error assumption to weight modeled OBP. The second one uses the estimated variable model error. In the title the location and the correlation of the two inversion solutions and OBPR are shown.



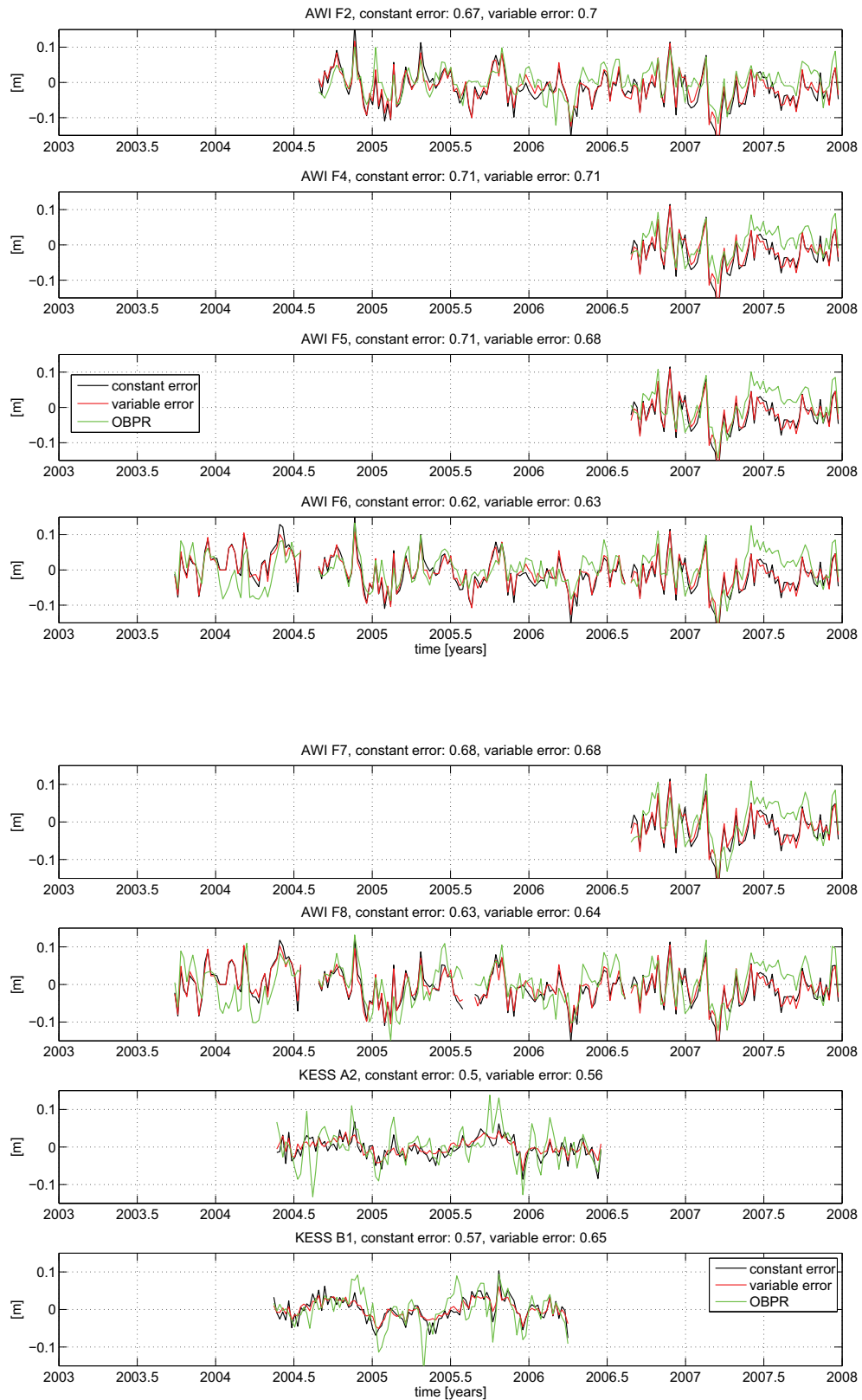
## D. COMPARISON OF TIME SERIES FROM OBPR AND INVERSE SOLUTIONS 150



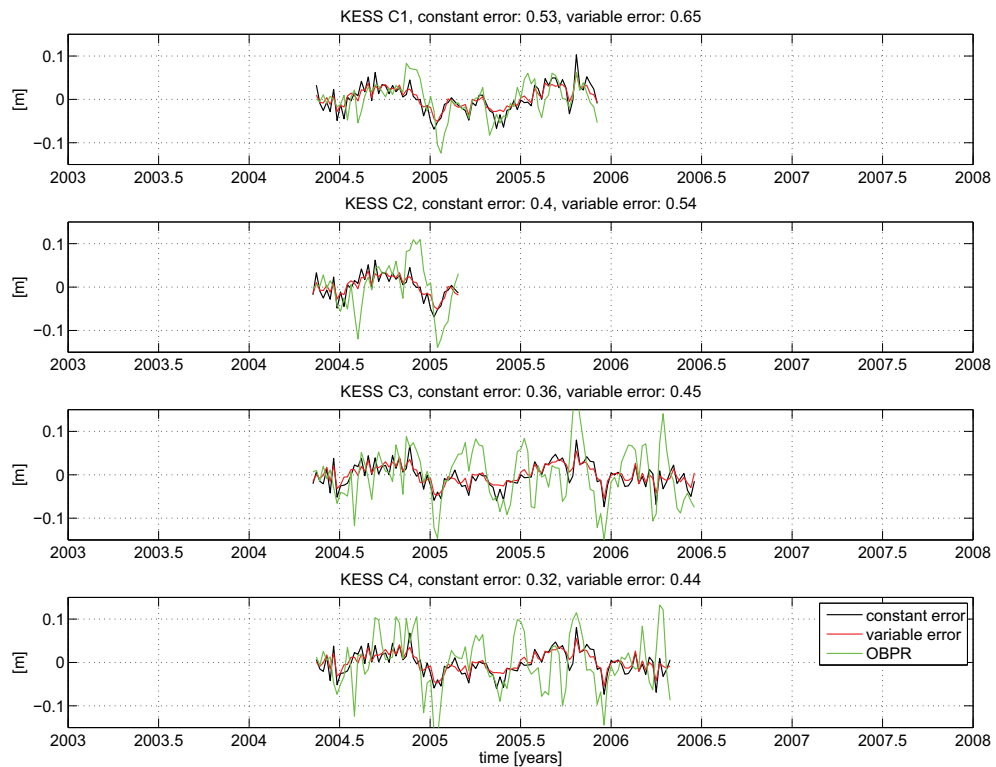
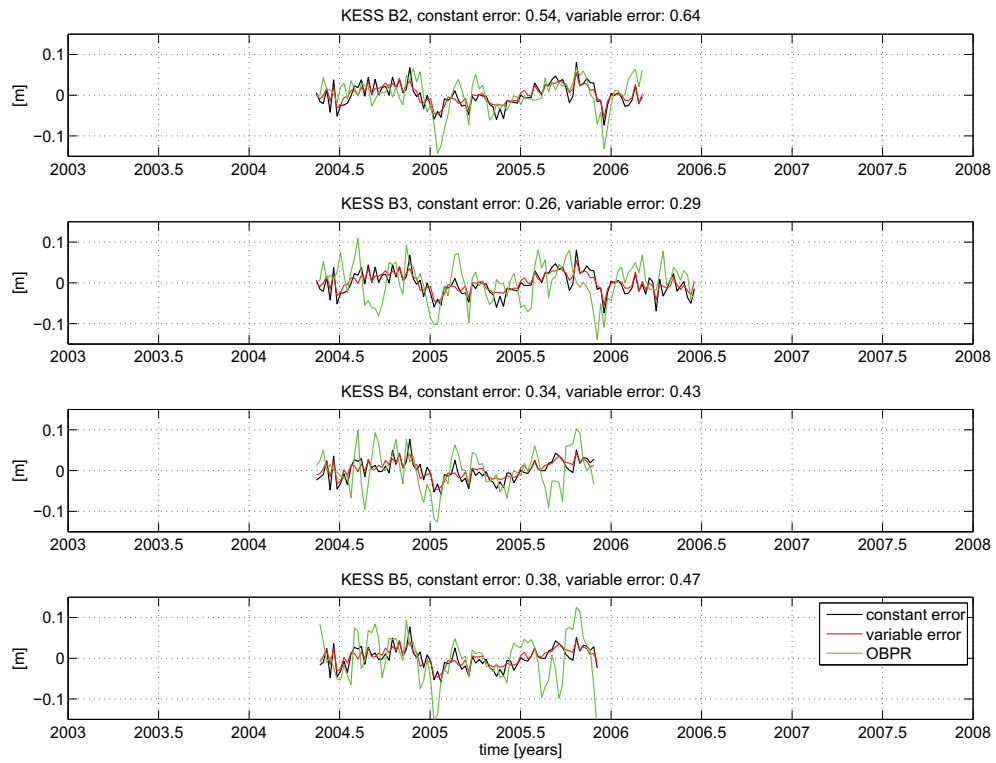
## D. COMPARISON OF TIME SERIES FROM OBPR AND INVERSE SOLUTIONS 151



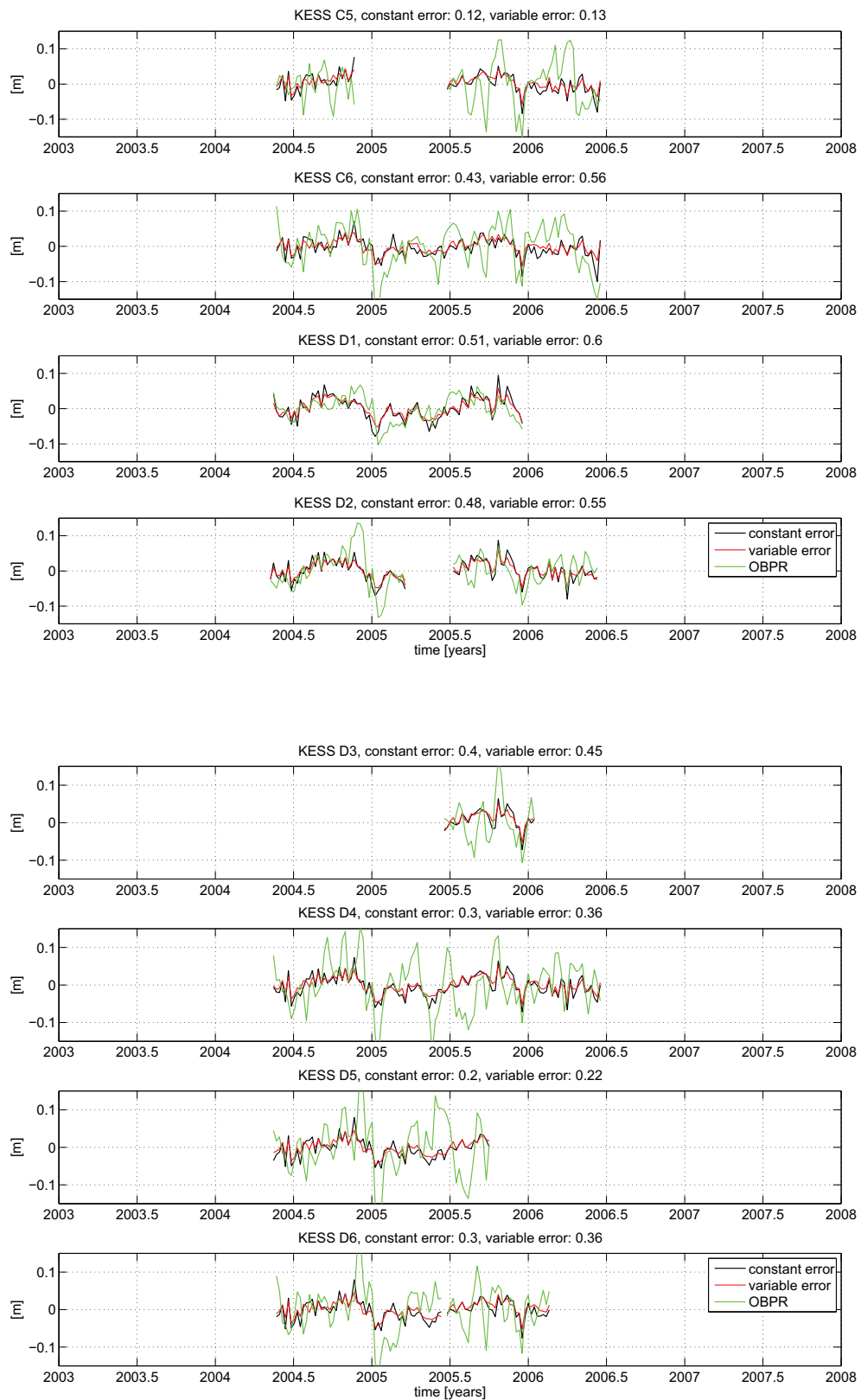
## D. COMPARISON OF TIME SERIES FROM OBPR AND INVERSE SOLUTIONS 152



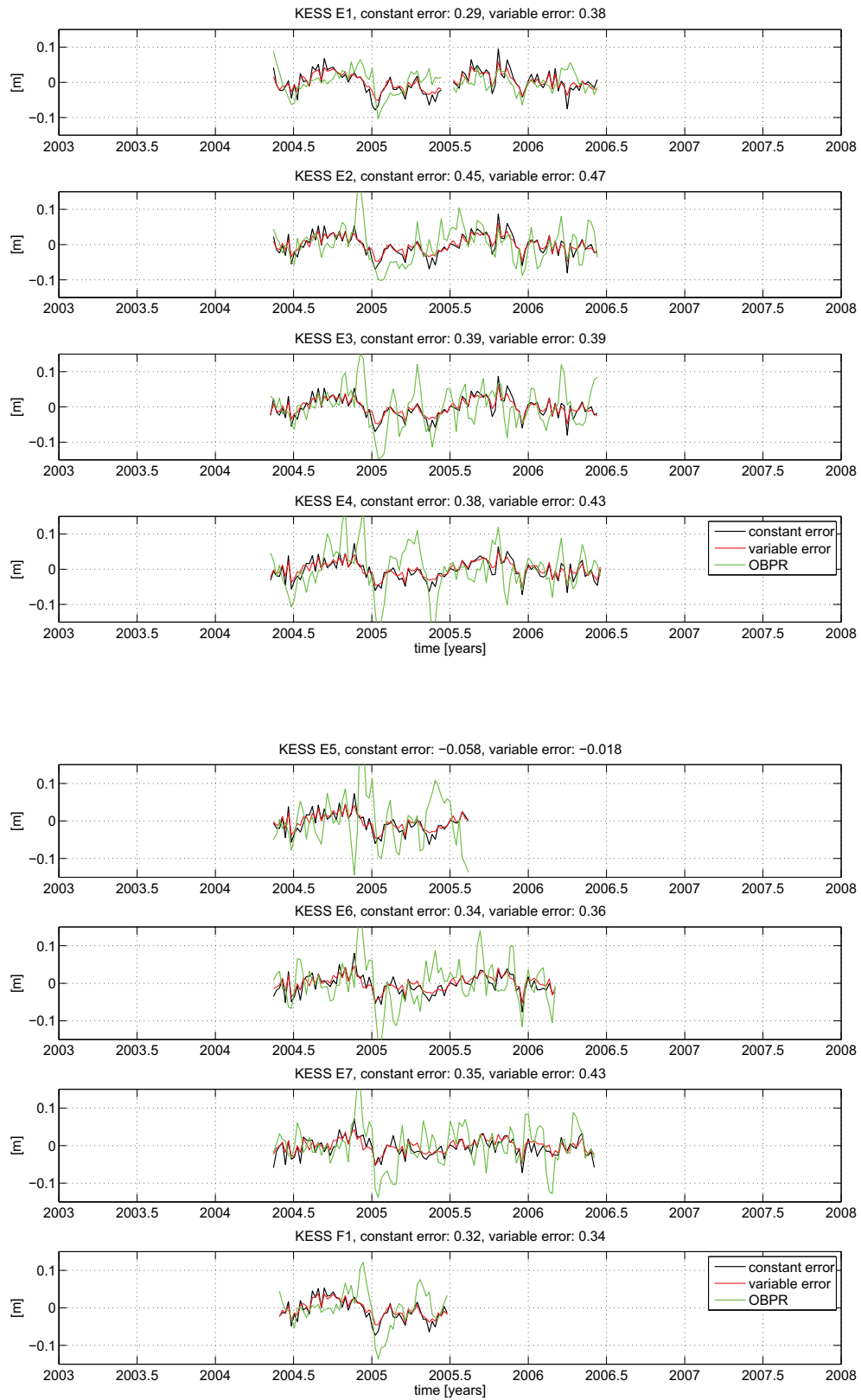
## D. COMPARISON OF TIME SERIES FROM OBPR AND INVERSE SOLUTIONS 153



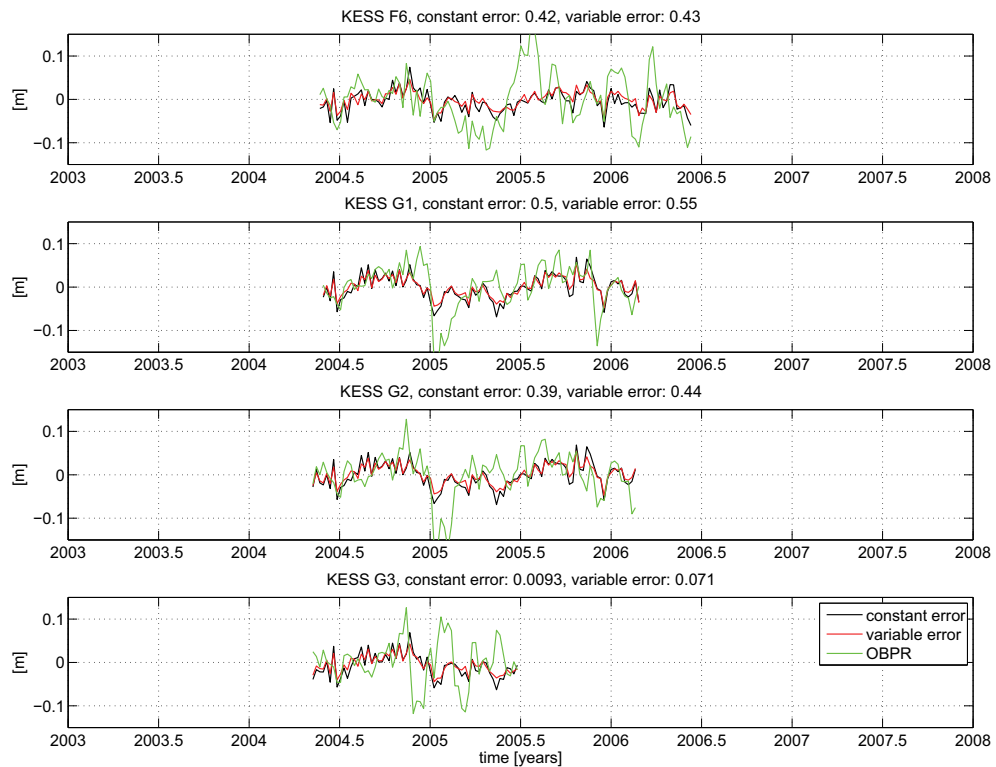
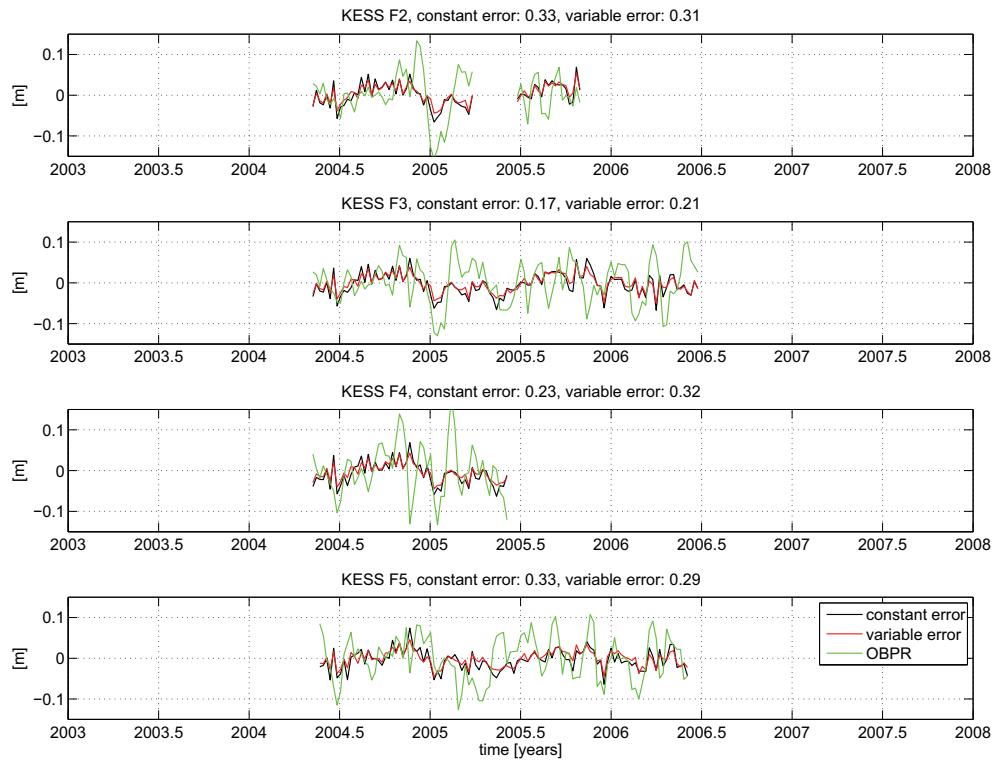
## D. COMPARISON OF TIME SERIES FROM OBPR AND INVERSE SOLUTIONS 154



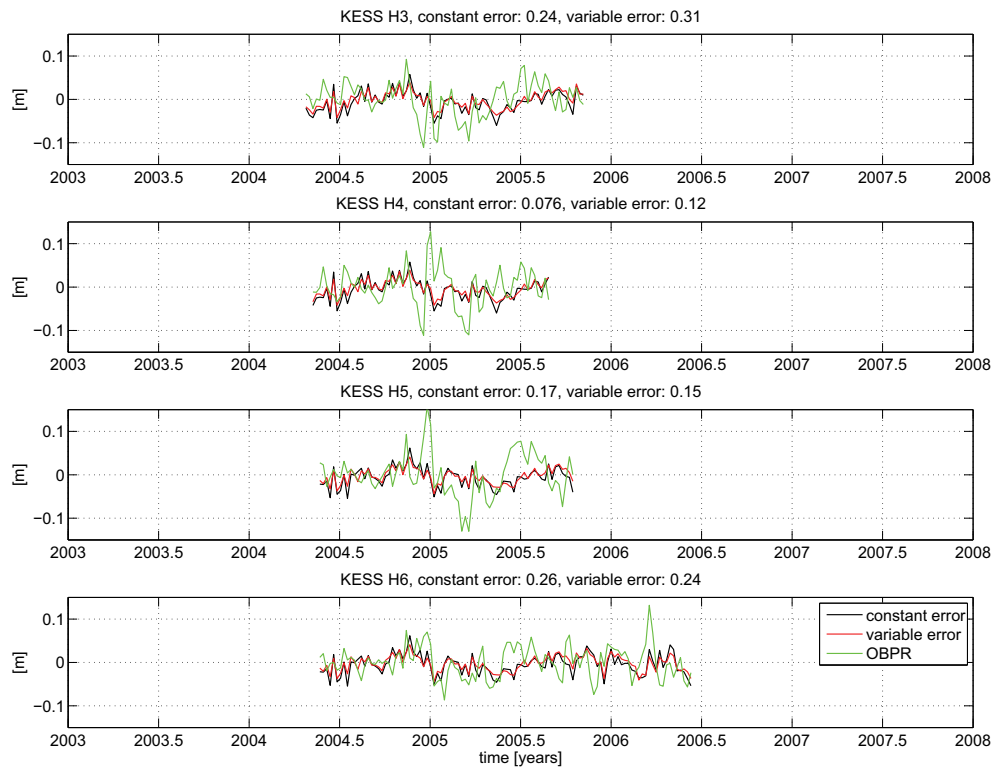
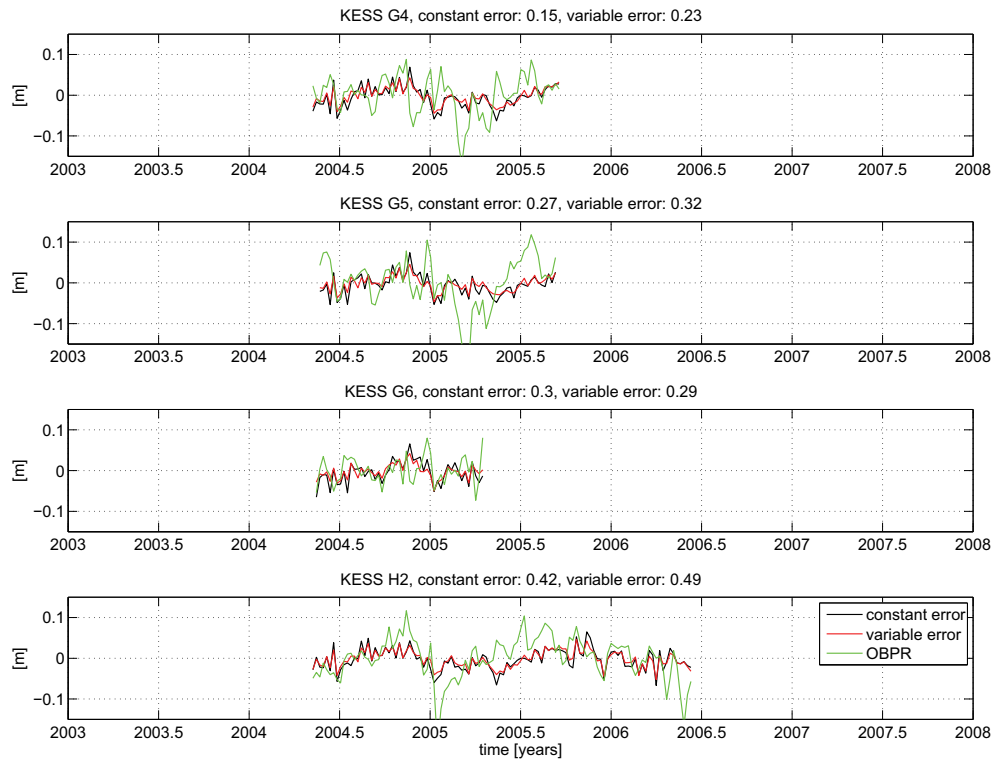
## D. COMPARISON OF TIME SERIES FROM OBPR AND INVERSE SOLUTIONS 155



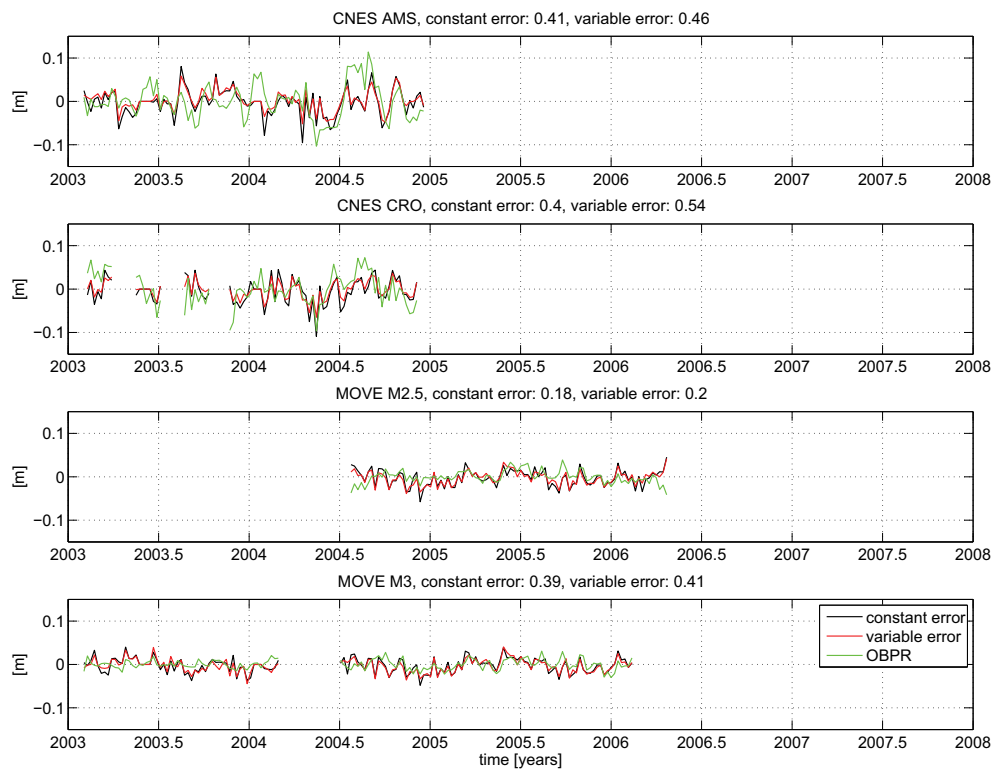
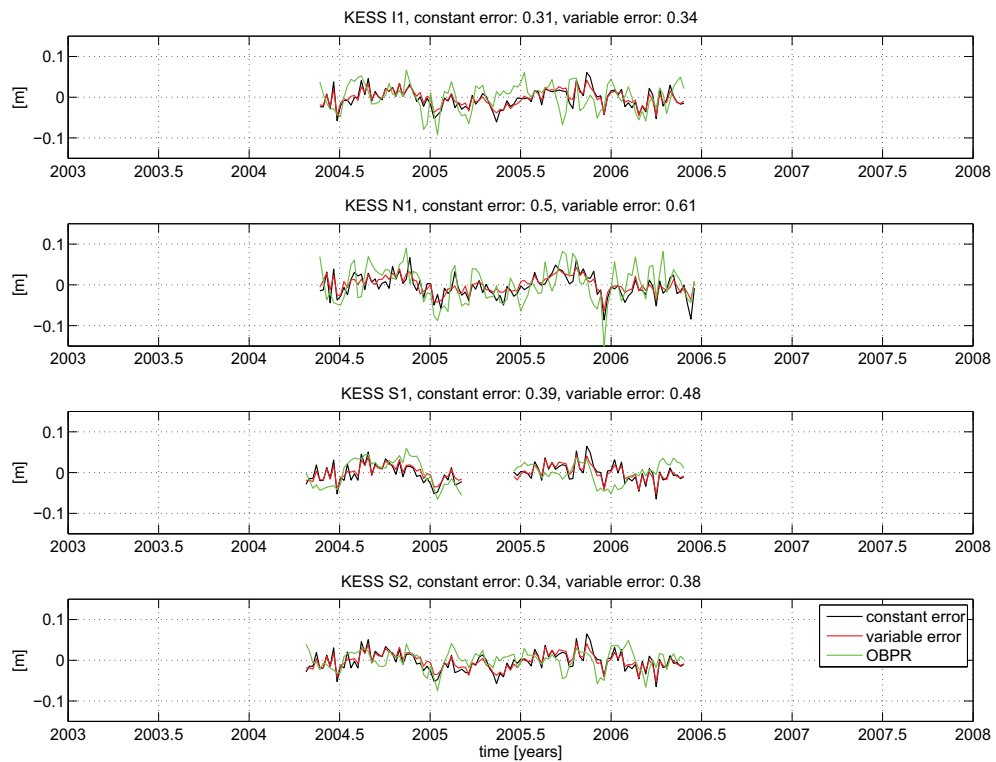
## D. COMPARISON OF TIME SERIES FROM OBPR AND INVERSE SOLUTIONS 156



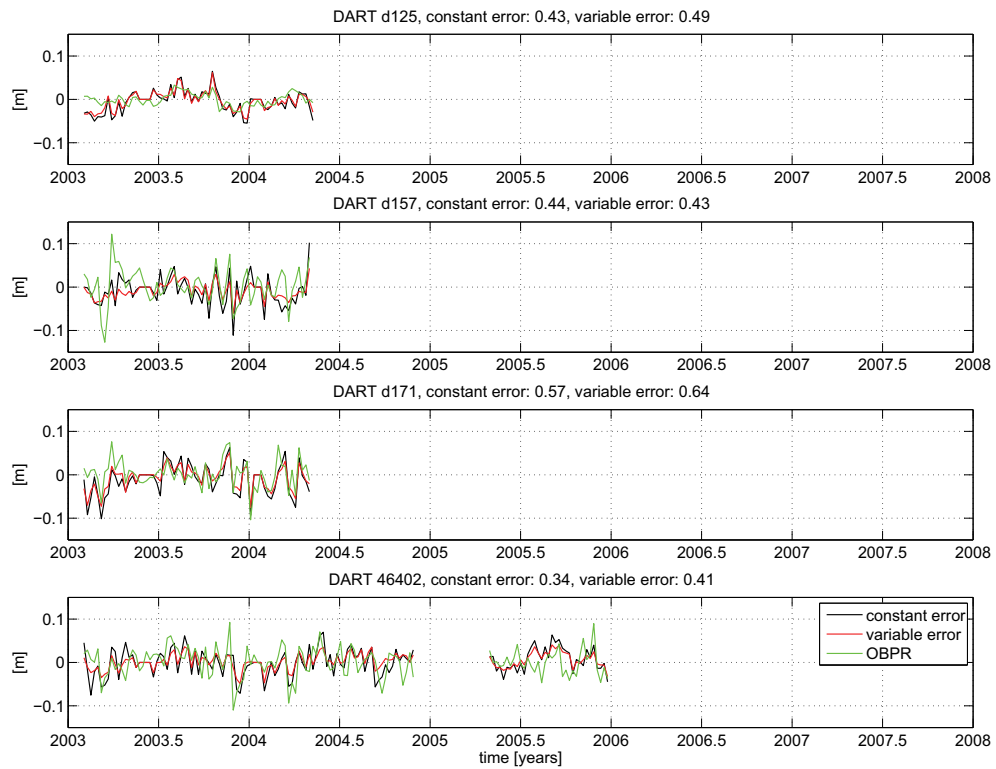
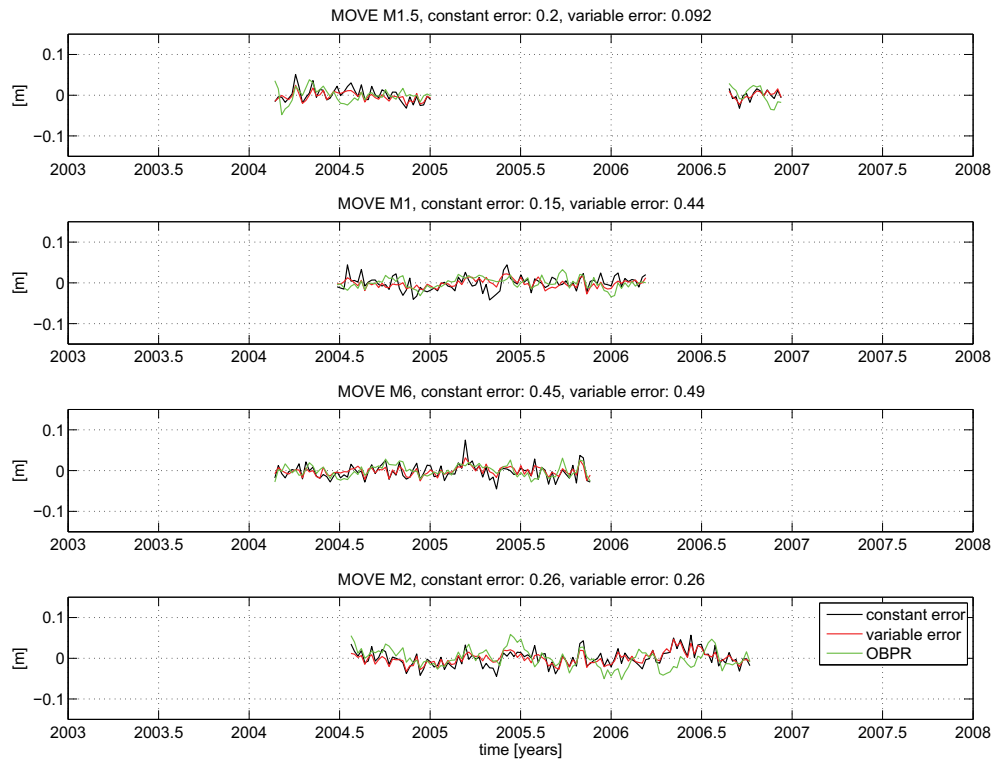
## D. COMPARISON OF TIME SERIES FROM OBPR AND INVERSE SOLUTIONS 157



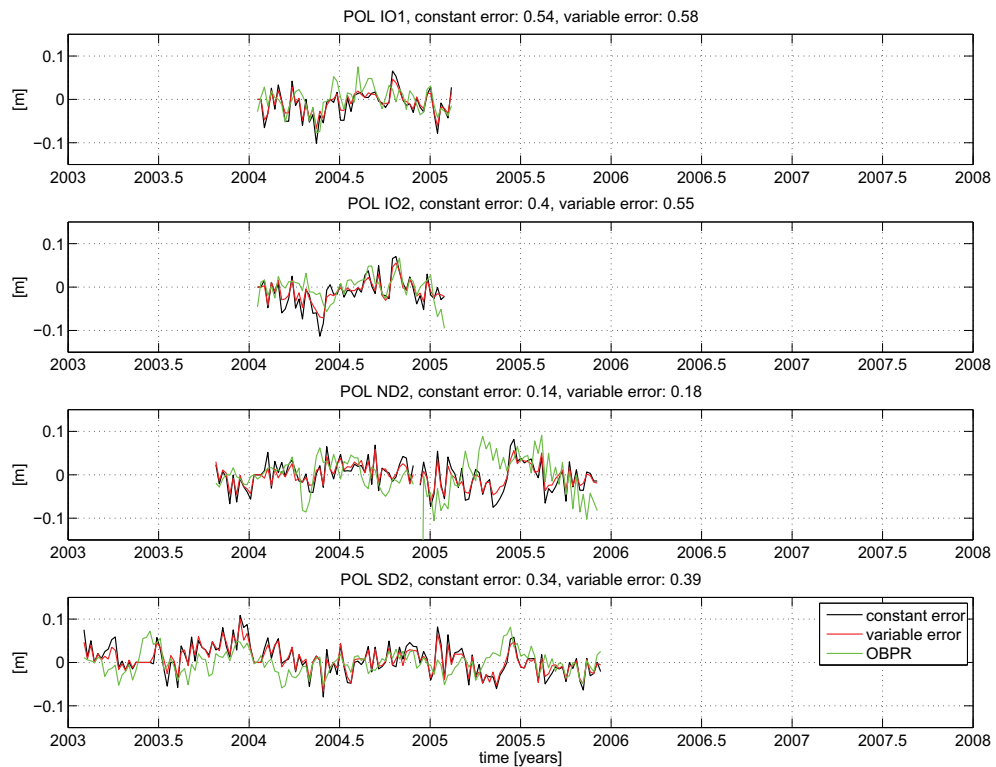
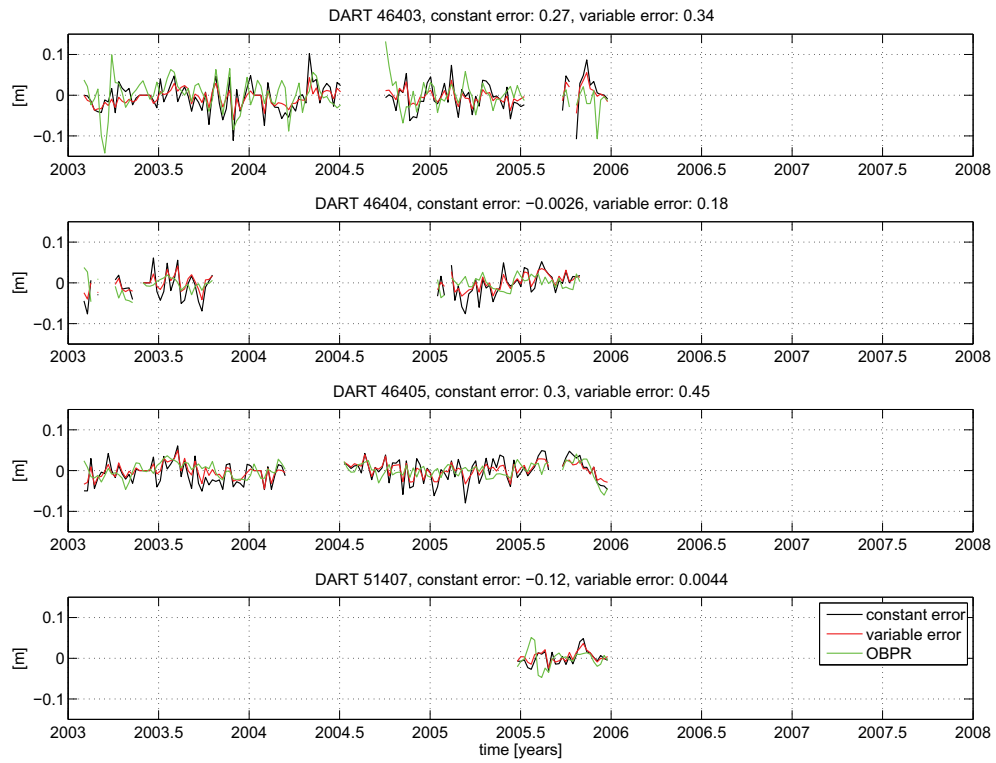
## D. COMPARISON OF TIME SERIES FROM OBPR AND INVERSE SOLUTIONS 158



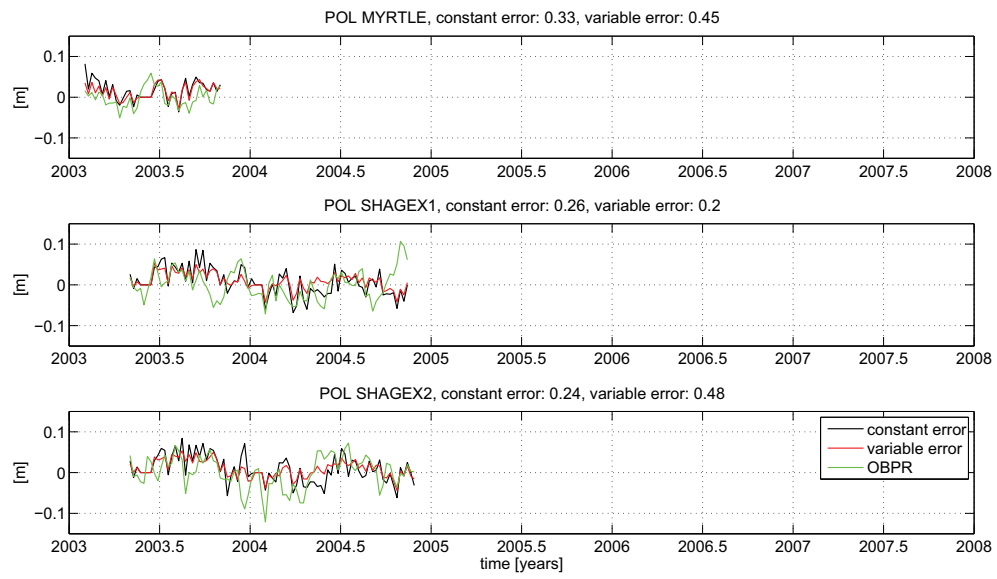
## D. COMPARISON OF TIME SERIES FROM OBPR AND INVERSE SOLUTIONS 159



## D. COMPARISON OF TIME SERIES FROM OBPR AND INVERSE SOLUTIONS 160

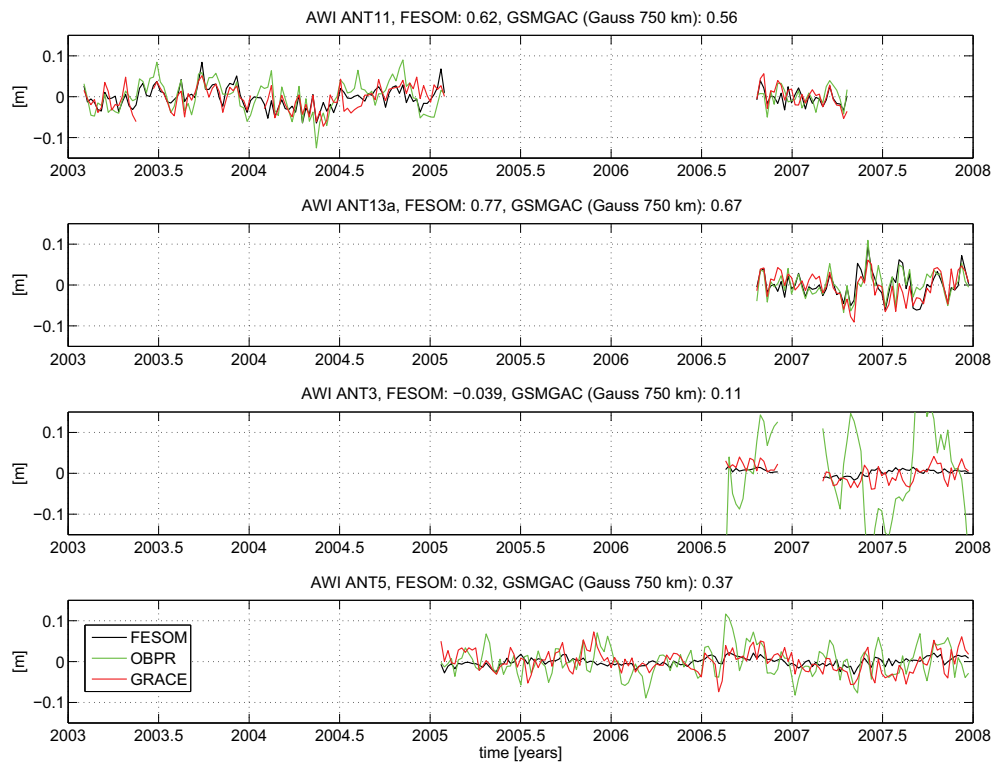


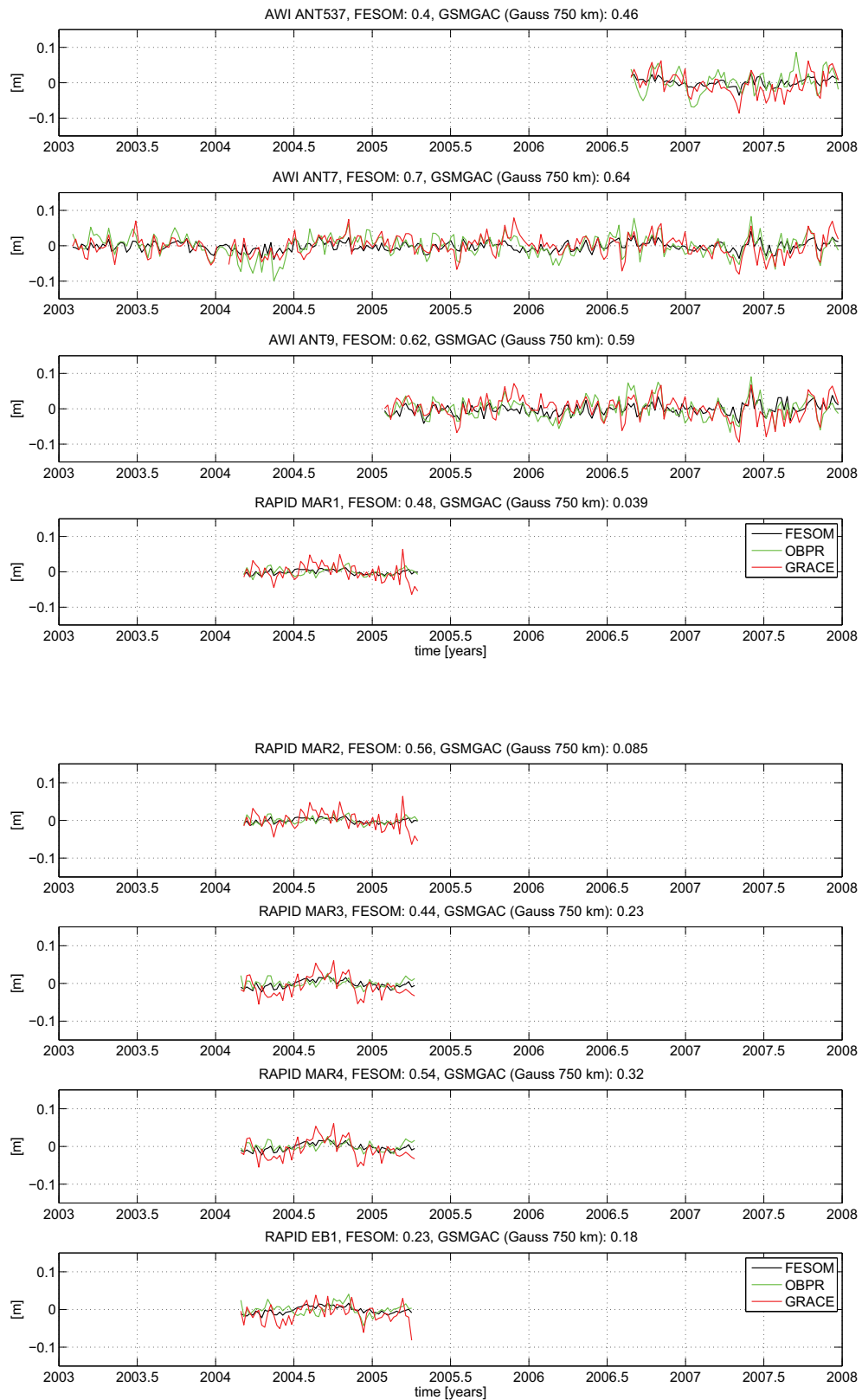
## D. COMPARISON OF TIME SERIES FROM OBPR AND INVERSE SOLUTIONS 161

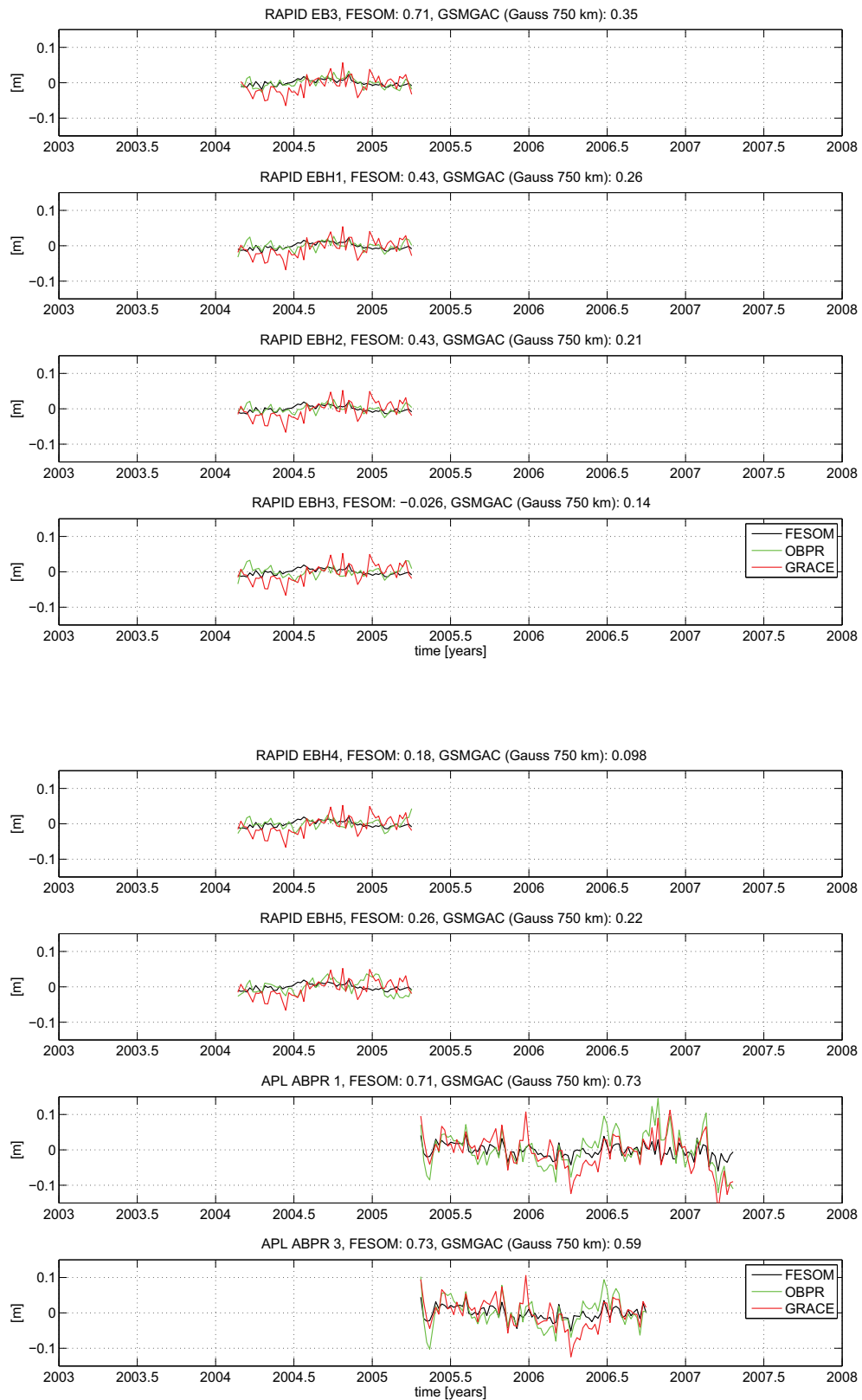


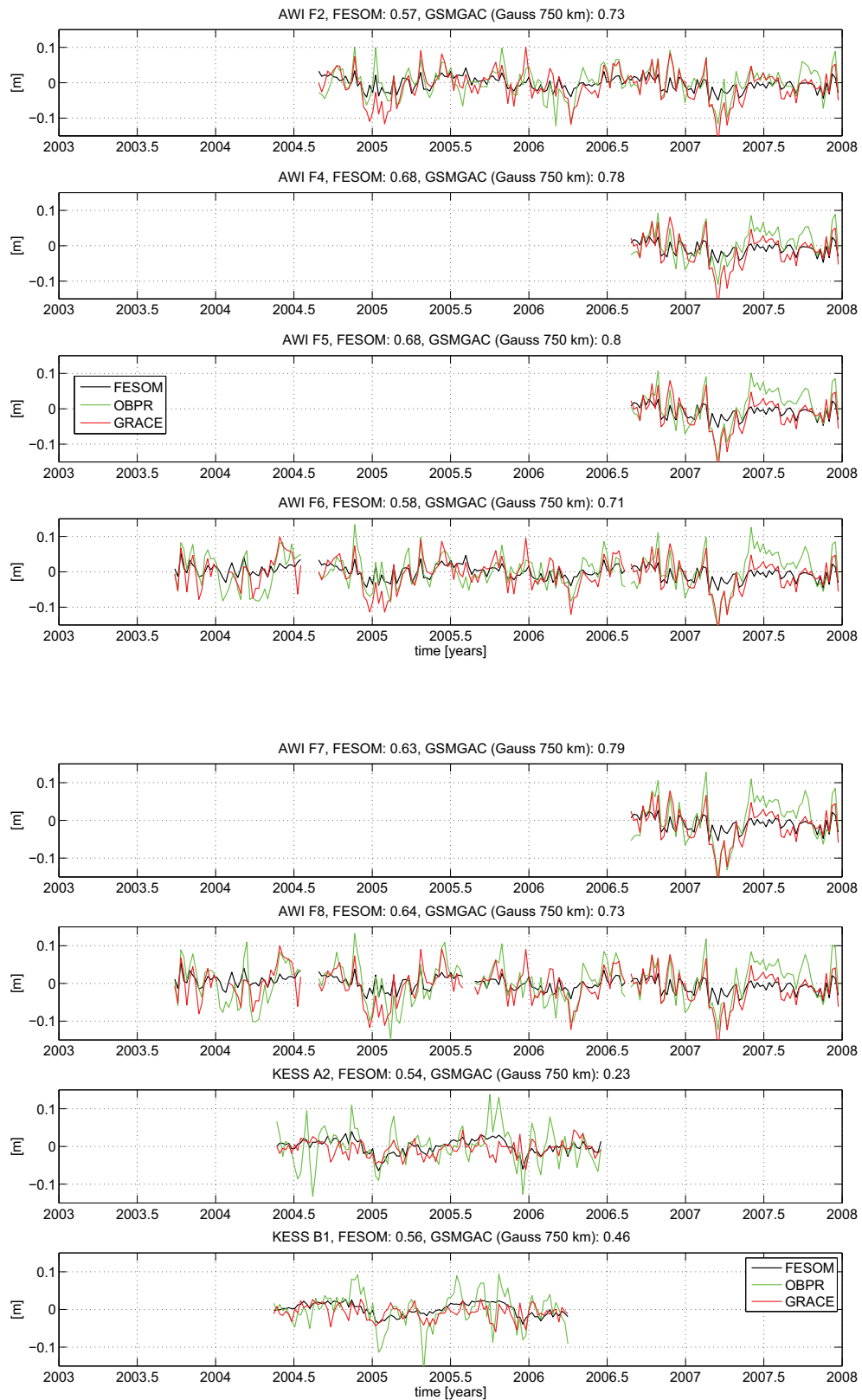
## E Comparison of time series from OBPR and GRACE Solutions

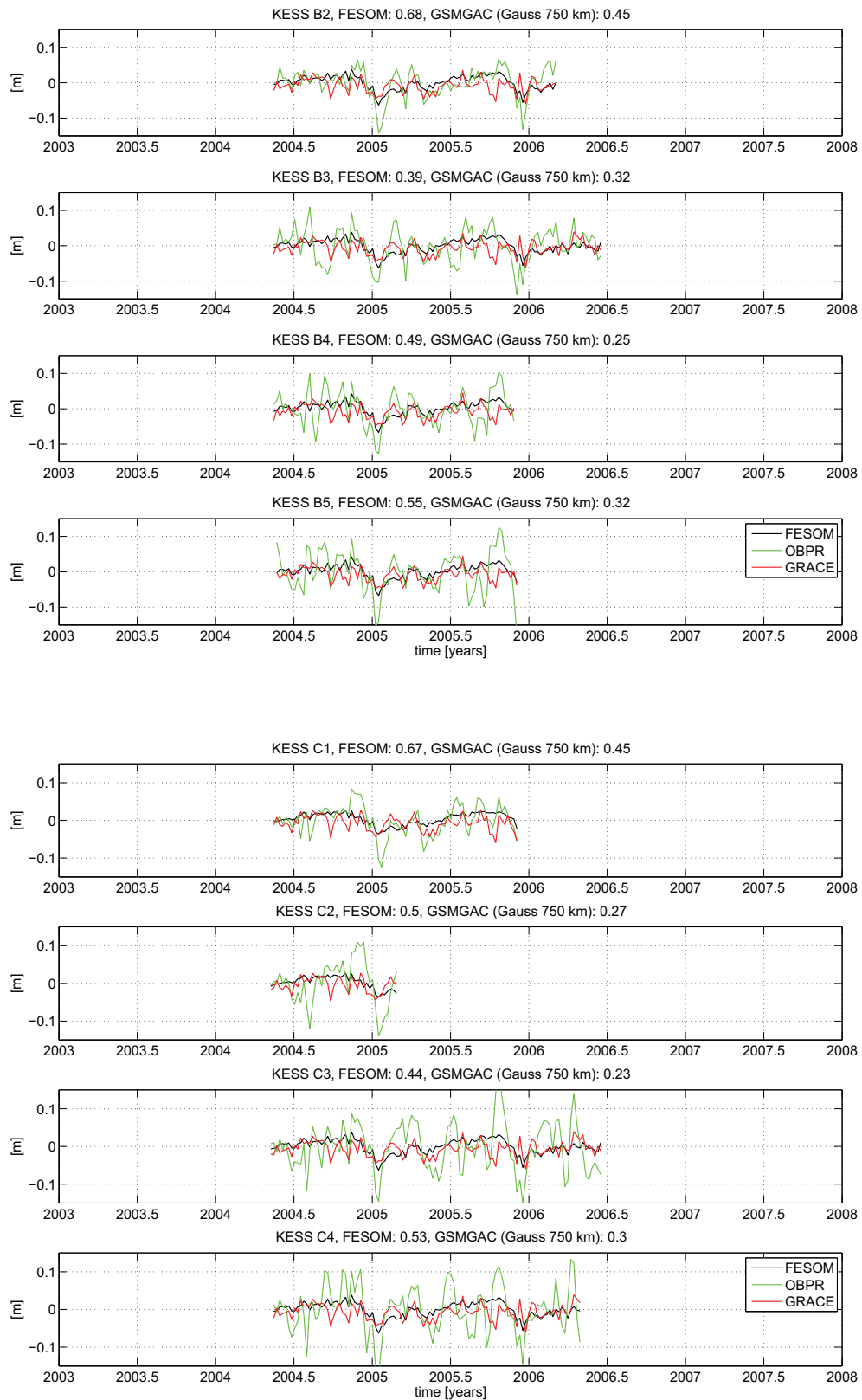
In the following all OBPR time series, which are longer than 20 weeks, are compared with time series of the GRACE solutions from GFZ (RL04) and modeled OBP (NCEP forcing). The GRACE solutions (GSMGAC) are filtered with a Gauss filter (radius: 750 km). In the title the location and the correlation of the GRACE solutions as well as the FESOM solution and OBPR are shown. As the weekly GRACE solutions have data gaps, only modeled OBP are taken into account for the weeks where also GRACE solutions are available. To avoid distortions from the estimates of the first weeks, the GRACE solutions of the weeks 1200 to 1203, if present in the OBPR time series, are not taken into account when computing the correlation.

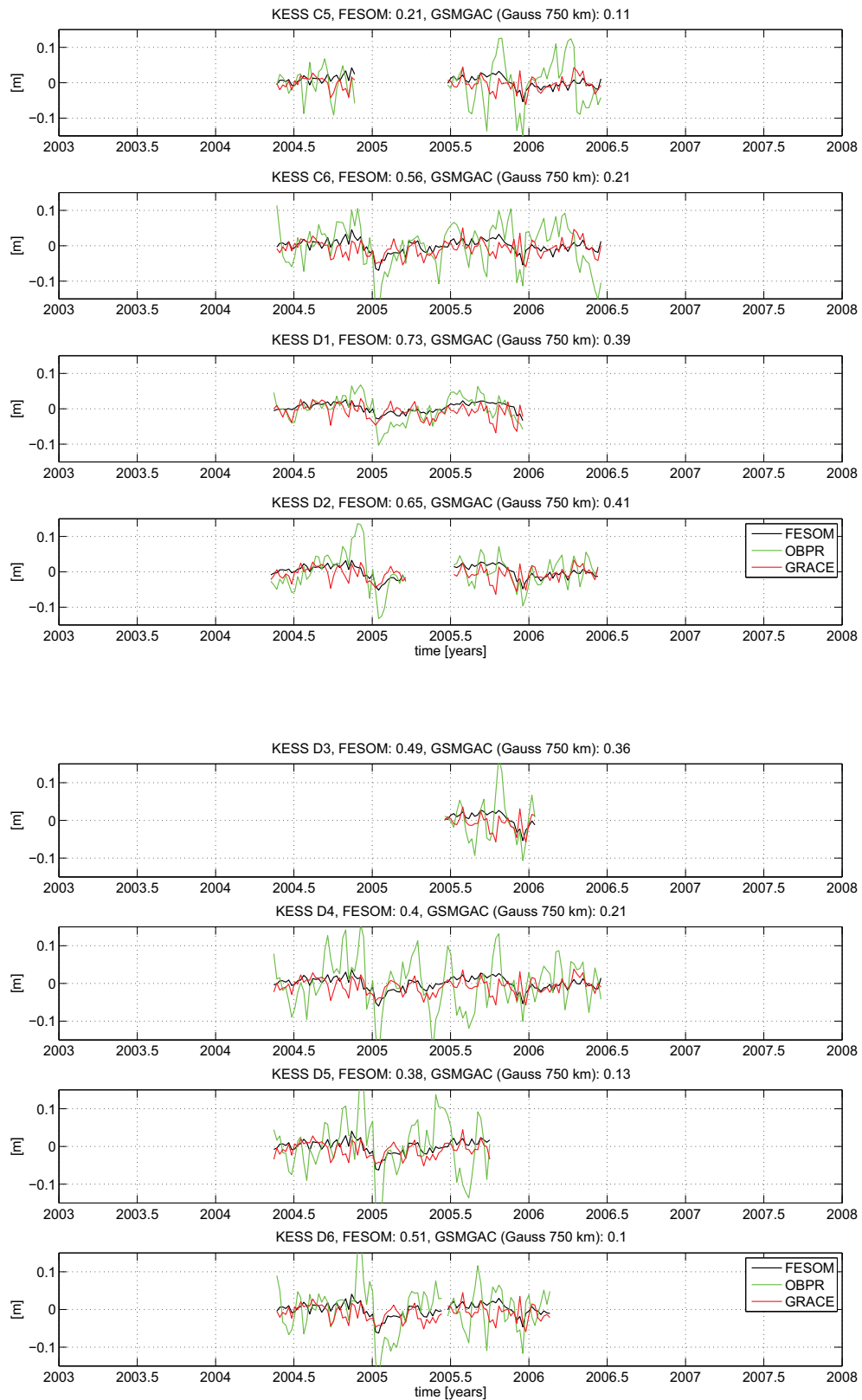


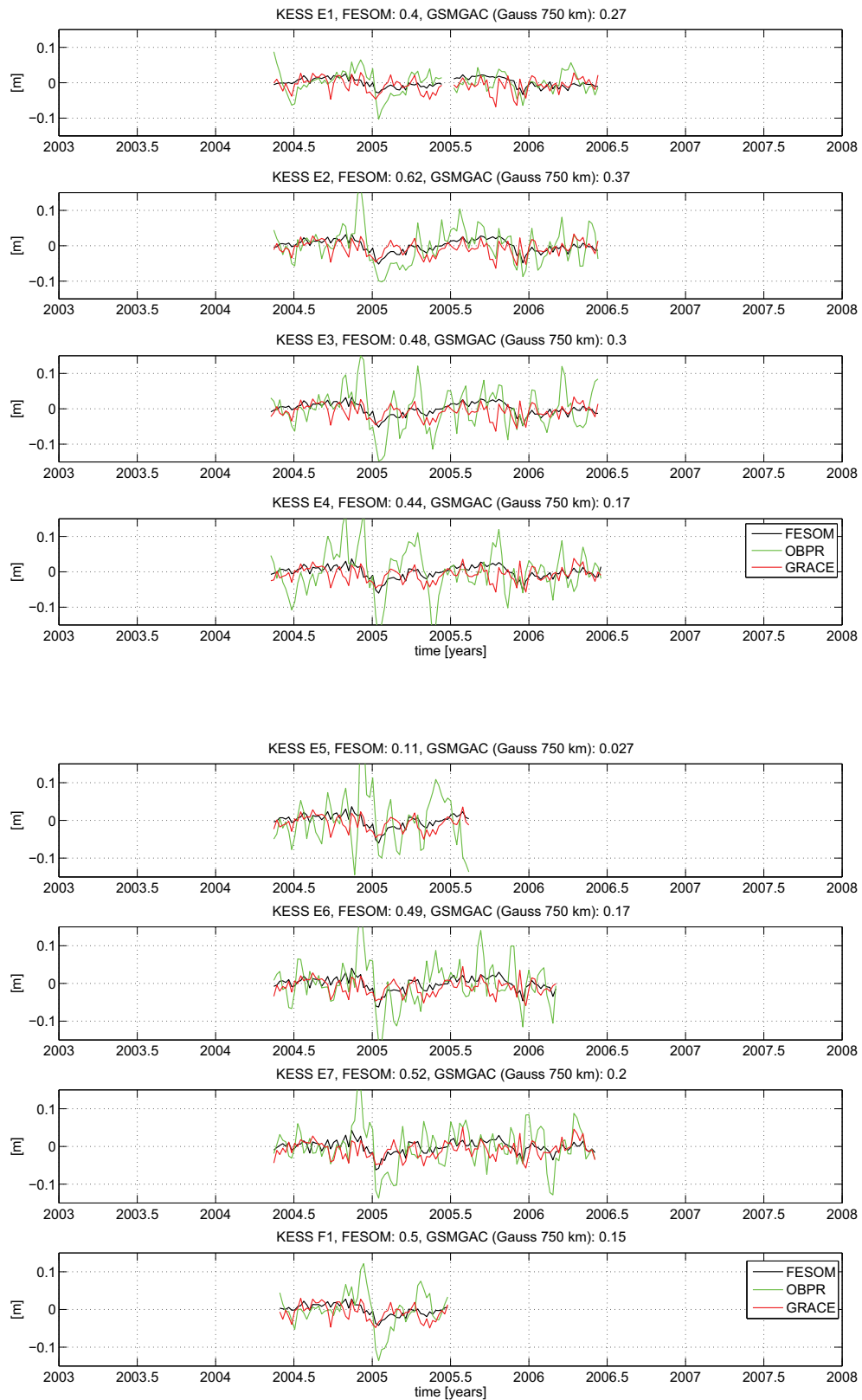


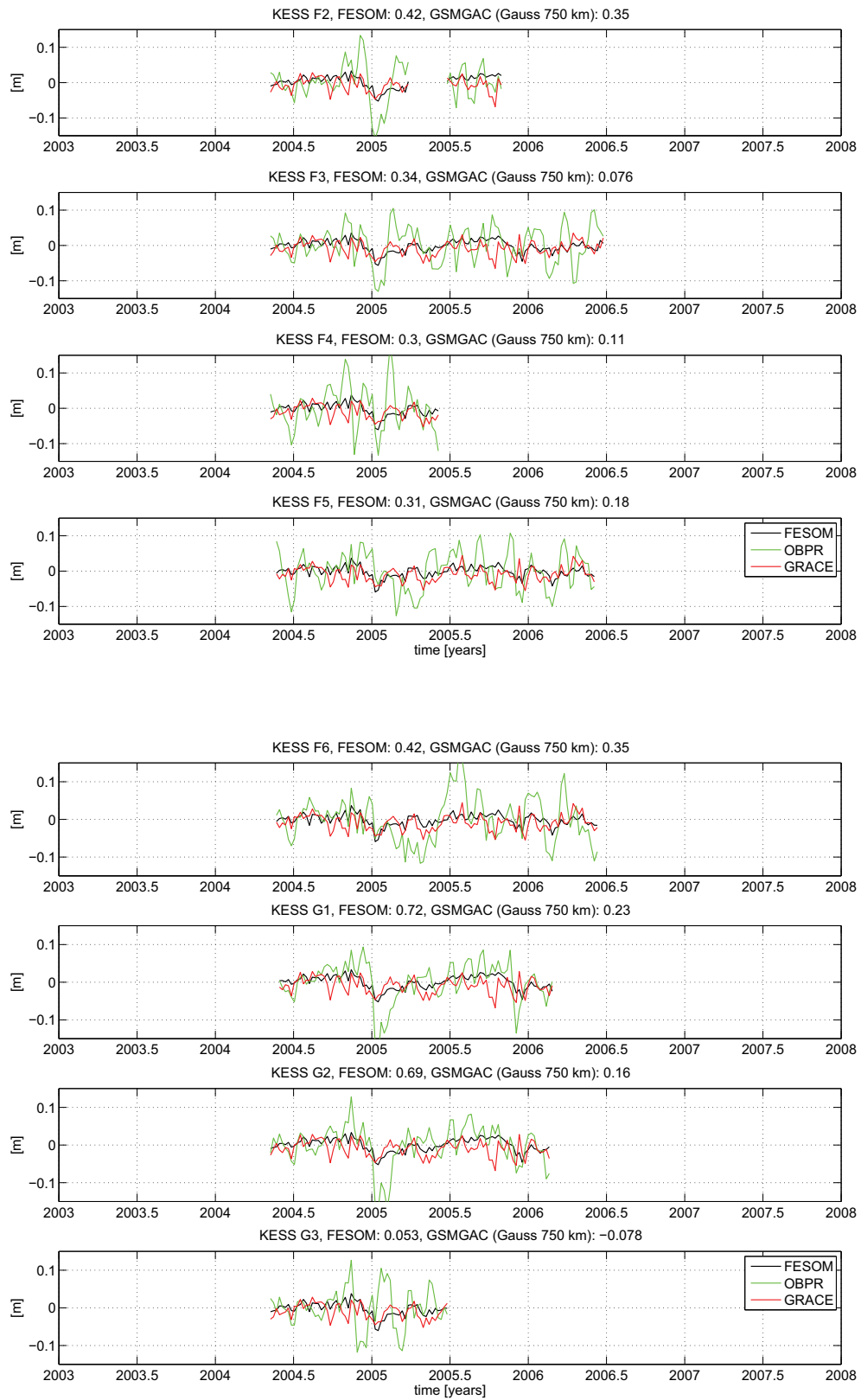


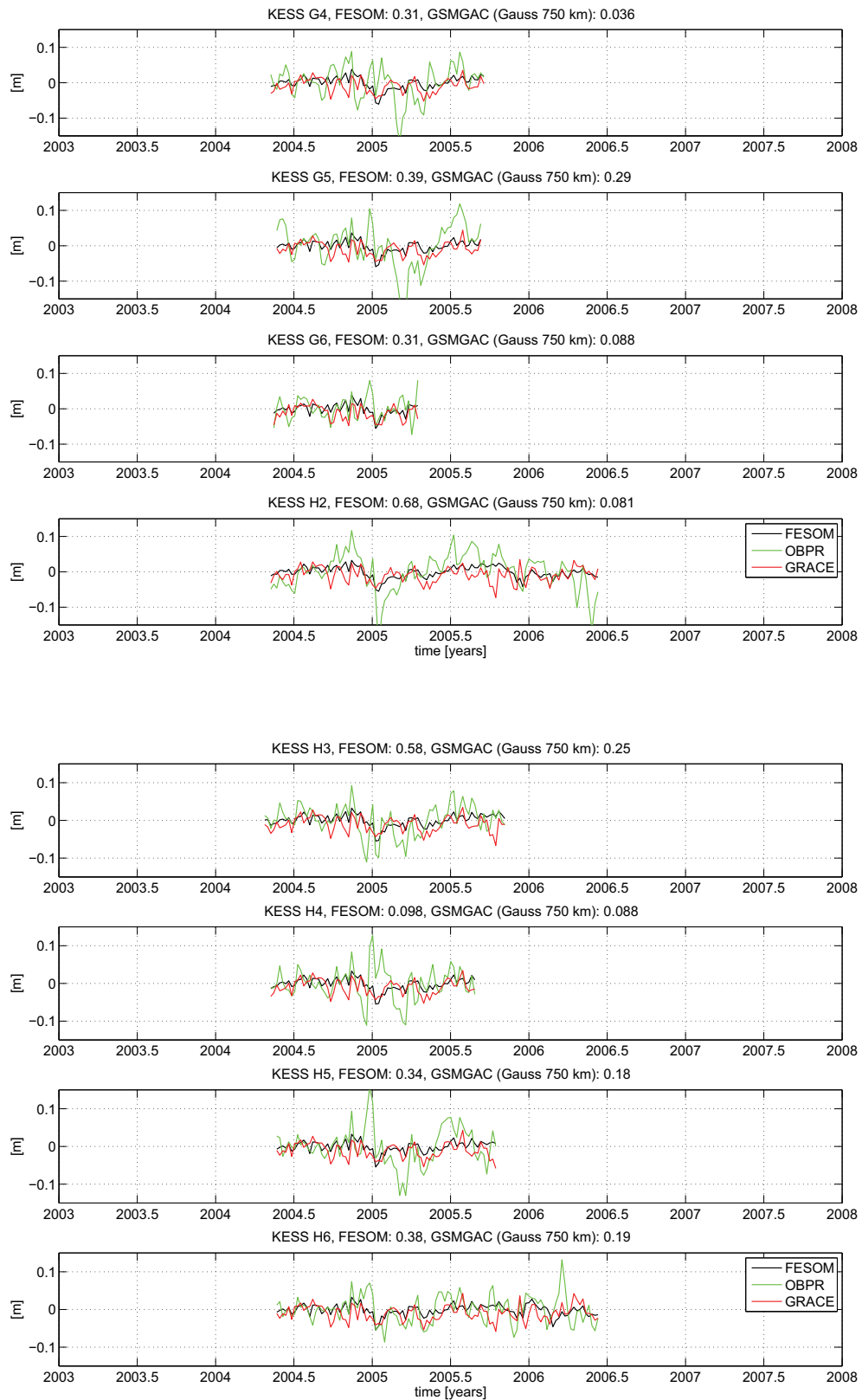


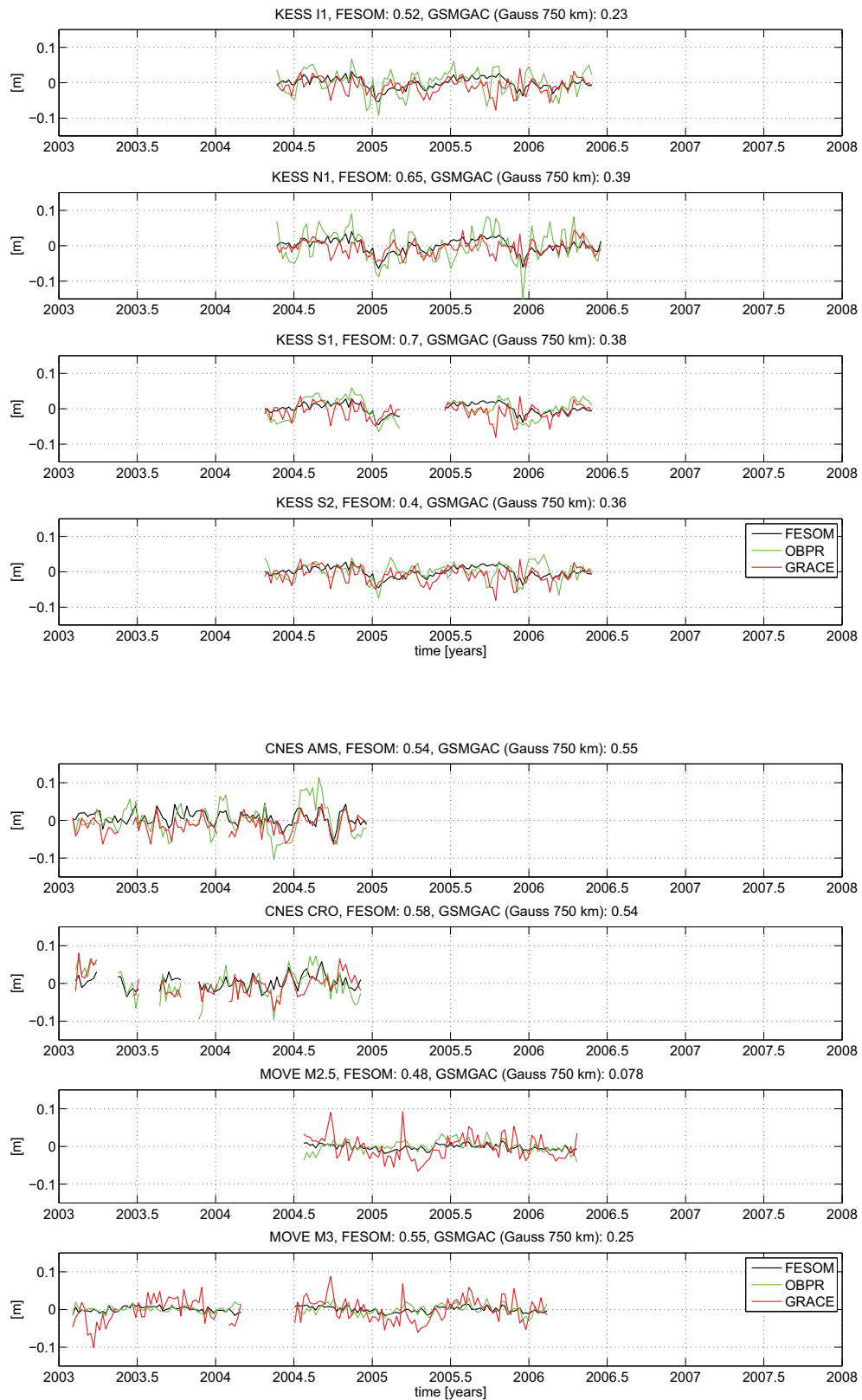


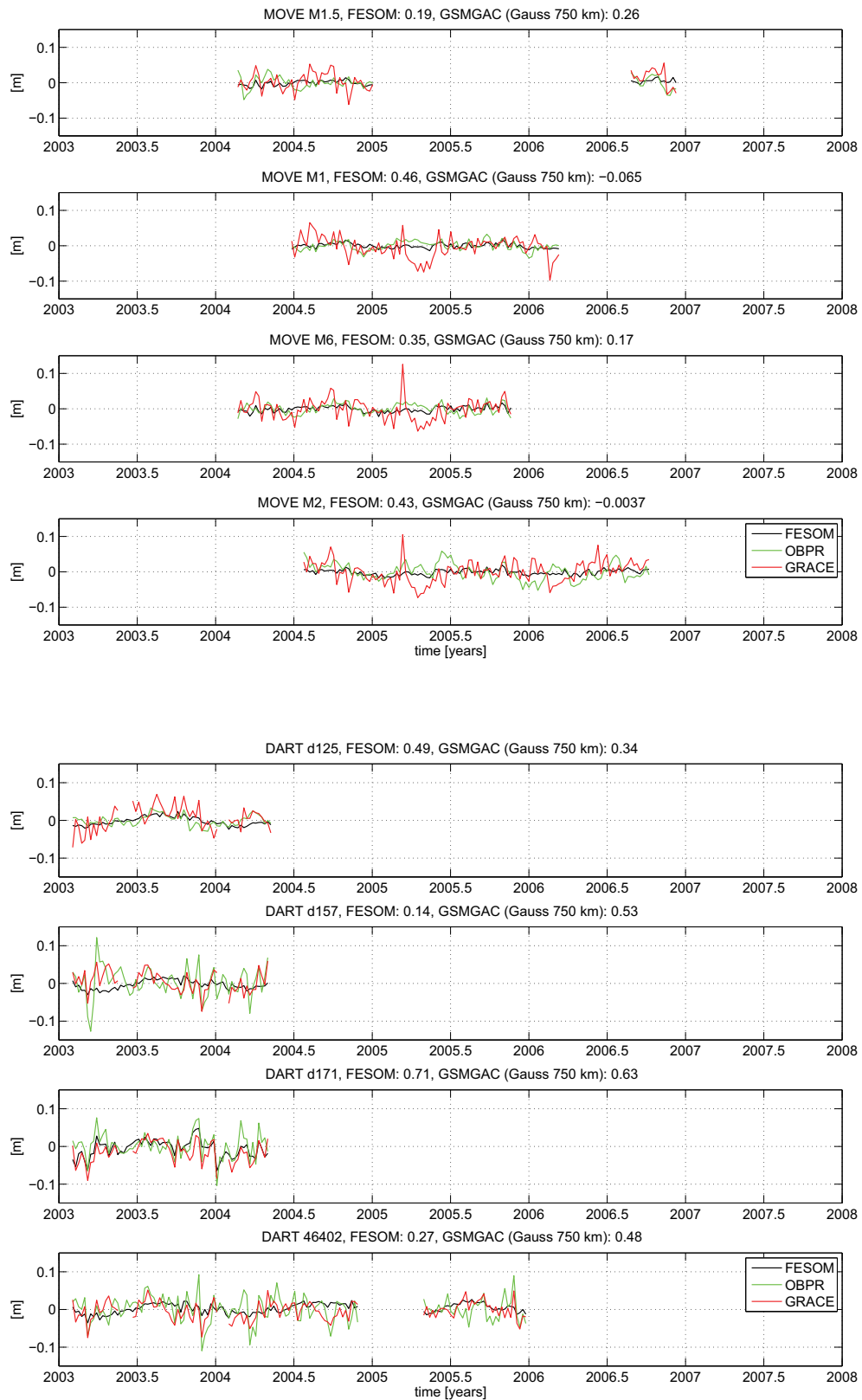


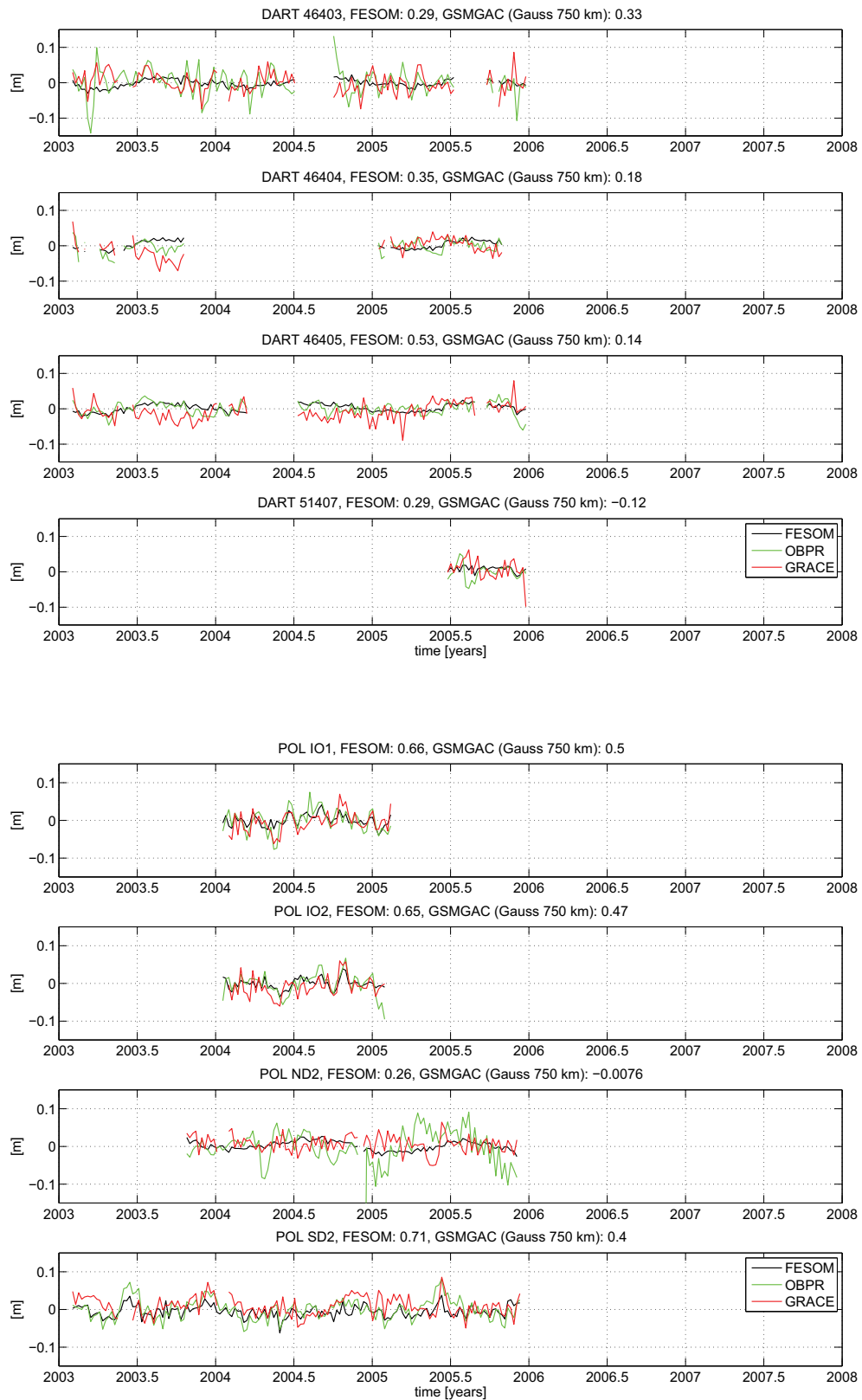


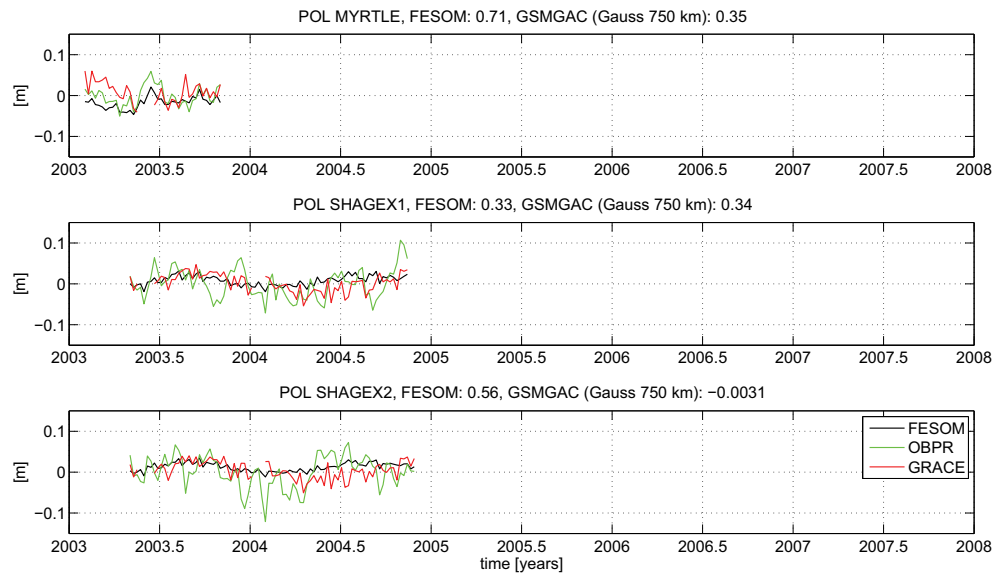






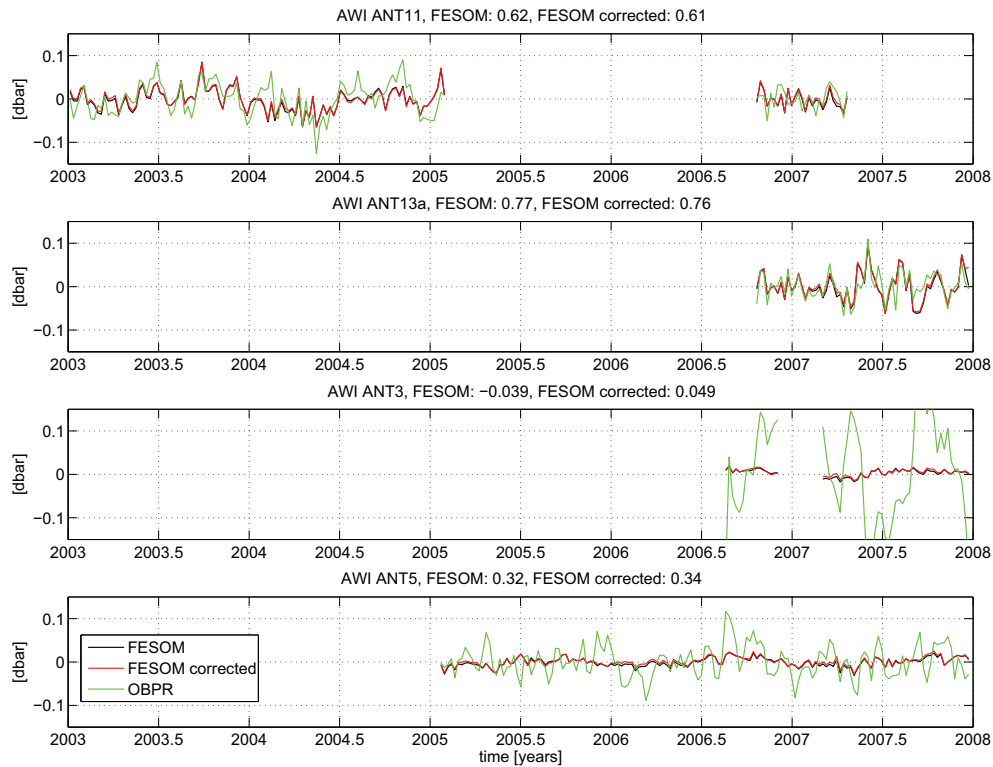




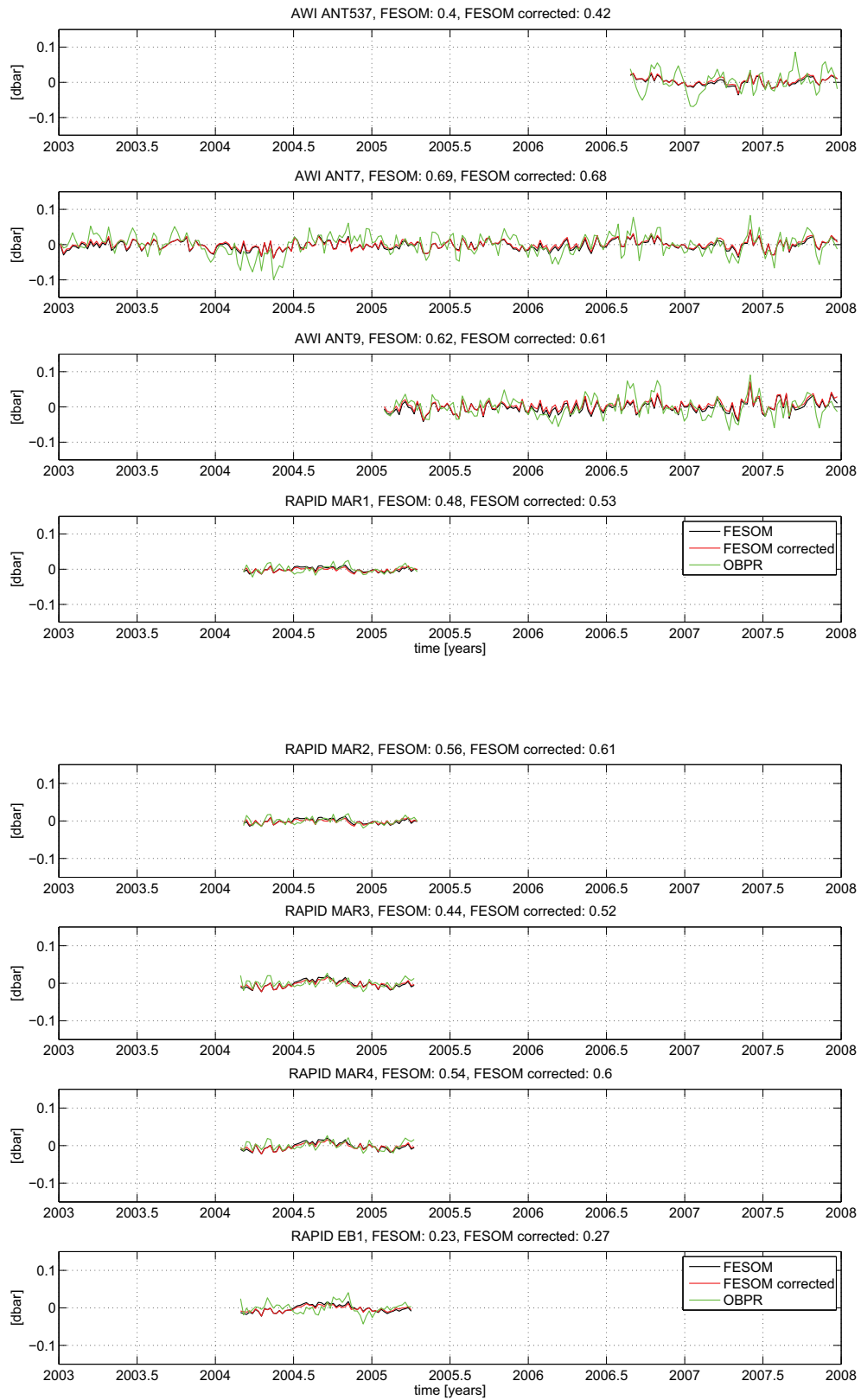


## F Comparison of time series from OBPR and corrected FESOM

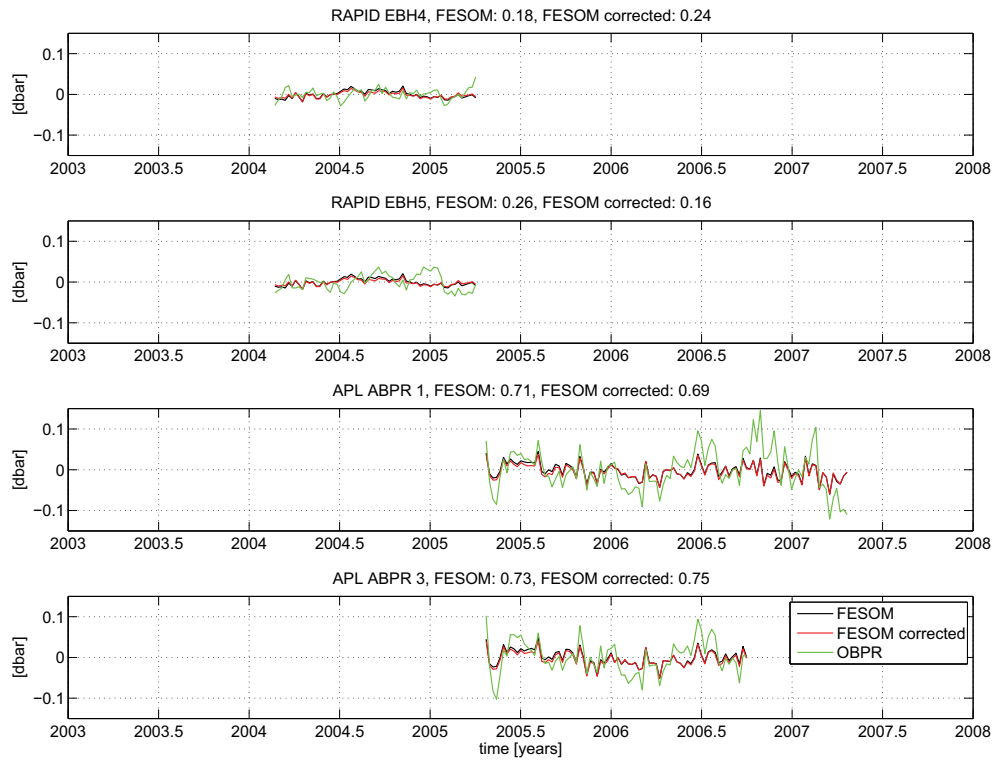
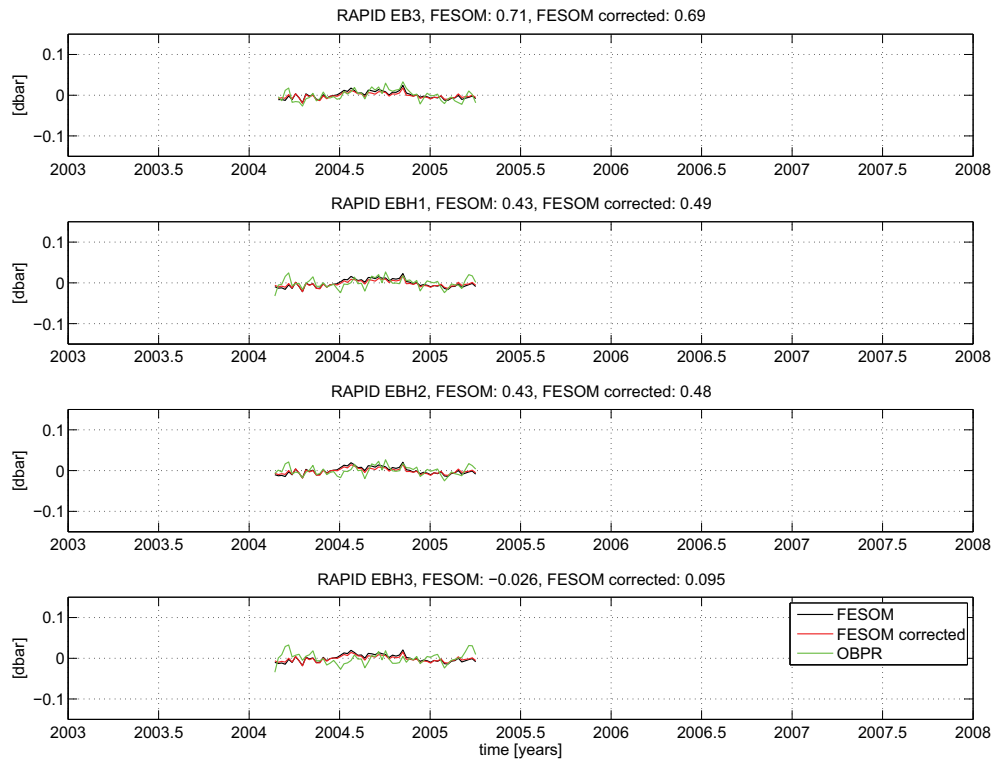
In the following all OBPR time series, which are longer than 20 weeks, are compared with time series and modeled OBP (NCAR/NCEP forcing), where the fresh water budget is corrected according to the mass correction term of the inverse solution (including the error of modeled OBP). In the title the location and the correlation of the FESOM solutions and OBPR are shown. The mass correction term of the first weeks are not used (weeks 1200 to 1203). Here, systematic differences occurred, as GRACE solutions, used in the inversion, are generated using only low amount of raw data. Therefore, the solutions of these time period are not trusted.



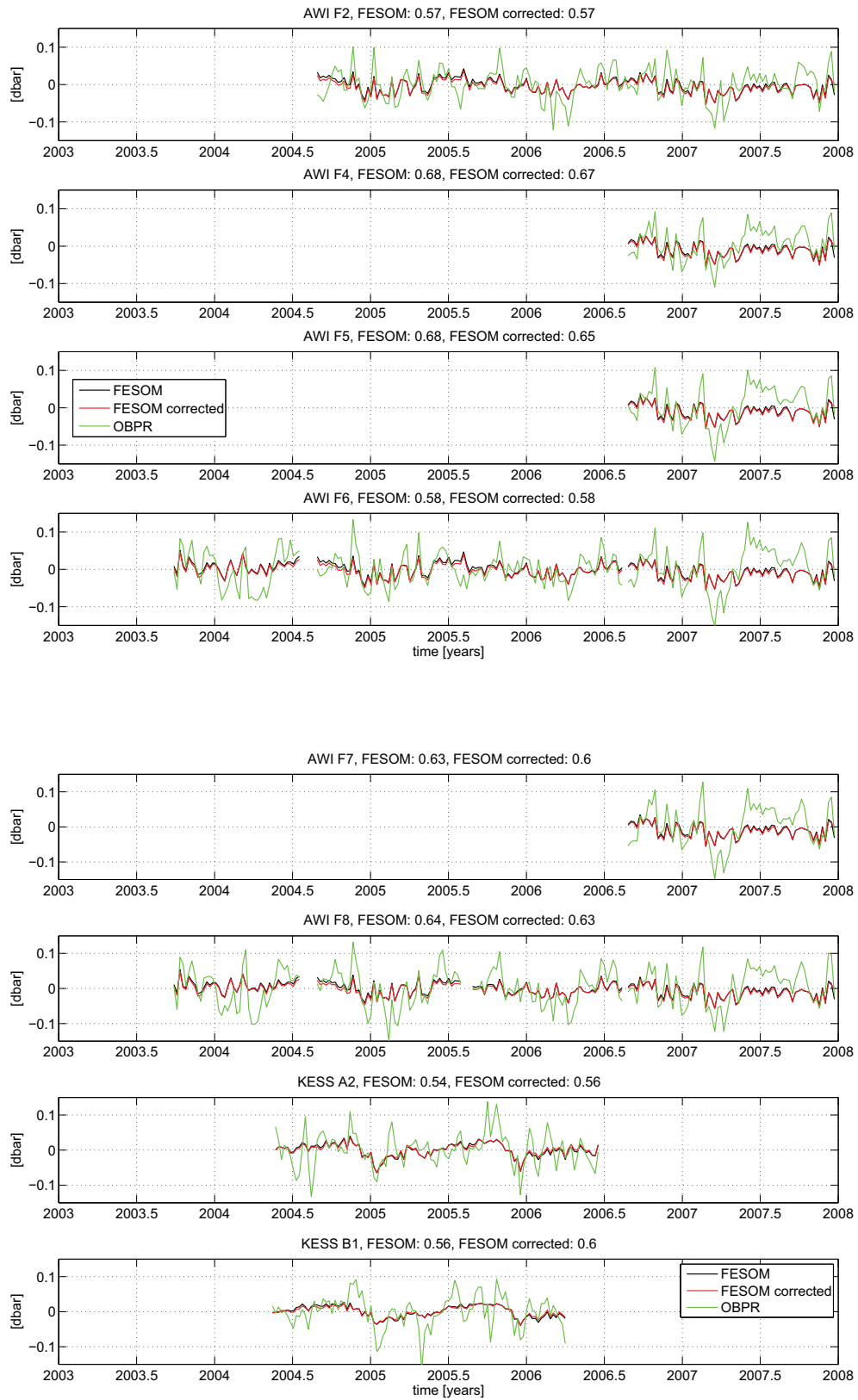
## F. COMPARISON OF TIME SERIES FROM OBPR AND CORRECTED FESOM 176



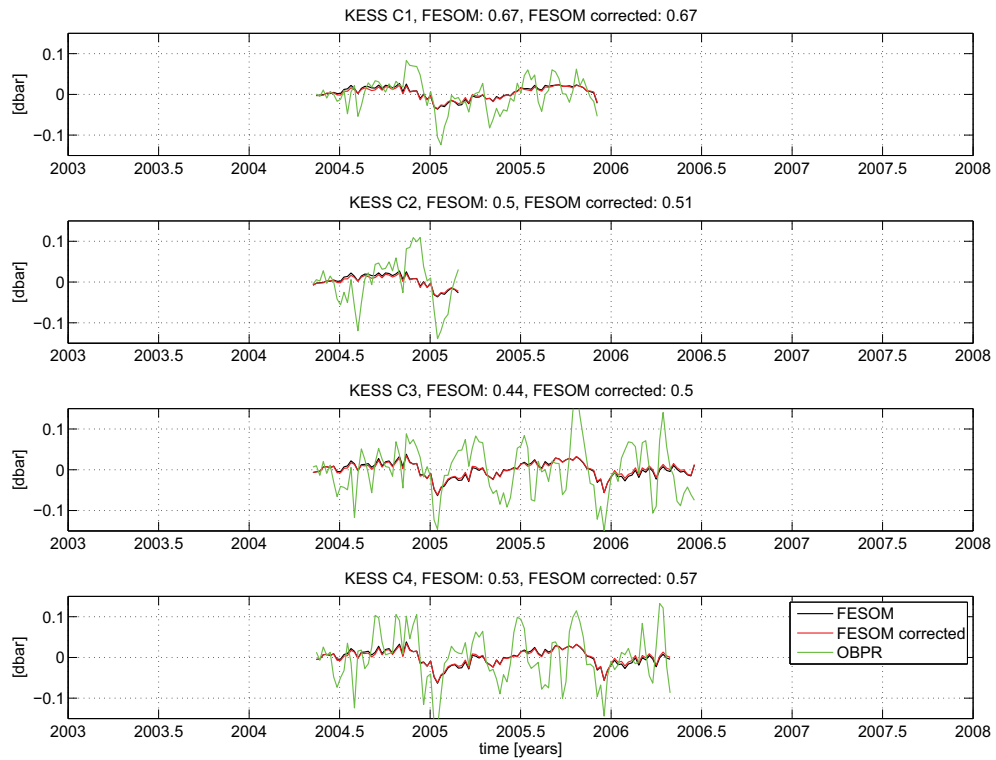
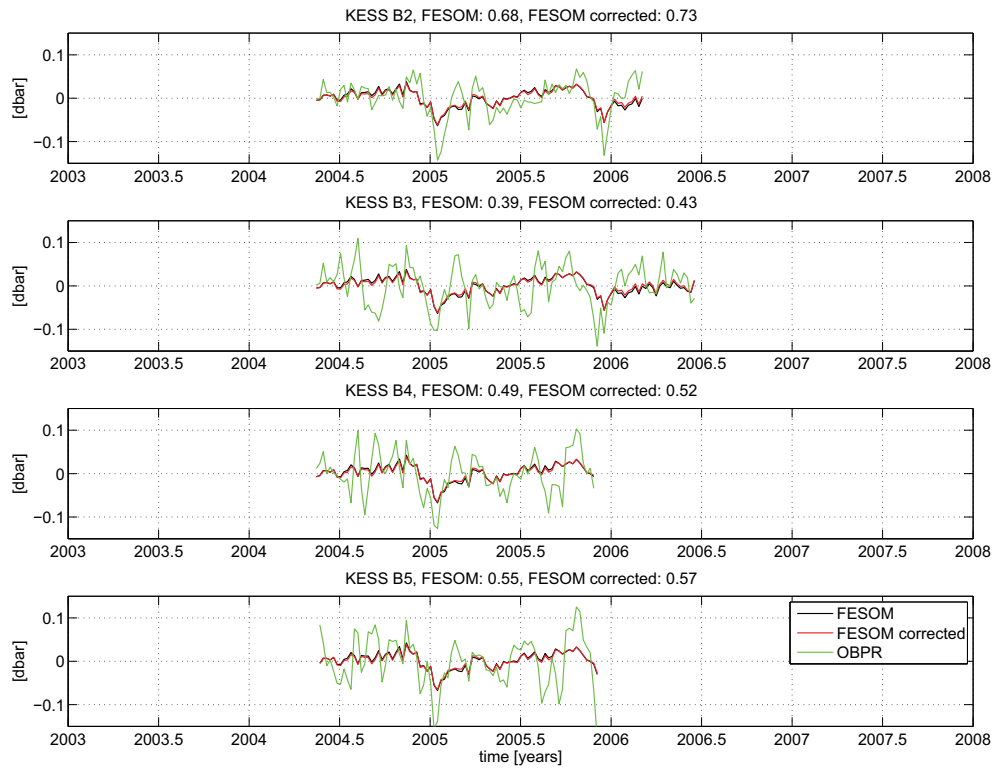
## F. COMPARISON OF TIME SERIES FROM OBPR AND CORRECTED FESOM 177



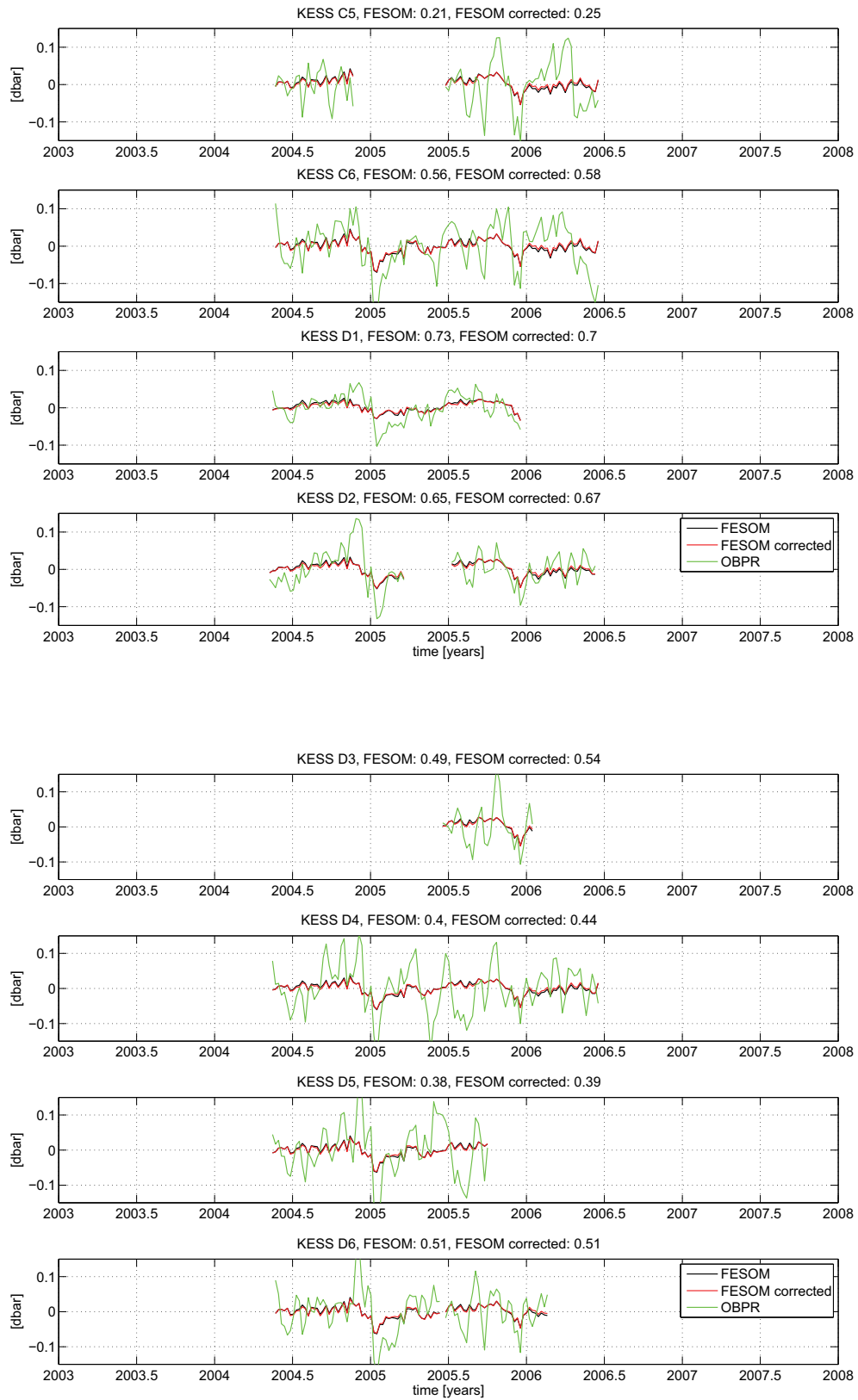
## F. COMPARISON OF TIME SERIES FROM OBPR AND CORRECTED FESOM 178



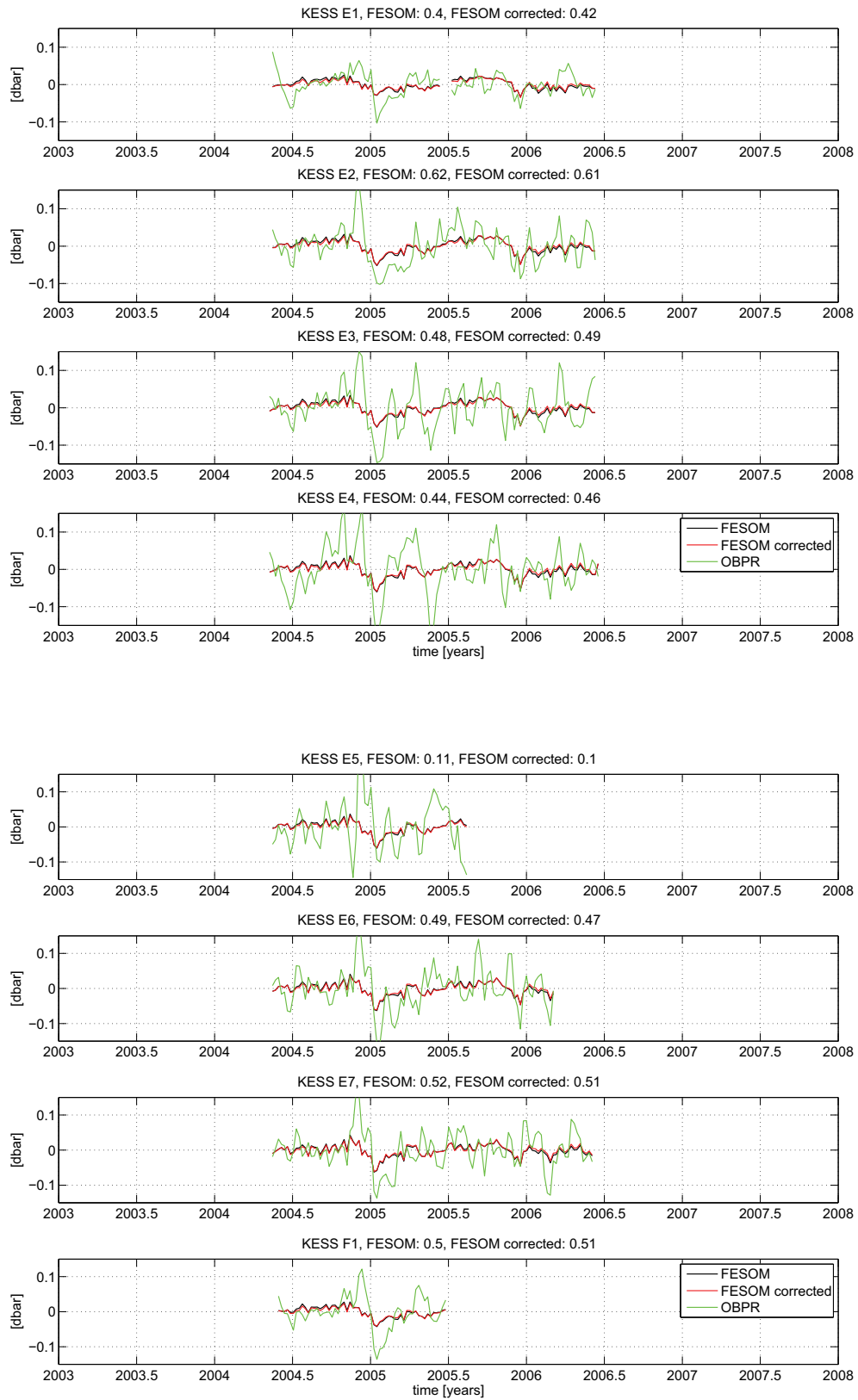
## F. COMPARISON OF TIME SERIES FROM OBPR AND CORRECTED FESOM 179



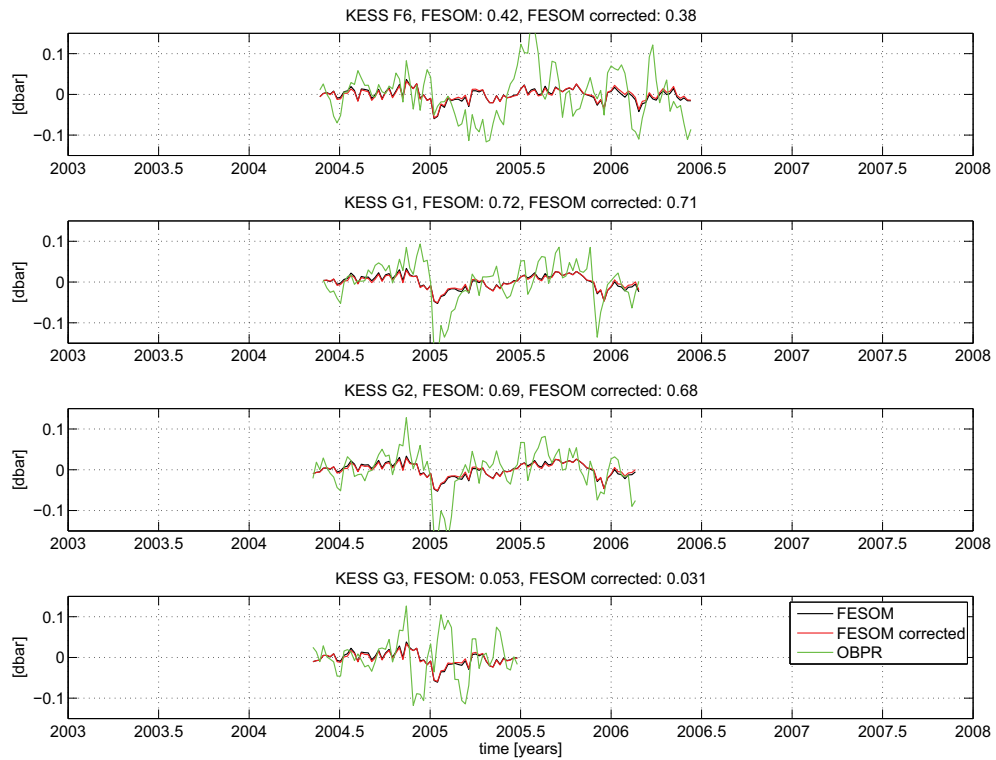
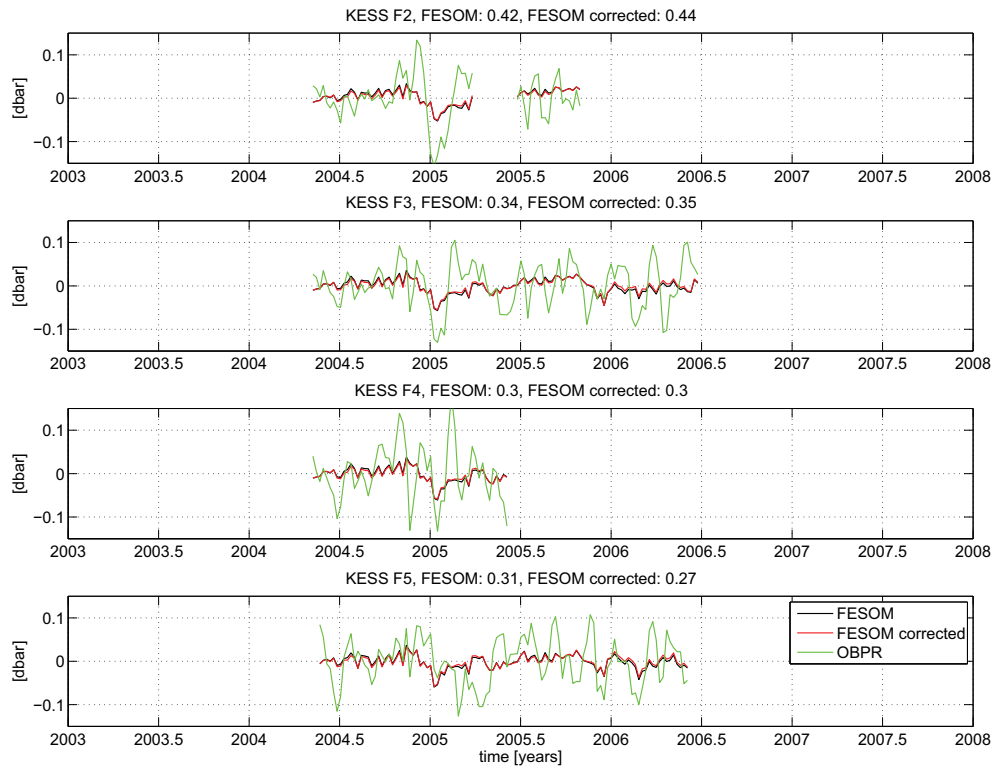
## F. COMPARISON OF TIME SERIES FROM OBPR AND CORRECTED FESOM 180



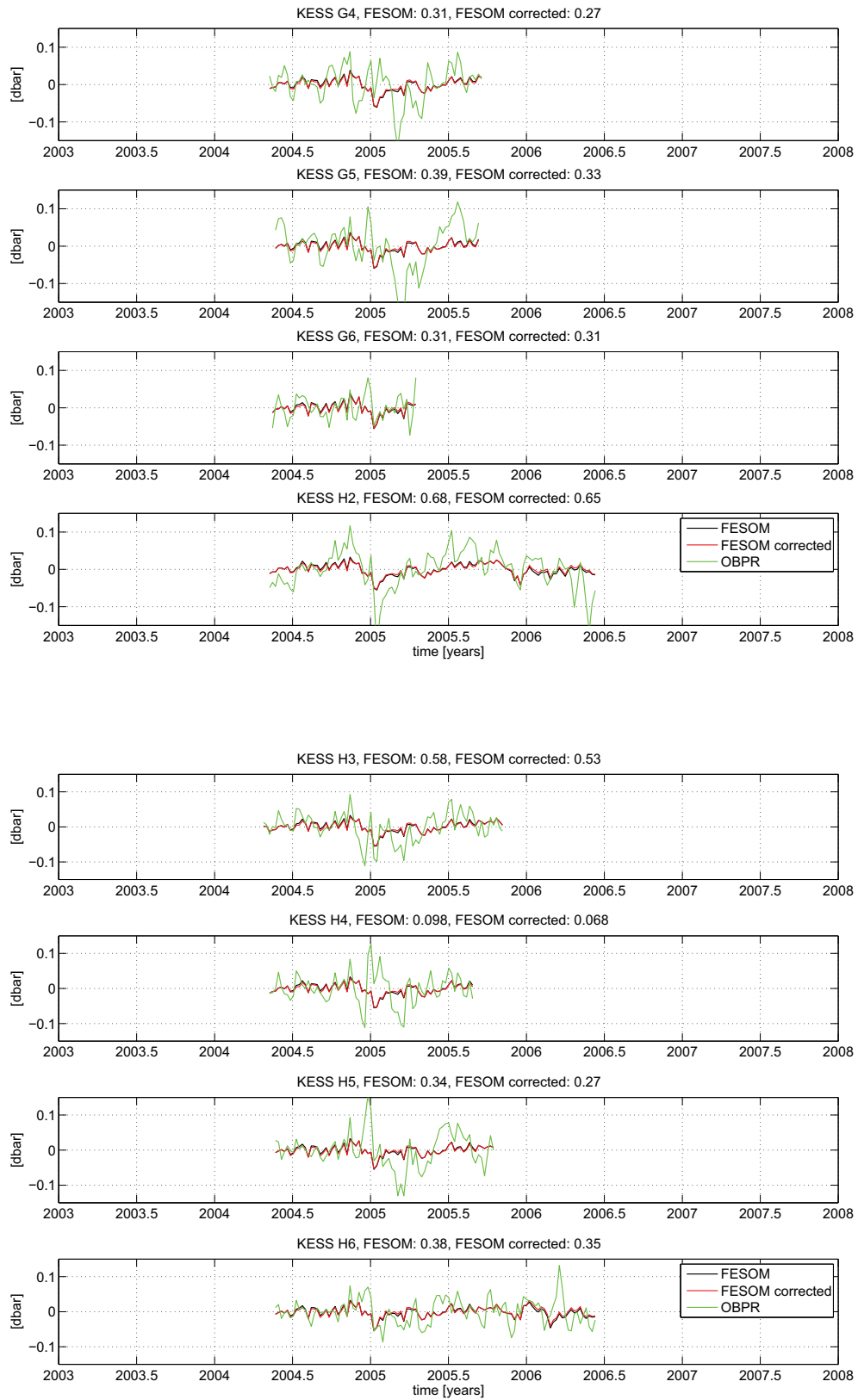
## F. COMPARISON OF TIME SERIES FROM OBPR AND CORRECTED FESOM 181



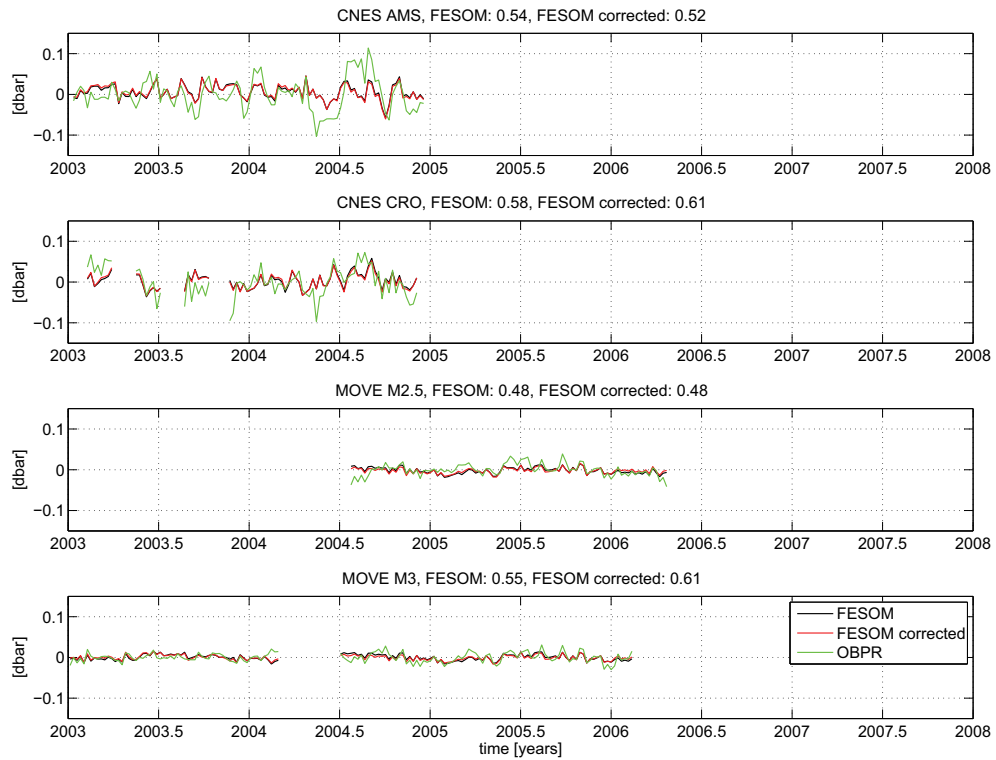
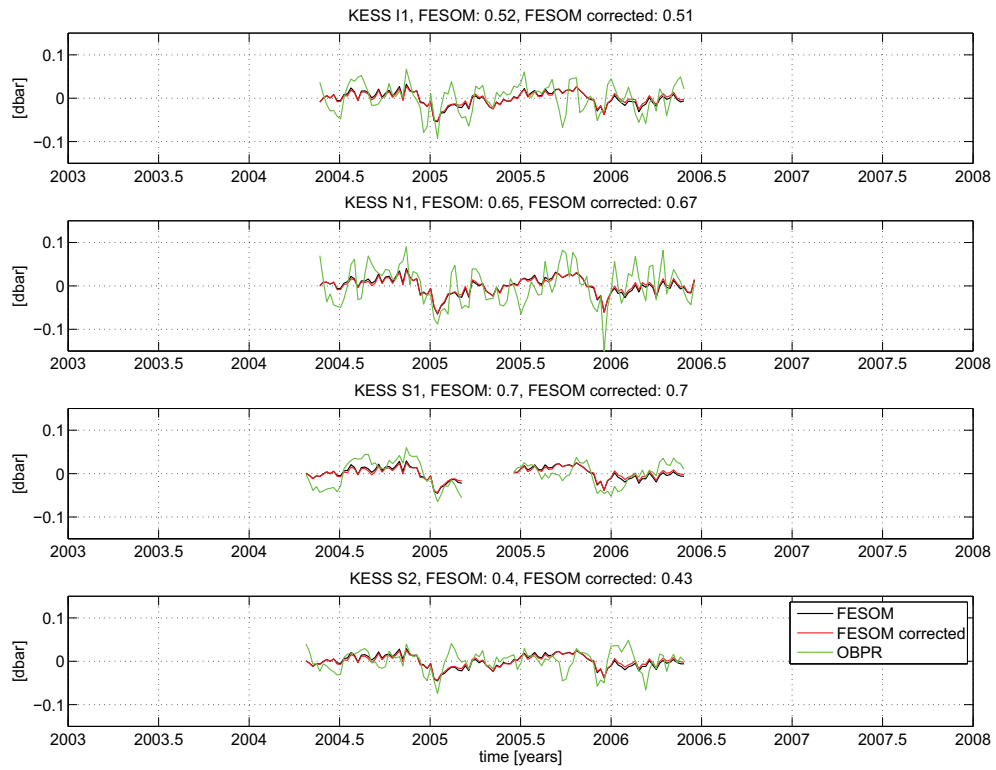
## F. COMPARISON OF TIME SERIES FROM OBPR AND CORRECTED FESOM 182



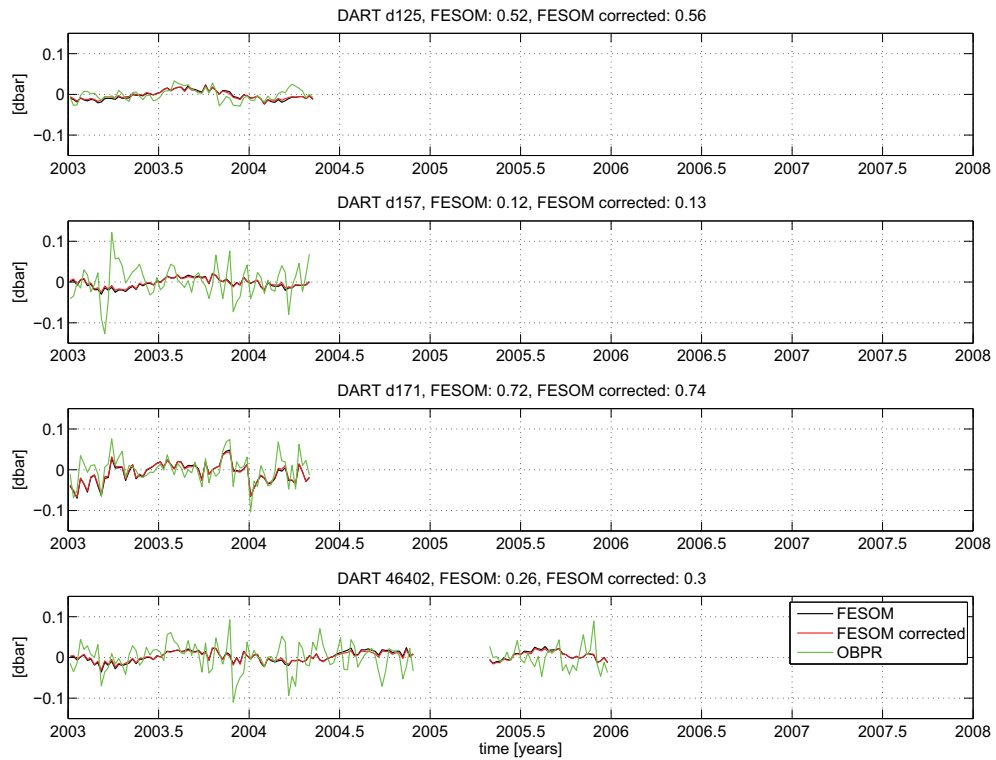
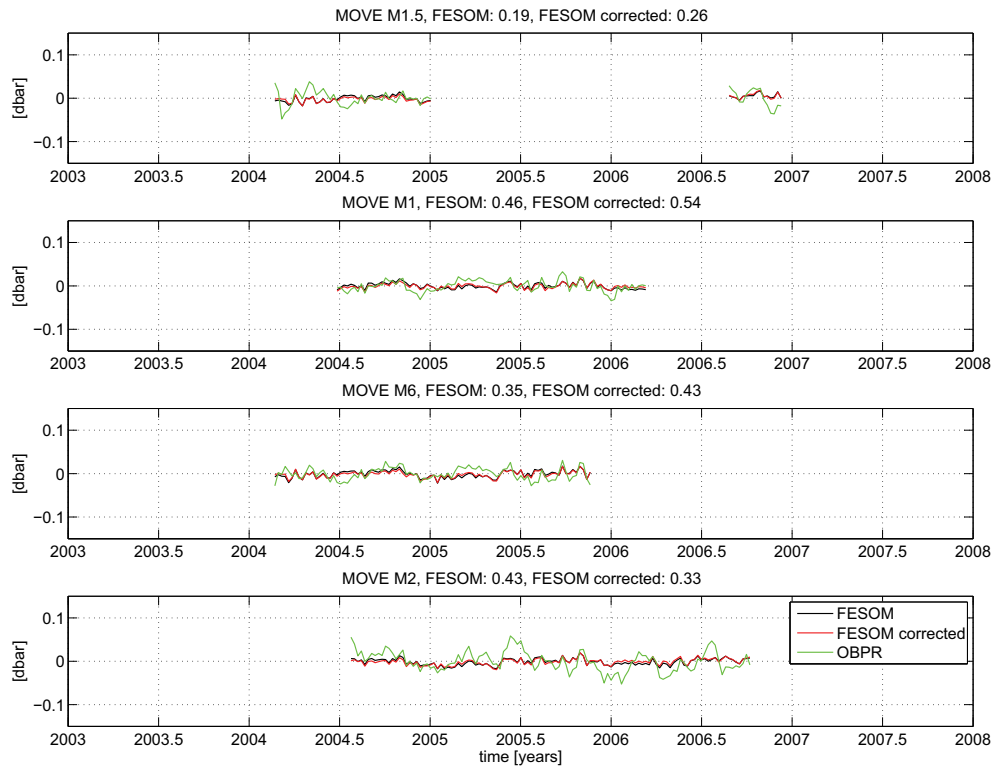
## F. COMPARISON OF TIME SERIES FROM OBPR AND CORRECTED FESOM 183



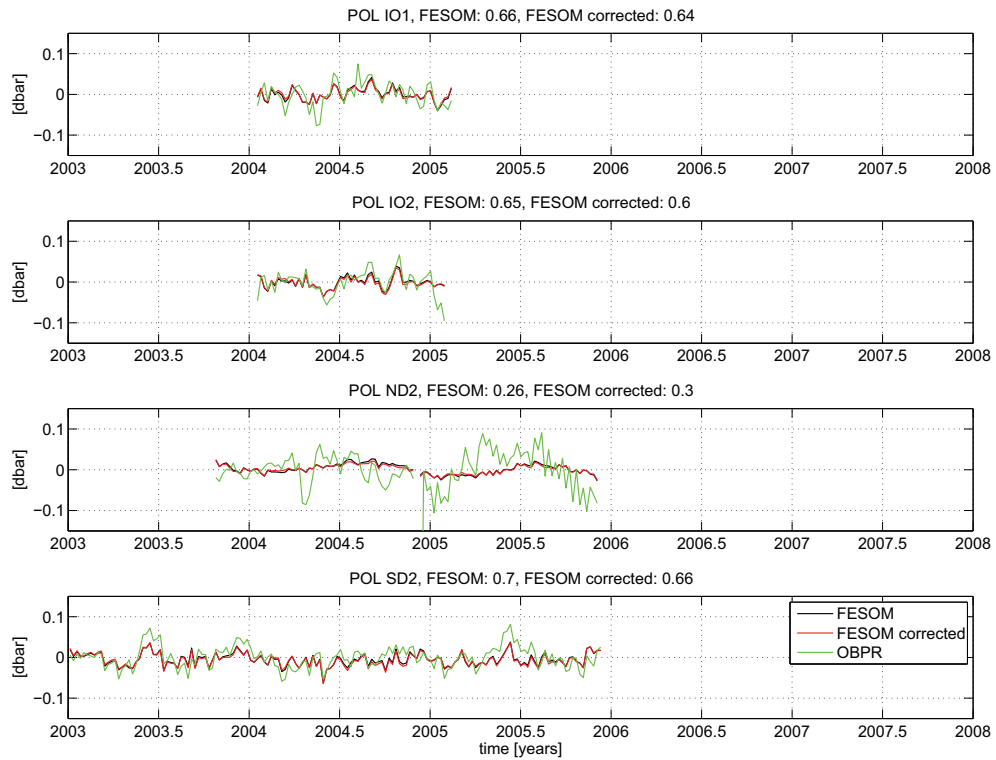
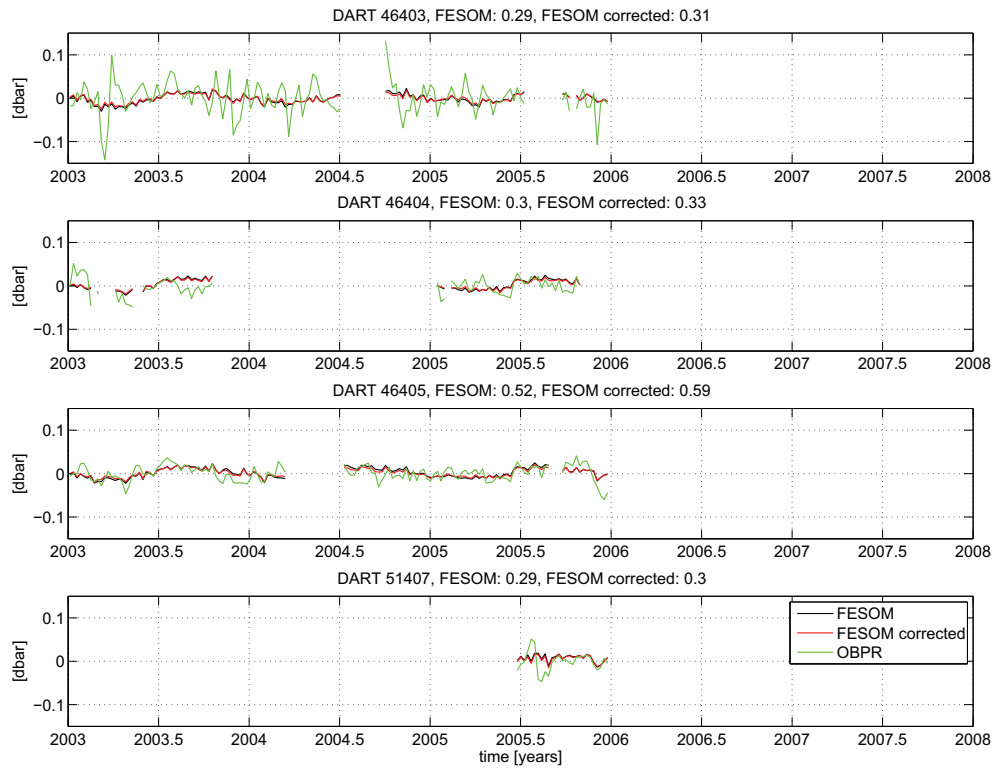
## F. COMPARISON OF TIME SERIES FROM OBPR AND CORRECTED FESOM 184



## F. COMPARISON OF TIME SERIES FROM OBPR AND CORRECTED FESOM 185



## F. COMPARISON OF TIME SERIES FROM OBPR AND CORRECTED FESOM 186



## F. COMPARISON OF TIME SERIES FROM OBPR AND CORRECTED FESOM 187

